THE MECHANISMS INVOLVED DURING THE DESATURATION PROCESS OF A POROUS MATRIX

BY

KURT J. SJOBLOM

B.S. GEOLOGY
STATE UNIVERSITY OF NEW YORK COLLEGE AT ONEONTA, 1987

M.S.E. CIVIL ENGINEERING
WEST VIRGINIA UNIVERSITY, 1994

SUBMITTED TO THE DEPARTMENT OF CIVIL AND ENVIRONMENTAL ENGINEERING IN PARTIAL FULFILLMENT OF THE REQUIREMENTS FOR THE DEGREE OF

DOCTOR OF PHILOSOPHY IN GEOTECHNICAL ENGINEERING
AT THE
MASSACHUSETTS INSTITUTE OF TECHNOLOGY

SEPTEMBER 2000

Signature of Author:____
Department of Civil and Environmental Engineering
June 30, 2000

Certified by:____
Dr. John T. Germaine
Principal Research Associate
Thesis Supervisor

Accepted by:____
Professor Daniele Veneziano
Professor of Civil and Environmental Engineering
Chairman, Departmental Committee on Graduate Studies

The Mechanisms Involved During the Desaturation Process of a Porous Matrix

By

Kurt J. Sjoblom

Submitted to the Department of Civil and Environmental Engineering in Partial Fulfillment of the Requirements for the Degree of
Doctor of Philosophy in Geotechnical Engineering, September 2000

Abstract

Traditionally, soil mechanics deals with soil in either of two states, saturated or dry. The effective stress concept proposed by Terzaghi has proven to be valid for soils in either of these states. However, when the water or air phase becomes large enough, the soil no longer behaves as two-phase system and the third phase must be considered.

Unsaturated soil behavior has been argued to be a function of negative pore pressure or matric suction. All the unsaturated soil behavioral issues contain a single underlying question; what is the *nature* of soil suction? Nature refers to the physical phenomenon that generates soil suction and changes with environmental factors. The goal of this work is to provide an understanding of the generation of soil suction.

Examining the drying process of porous material gave perspective into the development of negative pressures. The drying material was modeled by a regular packed matrix of equal diameter spheres. Configuring the water into the geometric shape of pendular rings simulated the water held in the matrix. A predictive model was then developed relating the water content of the matrix to the associated tension in the water.

The model was tested using a unique measurement technique to determine a continuous drying curve of a porous material. The technique required the development of a tensiometer capable of directly measuring the high negative pressures. Glass beads of narrow distribution provided insight into the behavior of the drying pendular rings. It was determined that the actual tension to initiate draining is much greater than that predicted by the largest pendular ring. This reduced size of ring was also observed by a series of photographs of drying spheres.

The information gained was then used to predict the tension of draining (or air entry pressure, AEP) for natural materials. Three types of soils were tested to validate this prediction. Finally, a literature search was done to obtain data for a wide variety of soils. The literature data provided a means to refine the prediction by relating the grain size distribution of the soil to the AEP.

Thesis Supervisor: Dr. John T. Germaine
Title: Principle Research Associate in Civil and Environmental Engineering

Acknowledgements

I would like to express my thanks and gratitude to the following people who during the course of my tenure at MIT contributed to my achievements;

Dr. John T. Germaine who served as my thesis supervisor, guidance counselor, professional advisor, friend and occasional sounding board for my complaints. Many, many thanks.

Professors Charles C. Ladd and Patricia J. Culligan who served on my committee and provided valuable assistance to the progress of this work.

Lt. Laurent (Larry) Levy who has played many roles; lab partner, labmate, officemate, traveling companion, housemate and best of friend. Your antics never cease to amaze me. Thanks for making this place bearable.

To Catalina Marulanda who provided an unending stream of support for all of my endeavors. Muchos gracias babe.

To Thomas (Tommy) Meyer, Dr. Greg Da Re and Dr. Douglas Cauble. Between the three of them, there was no problem, either academic or personal that could not be solved.

All of my officemates over the years, Sang Ratnam, Brad Ramsey, Lana Aref, Kortney Adams, Cathy Castenson, and Yogi Sanjay Pahuja. Thanks for the interesting conversations and advice.

Jorge Gonzalez, Frederico Pinto, Martin Neussbaumer, Professor Gouping Zhang, Erin Wood, Amy Varney, Alex Liakos, Hannes Lagger and Rami Tawil. An assorted band of castaways that provided me with good humor.

To my fellow Mac users, Carolyn Jundzilo and Alice Kalemkiarian both would go out of their way to help me.

To my housemates and friends Adam, Abigail, Sara, John, Tom, Ken, and Vivi. I only have good memories from you all.

To the only **true** Yankees I know, Stephen and Arthur Rudolph. Both provided outstanding mechanical advice and good-natured joking that remains one of the high points of my time here.

To all Dirtballs.

To all of my friends back home, their wives and families who over the years supported me by taking me to Red Sox games, opening their homes for me to stay and eat, and most importantly, never allowing me to pay for drinks. I hope I can repay.

Finally to my family. Dad, Mom, Nonnie, Don and Ares. Their strength and unwavering support are the only reason that I strived to excel.

For Nonnie

Table of Contents

Table of Figures

Table of Tables

Chapter 1 Introduction

1.1 Unsaturated Soil Mechanics

Traditionally, soil mechanics deals with soil in either of two states, fully saturated or completely dry. These two cases simplify the pore structure of the soil by elimination of one phase, either air or water. The effective stress concept put forth by Terzaghi in the early part of the 20th century has proven to be a valid stress state variable for soils in either of the above states. The effective stress concept has also been shown to work well for soils with either very high or very low degrees of saturation (Lambe and Whitman 1969). Although these soils may in fact contain three phases of state, (solid, water and air) the fraction of either the air or water is so small that its' effect on the overall soil behavior can be negligible.

However, when the water or air phase becomes large enough, the soil no longer behaves as two-phase system and the third phase must be considered. In recent years, many research groups have studied this problem of a soil containing three phases (Bennett and Wilson 1999). Collectively, the work these researchers have done has become an important field of study termed *Unsaturated Soil Mechanics.* As the name implies, the field deals with soils in the unsaturated state.

Ironically, many civil engineering projects involve unsaturated rather than saturated soils. Since the water table is typically located at depth below most foundations, the imposed stresses of a structure can, in many cases, be negligible once fully saturated soils are encountered. The uncertainty in the behavior of unsaturated soils has been shadowed in practice by use of correction factors that overcompensate for the design. The goal of unsaturated soil mechanics is to reduce this overcompensation by providing a better understanding of behavior of the soil in various states of saturation and stresses.

Generally, soil behavior is a function of three processes that are themselves interrelated. *Strength*, *Deformation* and *Flow* are responsible for all of the behaviors that an engineer considers in design. Strength and deformations are traditionally related by Hooke's Law and are incorporated in all constitutive soil models. Deformations are in turn related to flow by a parameter proposed by Biot and later Terzaghi as the coefficient of consolidation, c_v. Figure 1-1 shows this relationship and gives several examples of unsaturated soil engineering problems unique to each process.

Strength problems of unsaturated soils can typically involve foundation design. However, a very common engineering problem involving strength of unsaturated soils is retaining wall design. Many retaining walls involve unsaturated soils in the Rankine or Coloumb failure zones. Often the soil is given the saturated strength, which maybe less than the unsaturated strength. In fact, this is common practice for all strength problems. However, this can yield extremely conservative results that inevitably contribute to expensive designs. Another common example of unsaturated strength is the cut slope stability-type problems. These are especially troublesome in areas of the world where residual soils exist that are prone to sudden wetting. This scenario is very common in Southeast Asia where slope cuts for roads suddenly become unstable upon wetting due to months of a wet season.

Examples of deformations in unsaturated soils typically involve changes in moisture content of the soil under a constant load. The most expensive type of this problem deals with swelling soils. This is especially common in the western portions of the United States where there are high concentrations of Smectite minerals in the soils. Swelling soils in this region of the States cause more monetary damage to structures than all natural occurring disasters totaled (Fredlund and Rahardjo 1993). The damage arises when the in-situ smectitic unsaturated soil is constructed upon. The new structure disrupts the evapo-transpiration cycle that was in place. Moisture can accumulate beneath the structure and thus in the smectitic soil. Smectite minerals can swell to hundreds of times their initial size and also produce tremendous swelling pressures. This

combination of swelling potential and pressure crack and uplift foundations and abutments.

Transport problems have become the focus of many concerns in recent years due to ever increasing government environmental regulations. Many waste facilities are constructed on top of natural clay liners. These liners are compacted in a state that is less than saturated in efforts to make the densest liner possible. As a result, study of flow through the unsaturated liner becomes an important design element in the facilities construction. Several tests and design codes have recently been accepted as the standard when building these liners.

1.2 Goals and Scope of Research

Unsaturated soil behavior has been argued to be a function of the negative pore water pressure or matric suction. This matric suction is thought to arise from the soil imparting stresses on the water in the pore matrix. Since there is not enough water in an unsaturated soil to satisfy this stress, the water is stretched and thus a negative pressure occurs. All of the examples given in the previous section contain a single underlying question. What is the *nature* of soil suction? Nature refers to the physical phenomenon that causes the generation of soil suction and how it changes with changes in environmental factors. The nature of this process is the key to understanding unsaturated soil behavior.

The main goal of this work is to provide a better understanding of the generation of soil suction in an unsaturated soil. This needs to be done in both theory and the laboratory. In other words, a theoretical model that is conceptually valid needs to be introduced and then a laboratory experimental program developed to test the theory. In order to realize this goal several tasks have been identified as outlined below.

- Examination of the drying process of a porous material. This naturally occurring process gives insight into the development of soil suction over changes in moisture content.

- Measurement of the complete drying curve in the laboratory. Current state of the art measuring techniques only measure several points on a drying curve. Each point can take several days or weeks if the soil contains a significant fine fraction.
- Design and manufacturing of a device capable of measuring the high tensions associated with the drying process. A device with the ability to measure the suction directly is needed in order to measure a complete drying curve.
- Develop a conceptually realistic model of the drying process. The common capillary model is very simplistic and is not based on actual drying but on empirical data fits.
- Formulate the model analytically in order to predict drying behavior of porous materials.

Completion of the above tasks outlines the goals and scope of this body of work. It is thought that this will provide a clearer understanding of suction generation in unsaturated soils.

1.3 Thesis Organization

The completed tasks above outline the work contained in this thesis. The material has been divided into several chapters, each described in the following.

Chapter 2 contains a review of literature including all relevant topics. These topics include; water tension theory, a ceramic stone review, capillarity, soil suction measurement, and a review of the soil moisture characteristic curve. Chapter 3 describes the proposed desaturation model. A model is first presented in two dimensions and then expanded to three with respect to water volumes. The tension of the water held in pendular rings is derived. Packing of regular spheres is then examined. The model describes in a conceptually realistic fashion the process of a soil draining. The model is able to predict a continuous drying curve for a system of spheres of constant diameter. Chapter 4 presents the design and development of the devices and techniques required measuring the drying curve. Also included is the equipment needed in order saturate the measuring system. Finally, a description of the interface to the balance is given. The evaluation of the equipment is presented in Chapter 5. The stones are examined first and

then the various designs of the bases are evaluated. The materials and specimens used for the experiments in the thesis are discussed in Chapter 6. The physical properties of the glass beads and soils used are given first. The methods used to prepare the materials are then described. The results of the experimental program are presented in Chapter 7. Chapter 8 interprets the testing data and gives several conclusions and recommendations for further work to be carried out. The references for the thesis are given in Chapter 9. Several Appendixes have been included to supplement the thesis with information on the data acquisition BASIC code, drying test procedures, literature data, and plots of all the tests done.

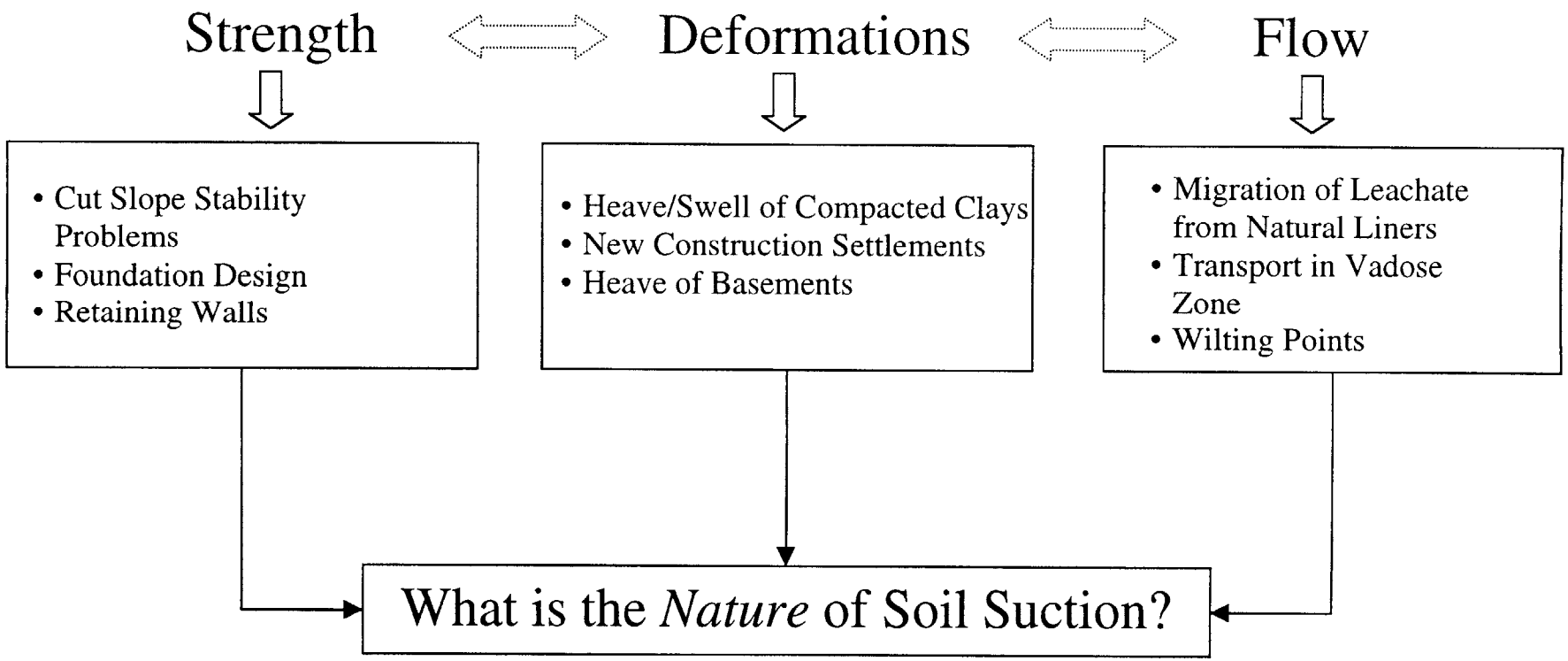

Figure 1-1. Interaction of several soil processes and examples.

Chapter 2 Review of the Literature

2.1 Water Tension Theory

2.1.1 Ultimate Tensile Strength of Water

The scientific discovery that water is able to withstand tensile stress was made in 1730 with the brothers Daniel and Jean Bernoulli. They worked in Basle, France developing relations between the pressure and velocity of moving water. Leonhard Euler in 1754 first described this relation mathematically, but the equation in present day form is called the Bernoulli Equation. This equation showed that when the fluid velocity increased, the pressure decreased. If the velocity were great enough, the fluid pressure would become negative. When the fluid pressure became too negative, the fluid would break with the formation of small cavities or voids. This phenomenon is today referred to as cavitation.

Next came François Donny who published a paper in 1844 while working at the University of Gent. The paper describes a U-tube device that was used to show that sulfuric acid could sustain a tension while in a static condition. Donny wrote that the tension must be attributed to two possible mechanisms, cohesion of the molecules to one another and the adhesion of the fluid to the walls of the container. He continued this work by increasing the height of the U-tube and by first degassing the fluid. He discovered that greater tensions could be sustained if the fluid was degassed prior to filling the U-tube.

The most famous advancement in water tension theory came in 1850 by Marcelin Berthelot at the College de France. His experiments consisted of a glass tube open at one end and filled with cooled pre-boiled water. He annealed the open end after filling with water. The sealed tube now contained two phases, air (with vapor) and water. The experiments then proceeded. The sealed tube was slowly heated until the water in the

tube completely filled the air space, i.e.; the air went into solution. This temperature was recorded as T_f. The tube was then slowly cooled to a temperature below T_f while the tube still remained filled with water. The water in the tube eventually 'broke' at a temperature, T_b. At this point the system made a 'metallic' click sound as cavitation bubbles formed within the tube. The tube also under went a sudden expansion in volume. This change in volume, ΔV, was recorded and from this Berthelot could indirectly calculate the tension in the tube. He calculated water tensions of approximately 50 atmospheres in this manner. Berthelot also concluded that this tension was not the ultimate tension of the water. He observed that the cavitation bubbles always occurred at the surface of the glass tube and not in the body of the water itself. He therefore postulated that he was measuring the adhesion of the water to the surface of the tube and not the true tensile strength of the water (Trevena 1987).

2.1.1.1 Estimated Tensile Strength of Water

As an estimate of the ultimate tensile strength of ordinary water, a simple calculation can be made. If the stress needed to pull apart two water molecules is considered, then this stress, P will be given by:

$$P = \frac{2\gamma}{r} \qquad [2.1]$$

where;

γ = the free surface energy of water, 72 mJ/m^2,

r = the radius of the sphere opened up in the fluid.

If r is assumed to be the diameter of a water molecule, i.e. 0.3 nm, then the stress in Equation [2.1] is approximately 4800 bar. Other estimates of this tensile stress have been made using the van der Waals equation to describe the fluid. These estimates are on the same order as that obtained by use of Equation [2.1] (Tabor 1979).

2.1.2 Current Measurement Techniques

Recent investigators (Henderson and Speedy 1987; Jones et al. 1981; Ohde et al. 1993) have been revising the technique used by Bethelot. The glass tube originally used has been replaced with a stainless steel chamber with an integral pressure transducer (Figure 2-1). The specimen chamber (approximately 1 cm^3) is sealed off by use of a metal plug. A degassed copper plug has been found to work satisfactorily (Ohde et al. 1988).

Ohde (1989) reached a sustained tension of regular water at 125 bar at 47°C. This value was reached after 3800 repeated cycles of heating and cooling the water in the chamber. Henderson (1980) used a glass specimen chamber as in the original Berthelot tube and recorded a maximum tension of 156 bar. The maximum recorded experimental value is 277 bar (Trevena 1987).

2.2 Ceramic Stones

Porous ceramics are widely used in the soil research industry. Due to the ceramics high porosity and low pore diameters, the material is an excellent boundary membrane between the soil and the measuring system. In general, the porous ceramic is exposed to the soil on one side and the other side is a chamber or reservoir of water. When the porous ceramic is fully saturated, there is a continuous hydraulic connection between the soil on one side, and the water reservoir on the other. There are many sources for porous ceramics used in soil research, both commercially and within academic institutions.

2.2.1 Composition

Although the composition of the ceramics will depend on the source and application, in general the material is composed of varying proportions of kaolin, talc, alumina, ball clay and feldspathic minerals. The main constituents of such ceramics are Al_3O_3, SiO_2, and MgO. Other minerals in lesser amounts can include Fe_2O_3, CaO, TiO_2, K_2O, and Na_2O.

2.2.2 Bubbling Pressure

The air entry value, or bubbling pressure, for a porous ceramic is the air pressure required to force air through a thoroughly saturated ceramic disc. The air entry value of a porous ceramic is defined by the capillary equation (which is derived in Section 2.4.1).

$$AEP = \frac{2T_s \cos\theta}{R_s} \qquad [2.2]$$

where;

AEP = the air entry pressure,
T_s = the surface tension of the water,
θ = contact angle between water and the ceramic (assumed to be = 0),
R_s = radius of pore channel in the ceramic.

From Equation [2.2] it can be seen that the smaller the pores in the ceramic, the higher the air entry value of the ceramic will be. Conversely, large pores in the ceramic will result in a lower air entry value. Figure 2-2 shows this concept schematically.

2.3 Soil Water Potential Energy

The concept of soil suction was developed in the early 1900's by the soil physics scientists. This concept was intended at that time for soil science and was used in the soil-water-plant system. Soil suction is commonly referred to as the free energy state of the soil water relative to pure water at the same temperature and atmospheric pressure. This free energy of the soil water can be expressed in terms of a thermodynamic context. This free energy can be related to the partial vapor pressure of the soil water (Aslyng 1963). The thermodynamic relationship between the total soil suction (free energy) and the partial pressure of the soil water is given by:

$$\psi = -\frac{RT}{\upsilon_{w_0}\omega_\upsilon}\ln\left(\frac{u_\upsilon}{u_{\upsilon_0}}\right) \qquad [2.3]$$

where;

ψ = free energy or total soil suction

R = universal gas constant (8.31432 J/mol•K)

T = absolute temperature (K)

υ_{w0} = specific volume of water (inverse of the density, m^3/kg)

ω_υ = molecular mass of water vapor (18.016 kg/kmol)

u_υ = partial pressure of the pore water vapor (kPa)

$u_{\upsilon 0}$ = saturation pressure of pure water vapor (kPa)

The term $u_\upsilon / u_{\upsilon 0}$ in Equation [2.3] is the relative humidity of the air in the equilibrium with the soil in the system. Figure 2-3 plots the total suction versus relative humidity for a system at 20°C.

Water added to a soil from a reference pool will undergo a change in potential energy. The work required to resist this change in potential energy is termed the potential. The following potentials of soil water are defined using definitions of a committee of the International Society of Soil Science (Aslyng 1963; Bolt 1976).

2.3.1 Total Potential

The total potential (ψ) of soil water is the amount of useful work that must be done per unit quantity of pure water to transfer reversibly and isothermally an infinitesimal quantity of water from a pool of pure water at a specified elevation at standard atmospheric pressure to the soil water at the point under consideration (Marshall et al. 1996).

Referring to Equation [2.4], the total potential (ψ) is the sum of the matric (ϕ) and osmotic (π) potentials described in Sections 2.3.2 and 2.3.3 respectively.

$$\psi = \phi + \pi \qquad [2.4]$$

2.3.2 Matric Potential

The matric potential (ϕ) is the amount of useful work that must be done per unit quantity of pure water to transfer reversibly and isothermally to the soil water an infinitesimal quantity of water from a pool that contains a solution identical in composition to the soil water and is at the elevation and the external gas pressure of the point under consideration (Marshall et al. 1996). The matric potential, or matric suction as it is commonly referred to, is thought to be the component of total suction that most greatly affects soil behavior. It is the component that acts on the soil skeleton or matrix.

2.3.3 Osmotic Potential

The osmotic potential (π) is defined as the amount of useful work that must be done per unit quantity of pure water to transfer reversibly and isothermally an infinitesimal quantity of water from a pool of pure water at a specified elevation at atmospheric pressure to a pool containing a solution identical in composition with the soil water at the point under consideration but in all other respects identical to the reference pool (Marshall et al. 1996). The osmotic potential is the component of total suction that is generated by the total concentration of salts in the bulk pore fluid. The ideal gas equation can be arranged to express the osmotic potential for a given concentration of salt. Referring to Equation [2.5], for a solution at standard temperature and pressure (STP), the osmotic potential (in bars) of the solution is approximately 24 times the total concentration of salt in the system. It should be noted that the concentration of the cations and the anions must be included to determine the osmotic potential (Petrucci 1989). For most soils, the osmotic potential does not change significantly over changes in water content that are to be expected (Fredlund and Rahardjo 1993).

$$P = \frac{n}{V} RT \qquad [2.5]$$

where;

P = the osmotic pressure (atm),
n/V = concentration of salt (cations and anions, mol/L),
R = Universal Gas Constant (0.082 L•atm/mol•K),
T = absolute temperature (K).

2.4 Capillarity

2.4.1 Surface Tension

Surface tension of a fluid results from the unbalanced forces acting on a molecule of fluid located at the gas-liquid interface. A molecule located within the fluid undergoes equal forces in all directions and therefore is in static equilibrium. However, a liquid molecule located at the air-water interface (for purposes of this work air and water are considered only) undergoes an unsymmetrical force balance due to the change of phase. In order to overcome this asymmetry, the surface of the water must undergo tension to compensate for the lack of forces above the interface. The result of this tension is a curved surface concave towards the unbalance. This curved surface can be modeled as a flexible membrane as shown in Figure 2-4. If two orthogonal directions in the plane of the membrane are considered, they will have radii of curvatures of R_1 and R_2. The corresponding components of surface tension will be T_1 and T_2. For a pressure perturbation of Δu, considering one direction, the force equilibrium in the vertical direction require that:

$$2T_s \sin\beta = 2\Delta u R_s \sin\beta \qquad [2.6]$$

where;

β = the angle between the membrane and the horizontal,
R_s = radius of curvature of the membrane in the given direction,
T_s = the corresponding tension in the membrane.

Simplifying Equation [2.6] yields:

$$\Delta u = \frac{T_s}{R_s} \qquad [2.7]$$

Equation [2.7] gives the pressure difference across a two dimensional membrane with a radius, R_s and surface tension, T_s. Extending this membrane to three dimensions by use of the Laplace equation yields:

$$\Delta u = T_s\left(\frac{1}{R_1} + \frac{1}{R_2}\right) \qquad [2.8]$$

If the radius of curvature is equal in both directions, (i.e. $R_1 = R_2 = R_s$), Equation [2.8] becomes:

$$\Delta u = \frac{2T_s}{R_s} \qquad [2.9]$$

When considering a multiphase system of air-water-soil, the pressure perturbation, Δu, arises from the difference in water and air pressure. This difference as defined in Section 2.2.2 is the matric suction. Updating Equation [2.9] with this definition yields:

$$\left(u_a - u_w\right) = \frac{2T_s}{R_s} \qquad [2.10]$$

where;

u_a = the pressure in the air phase,
u_w = the pressure in the water phase.

Equation [2.10] is referred to as the Kelvin capillary model. As the difference in air and water pressure increases, the radius of curvature decreases. Conversely, when the difference in air and water pressure approaches zero, the radius of curvature approaches infinity, i.e., a planar surface.

The surface tension is represented in units of force per length, typically expressed in N/m. Table 2-1 lists surface tensions as a function of temperature for air-water interfaces.

2.4.2 Capillary Rise

When a glass tube of small radius r, is inserted into water, the water will rise in the tube to a height of h_c. This phenomenon is called capillary rise and comes from the tendency of the water to wet the sides of the glass tube and of the tension developed in the surface of the rising water at the air-water interface. Considering the vertical force equilibrium in the tube will yield the following:

$$2\pi R_s T_s \cos\alpha = \pi r^2 h_c \rho_w g \qquad [2.11]$$

where;

r = radius of the capillary tube,
T_s = surface tension of the water,
R_s = radius of the curvature of the water,
α = contact angle between the water and the tube,
h_c = capillary height,
ρ_w = density of water,
g = acceleration due to gravity.

If the contact angle is assumed to be zero (Mayer and Miller 1992), then the radius of the tube will be the same as the radius of the meniscus R_s, and Equation [2.11] can be rearranged in the form of:

$$h_c = \frac{2T_s}{\rho_w g R_s} \qquad [2.12]$$

The actual height of capillary rise in soils may not be realized as described by Equation [2.12] due to variations in pore diameters (shown in Figure 2-5). If a simple model of a capillary tube is used to explain capillary behavior in soils then h_c should be expected. However, if a more realistic model is assumed, such as a pore being a series of bulbs of differing radii (the ink bottle effect), then h_c will also be dependent on whether the pore is wetting or drying. Consider a capillary tube with a radius R_1 and a bulb of radius R_2. Applying Equation [2.12] will give a height of rise of h_{c1}. If $R_2 >> R_2$ and the tube is

initially dry, the advancing water rise will reach the bulb of radius R_2 and stop. If the system is initially wet, then h_{c1} will be realized, as the driving radius will be the smaller R_1. The above phenomenon along with entrapped air, are the major causes of hysteresis in the Soil Moisture Characteristic (Fredlund and Rahardjo 1993).

2.5 Techniques of Matric Suction Measurement

2.5.1 Indirect Techniques

2.5.1.1 Filter Paper

The filter paper method was developed by the soil science community in the late 1930's. Since that time it has been looked at by numerous researches in both soil science and soil engineering. This techniques' ease of use and simple interpretation make it a convenient technique for comparison to other methods. The ASTM standard for this method is ASTM D5298-92.

To perform this technique, a representative soil sample of approximately 100-200 grams is placed into an airtight container with the oven-dried filter paper (approximately 5.5 cm in diameter) and allowed to equilibrate for one week. The filter paper is placed such that the paper is in direct contact with the soil. Generally it is recommended to sandwich the filter paper between two other filter papers to prevent the soil from contaminating the middle filter paper (Figure 2-6). After the appropriate equilibration time, the middle filter paper is removed from the sandwich and a water content determination of the paper is made. Based on a calibration curve for the filter paper, suction can be inferred from the equilibrium water content (Houston et al. 1994). The calibration curve is generated by allowing the oven dry filter paper to equilibrate in a chamber at different relative humidities. The relative humidity can be controlled by either salt or acid solutions. Once the paper is removed from the chamber, the water content is determined. This process is repeated for several different relative humidities and a curve can then be constructed. The relative humidity is converted to an equivalent suction by use of Equation [2.3].

Problems generally arise from several sources. This method is extremely sensitive to the temperature of equilibration. Therefore, a constant temperature should be maintained while the paper is equilibrating within the chamber. This will also eliminate any condensation of moisture on the container walls. Once the equilibration period is complete, care should be taken to remove the paper from the soil to a sealed container as quickly as possible to minimize moisture loss in the laboratory air. With some soils, particularly organic rich soils, fungal growth may occur due to the long equilibration period. A dilute solution of mercury chloride ($HgCl_2$) can be used to pretreat the paper in order to prevent any fungal growth. Houston et al (1994) found that the pretreatment with 0.02% by weight $HgCl_2$ showed no measurable affect on the final resulting suction.

2.5.1.2 Porous Plate

The porous plate method is used to determine the moisture – suction relationship for coarse and medium grained soils. The technique is recommended for suctions between 0.1 and 1 ATM. The use of this method is outlined in ASTM D2325-68. The experimental setup shown in Figure 2-7 consists of a pressure container, a 2 bar fine ceramic porous plate, 10-mesh brass screen, rubber (neoprene) membrane, sample rings, various tubing and spouts, and an air pressure source.

Approximately 25 grams of soil is placed into a retainer ring 10 mm high by 50 mm in diameter. The specimen and saturated porous plate are then placed into the pressure chamber where the air pressure is regulated by an outside source. By raising the air pressure in the chamber to the desired value, drainage of the soil pore water is initiated and the expelled water is removed from the system via the underlying brass screen and neoprene membrane. The chamber pressure is maintained until cessation of pore water flow. At this point, the chamber pressure is released and a water content is taken of the specimen. Since the pore water is free to drain to an outside source, the difference in chamber pressure to that of atmospheric pressure is assumed to be the matric suction imposed (ASTM 1993a).

Problems with this technique (and also with the pressure membrane) are outlined in Bocking (1980) and in general arise from saturation of the specimen being tested. Any occluded air in the pore water will not be effected by an increase in the chamber air pressure. Therefore, the specimen needs to be thoroughly saturated prior to testing. Also, specimens can undergo volume change as the pore water drains. Typically, the gravimetric water content of the specimen is converted to volumetric water content. In order to do this, a constant volume is assumed with known dry density. Depending upon type of soil, this can lead to large errors in presentation.

2.5.1.3 Pressure Membrane

The pressure membrane apparatus is identical in theory and similar in use to the porous plate apparatus described in Section 2.5.1.2. The major difference is the capacity of the system that is able to measure suctions up to 15 bars. The ASTM designation for this apparatus is ASTM D3152-72 and is shown in Figure 2-8.

Following ASTM, a soil specimen is packed into a sample ring 10.2 mm in height by 50.8 mm in diameter. The ring is capable of holding approximately 25 grams of soil. The specimen ring and soil are placed onto a cellulose membrane that rests upon a screen, and then a 15 bar ceramic plate. An air pressure is applied to the system and drainage of the pore water is initiated. By providing this differential pressure, constant contact between the membrane and the soil is assured. The setup is maintained in this fashion until equilibrium is reached (at least 1 to 2 days) at which point the pressure is released and the gravimetric water content is taken of the soil (ASTM 1993b).

2.5.1.4 Axis Translation Technique

This technique was developed by Hilf (1956) for measuring the negative pore pressures in compacted soils. The technique utilizes the properties of a fine porous plate as described in Sections 2.5.1.2 and 2.5.1.3 and high air pressure. A soil specimen is placed on a porous plate and the air pressure in the environment of the soil is elevated to a pressure that yields a zero or positive pore pressure. The pore pressure is measured by a

transducer connected to the water compartment below the porous stone. The difference of the air pressure and the pore pressure is taken as the matric suction. The limit of the technique is dictated by the rating of the fine porous stone. Usually a high air entry disk of 15 bars is used to avoid any measurement problems and extend the range of suction measurements. A typical setup is shown in Figure 2-9.

Bocking (1980) reviewed this technique and made several recommendations regarding the limitations. For soils with totally interconnected pores the technique should yield correct measurements. However, for soils with occluded air, the technique will over-estimate the actual suction. In order for the technique to work, a small amount of water must change in the system to register a pressure change in the transducer. This volume (water) change is minor and fully reversible for specimens with continuous air. When the soil contains discontinuous air, this volume change will be non-reversible. Bocking (1980) concluded with the following four considerations: (1) due to the asymptotic nature of the transient flow of pore water, flow equilibrium will never truly be attained. (2) air diffusion through the porous ceramics imposes a practical limit on the length of time that a test can be run. (3) the rate of application of the chamber pressure and the compressibility of the soil, the suction can be over-shot yielding a peak value which should not be interpreted as the actual suction of the soil. (4) the suction will be overestimated if the specimen contains significant amounts of occluded air.

2.5.1.5 Thermal Conductivity

The thermal conductivity of a soil will vary with the water content of the soil as water dissipates thermal energy differently than air. A thermal conductivity sensor consists of a heating element and a temperature sensor encased in a porous block (Figure 2-10). When the sensor is in contact with a soil, there will be a transfer of pore water between the soil and the porous block. The equilibrium moisture transfer of the soil water will be a function of the matric suction of the soil, i.e., the higher the suction, the more water transferred from the block to the soil. By measuring the thermal conductivity of the porous block over time, it can be determined at which point equilibrium has been

reached. Use of a calibration curve for the sensor is needed in order to convert the output of the sensor to equivalent soil suction (Fredlund and Rahardjo 1993).

2.5.2 Direct Techniques

2.5.2.1 Tensiometers

Richards (1936) originally developed the tensiometer for use in soil science. The basic tensiometer is composed of a porous ceramic cup, a water filled conduit, and a pressure measuring device. A pressure transducer, manometer or vacuum gauge can be used to make the pressure measurement. Stannard (1992) gives a complete review of current tensiometer design and use.

The tensiometer can be used in either the lab or the field depending upon the design of the device. In essence, a tensiometer directly measures the tension imparted on the water filled conduit due to the matric suction of the soil. The soil in contact with the porous cup exerts a flow of water from within the tensiometer to the soil. The magnitude of this flow is a measure of the matric suction of the soil. The resulting tension in the water filled conduit is then measured by one of the configurations mentioned above. The major drawback to the tensiometer is the limited range of tension that it can measure. Tensions measured are typically from 10 to 85 kPa with standard tensiometers. Beyond this limit, dissolved air in the tensiometer comes out of solution and accumulates in the measurement system.

2.5.2.2 Imperial College Tensiometer

Ridley and Burland (1993) describes a device capable of directly measuring soil suctions up to 15 bars. The device described is based on work performed by physicists investigating the tensile strength of water. As early as 1850, Berthelot measured tensile strengths of water to several bars. By reducing the volume of degassed water (with respect to standard tensiometers), recent researches have shown that water can withstand

several hundred bars of tension. Ridley and Burland utilized these concepts in the development of their Imperial College Tensiometer device (Figure 2-12).

By shrouding a miniature Entran EPX pressure transducer with a high air entry (15 bar) porous stone and stainless steel sheath, Ridley and Burland created a small reservoir of water (3 mm^3) within their measurement system. Saturation of the device was done by assembling the device dry and then subjecting the device to a high backpressure. The high pressure dissolved air entrapped in crevices and/or mismatches in the threads of the transducer. This pressure was sustained for 12 hours and then released. Soil placed in direct contact with the porous stone impartes a tension in the reservoir and a direct reading of the matric suction can be taken. The maximum tension sustained was found to be related to the volume in the reservoir and thickness of the porous stone. By decreasing the volume in the reservoir and keeping the porous stone as thick as possible, tensions above 10 bar could be maintained for several weeks.

Ridley and Burland (1995) revised the design to incorporate an internal strain gauge (Figure 2-13). This new design eliminates the Entran pressure transducer and thereby any mismatches in the threaded shroud and transducer. They reported much more consistent results and ease of saturation with no decrease in magnitude of tension measurements.

Guan and Fredlund (1997) describe a similar device to that of the original Imperial College Tensiometer (Figure 2-14). They compared the suction measurements made in their tensiometer to suction measurements made with pressure plate apparatus, filter paper method, and thermal conductivity sensors. They concluded that their tensiometer gave higher values of suction when compared to the filter paper and thermal conductivity sensor and lower values of suction when compared to the pressure plate.

2.6 Techniques of Osmotic Suction Measurement

2.6.1 Squeezing Technique

The osmotic suction of a soil matrix can be indirectly determined from the pore fluid salt concentration. The salt concentration can be determined by making a resistivity or conductivity measurement and then converting to an equivalent salt concentration. This concentration is then converted to an equivalent suction by means of Equation [2.5].

The removal of the pore fluid can be accomplished in two ways. The water content of the soil can be diluted to a known value and then the pore fluid decanted off and measured separately. However, Krahn (1972) found this procedure to be somewhat inaccurate. Manheim (1966) outlines the use of a pore fluid squeezer to extract the interstitial water from a soil. The device is also outlined in ASTM D4542-85. This device essentially consists of a piston chamber and a syringe affixed to the bottom. A wire screen separates the soil chamber and the syringe. A fine filter is placed upon the screen (5 to 10 μm) to remove fine soil particles from the extracted pore fluid. Approximately 50 grams of soil is placed into the apparatus and a pressure is applied to the chamber by depressing the piston. The expelled effluent passes through the filter and into the syringe. Approximately 25 mL of pore fluid can be extracted in this manner. Fredlund (1993) reports using this technique for osmotic suctions up to 350 bar while still maintaining agreement with the Subtraction method outline below.

2.6.2 Subtraction Method

The most common method of measuring the osmotic suction is by means of measuring the total suction and matric suction separately, and then subtracting the two values to obtain the desired result. This method appears to be relatively sufficient for most soils since the osmotic suction remains relatively constant for a given soil over a wide range of water contents (Fredlund and Rahardjo 1993).

2.7 Techniques of Total Suction Measurements

2.7.1 Humidity Chamber

Placing a soil sample in a chamber of known relative humidity will cause the soil to come into equilibrium with the surrounding air. The soil will either give up excess moisture to the environment or will sorb moisture from the environment. In either case the soil will eventually come into equilibrium with imposed relative humidity. A water content determination can then be made of the soil and the imposed total suction is known based on the relative humidity (by Equation [2.3]).

Placing a solution of salt or acid in the chamber can control the relative humidity. By changing the concentration of the solution, the relative humidity can be adjusted. Table 2-2 and Table 2-3 list the resulting suctions for solutions of NaCl at several different temperatures and for different saturated salt solutions at 20°C, respectively.

2.7.2 Filter Paper Method

As described in Section 2.5.1.1, the filter paper technique is a simple and relatively fast test to perform. When applying the technique to measure total suction the paper must not be in contact with the soil itself (Figure 2-15). By allowing only vapor exchange of water between the soil and the filter paper, an indirect measure of the chamber relative humidity is determined. Comparing the resulting water content of the filter paper to a total suction calibration (Houston et al. 1994) the total suction of the soil can be determined.

In accordance with ASTM D5298-92, calibration of the filter paper is accomplished by allowing the filter paper to equilibrate over salt solutions in a sealed container. A volume of at least 50 mL is recommended as the calibrating solution. The resulting relative humidity in the calibration chamber can be converted to an equivalent suction based on Equation [2.3].

2.7.3 Psychrometer Techniques

A psychrometer is an instrument that measures the difference between the ambient temperature and the equilibrium temperature needed to evaporate water at the same atmospheric pressure. The simplest psychrometer is the sling psychrometer that consists of two thermometers that can be rotated about a handle. One of the thermometers is covered with a sleeve of cloth that is wetted with water. The sling psychrometer is then spun about the handle until the wet sleeve is dry. At this point the ambient temperature is recorded along with the temperature of the 'wet bulb' thermometer. The difference in the temperature of the two thermometers is known as the wet bulb depression. This depression along with the known atmospheric pressure can be used to calculate the relative humidity of the air. Current psychrometers are variations on this principle by measuring the depression by either voltage differentials or by measuring current differentials. When used in a soil application, the relative humidity can be converted to an equivalent total suction as described above in Section 2.7.1.

2.7.3.1 Thermistor Psychrometer

A thermistor is a resistor that is sensitive to temperature. Thermistors may either increase or decrease in resistance due to a change in temperature depending upon the materials used and the type of construction of the resistor. The thermistor psychrometer is essentially the same idea as the simple psychrometer described in Section 2.7.3. Two thermistors are used in the setup of the device. One thermistor acts as the dry bulb, while the other acts as the wet bulb (see Figure 2-16). As the water evaporates from the wet thermistor, a depression in temperature is recorded. This depression is calibrated to a relative humidity, and thus, a total suction.

Richards (1987), who replaced the thermistors with transistors, have reported recent improvements to this design. The transistors give better stability and quicker response times. Truong (1995) and Holden (1995) provide details concerning calibration and use of the transistor psychrometer. The original design had a measurement range between 100 kPa and 10 MPa, however recent advancements by Woodburn (1995) have extended

this range to 71 MPa. Ridley and Wray (1996) report that the transistor psychrometer attains an equilibrium reading in under 3 hours.

2.7.3.2 Thermocouple Psychrometer

Currently there are two main types of thermocouple psychrometers in use today, the Peltier type (Spanner 1951) and the wet loop type (Richards and Ogata 1958). As with the thermistor psychrometer, a temperature differential is measured between an evaporating surface, the wet bulb, and a non-evaporating surface, the dry bulb. The differential can then be related to the relative humidity of the air in question. The main difference between the two types is the manner in which the evaporating junction is wetted. For the wet loop type, a drop of water is placed on a silver ring surrounding the evaporating junction. The Peltier type psychrometer (Figure 2-17) uses a Peltier current to cool the measuring junction to below the dew point of the air. This causes a small amount of water to condense on the junction. The junction is then further cooled by evaporation of the water droplet. Based on this depression, the relative humidity can be determined.

2.8 Soil Moisture Characteristic

2.8.1 General Description

The Soil Moisture Characteristic (SMC) is the relation between the degree of saturation or water content of the soil (either gavimetric or volumetric) and the associated matric suction in the pore water. It is a function of two components, the pore diameter and the tendency of water to be attracted to the surfaces of the soil. Distinguishing between the two components is complex and in general not necessary for most purposes. However, it can be assumed that for a soil with mostly coarse grains, the capillary effects dominate the SMC. Conversely, for a fine-grained material, water sorption becomes more influential.

The shape of the SMC is generally sigmoidal. This of course is dependent on the type of soil, particle size distribution, and degree of compaction (see Figure 2-18). Describing the genesis with respect to the shape of the SMC can be accomplished if the general case is considered. Starting with the pore water completely filling in the pore space of the soil and the water at hydrostatic pressure, this will yield the initial point on the SMC. As tension is applied to the soil water, the water will remain in the pore space until the tension is great enough to initiate drainage of the largest diameter pores. At this point, a break in the SMC occurs and water continues to flow out of the soil matrix as the tension increases. The point at which the pore flow is incipient is the air entry pressure, this is dipicted at the top in Figure 2-19. The next break in the curve happens as the residual water content is approached. This is the point at which the soil water is held so tightly that a large tension must be applied in order to remove the remaining water (bottom of Figure 2-19). Fredlund (1996) indicates that the largest tension that can exist in a soil matrix is approximately $1x10^6$ kPa, however Tabor (1979) gives a conservative derivation for the ultimate tensile strength of water to be slightly more than half of this value. From the residual water content it is assumed that the soil water continues to drain until this tension is reached.

2.8.2 Methods of Measurement

As described in Section 2.5.1.3, the pressure membrane apparatus is generally used to measure the SMC up to 15 bars of tension. This provides adequate results for the soil science industry, as this tension is usually the wilting point for most agricultural crops. To adequately describe the SMC, several points are needed. Due to the time limitations for equilibration, a test may take up to 3 to 4 months to complete for clay rich soils. In pursuit of faster results, researchers have modified the pressure membrane technique.

The present technique described above is attributed to Gardner (1937) which is a modification of the technique described by Haines (1927). Both techniques have remained essentially unchanged since their inception and are in use today.

Daniel (1983) presents a technique that uses a syringe pump located at one end of the specimen that forces water through at a predetermined rate. Although this technique was initially developed to measure hydraulic conductivity, with the addition of porous stones and suction psychrometers, the SMC can be determined (see Figure 2-20). Daniel discusses that this technique is operator dependent and also requires long equilibration times.

Fourie (1995) describes a technique to determine six to eight data points in 1 week. The modified apparatus essentially is the pressure membrane with a differential pressure transducer on the outflow line (Figure 2-21). The test was run by increasing the chamber air pressure and then opening the base valve to allow water to flow out of the specimen. Volume measurements are calculated by keeping a record of the amount of outflow and then back calculating from the final volume that is physically measured. After it was determined that the outflow had stopped, the base valve connected to the bubble trap was closed and the pore water pressure allowed to equilibrate. The equilibrium suction was determined directly from the differential pressure transducer reading.

2.8.3 Mathematical Models

Over the years numerous mathematical models have been developed to quantify the SMC. All the models are empirical curve fit equations and provide little or no theoretical background as to the expected relationship between the soil water and the resulting tension. Leong (1997) give an in depth review of many models and some rationale behind them. What will be presented in this review are several of the more popular models.

While the models have been developed independently, it is possible to combine all the essential detail into one generic governing equation (Leong and Rahardjo 1997). The general form of this equation is given by:

$$a_1\Theta^{b_1} + a_2 e^{a_3\Theta^{b_1}} = a_4\psi^{b_2} + a_5 e^{a_6\psi^{b_2}} + a_7 \quad [2.13]$$

where;

a_x and b_x = constants

ψ = suction pressure

Θ =normalized volumetric water content $(\theta_w-\theta_r)/(\theta_s-\theta_r)$ where θ_w = volumetric water content, θ_r = residual volumetric water content, θ_s = saturated volumetric water content

e = base of natural logarithms

2.8.3.1 Brooks and Corey (1966)

By substituting $b_2 = -\lambda$ and $a_4/a_1 = \psi_b^{\lambda}$ and setting $a_{2,5,7} = 0$ and $b_1 = 1$ in Equation [2.13] the Brooks and Corey equation (Brooks and Corey 1966) is developed in the form of:

$$\Theta = \left(\frac{\psi_b}{\psi}\right)^{\lambda} \quad [2.14]$$

This equation does not give a sigmoidal shape when evaluated. This type of curve fit equation best describes a narrowly distributed coarse-grained soil.

2.8.3.2 Gardner (1958)

By substituting $a_4/a_1 = a$, $b_1 = 1$, $b_2 = n$ and setting $a_{2,5} = 0$ and $a_1 = a_7$ in Equation [2.13] Gardner's equation (Gardner 1958) is obtained:

$$\Theta = \frac{1}{1 + a\psi^n} \quad [2.15]$$

2.8.3.3 van Genuchten (1980)

Probably the most common of all the models comes from the work of (van Genuchten 1980). As before, if by setting $a_{2,5} = 0$ and $a_1 = a_7$ and then substituting $a_4/a_1 = \alpha^n$, $b_1 = m$, $b_2 = n$ in Equation [2.13], the common form of van Genuchten is obtain as:

$$\Theta = \left[\frac{1}{1+(\alpha\psi)^n} \right]^m \qquad [2.16]$$

2.8.3.4 Fredlund and Xing (1994)

Fredlund and Xing (1994) used a theoretical basis for development of their SMC model. Assuming that the SMC is a function of the pore size distribution of the soil, Fredlund and Xing established a framework to develop a model. By considering a pore size distribution as a frequency function, Fredlund and Xing proposed the following general form of SMC equation:

$$\Theta = \left\{ \frac{1}{\ln\left[e + \left(\frac{\psi}{a} \right)^n \right]} \right\}^m \qquad [2.17]$$

where;

a,n,m = constants
e = base of natural logarithms

Equation [2.17] can be related to Equation [2.13] by setting $a_{1,5} = 0$ and $a_3 = 1$ and substituting $a_7/a_1 = e$, $a_4/a_2 = (1/a)^b{}_2$, $b_1 = m$, and $b_2 = n$.

2.8.3.5 Evaluation of Model Parameters

In order to provide some perspective on the above models, a simple parametric analysis was done by Leong (1997). The parameters a, m and n are common to the Gardner, van Genuchten, and Fredlund and Xing equations. It should be noted that the Gardner equation set m equal to 1 in all cases. Figure 2-22 shows plots of the effects of varying these three parameters. As shown in Figure 2-22a, as a is increased, this has the effect of shifting the model to the larger suction while maintaining the same shape. As the parameter n is increased, the models become steeper and show a more pronounced air entry value and residual water content. The effect of m is finally shown in Figure 2-22c.

As m decreases, the residual saturation decreases and the curves become slightly more shallow.

Table 2-1. Surface Tensions of Air-Water Interface (from Kaye and Laby 1973).

Temperature (°C)	Surface Tension (mN/m)
0	75.7
10	74.2
15	73.5
20	72.75
25	72.0
30	71.2
40	69.6
50	67.9
60	66.2
70	64.4
80	62.6
100	58.8

Table 2-2. Suctions of NaCl Solutions (after Lang 1967).

	Temperature (°C)				
	0	7.5	15	25	35
NaCl Molality	Osmotic Suction (kPa)				
0.0	0	0	0	0	0
0.2	836	860	884	915	946
0.5	2070	2136	2200	2281	2362
0.7	2901	2998	3091	3210	3328
1.0	4169	4318	4459	4640	4815
1.5	6359	6606	6837	7134	7411
1.7	7260	7550	7820	8170	8490
1.8	7730	8035	8330	8700	9040
1.9	8190	8530	8840	9240	9600
2.0	8670	9025	9360	9780	10160

Note: 1 bar = 100 kPa

Table 2-3. Saturated Salt Solutions and Vapor Pressures at 20°C (after Smith and Mullins, 1991).

Salt	Relative Humidity (%)	Potential (kPa)
$CaSO_4 \cdot 5H_2O$	98	-2730
$Na_2SO_3 \cdot 7H_2O$	95	-6935
$ZnSO_4 \cdot 7H_2O$	90	-14245
NaCl	75	-38893
$Ca(NO_3)_2 \cdot 4H_2O$	56	-78389
$CaCl_2 \cdot 6H_2O$	32	-154125

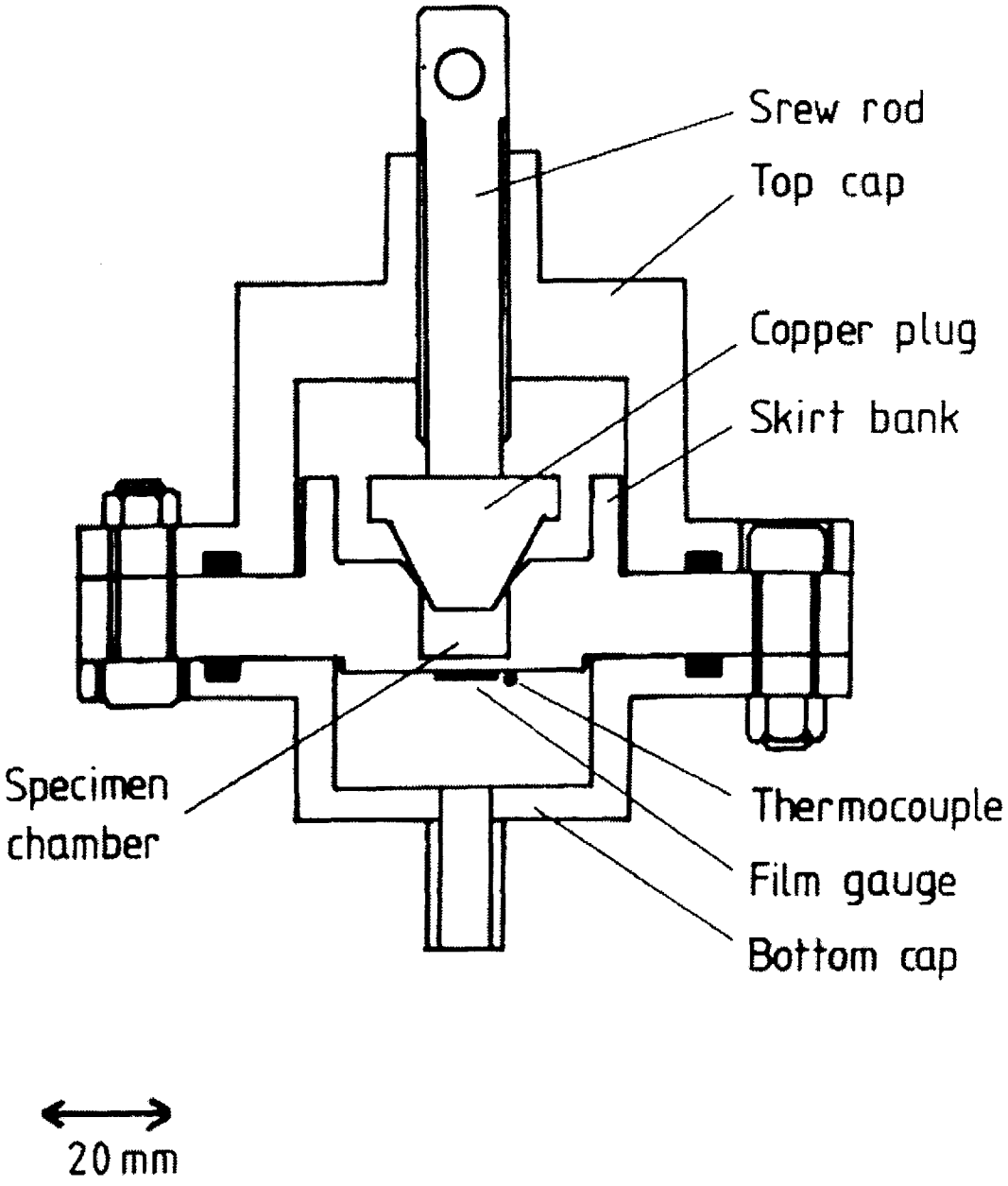

Figure 2-1. Stainless steel Berthelot tube (after Ohde et al. 1991).

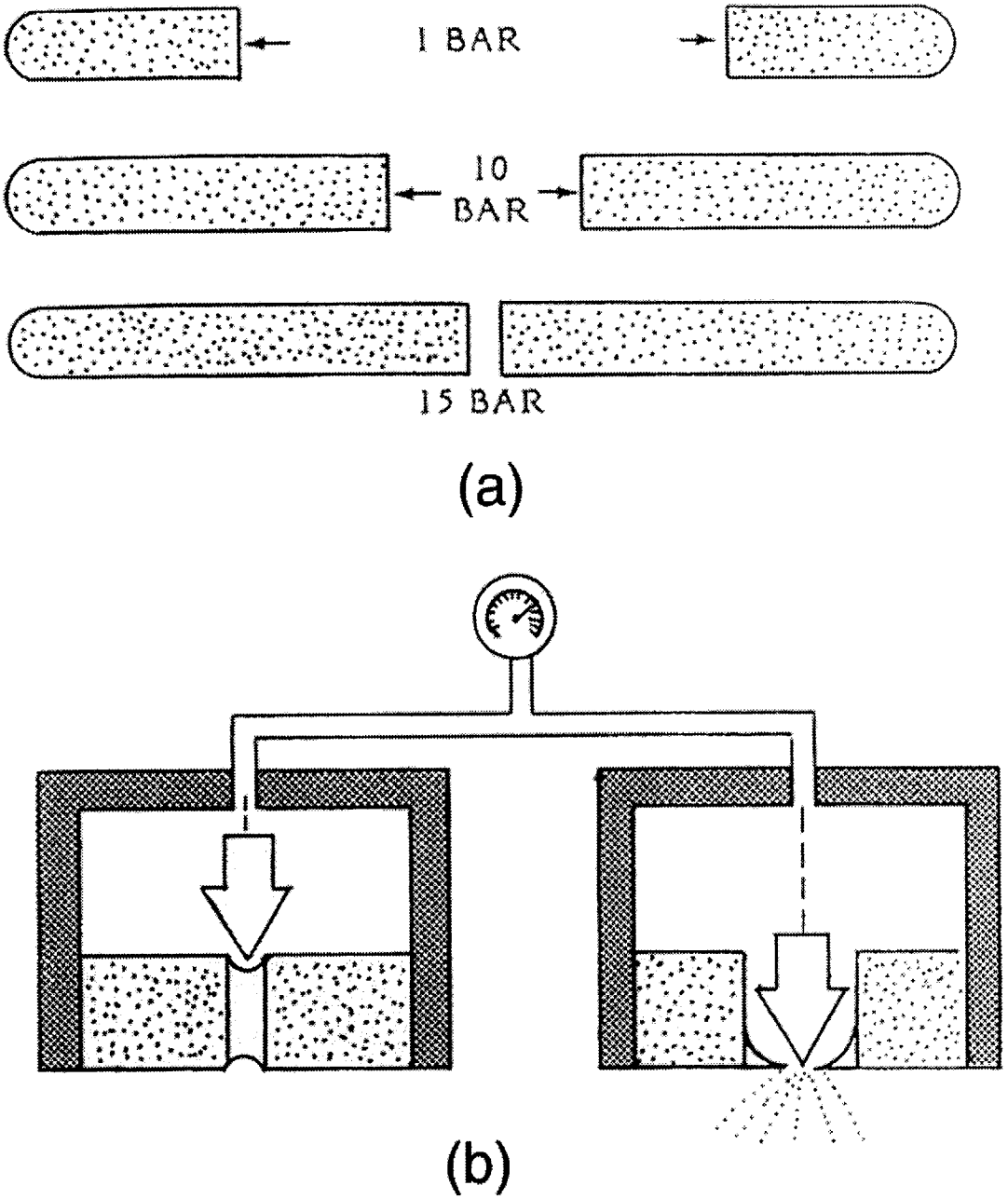

Figure 2-2. Schematic of (a) relative pore size (b) bubbling pressure (Soil Moisture Equipment Corp 1995).

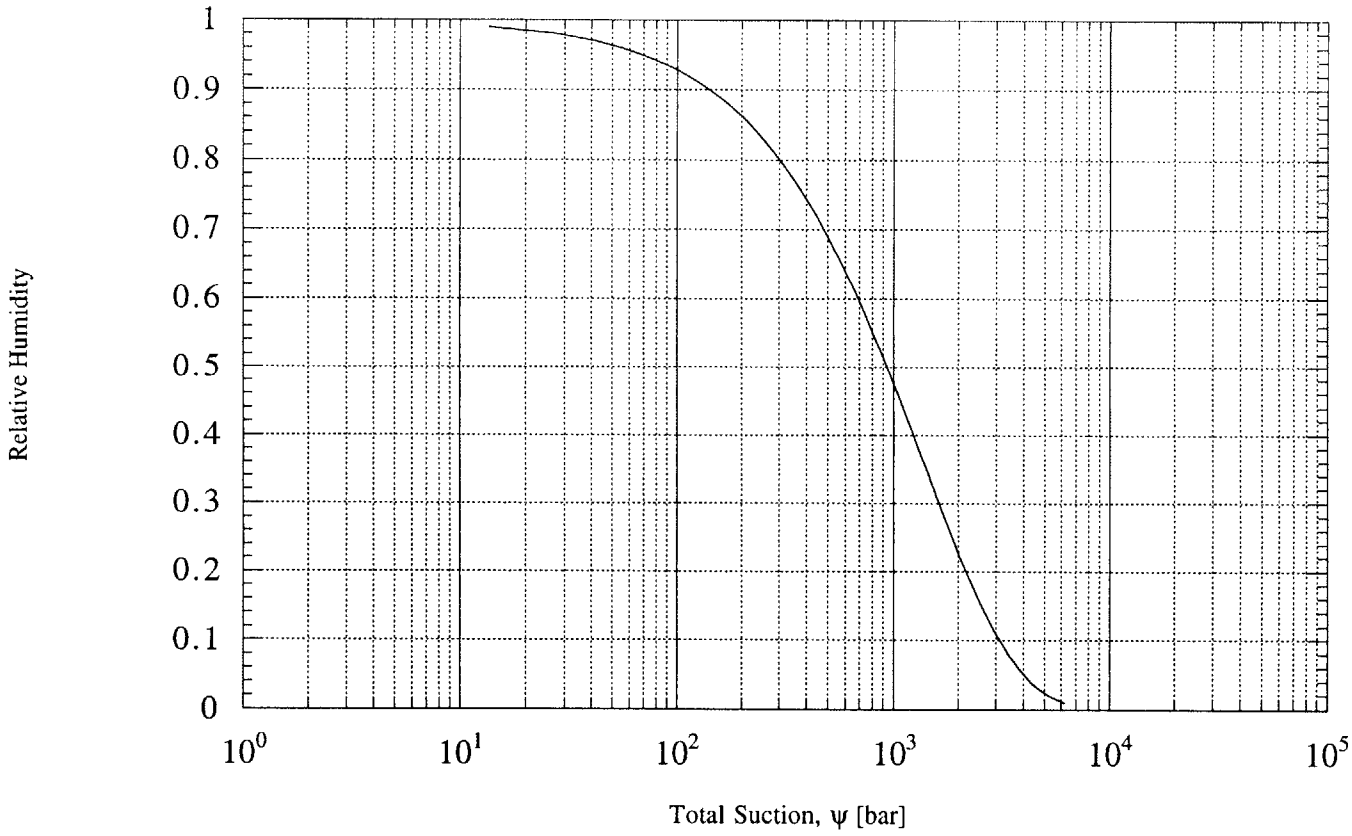

Figure 2-3. Total suction vs Relative Humidity at 20°C.

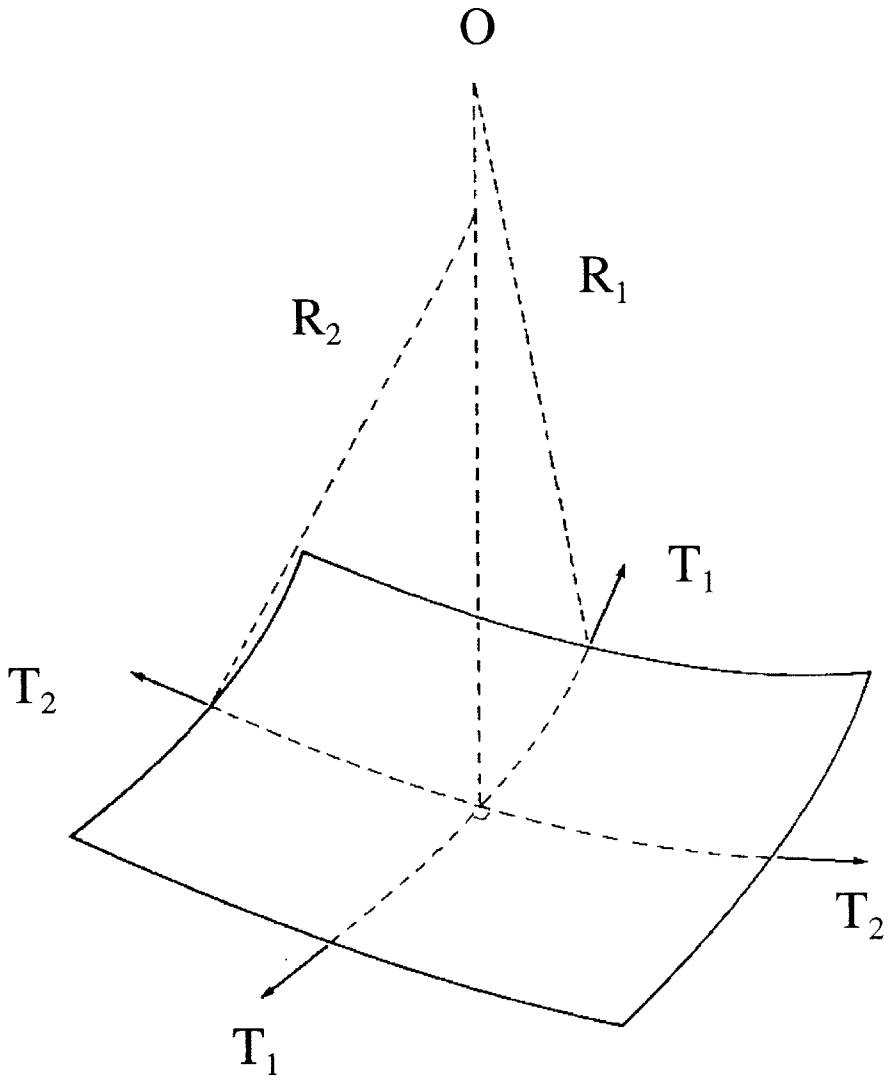

Figure 2-4. Surface tension on a warped membrane (after Fredlund and Rahardjo 1993).

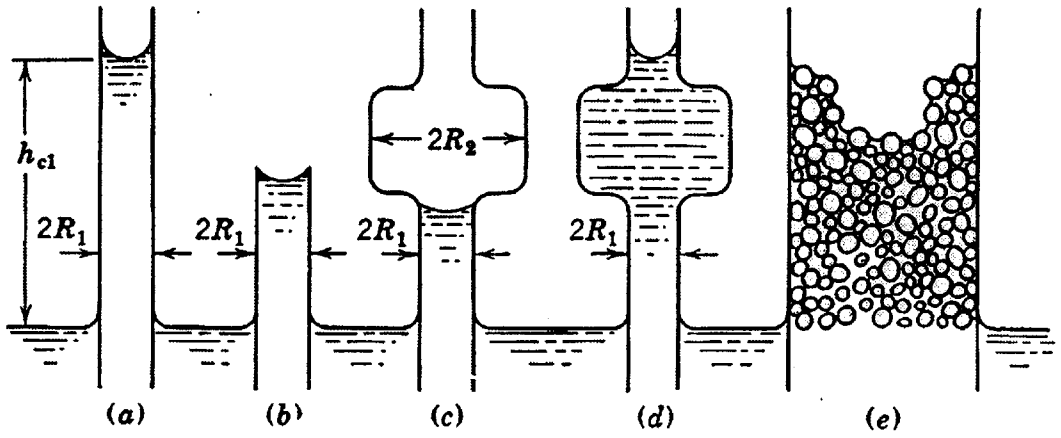

Figure 2-5. Capillary rise in tubes (after Taylor 1965).

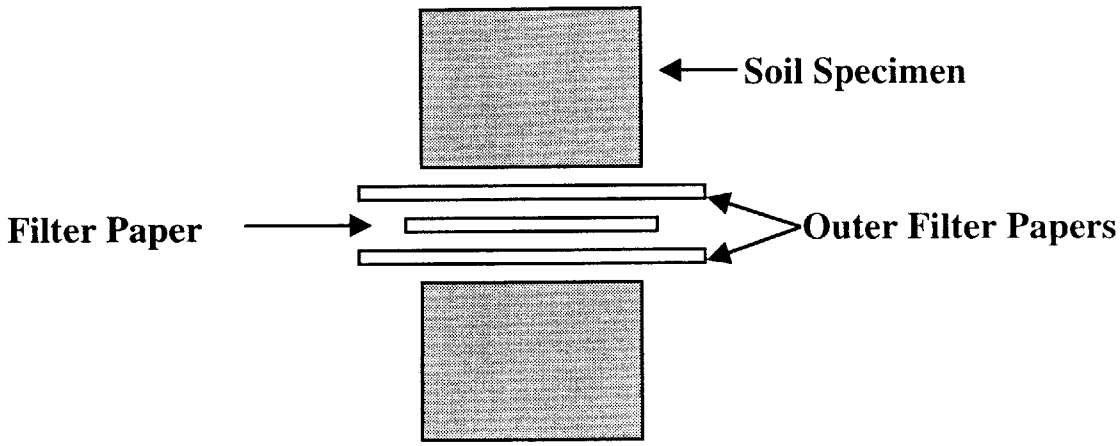

Figure 2-6. Filter paper method for matric suction measurement.

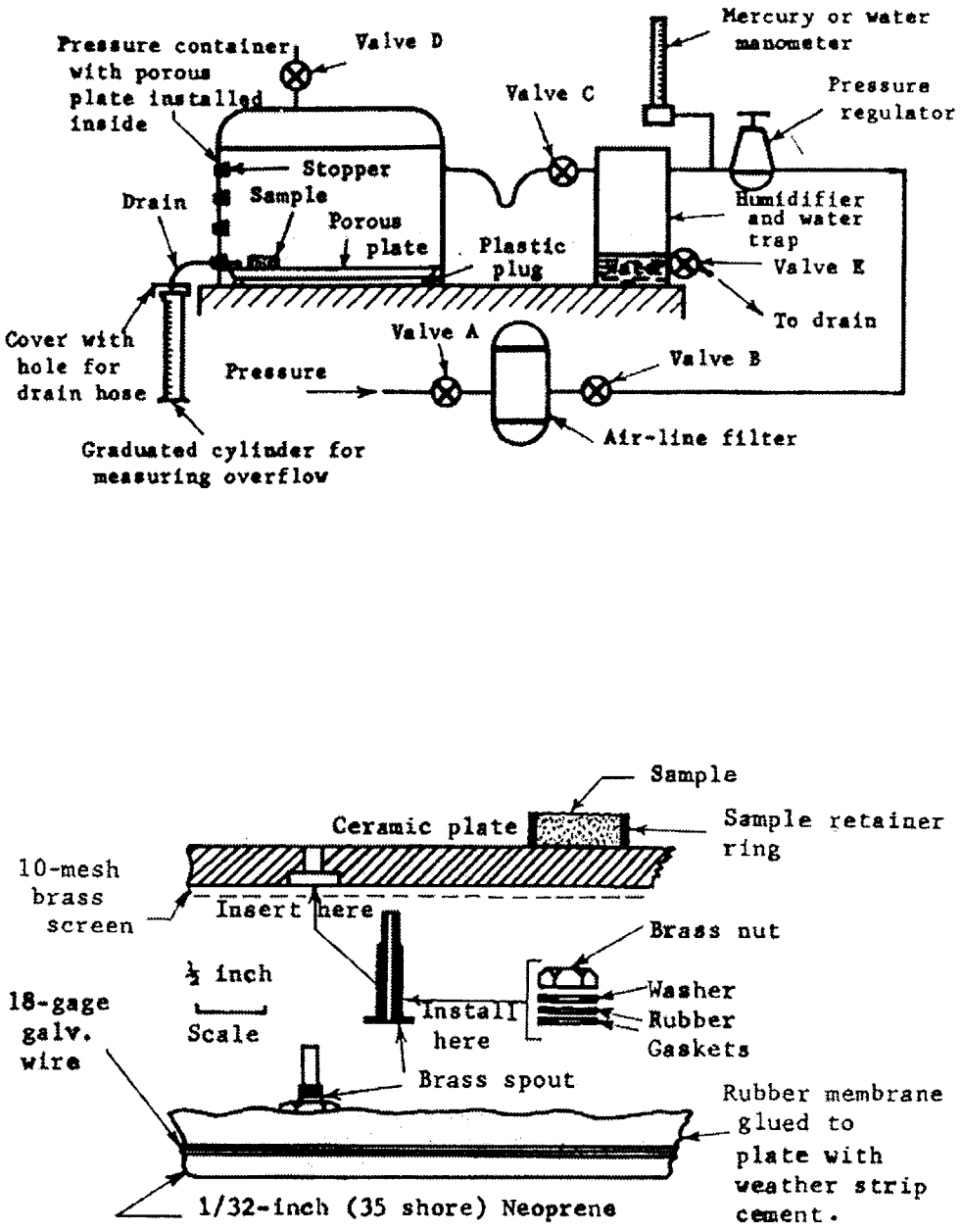

Figure 2-7. Schematic of Porous Plate method (ASTM 1993a).

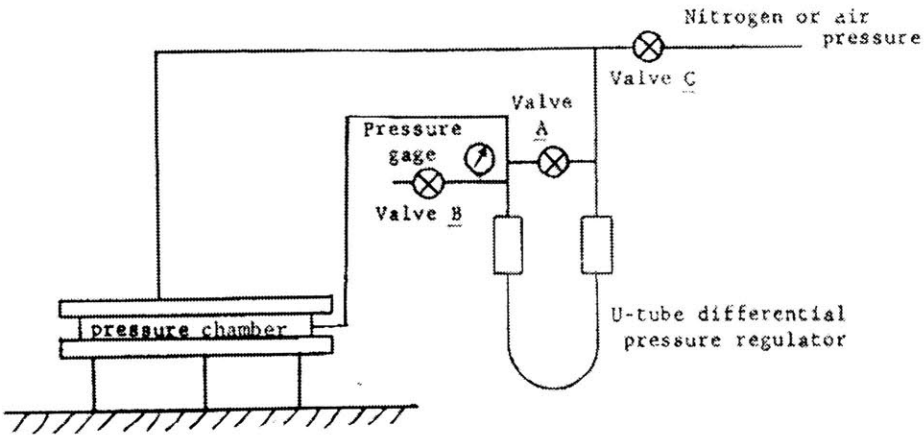

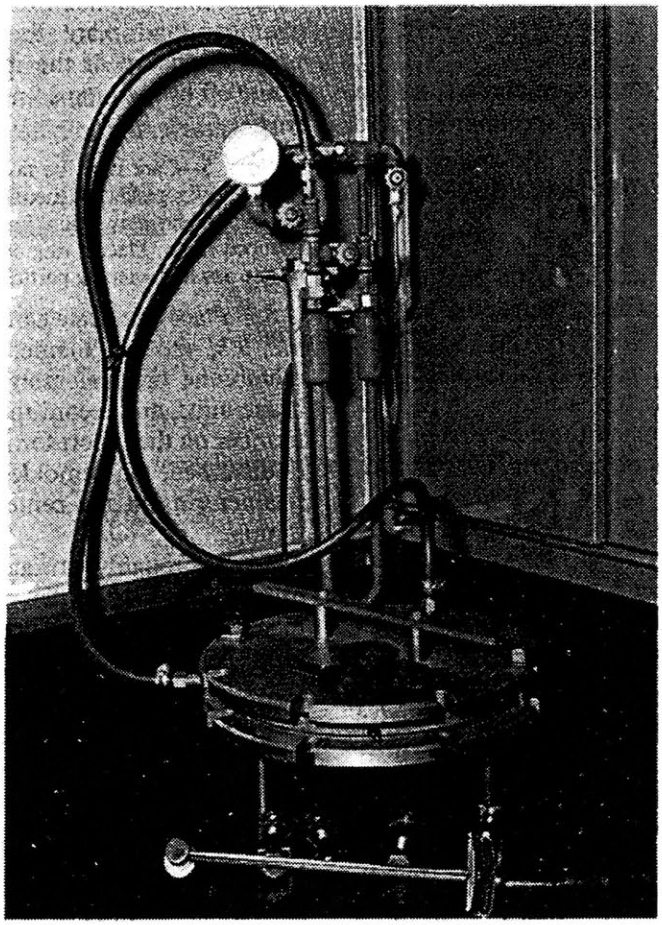

Figure 2-8. Pressure Membrane apparatus (ASTM 1993b).

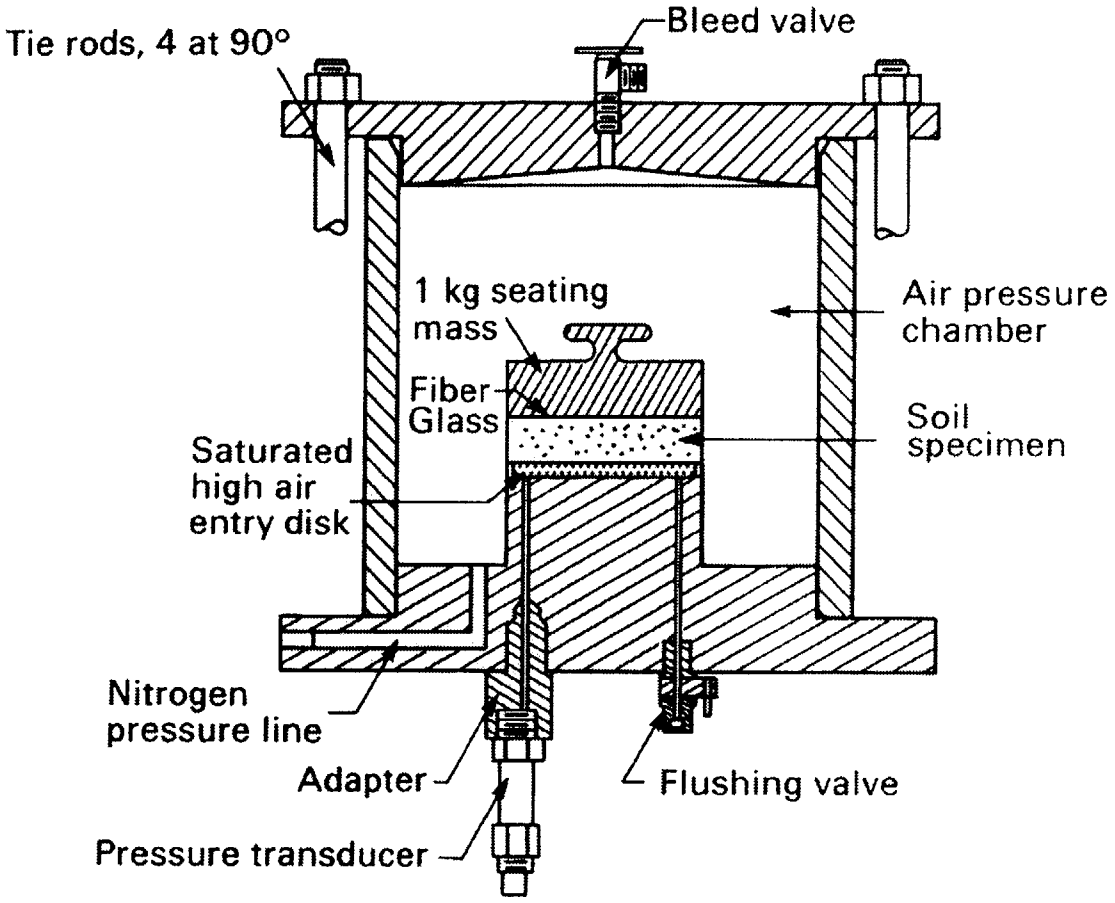

Figure 2-9. Axis Translation apparatus (from Olson and Langfelder 1965).

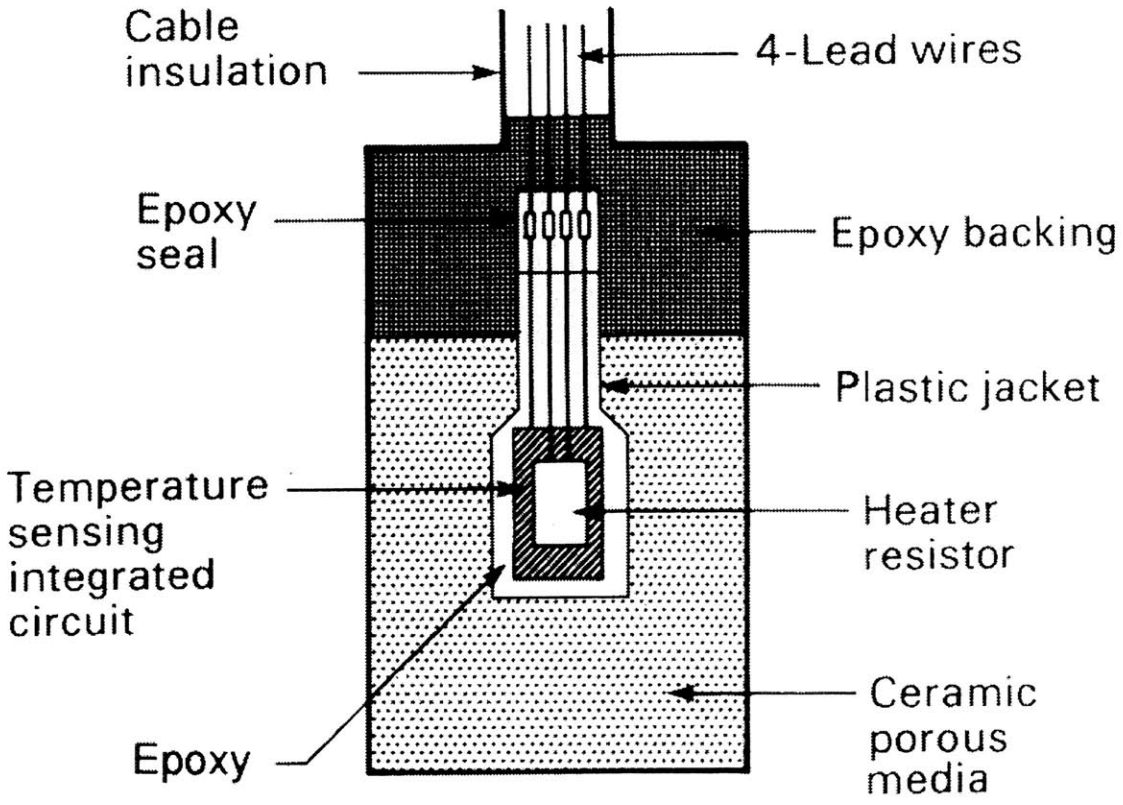

Figure 2-10. AGWA-II Thermal conductivity sensor (after Fredlund and Rahardjo 1993).

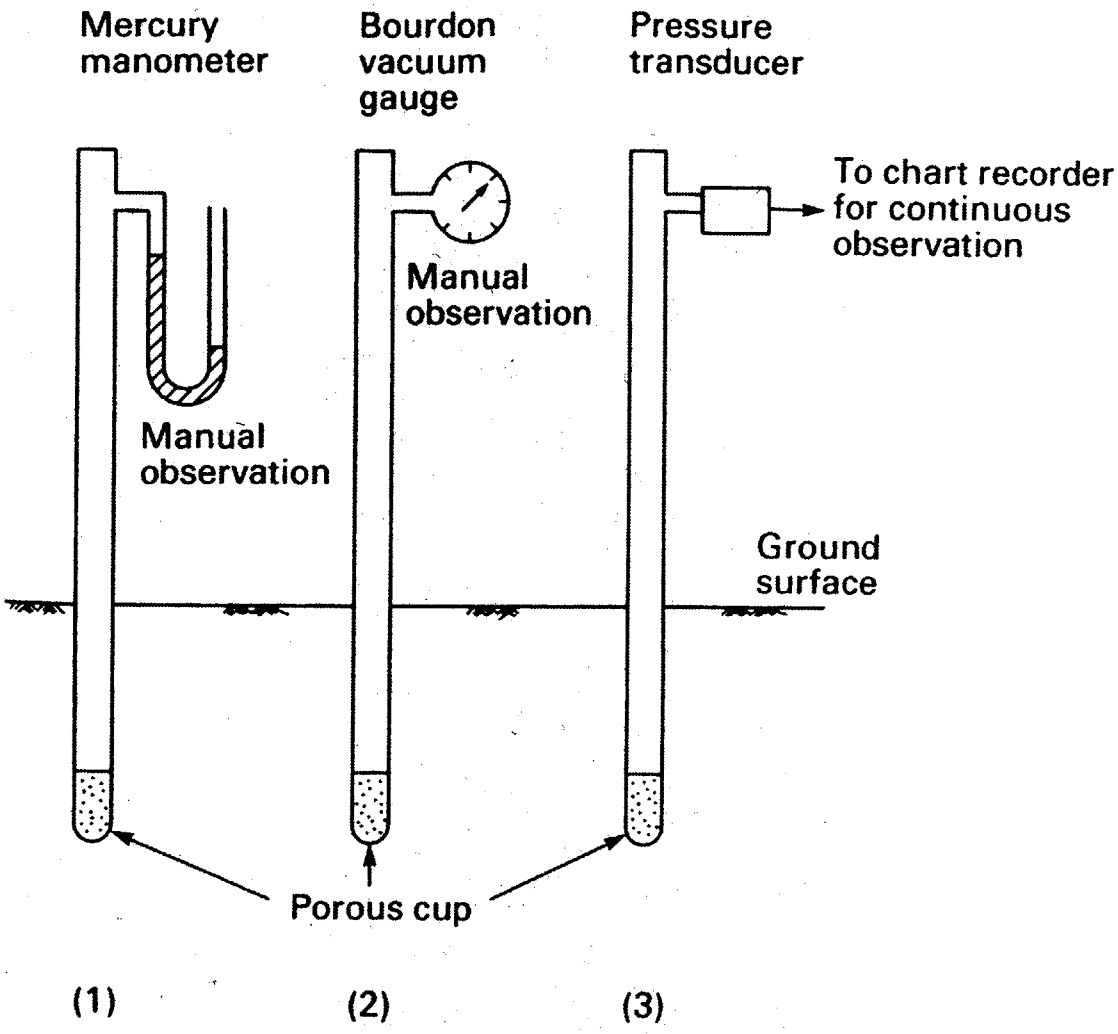

Figure 2-11. Common tensiometers (after Stannard 1992).

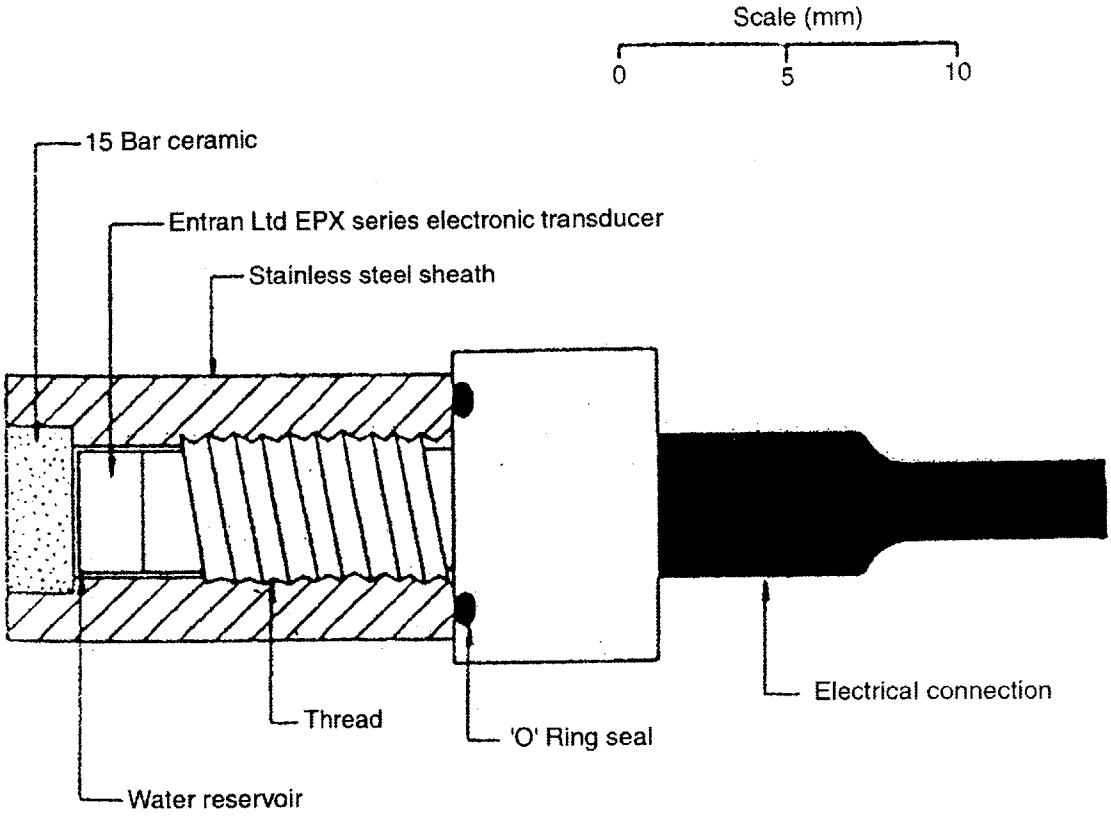

Figure 2-12. New type of tensiometer (after Ridley and Burland 1993).

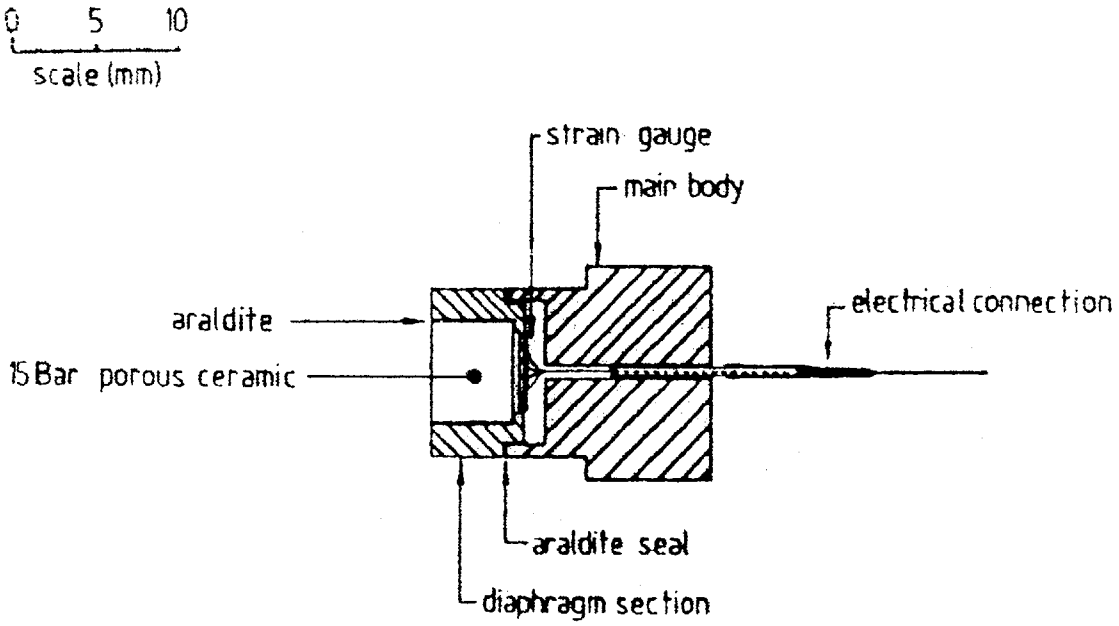

Figure 2-13. Tensiometer design (after Ridley and Burland 1995).

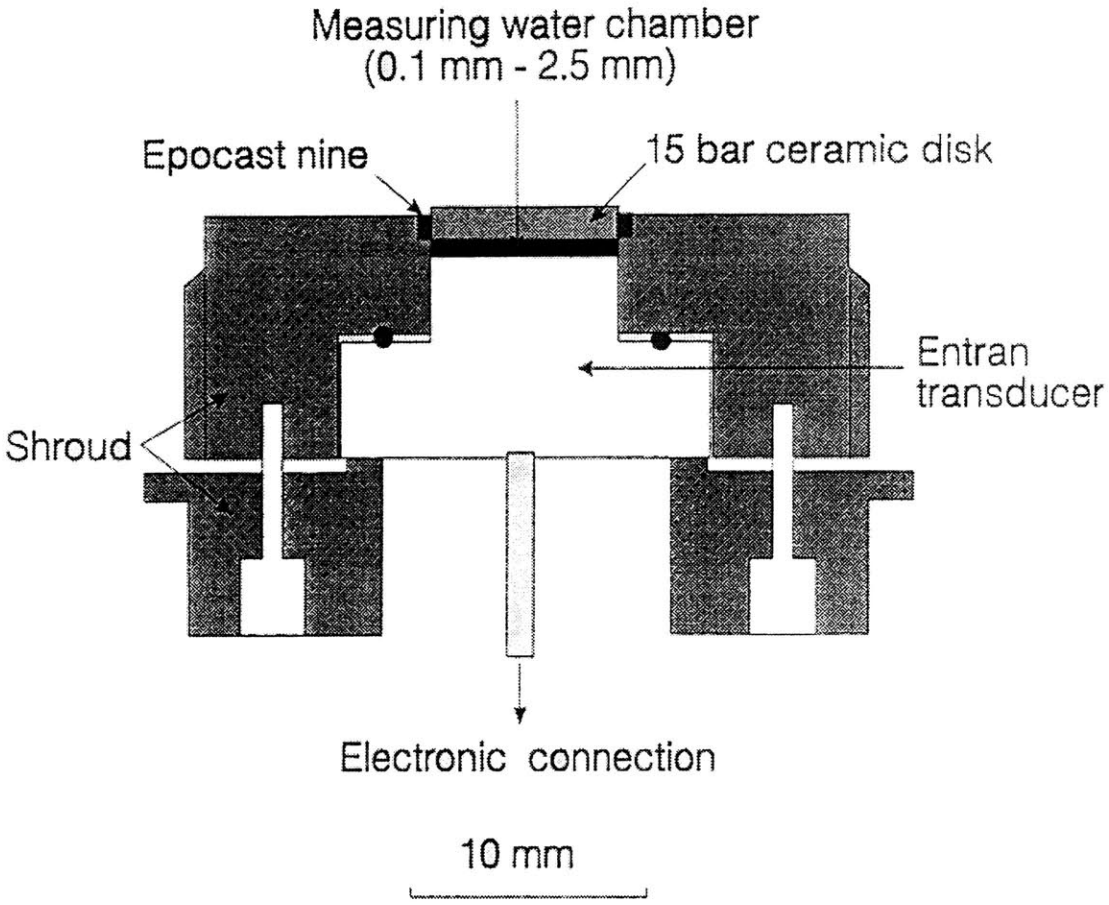

Figure 2-14. Saskatchewan tensiometer (Guan and Fredlund 1997).

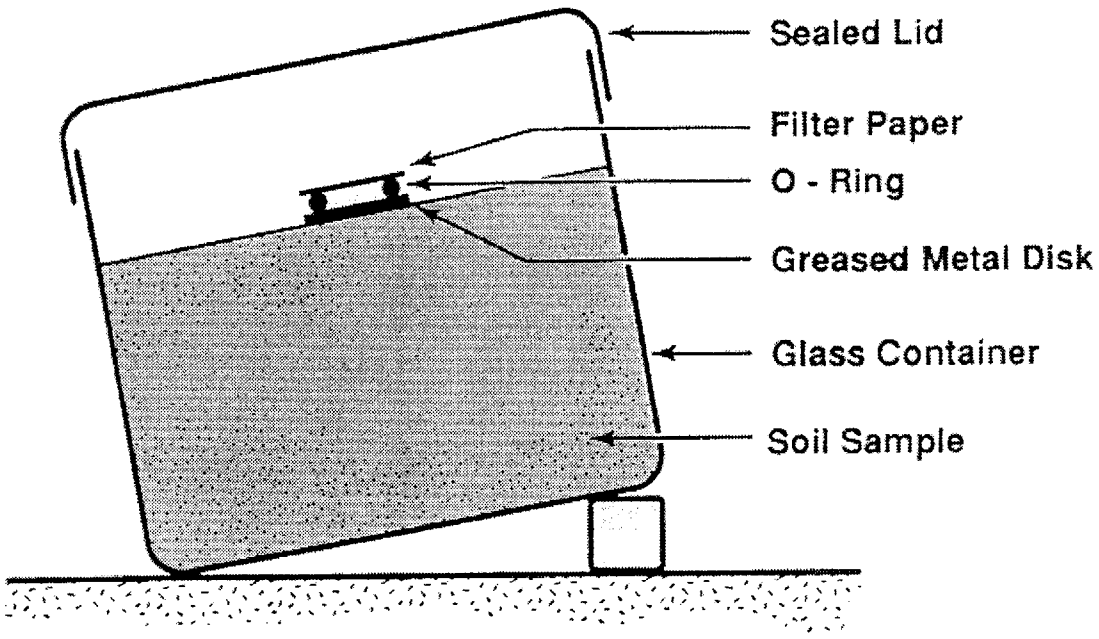

Figure 2-15. Total suction measurement using filter paper (after Houston et al. 1994).

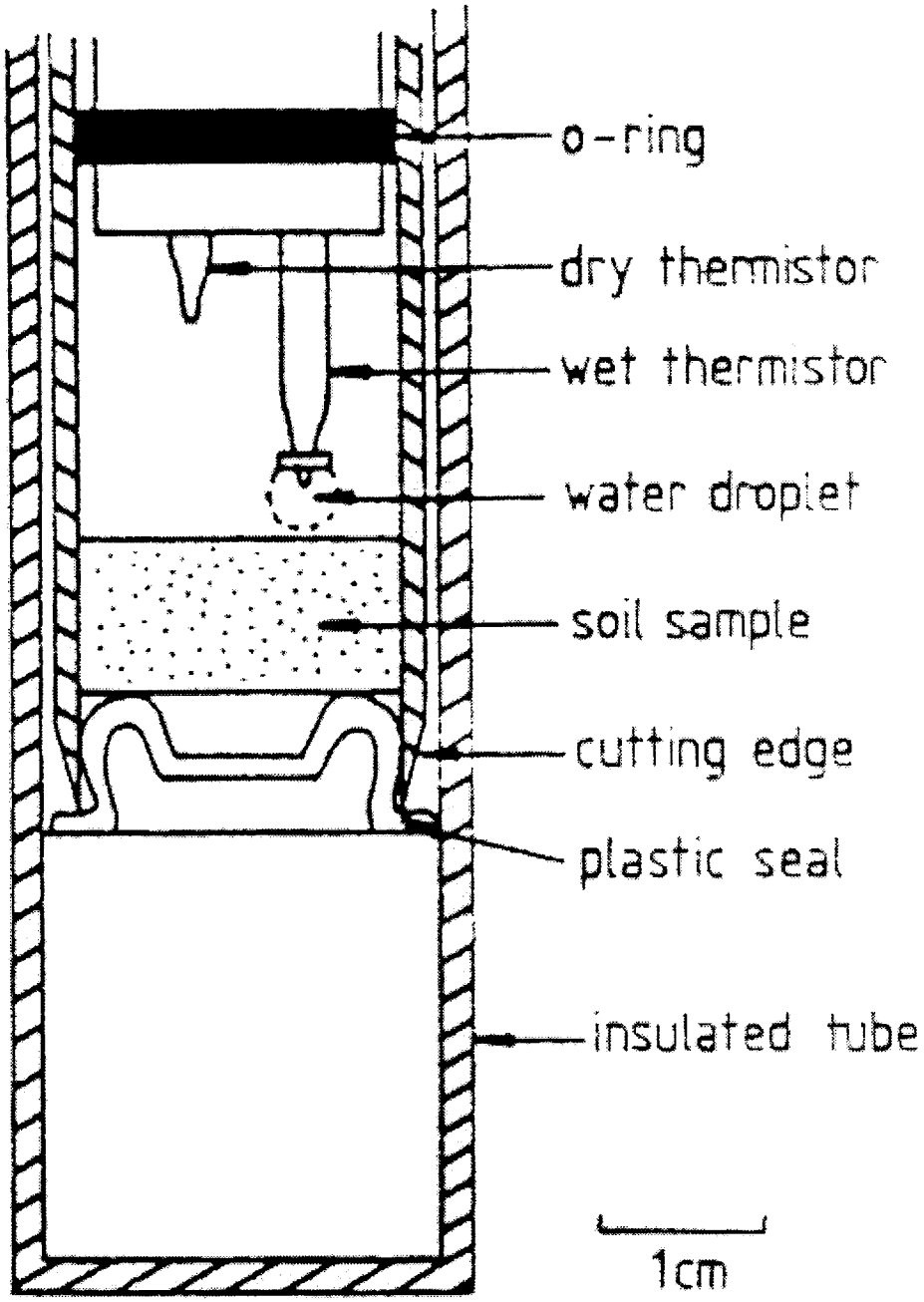

Figure 2-16. Thermister psychrometer (from Ridley and Wray 1996).

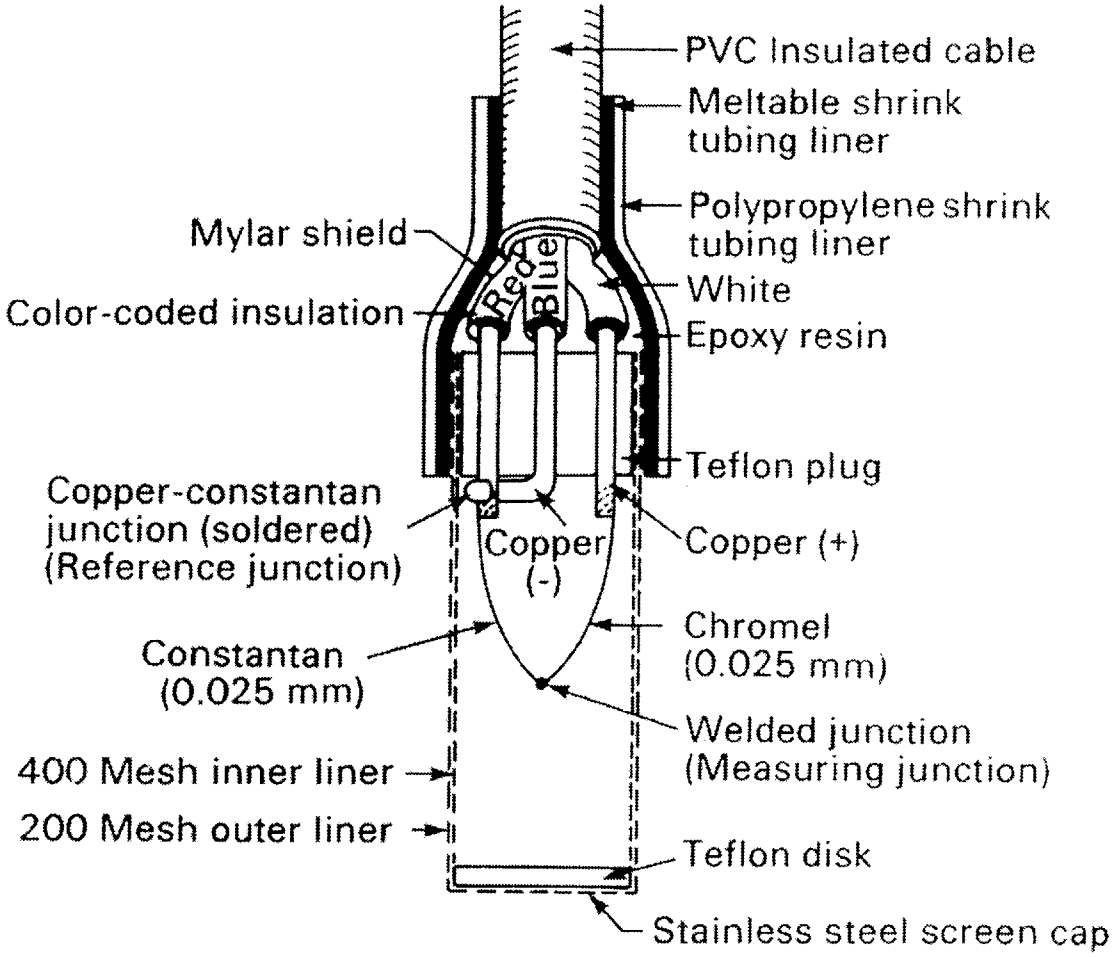

Figure 2-17. Thermocouple psychormeter (Fredlund and Rahardjo 1993).

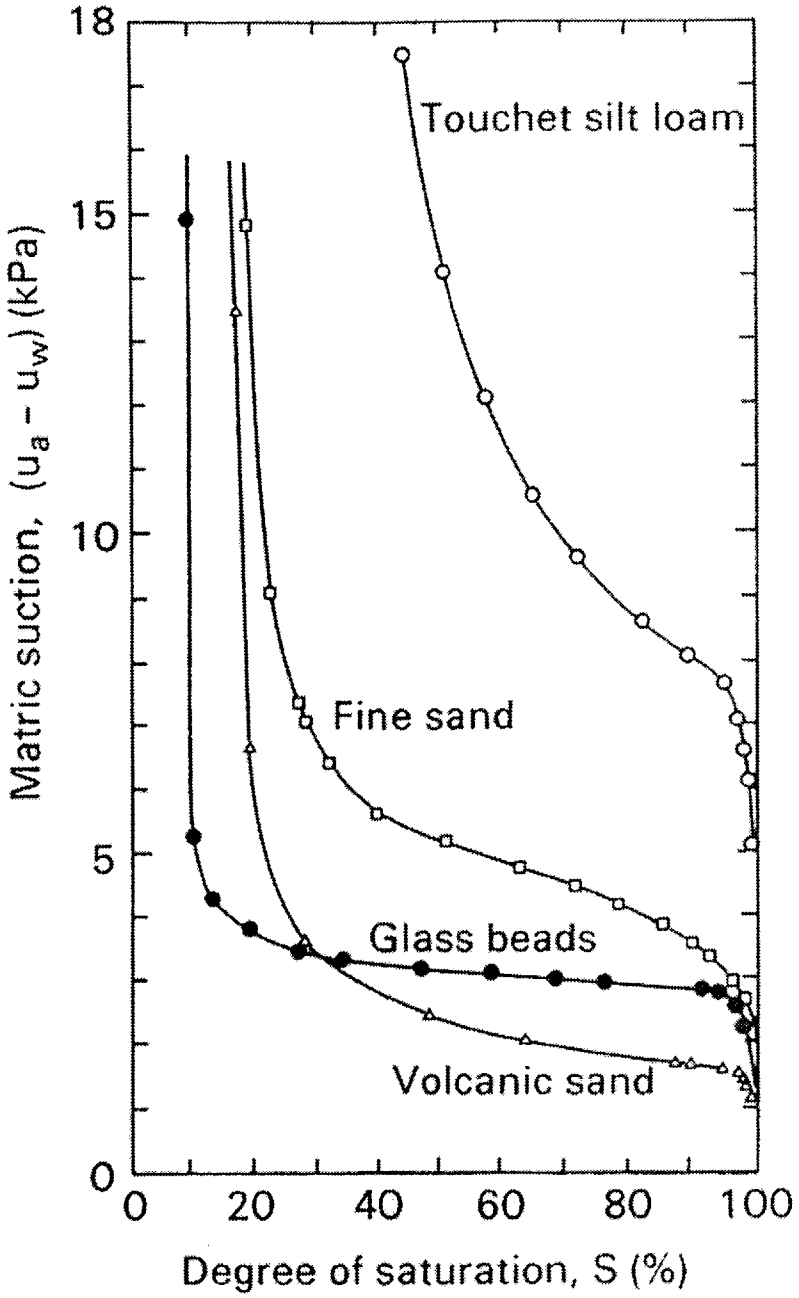

Figure 2-18. Retention curves of various materials (from Brooks and Corey 1966).

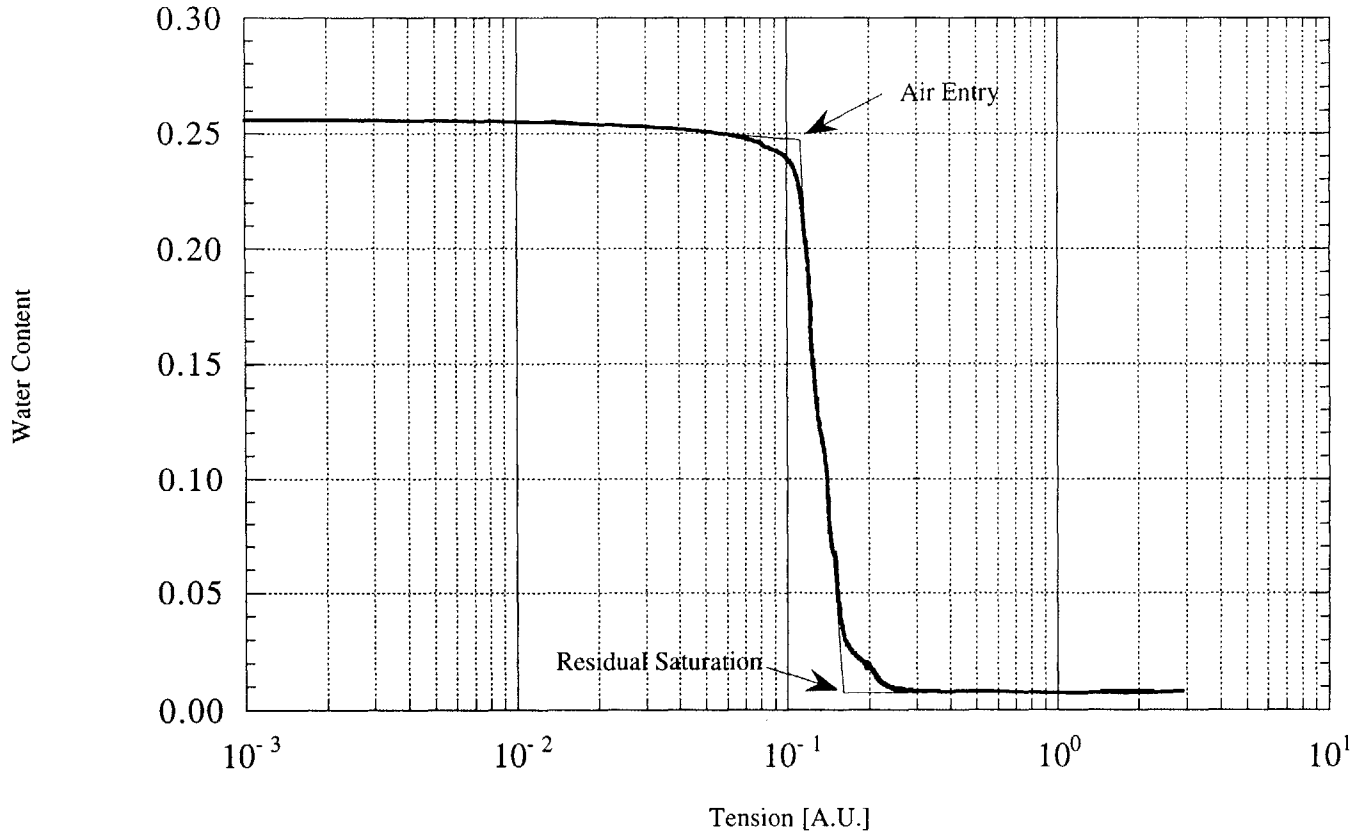

Figure 2-19. General SMC for a porous material with Air Entry and Residual Saturation.

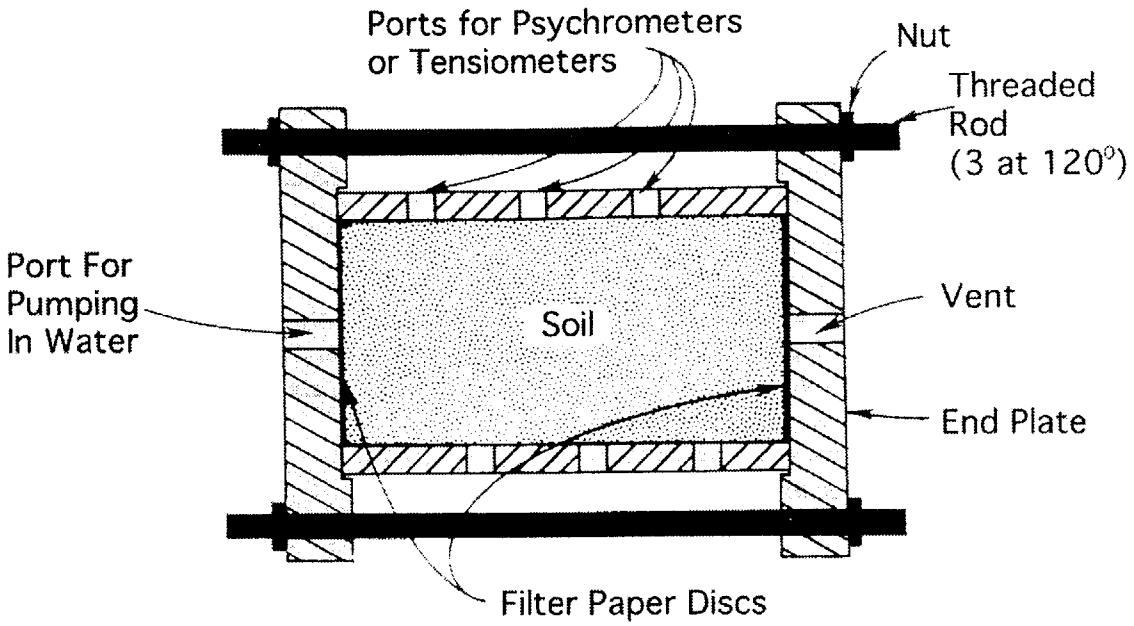

Figure 2-20. Modified permeameter (after Daniel 1983).

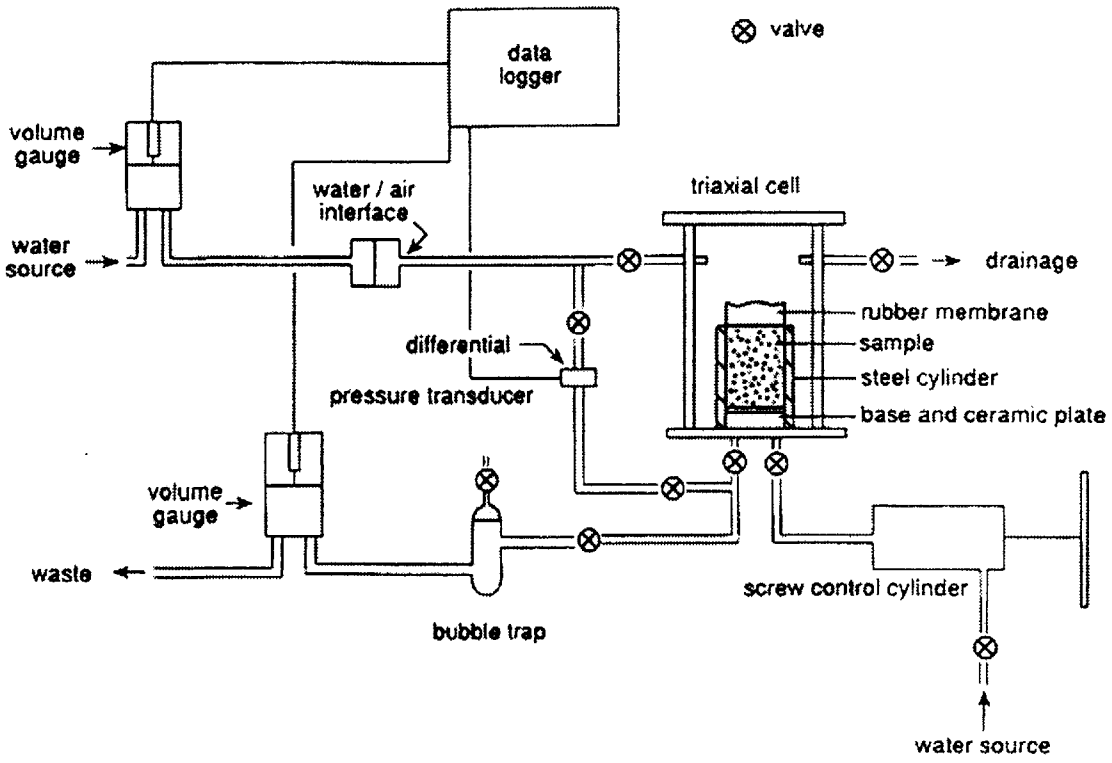

Figure 2-21. Schematic of experimental setup for rapid SMC determination (from Fourie et al. 1995).

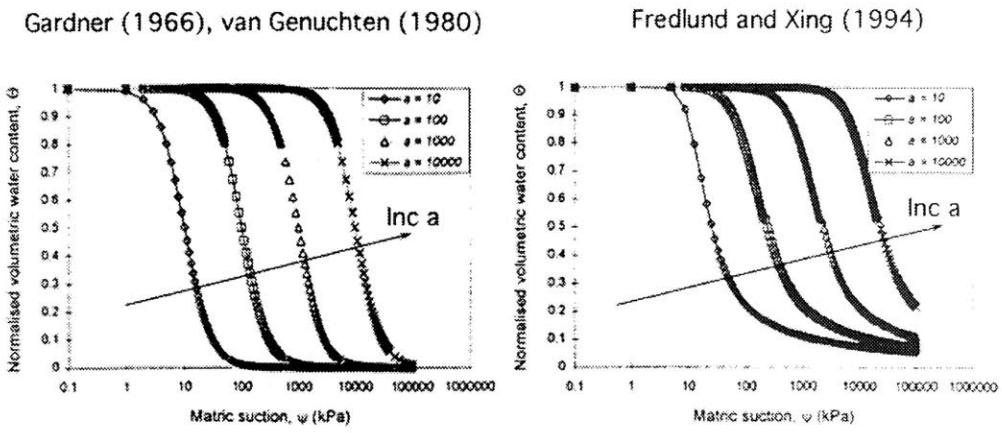

(a) Effect of parameter a with $n = 2$ and $m = 1$

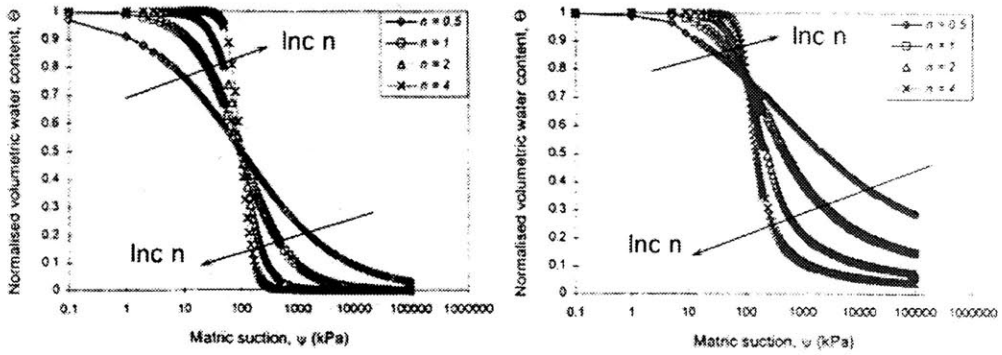

(b) Effect of parameter n with a =100, $m = 1$.

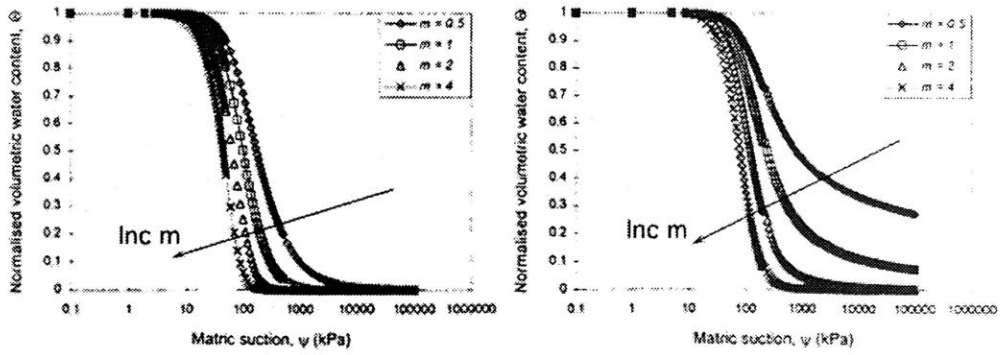

(c) Effect of parameter m with a =100, $n = 2$.

Figure 2-22. SMC model evaluation (after Leong and Rahardjo 1997)

Chapter 3 Desaturation Model

3.1 Introduction

The draining of a porous material has been studied by researches for many years. The process is important in various fields from packed bed reactor design (Mao et al. 1994; Turner and Hewitt 1959) to contaminant transport and migration (e.g. Mayer and Miller 1992). The questions asked are different in each of the fields, however there is a common goal to model the porous medium in an accurate manner.

In general, porous media are described by simple capillary models. These models assume that the porous material is a series or distribution of capillary tubes of varying diameters (Bear and Verruijt 1992; Dullien 1992; Levine and Neale 1974; Levine et al. 1977; Marmur 1992; van Brakel and Heertjes 1977). Various material properties can then be examined empirically. For example, the effective pore diameter governing flow is found to correlate reasonably well with the D_{10} of the grain size distribution (Lambe and Whitman 1969).

Another approach was examined by Mason (1972). Mason assumed all pores in the media were tetrahedral in shape. By using a randomly distributed model to describe the length of each of the six edges of the tetrahedra, each of the four faces of the tetrahedra could be described independently. Mason then assumes that the drainage of the pore will occur when the meniscus of curvature of one of the faces is large enough to allow a sphere of the same curvature to pass through the face. The fluid can drain in the model in two ways, bulk flow from one pore to the other and pendular ring transport. A pendular ring is the saddle shaped geometry resulting from the adhesion of a liquid to two spherical surfaces (see Figure 3-1). Mason concluded that the residual saturation (by volume) of the media reduces from about 9% to 2.8% of saturated cells (pores) when pendular flow is accounted for.

Alternatively, some researchers have assumed that the porous material is comprised of a matrix of packed spheres. This approximation lends to easier math functions to describe the pore structure and any interacting fluids. Fisher (1926) describes a system of regularly packed spheres of equal diameter. Fisher then relates the tensile force to the volume of the water held in the system. Fisher assumes that the water is held at the contacts between the spheres in pendular rings. The surface of the pendular ring is derived as circular (toroidal) in this model.

The desaturation model described in this Chapter makes this assumption of a regular packed media. For a series of regularly packed spheres, the process of drying is examined from a fully saturated medium to partially saturated medium with channels of air formed. The Chapter begins with a brief overview of relevant past work and then derives the model in full detail, first in two dimensions and then extending the model to three.

3.2 Previous Work

3.2.1 Pendular Ring Geometry

The surface of a pendular ring is defined by a series of functions (surfaces) termed nodoids. Nodoids are functions that have constant curvature throughout all or a portion of their arc lengths. Curvature is the change in angle (ϕ) a tangent vector makes with an arbitrary axis at a point on the function with respect to the change in arc length (s). Using vector calculus the curvature, κ is defined by:

$$\kappa = \left| \frac{d\phi}{ds} \right| \qquad [3.1]$$

By convention the curvature is taken as the absolute value of this rate. As an example, all circles have a constant curvature. However, functions other than circles can also have a

constant curvature, if evaluated over a portion of their total arc lengths. Since the curve of interest lies between the points of intersection of the water surface to the spheres, this surface is not necessarily circular. From observations made by Clark et al (1968) and others, the surface of a pendular ring is not circular or toroidal. For ease of calculation, researchers have adopted the toroidal approximation as a starting point. This has been shown by Clark et al to be a very reasonable approximation to the experimental data.

3.2.2 Static Liquid Holdup

A study was conducted by Turner and Hewitt (1959) to determine the amount of liquid that could be sustained by two spheres in contact with each other. Turner and Hewitt glued two spheres to threaded rods. The rods were then mounted in a ring such that the rods and the spheres were on the same axis. The threaded rod allowed for adjusting the distance between the spheres. This allowed for precise control of sphere separation or to bring them in contact with each other. The ring also allowed the axis to be rotated 90° from the horizontal. Two types of spheres were used, glass and steel. The diameters of the steel spheres used were; 0.5, 0.625, 0.75, 0.875 and 1 inches. Two sizes of glass spheres were used, 0.389 and 0.684 inches. Several types of liquids were used in experiments, n-octyl alcohol, paraffin oil, ethylene glycol, glycerol and water.

The experiments were conducted by bringing the spheres in contact with each other at a predetermined axis angle. The liquid was then introduced onto the spheres by injection of a hypodermic syringe. When the excess liquid had drained from the spheres, the adhered liquid was removed by a pre-massed and dried filter paper. This procedure was carried out for various angles of inclination and liquid/sphere combinations. They concluded that when the angle of inclination was greatest (90°), the most liquid was retained in all cases. They also observed that the smaller the sphere, the less the difference in retained mass over the inclination range. Most relevant to this research is the finding that the volume of water held in the pendular ring normalized to the diameter of the glass sphere cubed was equal to 0.0536 and 0.0217 for the 0.389 and 0.684 diameter spheres, respectively.

Another study of the same problem was conducted by Mao (1993; 1994). Mao used a theoretical thermodynamic approach to estimate the maximum retention of a liquid to two spheres in contact with each other. The values obtained by Mao agree closely with the experimental results of Turner and Hewitt (1959).

3.2.3 Liquid Bridge Rupture

Lian et al (1993) describes a theoretical model to determine the maximum separation that two spheres of equal diameter can have while still maintaining a liquid bridge. The liquid bridge is described as a pendular ring. Lian et al uses two separate derivations to solve this problem. The first is a geometric approach using dimensionless parameters. This enables Lian et al to solve the problem without needing to fully describe the actual geometry of the surface of the bridge. The bridge is described in a dimensionless volume and thus, shape is not needed. The second approach Lian et al uses is a free energy approach. By accounting for the total free energy of the system, a maximum separation distance is determined. Both techniques provided the same result. A good approximation of the maximum dimensionless separation, S_c^* as a function of dimensionless volume, V^* is given by:

$$S_c^* \cong \frac{1}{2}\left(1+\frac{\theta}{2}\right)\sqrt[3]{V^*} \qquad [3.2]$$

where;

S_c^* is the dimensionless separation or half the distance between the spheres normalized by the radius of the sphere

V^* is the dimensionless volume or the volume of the pendular ring normalized by the radius of the spheres cubed

θ is the contact angle between the fluid and the spheres expressed in radians

3.2.4 Tensile Force Developed

Fisher (1926) describes a soil model by a regular packing of equal spheres. The water attracted in the pore space of the spheres is held in pendular rings at the contacts between the spheres. Fisher uses a simplified geometry to describe the pendular rings as a toroid.

In order to show the total tensile force developed in the pendular ring between two spheres, Fisher breaks the force into two components. The first component is the tension exerted at the air-water interface. The second component is the force due to the negative pressure in the water acting on the reminder of the sphere. The sum of these forces gives the total force acting between the two spheres. This force, F_T is given by:

$$F_T = \frac{2\pi r T}{1 + \tan\frac{\beta}{2}} \qquad [3.3]$$

where;

T is the surface tension of the water
r is the radius of the sphere
β is the half filling angle (the equivalent of $\alpha/2$ in Figure 3-2)

This force, F_T is the projected force in the axis of the contact point of the spheres. Clark et al (1968) measured the force necessary to pull apart two spheres connected by a water bridge. They also measured the force required to pull a sphere from a plate. Their results are compared to the predictions of Fisher and show very good agreement.

3.2.5 Desaturation

In studying the draining of porous materials, there are some inherent testing effects that need to be addressed. The following sections briefly discuss these effects and some conclusions of previous researchers.

3.2.5.1 Boundary Effects

White (1972) examines the effect of specimen cross-sectional area with respect to volume of the specimen to the resulting desaturation curve. A horizontal permeameter was used with varying head capabilities. Specimens were consolidated sandstone from the Colorado area. Nine types of sandstones were used. Porosity ranged from 0.0863 to 0.240. The fluid used was a petroleum core test fluid obtained from Phillips Petroleum

Company. Physical properties of the fluid are; surface tension = 22.9 dynes/cm, dynamic viscosity = 1.45 centipoises, and density = 0.755 g/ml at room temperature. White found that varying the surface area exposed to the capillary pressure caused up to 15% difference in saturation for a given capillary pressure. The boundary effects were negligible once the specimens were desaturated to a point where air formed continuous channels. At this point it was concluded that fluid loss was uniform throughout the system.

3.2.5.2 Residual Saturation

Numerous researchers have investigated the residual saturation effects upon drying, esp. when considering organic liquids (Adler and Brenner 1988; Bear and Verruijt 1992; Demond and Roberts 1991; Mayer and Miller 1992). In a series of detailed experiments Morrow (1970) found that the residual saturation of packing of discrete particles was about 7% of the pore space, independent of particle size and shape, porosity of the packing and even independent of the composition of mixtures of different particle sizes. If the porosity of the media was decreased by sintering, then the residual saturation increased. Morrow concluded that the residual saturation is not a function of the pore size distribution but rather a function of the degree of consolidation. In other words, different materials would result in the same residual saturation regardless of the grain size distributions. However, if these materials were consolidated, the residual saturation would increase over the unconsolidated state.

3.2.5.3 Adsorbed Layer Effects

Kim (1979) experimentally studied the effects of particle size on the partitioning of adsorbed gas on spherical particles. Kim separated the adsorbed gas into two fractions, the adsorbed layers over all of the particles and the adsorbed gas at the contact points of the spheres. This adsorption (condensate) at the contact points forms a pendular ring. They concluded that the pendular ring condensation became appreciable to the overall adsorption only when the particle size was greater that 800 Å. In other words, the pendular condensate dominates the adsorption for particles greater in diameter than 800

Å. Gvirtzman and Roberts (1991) neglect the adsobed layers of water in their analysis by limiting the spheres to larger than 10^{-3} mm. They found that this did not produce any discernable errors in there analyses.

3.3 Model Derivation

3.3.1 Introduction

The following sections describe a simple model of a draining porous media. The porous media is assumed to be a matrix of regularly packed equal spheres. Inherent to the model is the assumption that the contact angle between the water and the spheres is negligible. A circular function is chosen as the shape of the pendular ring. This assumption has been shown in Section 3.2.1 to be satisfactory in it's approximation to the true surface.

The model is first developed in two dimensions that lay a foundation for the extension to three dimensions. The mathematics involved are basic integral calculus and therefore no reference is given as to the formulations. However, the earliest porous matrix model using regularly packed equal spheres with water attracted at the contacts as pendular rings was given by Haines (1925).

3.3.2 Model Derivation in 2D

Figure 3-2 shows schematically two equal diameter circles adjoining at a point. Two smaller circles are inscribed to the adjoining circles and are tangent to both larger circles. If it is assumed that the larger circles are a 2D representation of spheres of equal diameter, then the smaller circles can describe a radius of curvature of water attracted to the spheres. The attracted water is shown as the shaded area in the figure. As water leaves the system, the radius of curvature will decrease as the smaller circles become smaller and approach the adjoining point of the larger circles. This process can be easily modeled in this system by varying the angle $\alpha/2$. Mathematically $\alpha/2$ must be in the

range of $\pi/2 > \alpha/2 > 0$, however it will be shown that the range of $\alpha/2$ will be much less.

From the figure it can be seen that the cosine of the angle $\alpha/2$ is given by:

$$\cos\frac{\alpha}{2} = \frac{R}{R+r} \qquad [3.4]$$

where;

r is the radius of curvature of the tangent circle
R is the radius of the adjoining circles
$\alpha/2$ is the angle between the centers of the adjoining circle and tangent circle

Solving Equation [3.4] for the radius of curvature, r yields:

$$r = \frac{R\left[1-\cos\left(\frac{\alpha}{2}\right)\right]}{\cos\left(\frac{\alpha}{2}\right)} \qquad [3.5]$$

Once the radius of curvature, r is determined, the equivalent suction of the water can be calculated by use of the Capillary Equation (Bear and Verruijt 1992):

$$u_w = \frac{2\sigma\cos\theta}{r} \qquad [3.6]$$

where;

u_w is the tension of the water
σ is the surface tension of water
θ is the contact angle between the water and the surface of the circle
r is the radius of curvature of the water

Substitution of Equation [3.5] into Equation [3.6] yields an expression for the tension of the water in terms of α and R:

$$u_w = \frac{2\sigma\cos\theta\cos\left(\frac{\alpha}{2}\right)}{R\left[1-\cos\left(\frac{\alpha}{2}\right)\right]} \qquad [3.7]$$

3.3.2.1 Area Calculations

The area occupied by the water between the adjoining circles can be calculated by integrating the functions of the curves that bound the shaded region. Referring to Figure 3-2, it can be seen that the shaded region is axisymmetric about the x-axis. By considering only the shaded portion in the first quadrant, the entire area can be found by multiplying the result by 4. Assuming that the origin lies at the adjoining point of the larger circles, the equation for the larger circle in the figure is given by:

$$x^2 + (y - R)^2 = R^2 \qquad [3.8]$$

The equation of the smaller circle is given by:

$$(x - a)^2 + y^2 = r^2 \qquad [3.9]$$

where a is the location of the center of the circle on the x-axis.

The entire shaded area can be found by the integral:

$$A = 4\iint_R dx\,dy \qquad [3.10]$$

where R is the region bounded by x-axis, Equation [3.8] and Equation [3.9].

Evaluation of Equation [3.10] over the proper limits yields the following result:

$$A_w = \frac{R^2\left[2\sin\left(\frac{\alpha}{2}\right)\cos\left(\frac{\alpha}{2}\right) - \pi + 2\pi\cos\left(\frac{\alpha}{2}\right) - \pi\cos^2\left(\frac{\alpha}{2}\right) + \alpha - 2\alpha\cos\left(\frac{\alpha}{2}\right)\right]}{\cos^2\left(\frac{\alpha}{2}\right)} \quad [3.11]$$

3.3.2.1.1 Area Water Content

To give a relation in 2 dimensions between the amount of water in the system and the amount of matrix material, a water content based on areas can be formed. The area water content, w_a can be defined as:

$$w_a = \frac{A_w}{A_c} \quad [3.12]$$

where;

w_a is the area water content
A_w as defined before
A_c is the area of the circle

Substitution of the appropriate terms into Equation [3.12] gives an expression for the area water content in terms of α only:

$$w_a = \frac{2\sin\left(\frac{\alpha}{2}\right)\cos\left(\frac{\alpha}{2}\right) - \pi + 2\pi\cos\left(\frac{\alpha}{2}\right) - \pi\cos^2\left(\frac{\alpha}{2}\right) + \alpha - 2\alpha\cos\left(\frac{\alpha}{2}\right)}{\cos^2\left(\frac{\alpha}{2}\right)\pi} \quad [3.13]$$

Assigning an appropriate value of contact angle and surface tension to Equation [3.7] permits a parametric plot to be constructed from Equations [3.7] and [3.13] for any given value of R. Figure 3-3 shows the relation between *area water content* and water tension for circles having radii of 1mm.

3.3.3 Model Derivation in 3D

Figure 3-4 shows two spheres of equal radii. Using this as a basis for more complicated arrangement of spheres, basic derivations of volumes of water can be examined. The same basic ideas in the 2D case can be applied in 3D, however slightly different methods are required. As done previously, basic geometric relations will be introduced to form the framework for a parametric relation between amount of water held between the spheres and the associated tension in the held water.

3.3.3.1 Volume Calculations

Two volumes need to be examined in the two sphere system of Figure 3-4. These two volumes are presented in the following sections.

3.3.3.1.1 Water Volume

In order to calculate the volume of water held between the spheres the shaded area of Figure 3-2 needs to be integrated over 2π radians. This is most easily accomplished by taking 1/4 of the shaded area and rotating this area about the y–axis. The resulting volume of revolution is then doubled to determine the full volume of the saddle-shaped water. This saddle shape is commonly referred to as a pendular ring (Bear and Verruijt 1992). This shape is most easily integrated by the method of cross sections (Edwards and Penney 1990). The general form of the integral is given by:

$$V_w = 2\int_R \pi[x_{Right}^2 - x_{Left}^2]dy \qquad [3.14]$$

Substitution of Equations [3.8] and [3.9] into Equation [3.14] yields:

$$V_w = \frac{R^3\pi\left[\cos\left(\frac{\alpha}{2}\right)-1\right]^2\left[2\cos\left(\frac{\alpha}{2}\right)-\sin\left(\frac{\alpha}{2}\right)\pi+\sin\left(\frac{\alpha}{2}\right)\alpha\right]}{\cos^3\left(\frac{\alpha}{2}\right)} \qquad [3.15]$$

3.3.3.1.2 Sphere Volume

The total volume of the spheres involved reduces to the volume of a single sphere since h in Figure 3-2 equals $2R$ when $\alpha = \pi$. This indicates that the smallest unit of sphere required to model the system is one single sphere, or a *unit sphere*. Therefore the volume of the sphere (matrix material) is:

$$V = \frac{4}{3}\pi R^3 \qquad [3.16]$$

3.3.3.2 Volume Water Content

A new relation for a 3D system of spheres between the amount of water and amount of matrix material can be presented as the *volume water content*. The *volume water content* can be expressed by:

$$W_v = \frac{V_{water}}{V_{matrix}} \qquad [3.17]$$

Substitution of Equations [3.15] and [3.16] into Equation [3.17] gives the following:

$$W_v = \frac{3}{4}\frac{\left[\cos\left(\frac{\alpha}{2}\right)-1\right]^2\left[2\cos\left(\frac{\alpha}{2}\right)-\sin\left(\frac{\alpha}{2}\right)\pi+\sin\left(\frac{\alpha}{2}\right)\alpha\right]}{\cos^3\left(\frac{\alpha}{2}\right)} \qquad [3.18]$$

Defining the *volume water content* in this fashion makes for a convenient means to convert to the more common mass based water content. Conversion between the two types of water contents is given by:

$$w = \frac{W_v}{G_s} \qquad [3.19]$$

where;

G_s is the specific gravity of the matrix material
w is the gravimetric water content

As done previously in Section 3.3.2.1.1, values of surface tension and contact angle are applied to Equation [3.7] and a parametric plot is created relating capillary tension and volume water content for a given radius of sphere. Figure 3-6 plots water tension versus volume water content for spheres of equal radii of 1 mm. Due to the unit system being one sphere, this would correspond to an infinitely long assemblage of spheres in contact with centers aligned along a single line.

3.3.4 Tension of Pendular Ring

In order to predict the tension of the water held in the pendular rings, a modification needs to be made to Equation [3.6]. There are two radii that need to be considered. One is the radius of the tangent circle in Figure 3-2. The other is the radius of the tangent circle to the point of adjoining of the spheres. This second radius is measured from the point of adjoining to the tangent circle. This is the radius of revolution as described in Section 3.3.3.1.1. Following the derivation for a membrane of differing radii, a small element of the saddle is considered (Bear and Verruijt 1992).

Shown in Figure 3-5 is a differential element of the saddle with width, *ds* and height *dn*. If the radii of curvatures for the two opposing curves are r and $\tilde{R}$, then the resulting tension in the membrane, u_m is given by (assuming the surface contact angle is zero):

$$u_m = \sigma\left(\frac{1}{r} - \frac{1}{\tilde{R}}\right) \qquad [3.20]$$

The radius, $\tilde{R}$ can be related to r and α by:

$$\tilde{R} = (R + r)\sin\left(\frac{\alpha}{2}\right) - r \qquad [3.21]$$

Substitution of Equations [3.5] and [3.21] into Equation [3.20] gives an expression for the tension in the pendular ring in terms of R and α. Equation [3.20] becomes:

$$u_m = \frac{\sigma}{2}\frac{\left[1 + \sin\left(\frac{\alpha}{2}\right) - 3\cos\left(\frac{\alpha}{2}\right)\right]}{R\left[\cos\left(\frac{\alpha}{2}\right) - 1\right]} \qquad [3.22]$$

From Equation [3.22] it can be seen that the value of the tension predicted in the pendular ring model is substantially smaller than that predicted with a simple capillary model. Figure 3-6 compares the predictions of the two models assuming the radius and surface tension in both models the same. As can be seen, the pendular model gives a lower tension for a given volume water content. It should also be noted that the pendular model starts at a much lower water content. This is due to the fact that for values of α greater than 1.855 radians, r is larger than $\tilde{R}$, thus giving a negative value for Equation [3.22]. This fact becomes more evident if the limits of the two radii are considered:

$$\lim_{\alpha \to \pi} \Rightarrow \begin{cases} \tilde{R} \to 1 \\ r \to \infty \end{cases} \qquad [3.23]$$

A plot of the normalized saddle radii to the sphere radius (R) versus α is shown in Figure 3-7. This plot puts an upper limit on α at 1.855 radians. This is in close agreement with the published experimental data of Section 3.2.2.

3.3.5 Sphere Packing

The arrangement of the particles is another important consideration. In order to investigate this effect one basic packing scheme is discussed in the following section.

Cubic packing is examined, as it is the simplest regular packing to analyze. A variation of the packing is also examined by adding a regular spacing between the spheres.

3.3.5.1 Cubic Packing

The simplest arrangement for spheres of equal radii is cubic packing or orthogonal packing. The packing is characterized by each sphere having six tangent neighbors. Each of the tangent spheres has their centers at orthogonal positions to one another. This arrangement is shown in Figure 3-8 with the corners of the box representing locations of the centers of the spheres. As shown in the figure, the face angles *a, b,* and *c* are at right angles to each other with sides *l, w,* and *h* equal to $2R$. This is the smallest unit needed to construct a system of orthogonally packed spheres. This cubic unit consists of eight - 1/8 spheres at the corners with a unit void space occupying the center regions. Figure 3-9 shows the cubic unit with the sphere centers at the corners. This arrangement has spatial properties shown in Table 3-1.

3.3.5.1.1 Tension developed

Inscribing a circle on a face of the cube of Figure 3-9 gives the initial geometry of the pendular rings of each of the spheres. This occurs at an α angle of $\pi/2$ since any larger angle would cause the pendular rings to overlap. Thus this inscribed circle can be used to calculate an entry pressure. This *rooting* radius of the inscribed circle is given by:

$$r = \left(\sqrt{2} - 1\right)R \qquad [3.24]$$

By assuming that the rooting radius predicts the initial geometry of the pendular rings when draining of the pores is incipient, a complete characteristic drying curve can be calculated by varying α from $\pi/2$ to 0 and using Equations [3.18] and [3.22]. A plot of volume water content versus tension is given in Figure 3-10 for spheres of 1 mm radii. As shown in the Figure, the volume water content remains constant until the entry pressure is reached, at this point all of the water that is not held in pendular rings is

released. Continued desaturation occurs, as the pendular rings become smaller thus increasing the tension in the water. For comparison, the figure also plots a retention curve based on the capillary model. Clearly, the capillary model predicts larger tensions held in the spheres for the same volume water content.

3.3.5.2 Cubic Packing with Spacing

A slight variation of cubic packing can be examined by placing a small separation, d between the spheres. This spacing is a rough estimation of changing relative density. By adding spacing, the overall relative density decreases. As shown in Figure 3-11, two spheres of equal radii are separated by a distance, d. Using the approach of Section 3.3.3, the same types of relations can be formed. The concave radius of the pendular ring is now given by:

$$r = -\frac{1}{2}\frac{2\cos\left(\frac{\alpha}{2}\right)R - 2R - d}{\cos\left(\frac{\alpha}{2}\right)} \qquad [3.25]$$

Similarly the convex radius of the pendular ring is given by:

$$\tilde{R} = \frac{1}{2}\frac{2\sin\left(\frac{\alpha}{2}\right)R + \sin\left(\frac{\alpha}{2}\right)d + 2\cos\left(\frac{\alpha}{2}\right)R - 2R - d}{\cos\left(\frac{\alpha}{2}\right)} \qquad [3.26]$$

Inserting Equations [3.25] and [3.26] into Equation [3.20] gives the expression for the tension held in the pendular ring as:

$$u_m = -2\frac{\sigma\cos\left(\frac{\alpha}{2}\right)\left\{2R\left[\sin\left(\frac{\alpha}{2}\right)+2\left(\cos\left(\frac{\alpha}{2}\right)-1\right)\right]+d\left[\sin\left(\frac{\alpha}{2}\right)-2\right]\right\}}{\left\{2R\left[\cos\left(\frac{\alpha}{2}\right)-1\right]-d\right\}\left\{2R\left[\sin\left(\frac{\alpha}{2}\right)+\cos\left(\frac{\alpha}{2}\right)-1\right]+d\left[\sin\left(\frac{\alpha}{2}\right)-1\right]\right\}} \qquad [3.27]$$

Applying Equation [3.14] to this system gives the volume of water held in the pendular ring. This is given by:

$$V_w = \frac{1}{8}\frac{\pi(2R+d)\left[2R+d-2\cos\left(\frac{\alpha}{2}\right)R\right]^2\left[2\cos\left(\frac{\alpha}{2}\right)-\sin\left(\frac{\alpha}{2}\right)\pi+\sin\left(\frac{\alpha}{2}\right)\alpha\right]}{\cos^3\left(\frac{\alpha}{2}\right)} \quad [3.28]$$

Equations [3.27] and [3.28] simplify to Equations [3.15] and [3.22] when $d = 0$.

3.3.5.2.1 Range of d

The spacing variable d is examined in this section. It is expected that d has a maximum length that is less than $2R$. At this point, another sphere of radius R would be able to fit into this space. To examine this maximum distance, it is assumed that the minimum tension in the pendular ring occurs at a maximum spacing. This minimum tension is set to zero. By setting Equation [3.20] equal to zero it is found that the two radii of the pendular ring become equal. Therefore setting Equations [3.25] and [3.26] equal to each other and solving for d yields:

$$d = \frac{2R\left[2-2\cos\left(\frac{\alpha}{2}\right)-\sin\left(\frac{\alpha}{2}\right)\right]}{\sin\left(\frac{\alpha}{2}\right)-2} \quad [3.29]$$

To determine a maximum value of d the partial derivative with respect to α of Equation [3.29] is taken and set equal to zero. This gives:

$$\frac{\partial d}{\partial \alpha} = 2\frac{2\sin\left(\frac{\alpha}{2}\right)-1}{\cos^2\left(\frac{\alpha}{2}\right)+4\sin\left(\frac{\alpha}{2}\right)-5} = 0 \quad [3.30]$$

Solving Equation [3.30] for α gives a value of $\pi/3$. This value of α gives a maximum d of:

$$d_{\max} = \frac{4}{3}R\left(\sqrt{3} - \frac{3}{2}\right) \qquad [3.31]$$

The practical result of Equation [3.31] is that any separation greater than approximately $0.309R$, no pendular ring will develop and thus no tension between the particles. The variation of d with α is shown in Figure 3-12. From the Figure it is clear that for a given spacing there are two geometry's of pendular ring which gives zero tension.(except at d_{max}). This represents a range of α over which for a given R and d the tension can be evaluated. The lower limit of α indicates the limit at which the concave radius of the pendular ring r intersects the axis of sphere centers. At this point the pendular ring is no longer geometrically stable.

3.3.5.2.2 Unit void with spacing

By adding a uniform spacing, d to the unit void of Section 3.3.5.1, the system expands to the unit void shown in Figure 3-13. The unit void has a side length of $2R+d$ and a volume of $(2R+d)^3$. The inscribed circle shown has a rooting radius equal to:

$$r = \frac{\sqrt{2}(2R+d) - 2R}{2} \qquad [3.32]$$

As before, a theoretical plot of the retention curve can be calculated for a given sphere radius R and spacing d. Figure 3-14 plots several spacing lengths for a system of spheres with radii equal to 1 mm. As shown in the Figure, as the spacing becomes larger, the entry pressure decreases significantly. It should also be observed that the residual water content also increases significantly with respect to packing without any spacing. Figure 3-15 plots spheres of various radii with a constant spacing equal to $0.1R$.

3.3.5.2.3 Density of unit void

To quantitatively define the spacing of the unit void, the unit void density is introduced. The unit void density is a measure of the separation of spheres since the cubic packing is assumed to hold. It is defined as the mass of the matrix material divided by the volume of the unit void:

$$\rho_{uv} = \frac{M_m}{V_{uv}} \qquad [3.33]$$

where;

M_m is the mass of the matrix material
V_{uv} is the volume of the unit void

Equation [3.33] can be rewritten to include the specific gravity of the solid material. This provides a more convenient means of comparing different types of matrix materials. Rewriting Equation [3.33] in terms of specific gravity, G_s and the dimensions of the void gives:

$$\rho_{uv} = \frac{4}{3}\frac{\pi R^3 G_s}{(2R+d)^3} \qquad [3.34]$$

It should be noted that Equation [3.34] reduces to Equation [3.35] when $d = 0$:

$$\rho_{uv} = \frac{\pi}{6} G_s \qquad [3.35]$$

Table 3-1. Spatial properties of packing schemes.

Packing System	Face Angles a,b,c	Face Length l,w,h	Coordination Number	Unit Volume	Matrix Volume	Void Volume	Porosity n	Void Ratio e	Layer Spacing
Cubic	$\pi/2$	2R	6	$8R^3$	$4/3\pi R^3$	$4/3(6-\pi)R^3$	$1-\pi/6$	$6/\pi-1$	2R
Cubic with spacing, d	$\pi/2$	2R+d	6	$(2R+d)^3$	$4/3\pi R^3$	$(2R+d)^3-4/3\pi R^3$	na	na	2R+d

na - not applicable: porosity and void ratio not easy expressed

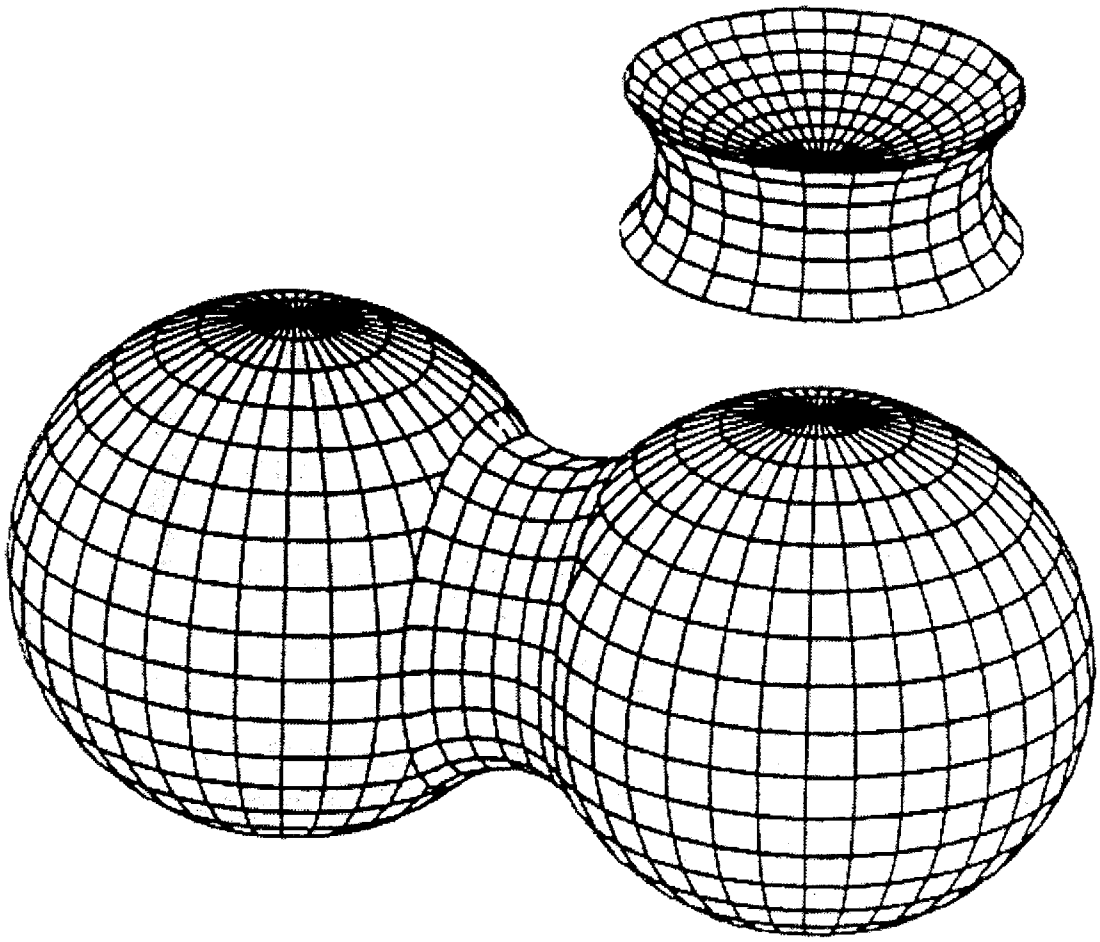

Figure 3-1. Pendular ring formed between two spheres of equal diameter (from Gvirtzman and Roberts 1991).

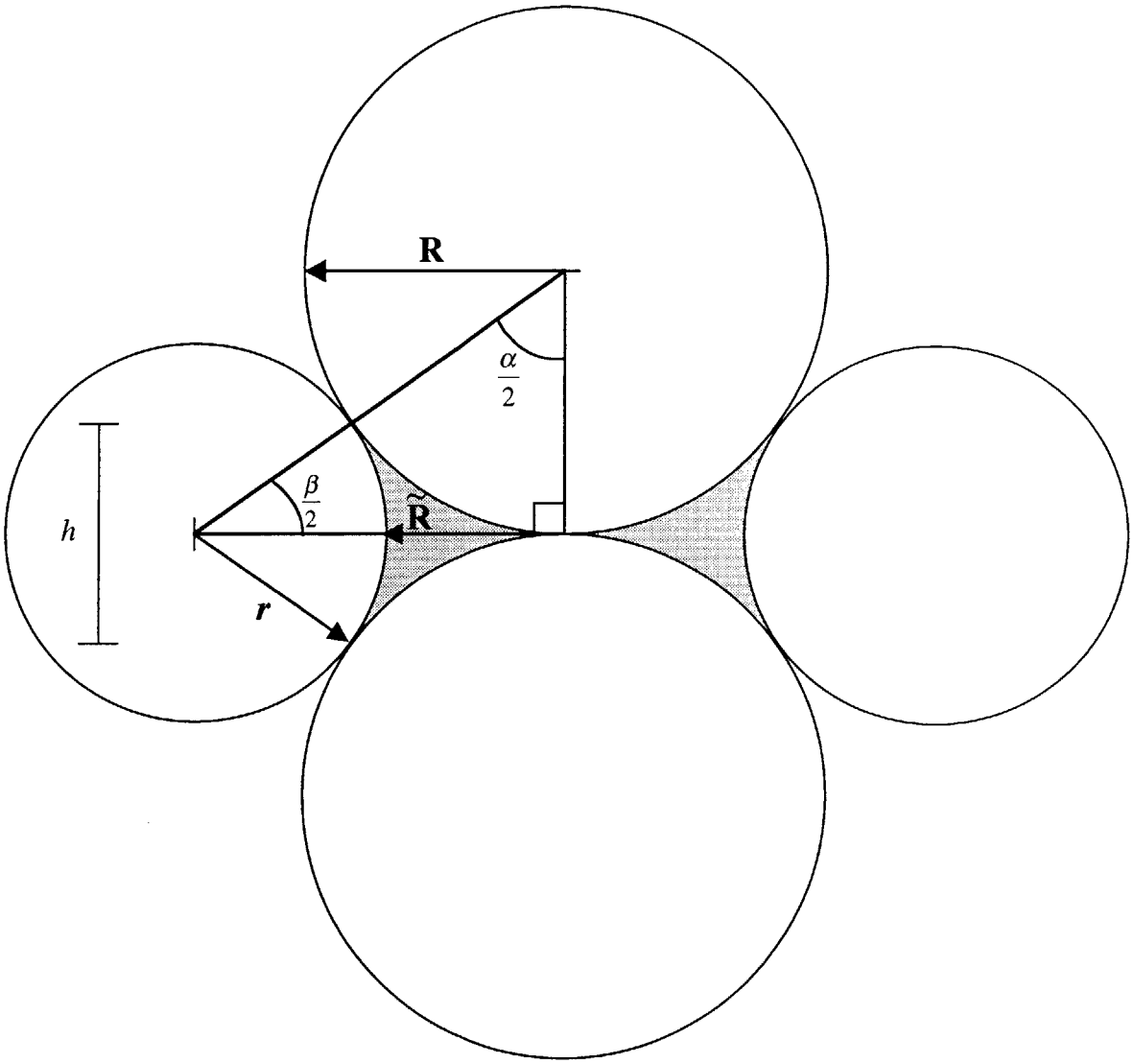

Figure 3-2. Geometric relations for maximum curvature of a tangent circle to two adjoining circles.

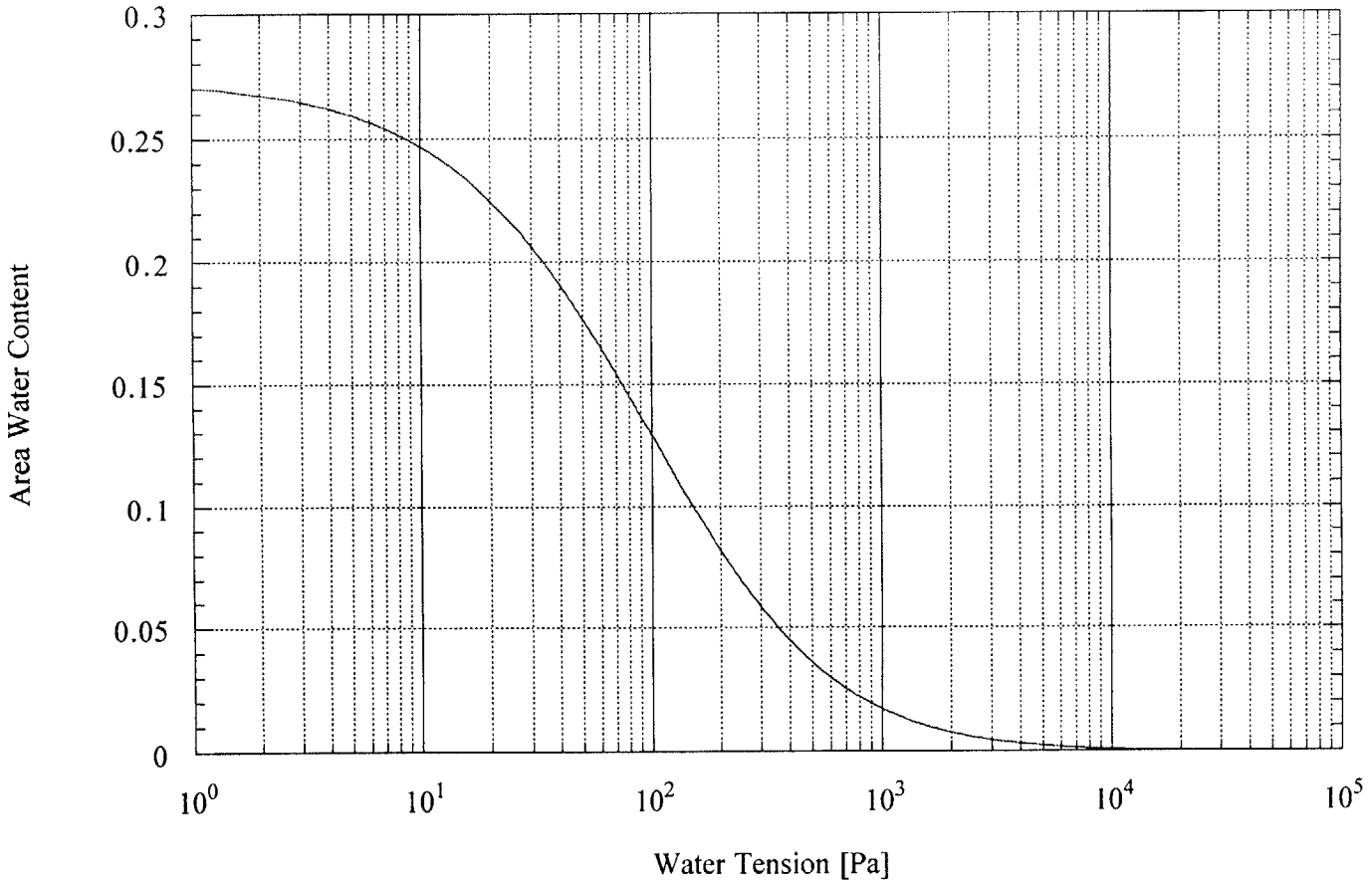

Figure 3-3. Calculated retention curve based on 2D predictions for circles of 1 mm radii.

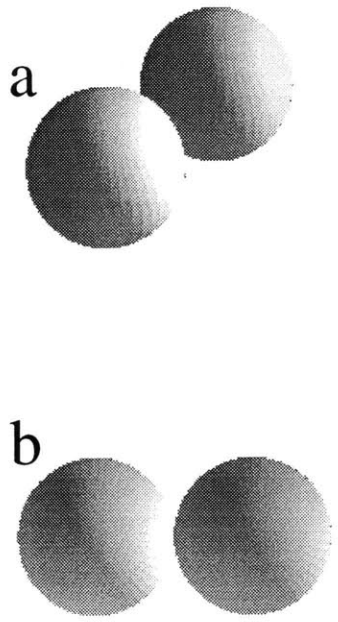

Figure 3-4. Two spheres of equal size in (a) perspective and (b) orthogonal views.

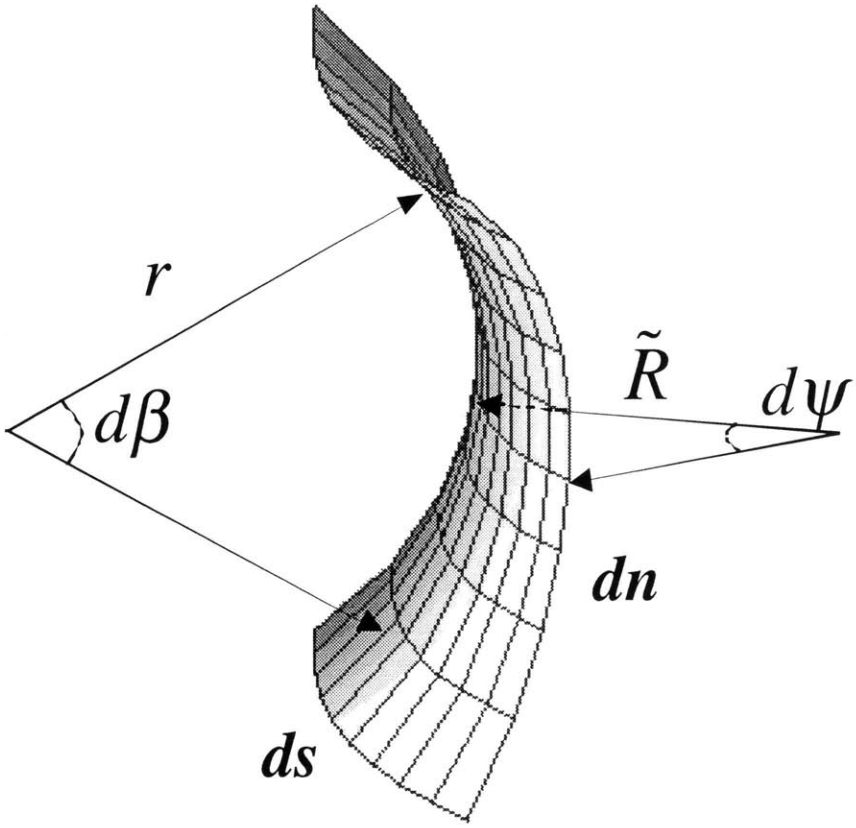

Figure 3-5. Section of saddle surface for tension derivation.

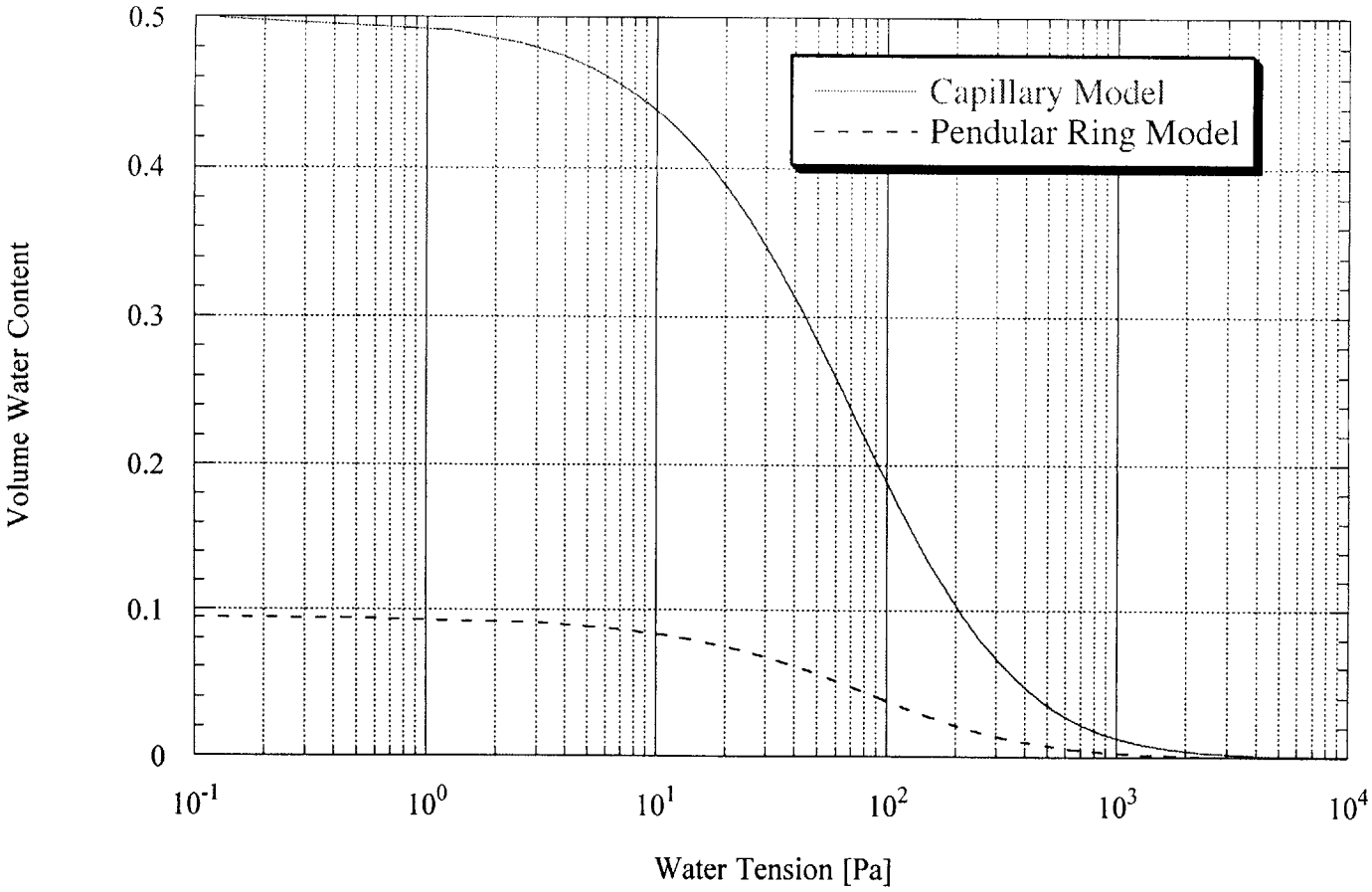

Figure 3-6. Comparison of Capillary Model and Pendular Ring Model for spheres of 1 mm radii.

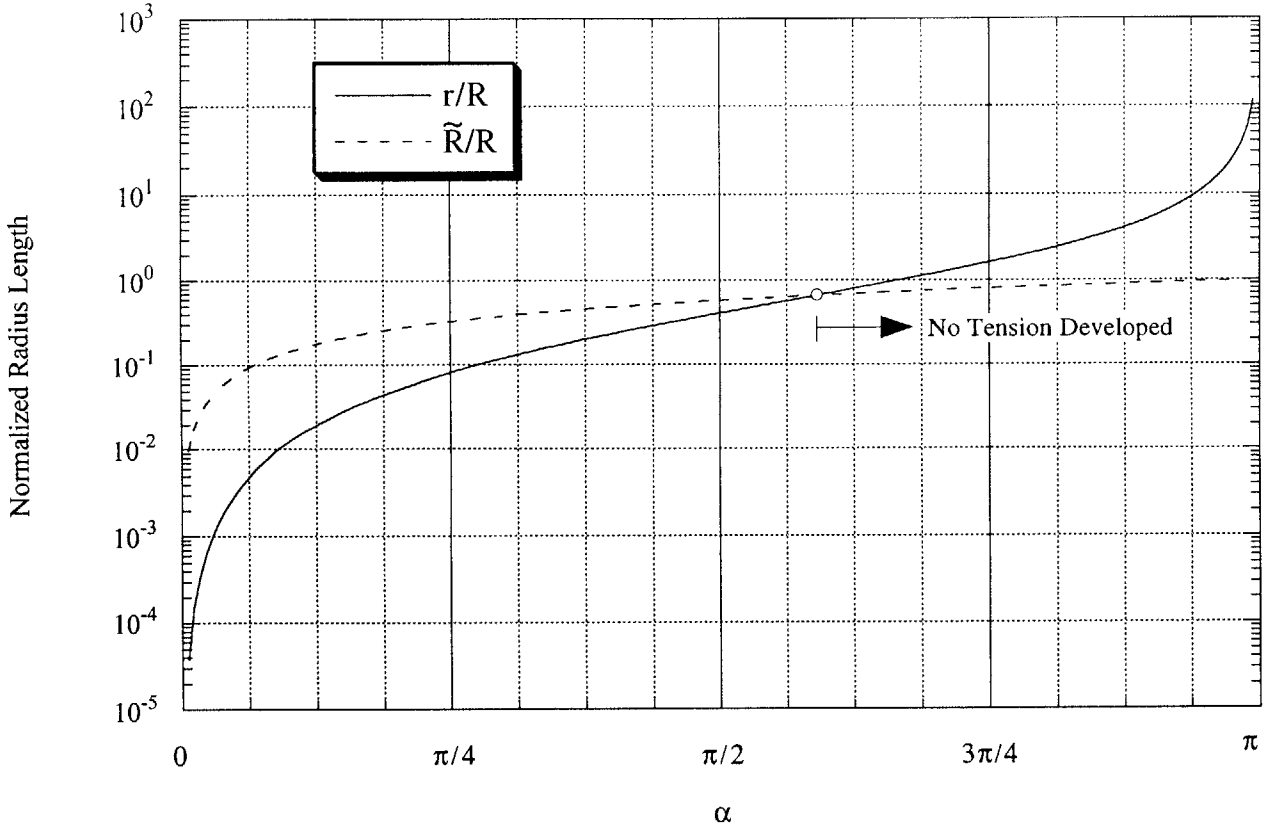

Figure 3-7. Saddle radii versus α angle.

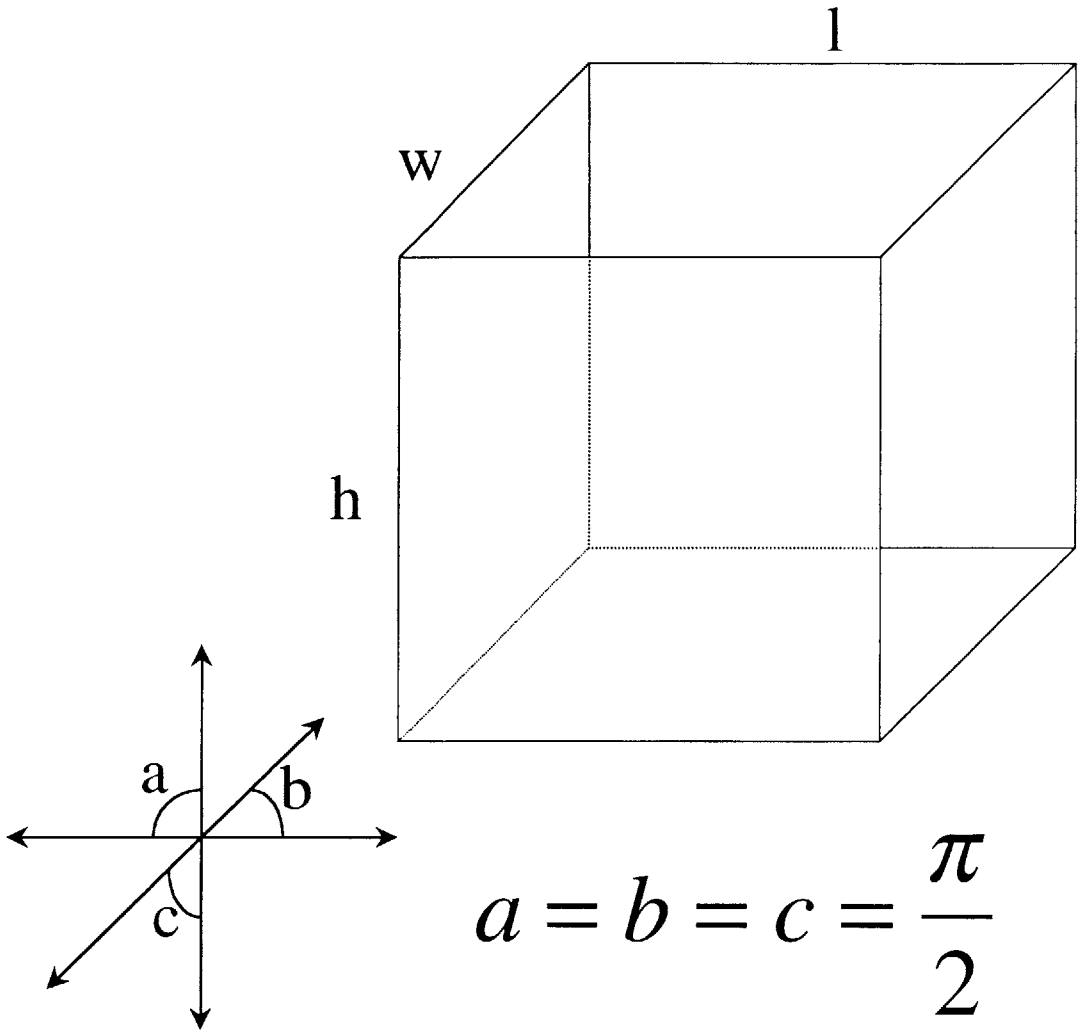

$$a = b = c = \frac{\pi}{2}$$

$$l = w = h = 2R$$

Figure 3-8. Cubic packing arrangement and face angles.

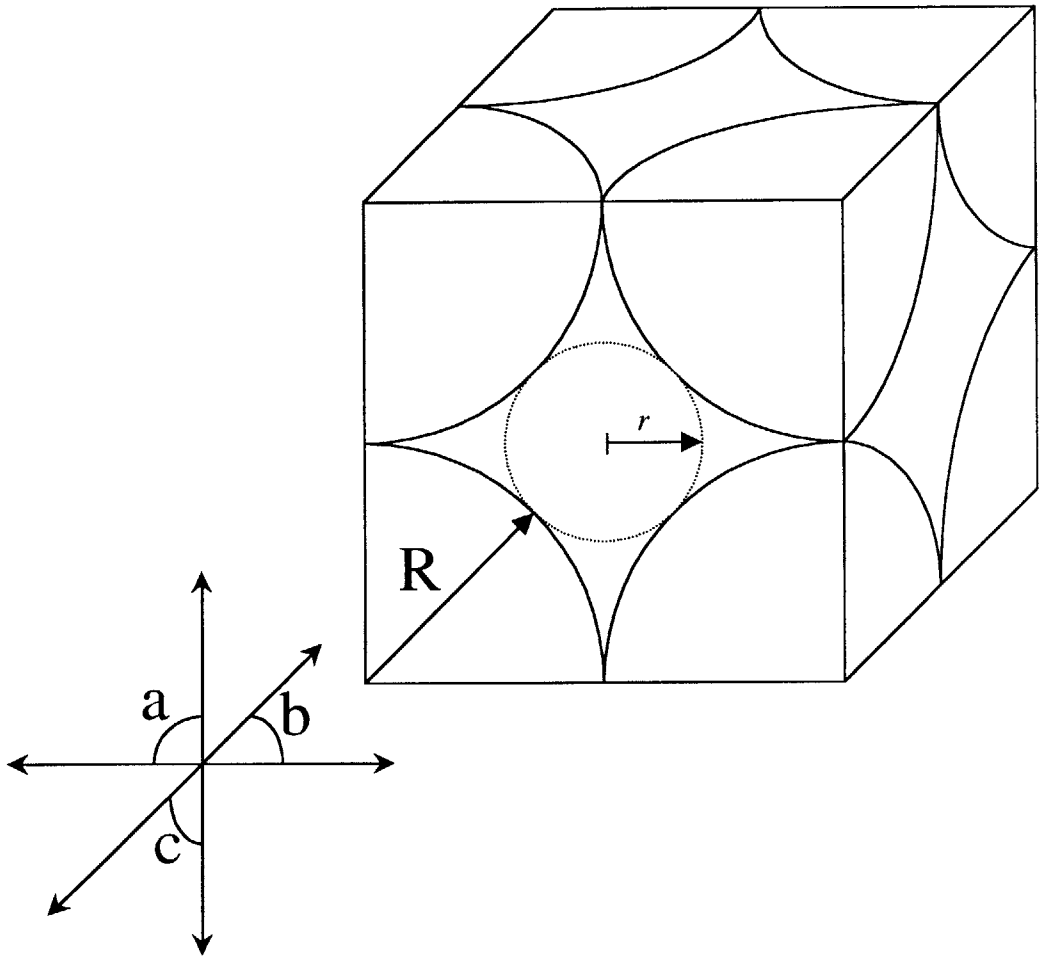

Figure 3-9. Unit void for cubic packing scheme.

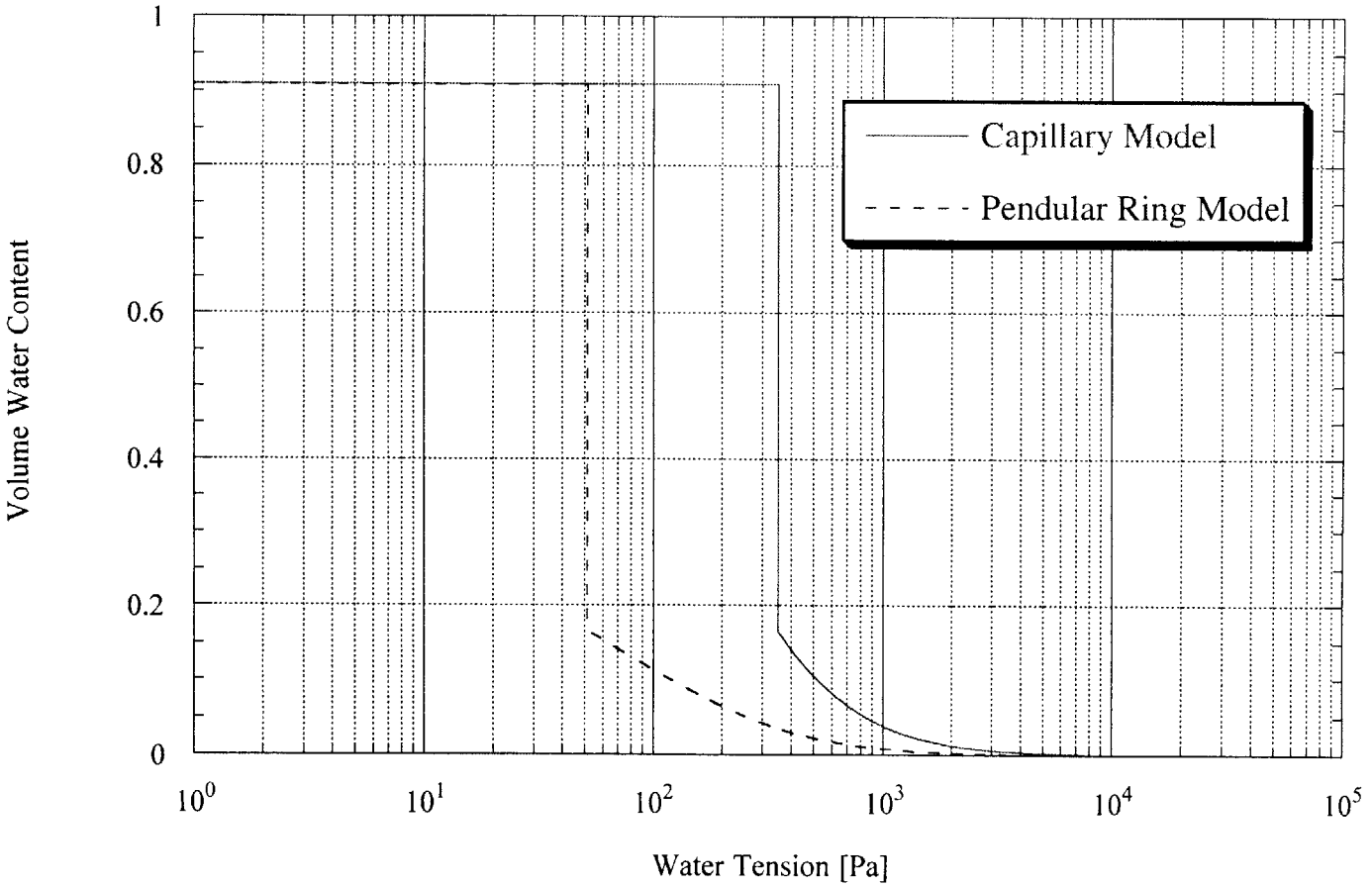

Figure 3-10. Calculated Retention curve for spheres of 1 mm radii with cubic packing.

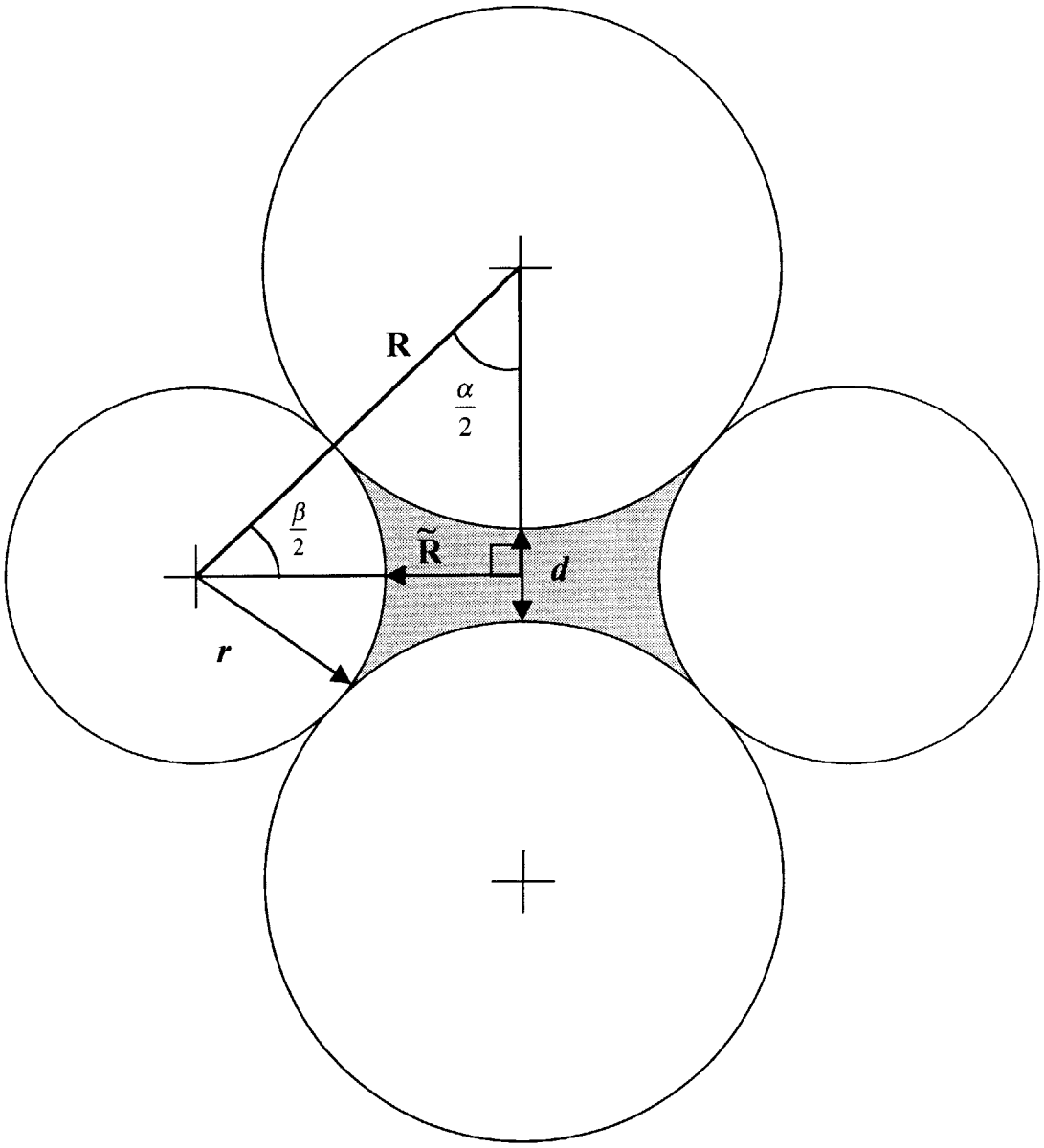

Figure 3-11. Geometric relations for spheres of equal radii with spacing, *d*.

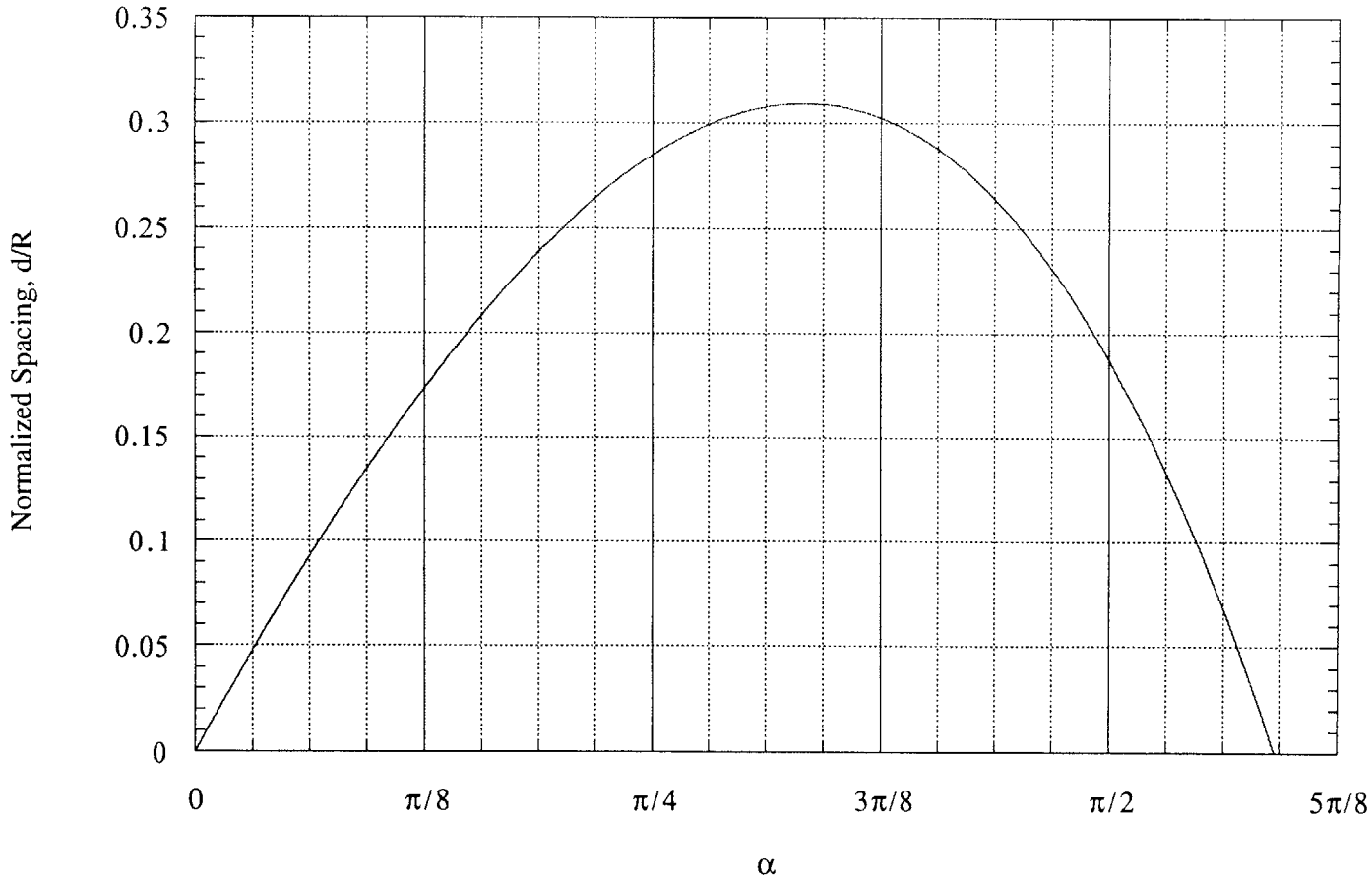

Figure 3-12. Variation of *d* with α.

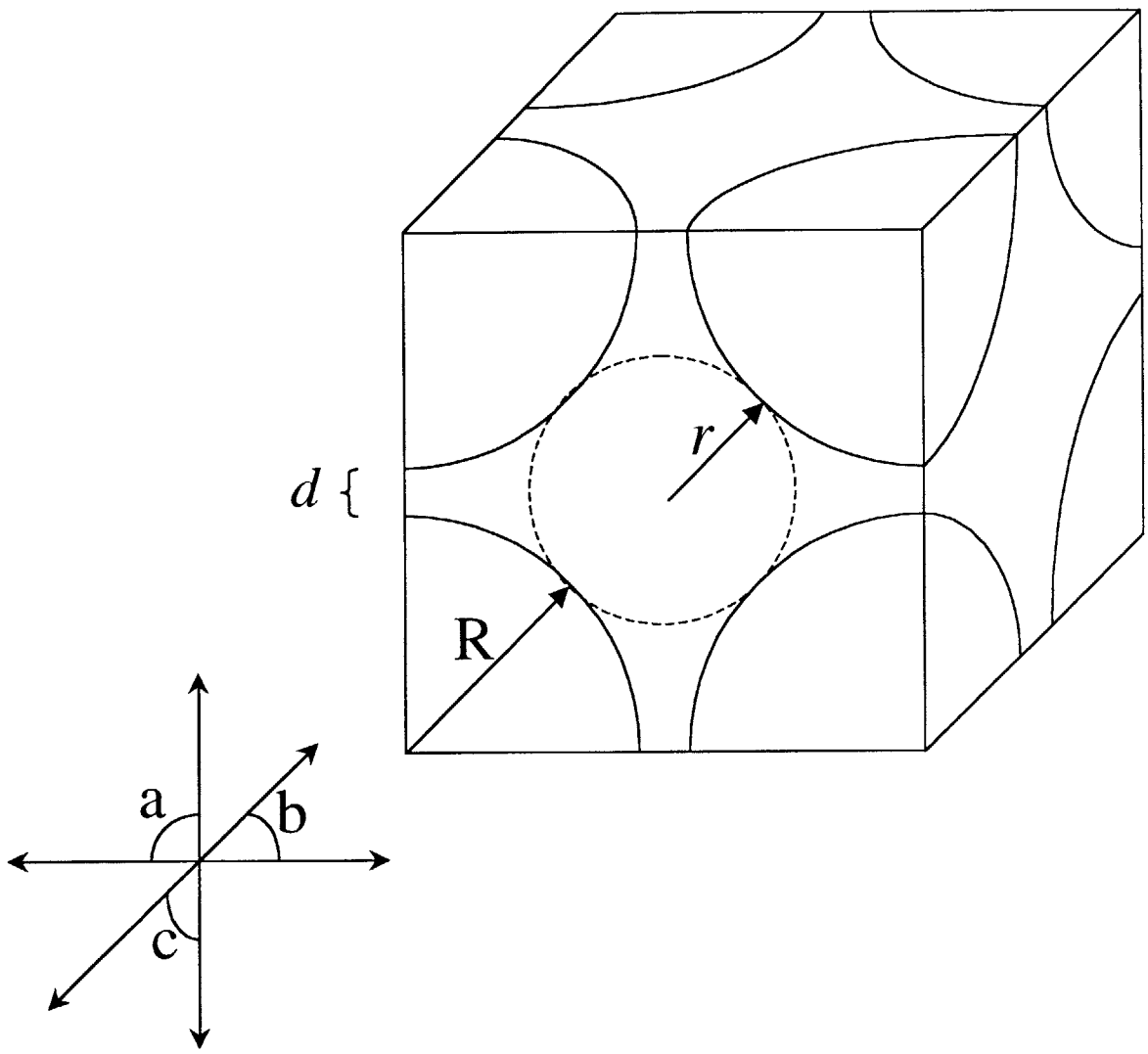

Figure 3-13. Unit void with spacing between particles of *d*.

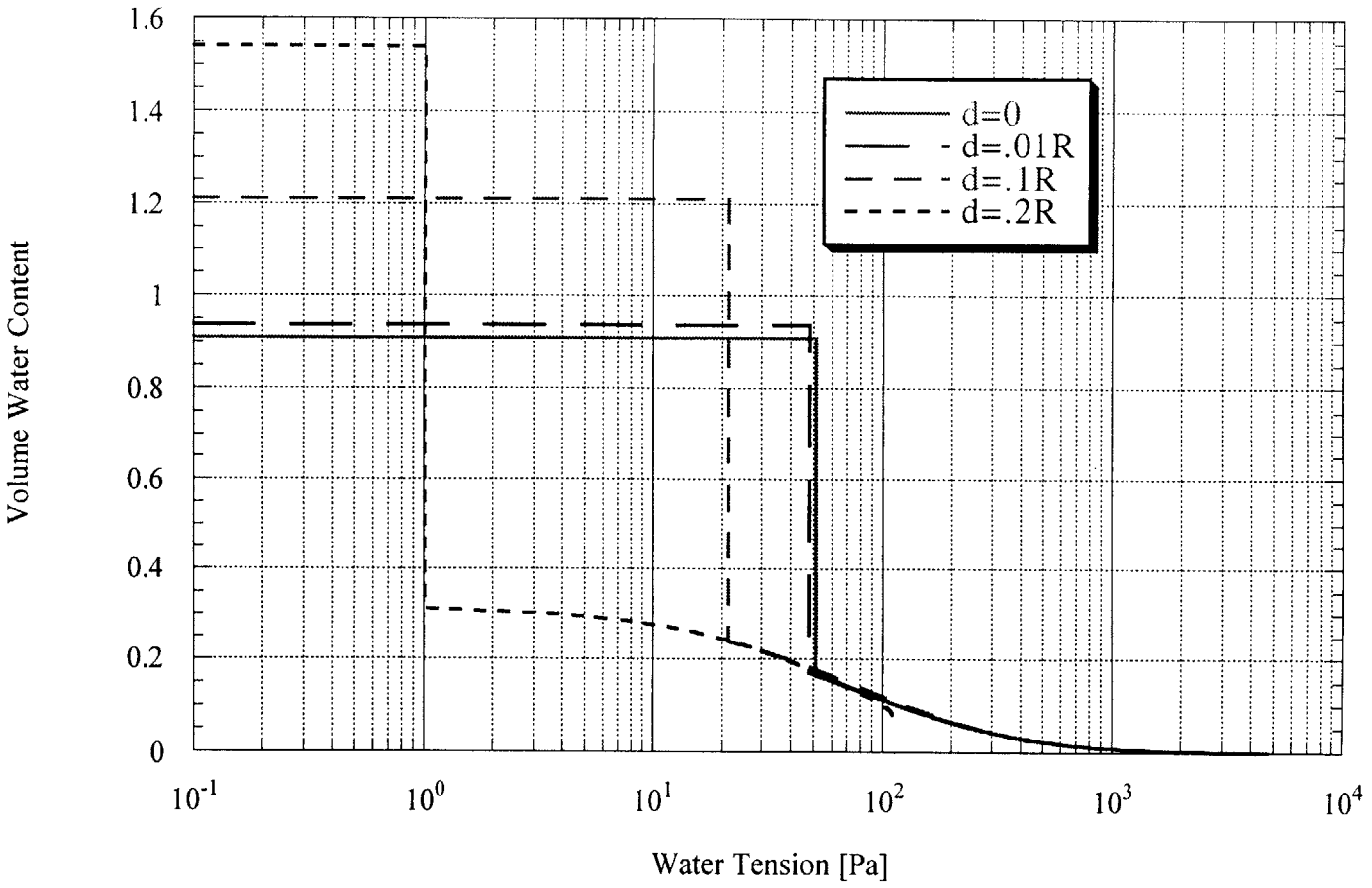

Figure 3-14. Calculated retention curves for spheres of radii equal to 1 mm at various spacings.

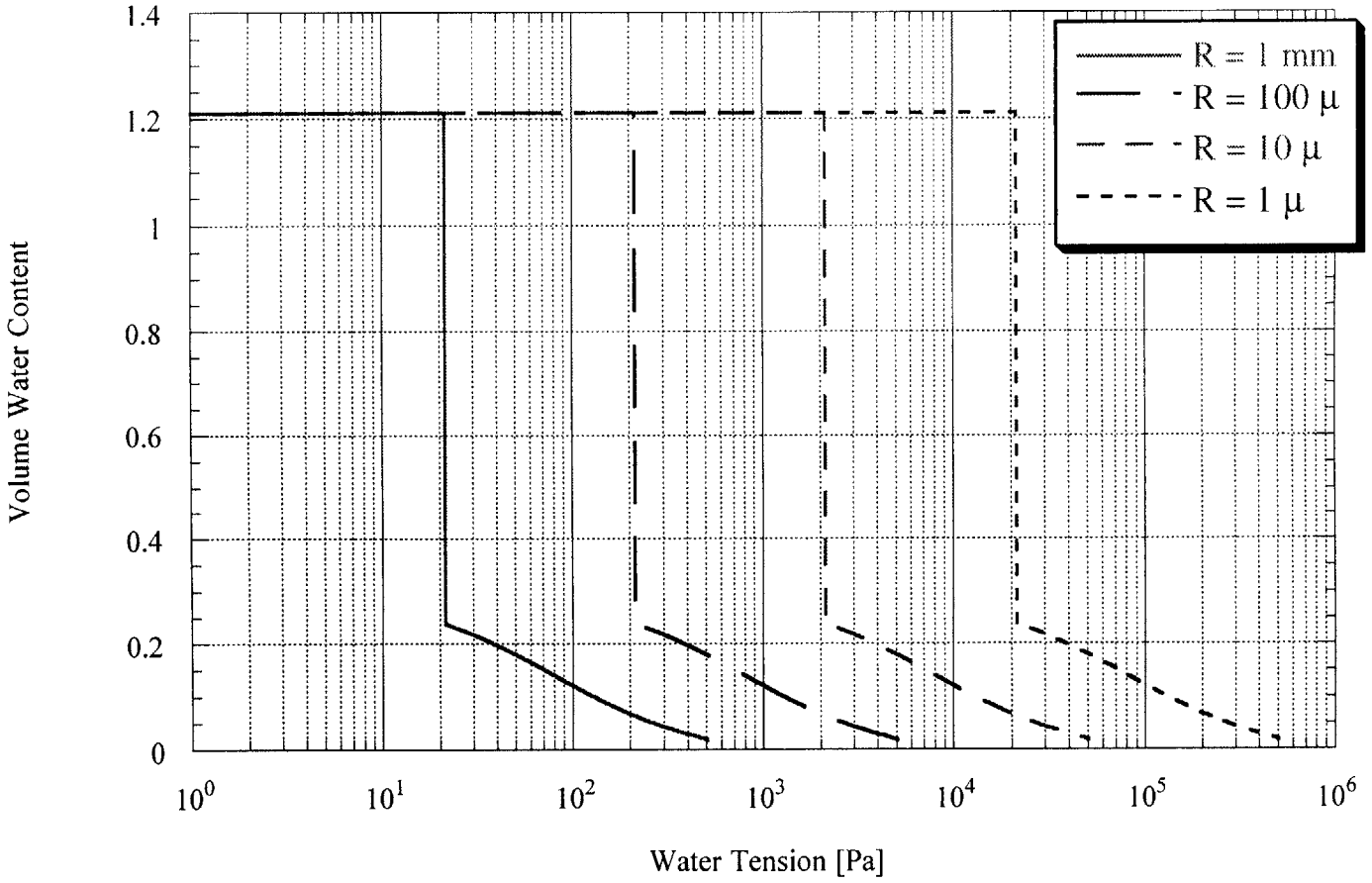

Figure 3-15. Calculated retention curves for spheres of various radii and spacing equal to 0.1R.

Chapter 4 Equipment Development

4.1 Introduction

In order to examine the drying process of a porous material from a saturated condition to a condition of continuous air, unique equipment and methods were developed. The desaturation was measured by placing the material on tensiometer and allowing the it to evaporate in the laboratory air. A mass balance recorded the moisture loss while the tensiometer measured the tension in the pore water. This method required the development of several pieces of equipment. It also involved interfacing the mass balance to allow for data acquisition readings.

This Chapter focuses on the development of the equipment used in the research. Section 4.2 describes the tensiometer construction in various stages and the integral components. Saturation of the tensiometer was accomplished with two separate pieces of equipment discussed in Section 4.3. Finally, the laboratory balance that was interfaced is described in Section 4.4.

4.2 MIT Tensiometer

4.2.1 Design Evaluation

Over the course of this research several designs of the MIT Tensiometer were built. Each of the designs was completed in order to overcome the deficiencies of the previous design. The following sections describe the MIT Tensiometer in various stages of development.

4.2.1.1 Version 1.0

The design of Version 1.0 was driven by the desire to incorporate a tensiometer into the standard triaxial equipment of the MIT Geotechnical laboratory. The dimensions for the tensiometer where therefore set by this constraint as well as the general configuration.

The first version of the tensiometer is shown in Figure 4-1. The device consisted of four basic components, a porous ceramic stone, a brass pedestal or body, a brass stem and a pressure transducer. The porous ceramic stone was a 15 bar stone obtained from Soil Moisture Corporation and is described in more detail in Section 4.2.2.1.1. The pressure transducer is discussed in Section 4.2.2.4.

The device body has dimensions of the common triaxial pedestal of the MIT Geotechnical Laboratory at 1.4 inches in diameter by 1.125 inches high. The stem of the device served two purposes. It allowed the pedestal to be installed in a standard triaxial base that is 1.5 inches thick by allowing the transducer to be secured from underneath. This enabled the device to be adapted to any of the triaxial bases in the lab. The stem also served as a pressure conduit from the stone to the pressure transducer. The stem was sealed to the pedestal by means of two o-rings. The ceramic stone was affixed to the pedestal by the epoxy described in Section 4.2.2.2.

4.2.1.2 Version 2.0

Due to the poor performance of Version 1.0, it was decided to redesign the tensiometer. It was suggested in the literature, that the reservoir of a tensiometer should be made as small as possible (Ridley and Burland 1993). Bringing the transducer directly up to the underside of the ceramic stone eliminated the stem and thus reduced the volume in the reservoir. This left a small gap between the face of the transducer diaphragm and the bottom of the ceramic stone. A different transducer was used, as it was important to minimize the area of the diaphragm. This miniature transducer was obtained from Kulite Corporation and is described in Section 4.2.2.4. The transducer was sealed to the underside of the stone with an o-ring and threads were cut into the device body. Figure

4-2 shows the design schematically. The material was also changed from brass to stainless steel. This provided much better resistance to surface corrosion and deposits due to repeated cycles of wetting and drying.

4.2.1.3 Version 3.0

Version 3.0 is radically different from the previous two versions. The previous versions used a pressure transducer as a separate device. This version eliminated the transducer by making the pressure-sensing diaphragm an integral part of the pedestal body. This eliminated the need for an o-ring seal and threads thereby avoiding the problems associated with these. Version 3.0 also incorporates the ability to underpressure the device. This allows for a direct calibration of the device. It was desired to have a direct calibration of the integral diaphragm by providing a pressure to the underside of the diaphragm. This would then deflect the diaphragm in the same direction as a tension applied to the reservoir on top of the diaphragm. The underpressure also gives the advantage of allowing the diaphragm to be designed for the limit of the stone and not of the overpressure required for saturation. By applying a pressure to the top and bottom of the diaphragm during the saturation process, the deflection of the diaphragm was eliminated.

At the top of the device is a porous ceramic as in prior versions. However, below this the changes are incorporated. As shown in Figure 4-3, a small depression below the ceramic was machined out of the stainless steel body to form a water reservoir. This depression acts as the pressure sensing face of a transducer. To the underside of the reservoir, the body was bored out to create a very thin diaphragm. The diaphragm is 0.024 inches thick. This provided a sufficient factor of safety against plastic deformations. The diaphragm was designed for applied pressures of up to 30 bars in either direction. This was based on elastic fixed disc equations (Roark and Young 1975). To the underside of the diaphragm was bonded a rosette styled strain gage. The gage is described in full detail in Section 4.2.2.3. The electronic wiring for the strain gage is fed out the bottom of the pedestal through a stainless steel stem. The wires from the gage are soldered to

stainless steel pins. The pins are then epoxied in place to form a seal from within the stem. The seal extends from the end of the stem for nearly 3 cm into the stem. This was found to be adequate against leaks caused by subsequent pressures. Approximately 1 cm of the pins are exposed out of the stem. These pins were then bent into a configuration for an Amphenol® electrical connector.

Three small holes were drilled offset into the stem above the epoxy connection at 120° intervals. The holes provided a conduit for the under-pressure fluid to pass into the stem and up into the body of the pedestal. The fluid needed to be non-conducting since it was in contact with the electrical connections of the strain gage. Silicon oil was chosen as it is readily available in the laboratory and has the required characteristics. The product used was manufactured by Dow Corning and marketed as 200 Fluid 20 cs. The physical characteristics are listed in Table 4-1.

A Swagelok® Tee connection was fitted over the stem and centered about the three holes. The tee connection allowed for the line of the silicon oil to be attached to the device. The other end of the silicon oil line was attached to the pressure-volume-device that is described in Section 4.3.2.

4.2.1.4 Version 3.1

A modification was made to Version 3.0 by incorporating a new type of ceramic stone. The Kochi University stones described in Section 4.2.2.1.2 were used instead of the Soil Moisture stones.

It was found that the Kochi University stones did not need the high saturation pressures that the Soil Moisture stones needed. It was therefore not necessary to under-pressure the device. Hence, Figure 4-4 does not show the oil under-pressure line. This version is essentially the same as the previous except the oil line is omitted and the stone has been replaced.

4.2.1.5 Version 4.0

During testing of Version 3.0 it was observed that some materials did not dry evenly on the device, particularly plastic materials showed uneven deformations. It was discovered that these materials showed what appeared to be one dimensional deformations over the area occupied by the stone. The material that was not in contact with the stone tended to become drier and warped upward. This caused the material to peel from the metal surface. The aim of Version 4.0 of the Tensiometer was to eliminate the up warping by extending the surface area of the stone to the entire cross section of the device.

The modification made to Version 3.0 to develop Version 4.0 was very minimal. The pedestal body and stem essentially remained unchanged. The modification came from enlarging the porous ceramic to the full diameter of the pedestal (see Figure 4-5). The shoulder rim that contained the stone on Version 3.0 was machined down to provide a channel for the epoxy to bond the ceramic. Since the Kochi University ceramics could not be supplied in diameters greater than 2.0 cm, the Soil Moisture stones were used. Therefore, the oil under-pressure capabilities were left intact.

4.2.1.6 Version 5.0

Although the performance of Versions 3.0 and 3.1 was very satisfactory, the major problem was the electronic drift of the strain gage. To overcome this, it was decided to incorporate a manufactured pressure transducer. A Data Instruments (DI) pressure transducer was chosen as it has superior electronic stability and reliability. This transducer is outlined in Section 4.2.2.4.

A new body was developed to fit the DI transducer. A detailed drawing is presented in Figure 4-6. A simplified schematic of the device is shown in Figure 4-7. As shown in the Figure, the DI transducer is epoxied to the stainless steel body thereby creating a permanent union. A Kochi University ceramic is epoxied to the top of the body. This configuration eliminates the need to under-pressure, and hence a much simpler design.

4.2.2 Design Components

4.2.2.1 Stones

Two types of ceramic stones were used in this research in order to provide an interface between the material being measured and the device itself. The interface element serves several purposes; the interface supports the soil particles, transmits effective stress and holds the tension. The properties of the ceramic stones most favorable were small uniform pore sizes, durability to withstand many wetting and drying cycles and strength to resist deformations.

4.2.2.1.1 Soil Moisture Stones

Soil Moisture Corporation provided stones that were readily available from their production plant. The stones are manufactured under a proprietary formula not released to the public. According to the documentation provided, the stones are mixtures of kaolin, talc, alumina, Ball clay and other feldspathic minerals. The stone properties given by the manufacturer are listed in Table 4-2.

4.2.2.1.2 Kochi University Stones

As a result of an extensive literature search, a source of fine porous ceramic stones was found in the academic environment. Professor Kazumichi Yanagisawa of Kochi University developed a hydrothermal sintering process of silica gels that produced fused ceramics of very fine pore distributions (Yanagisawa et al. 1994).

Professor Yanagisawa provided an assortment of stones with only the preparation parameters varied slightly. After evaluation of the stones in the MIT Tensiometer, the selected stones had been prepared with the parameters listed in Table 4-3. This stone appeared to give the most desirable results when incorporated into the MIT Tensiometer. A pore size distribution for the stone was given in Yanagisawa(1994) and is reproduced

in Figure 4-8 (curve b). Figure 4-9 shows the bulk density and compressive strength of the ceramics chosen.

4.2.2.2 Epoxy

The epoxy used to bond the porous ceramics to the pedestal bodies was obtained from Ellsworth Adhesive Systems in Billerica, MA. The product chosen was a two-part epoxy manufactured by Emerson and Cuming. The product number is 2651MM Stycast, and the physical properties of the epoxy are given in Table 4-5. This product was chosen as it fulfilled two main constraints. Of most importance was the ability to machine the epoxy. Once the ceramic stone was epoxied in place, the surface of the stone/epoxy bond needed to be machined to a flat surface. Stycast 2651MM was developed for machining applications (the suffix of the model number MM stands for mostly machinable). The other property of the epoxy was its resistance to water, particularly repeated wetting and drying cycles.

4.2.2.3 Strain gage

The strain gage used was obtained from BLH Electronics, Inc. located in Canton, MA. The style chosen was a full bridge rosette and is shown in Figure 4-10. The dimensions of the gage are given in Table 4-4. The gage grid is constructed of Constantan Foil with a Polymide carrier material.

A full bridge gage was used to eliminate configuring any excess resistors. The placement of the gage instalation was very limited and space was a major concern. The full bridge also reduces any electronic drift due to thermal variations (see Figure 4-11).

4.2.2.4 Pressure Transducers

Two different types of pressure transducers were used in this research. Each of the types is described in the following sections as well as the expected response time of the transducers.

4.2.2.4.1 Kulite Semiconductor

Revisions of Version 1.0 of the MIT Tensiometer led to the development of Version 2.0. This version's main objective was to reduce the volume of water in the reservoir. Therefore, a miniature pressure transducer was required. The transducer was mounted close to the underside of the ceramic creating a small water reservoir between the transducer and the ceramic. This allowed the reservoir to be as small in cross section as the transducer diaphragm.

A transducer was obtained from Kulite Semiconductor Products, Inc. located in Leonia, New Jersey. The transducer model is XTM -190. The technical specifications are given in Table 4-6 and the transducer schematic is shown in Figure 4-12.

4.2.2.4.2 Data Instruments

Versions 1.0 and 5.0 of the MIT Tensiometer incorporated a Data Instruments pressure transducer. The model chosen was the AB/HP with a range of 0-200 psig. A schematic of the transducer is shown in Figure 4-13. This model has been in use in the MIT Geotechnical laboratory and is now considered a standard in the lab. The electrical characteristics of the transducer are given in Table 4-6.

4.2.3 Time Response of Tensiometer

Following the technique of Henderson (1994), a simple estimate of the time response of the transducer can be made. The derivation of Henderson assumes a uniform instantaneous pressure on the interface of the probe (tensiometer). This estimate is expected to be lower than the actual time response of the MIT Tensiometer with soil due to the compressibility of the soil that is imparting the stress on the pore water. However, for design purposes the estimate was useful to determine if the expected response time was favorable. Henderson gives the following equation as a solution to a probe response:

$$y = \left(1 - e^{-bt}\right) \qquad [4.1]$$

where;

y is the normalized pressure (i.e., pressure read by the probe at time, t /pressure applied)
e is the base of natural logarithms
b is a constant of the system (T^{-1})
t is the time

Using the appropriate values in Equation [4.1] it was estimated that the MIT Tensiometer would reach 95 % of the applied tension in 12 seconds. This was compared to the actual response of the Tensiometer with soil imposing a tension. The measured response was nearly 120 seconds (these data are discussed in Chapter 5) indicating an order of magnitude delay due to the soil.

4.2.4 Tensiometer Calibration

Calibration of the various versions was performed on the pressure transducer calibration equipment available in the laboratory. For Versions 1.0 and 5.0, the Data Instruments pressure transducer was calibrated in the equipment as normally done in the lab. A special fitting was created for the Kulite miniature pressure transducer of Version 2.0. Essentially a threaded bushing was created to adapt the smaller threads of the Kulite to the larger threads of the equipment. In either case, the transducers were calibrated by applying a positive pressure to the topside of the diaphragm. This pressure caused the diaphragm to deflect in a direction into the device. It should be noted that this is a direction that is opposite to which the diaphragm would deflect when a tension is applied to the reservoir fluid. Due to the sealed nature of the transducers, it was not possible to calibrate the diaphragm in the opposite direction. It was therefore assumed that the calibration would still be linear in the opposite direction.

For all other versions (3.0, 3.1 and 4.0), a Swagelok® connection was fitted to the equipment and a copper line was run to the stem of the tensiometer. As described before,

this line was connected to a Swagelok® tee fitting over the stem. The underside of the tensiometer, including the stem and copper line was filled with the silicon oil discussed in Section 4.2.1.3. This provided a means to increase the pressure in the tensiometer from the underside of the diaphragm. This deflection is in the same direction as a tensile stress applied to the top of the diaphragm or in the water reservoir/ceramic stone.

4.3 Saturation Equipment

To prepare the MIT Tensiometer (all versions) for use, a saturation process was first required. Two steps are needed in order to saturate the MIT Tensiometer. First a vacuum is applied to the tensiometer to remove most of the air in the system. This vacuum is held for approximately 0.5 hours and is on the order of 100 mTorr. After this time, the tensiometer is flooded with distilled and de-aired water while still under a vacuum. The pressure in the water is then raised to a sufficient value to drive any entrapped air into solution.

The equipment developed to execute this process consists of essentially three components; a saturation chamber, a pressure volume device and an electronic controller to deliver and maintain the pressure. Each of these components is discussed below.

4.3.1 Pressure Chamber

The MIT Tensiometer was affixed to a standard triaxial base in the lab. The Tensiometer is secured to the base from beneath by 4 screws. An o-ring maintains the seal. A chamber (Figure 4-14) was then fitted onto the base and covered the Tensiometer. The chamber is attached to the base by 6 screws and made use of the existing o-ring seal in the base. The chamber was machined from solid brass. A series of fittings are attached to the top of the chamber to allow for the necessary pressure lines. A 1,000 psi pressure transducer was also fitted to the top of the chamber to monitor the pressure being applied to the tensiometer.

4.3.2 Pressure Volume Device and Interface

Figure 4-15 shows a drawing of the standard pressure volume device used in the lab. It consists of three components; a steel chamber, a steel piston sealed to the chamber, an actuator that moves the piston, and a servo drive motor that drives the actuator.

The chamber was filled with water and a line was connected directly to the saturation chamber. A tee fitting was attached to this line and attached to an oil water interface setup. This setup consisted of nothing more that a 0.5 inch copper pipe. The pipe was 3 inches in length. Figure 4-16 shows the configuration of this setup. As shown in the figure, the water line from the pressure volume device is attached to the bottom of the pipe. The pipe is filled with silicon oil discussed in Section 4.2.1.3. A copper line is attached to the top of the interface and fed directly to the bottom of the MIT tensiometer. This allowed for equal pressure from one pressure volume device to deliver both the overpressure on the top of the tensiometer and the underpressure on the bottom.

4.3.2.1 Analog-Analog Feedback Control

During the saturation process, a constant pressure is maintained on the tensiometer. This is accomplished by setting a reference pressure and comparing it to a measured pressure. Since the pressures are measured by an electronic transducer, the comparing can be done by a circuit.

A basic block diagram of the feedback system is shown in Figure 4-18. As explained above, the transducer output from the saturation chamber along with a reference voltage is input into a circuit. The output of the circuit is then input into the control card for the VDC servo motor. The Max100 control card sends a variable voltage to the motor to cause rotation to match the control signal. The motor tachometer generates a signal that is fed back to the Max100. This voltage is proportional to the rpm of the motor. The Max100 compares the tachometer output to the command signal to determine the output

voltage to the motor. Since a gain of 10× was wired into the output of the circuit, a very fast response time is initiated in the motor. The motor can also be controlled manually by way of a variable resistor to set the command signal. This manual tachometer is used primarily to reduce the pressure in the chamber once saturation is completed.

The basic circuit design is shown in Figure 4-17. As shown, the circuit is simply made of three instrument amplifiers. The amplifiers were purchased from Analog Devices and are common in the laboratory. The model number of the amplifiers is AD524.

The circuit takes the output of the measured pressure in the chamber and directs it through one amplifier. The output of the amplifier is now referenced to a ground of the system. The same is done for a reference voltage. The two outputs are then directed into a third amplifier. The output of this third amplifier is now the absolute difference in voltage between the two supplied voltages. The amplifiers are powered by a ±15 VDC supply.

4.4 Mass Balance Interface

Measuring the drying curve of porous materials was done by making frequent measurements of water tension with the tensiometer and mass measurements with a laboratory balance. The MIT Tensiometer (with specimen) was placed upon a balance and allowed to dry. Automatic measurements of mass were made by interfacing the balance with a personal computer. The following two sections describe this in detail.

4.4.1 Hardware

The balance used in this research was manufactured by Mettler-Toledo company. The model number of the balance is Basic Balance BB2400. The capacity of the device is 2,400 grams with a resolution of 0.01 grams. In order to acquire the periodic measurements of mass during a test, an IBM compatible computer was interfaced to the

balance. The BB2400 has a RS232 port built into the rear of the balance. An interfacing cable was purchased from Mettler-Toledo to connect the BB2400 to the computer. The model number of the cable is ME-33783.

Once the BB2400 was configured in constant send mode, the BB2400 sends a digital signal following RS232 protocols to the computer. The constant send mode is simply accessed during startup of the balance. The computer then reads the digital data at the communications port whenever required.

4.4.2 Software

A simple program was written in QuickBasic© to access the communications port of the computer and to acquire the data from the balance. A complete listing of the code is given in the Appendix, however the main communication between the computer and the BB2400 is given in the following BASIC code:

```
OPEN "com1:2400,E,7,1,CS,CD,DS,RS,LF" AS #1
IF LOC(1)>0 THEN PRINT INPUT$(LOC(1),#1);
```

The above code essentially handshakes with BB2400 and then determines if there are data being sent in the port. If there are data, then the data are displayed, if not, then a simple loop can run this code again.

Table 4-1. Physical properties of Dow Corning 200 Fluid 20 cs.

Composition	$(CH_3)_3SiO[SiO(CH_3)_2]_nSi(CH_3)_3$
Appearance	Crystal clear liquid
Specific Gravity at 25°C	0.960
Flash Point [°C]	318
Melting Point [°C]	-41
Surface Tension at 25°C [dynes/cm]	20.8
Coefficient of Expansion [$cm^3/cm^3/°C$]	0.00104
Refractive Index at 25°C	1.4022

Table 4-2. Physical properties of porous ceramics (Soil Moisture Equipment Corp 1995).

Air Entry Value	Bubbling Pressure (psi)	Approx Porosity (% Vol)	Saturated Hydraulic Conductivity (cm/sec)	Pore Size (μm)	Flow Rate Through 1/4" Plate (ml/hr/cm^2/14.7 psi)
1/2 bar	7 - 9	50	3.11×10^{-5}	6.0	180
1 bar High Flow	19 - 28	45	8.6×10^{-6}	2.5	50
1 bar Standard	20 - 30	34	3.46×10^{-7}	2.1	2
2 bar	35 - 45	38	1.73×10^{-7}	1.2	1
3 bar	46 - 70	34	1.7×10^{-7}	0.8	1
5 bar	80	31	1.21×10^{-7}	0.5	0.7
15 bar	220	32	2.59×10^{-9}	0.16	0.015

Table 4-3. Parameters used in Kochi University ceramics.

Preparation Water Content (%)	Preloaded Time (min)	Sintering Pressure (MPa)	Sintering Time (hr)	Sintering Temperature (°C)
10.2	10	2	1	300

Table 4-4. Characteristics of BLH strain gage.

Grid Diameter (inches/mm)	Overall Diameter (inches/mm)	Matrix Diameter (inches/mm)	Resistance (Ohms)	Part Number	Gage Factor
0.220/5.59	0.220/5.59	0.282/7.16	350±3	FAES4-22-35-S6-4	2.1

Table 4-5. Physical properties of STYCAST 2651MM (data from Emerson and Cuming).

Viscosity at 25°C (cP)	Specific Gravity	Temp range of use (°C)	Hardness Shore D	Thermal Conductivity (W/m-K)	Dielectric Constant @ 1mHz	Dielectric Strength (V/mil)	Comments
14,000	1.58	-40 to ±130	88	0.6	4.4	450	Low viscosity, low abrasion, superior machinability

Table 4-6. Electrical characteristics of the transducers.

Transducer	Range	Overload	Span (FSO)	Excitation	Zero Balance	Accuracy	Operating Temperature
Kulite XTM-190	0-250 psig	3x - burst pressure	75mV	10 Vdc	±3% FSO	±1% FSO	0°F to 250°F
Data Instruments	0-200 psig	2x w/o damage 5x w/o bursting	100 ±1mV at 5 Vdc at 77°F	5.0 Vdc	0 ±5.0 mV at 77°F	±0.25% span	30°F to 160°F

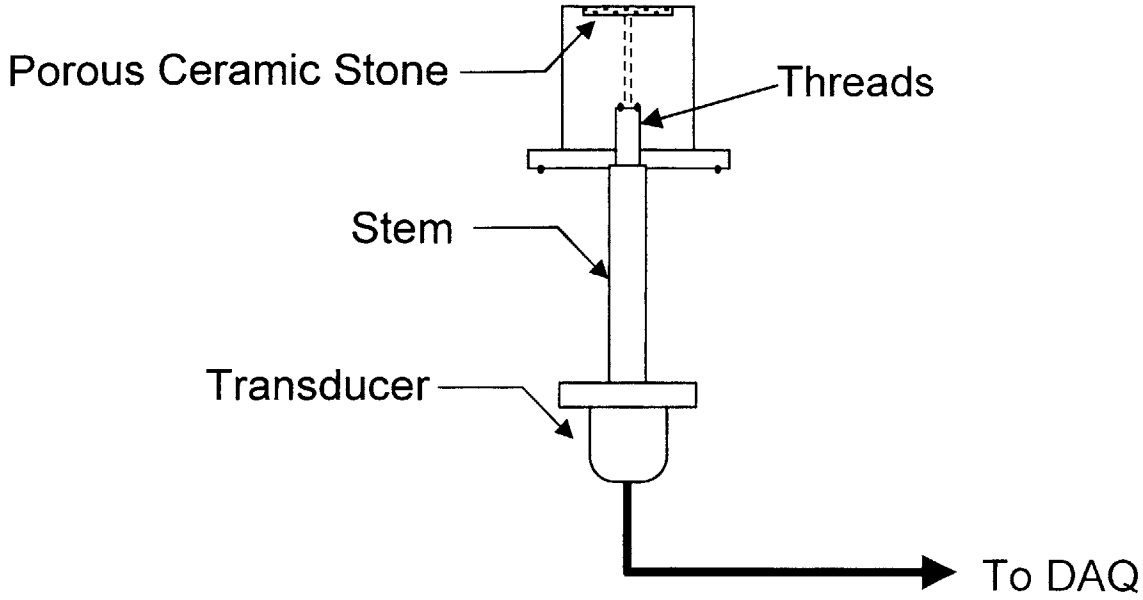

Figure 4-1. Version 1.0 of the MIT Tensiometer.

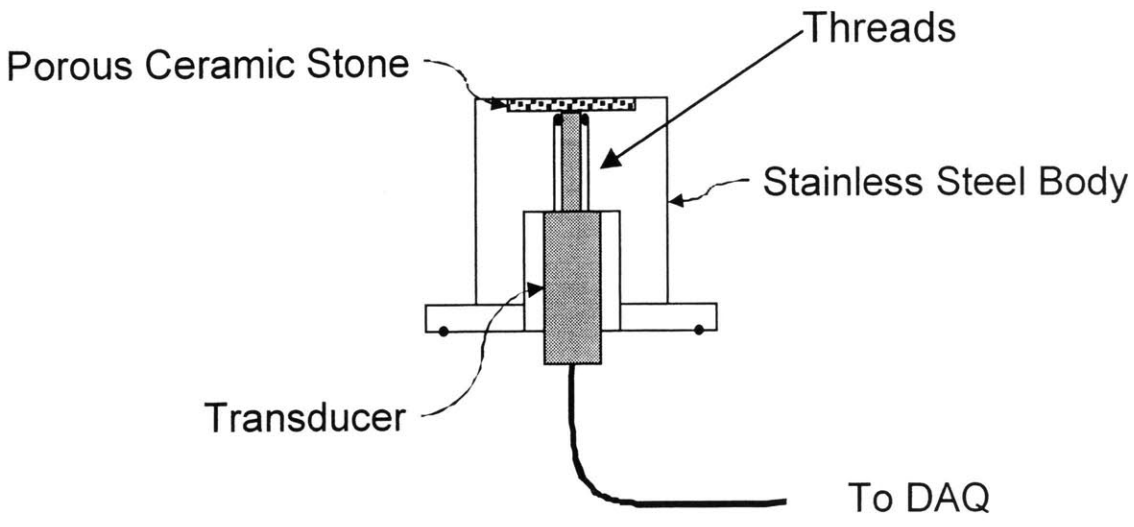

Figure 4-2. Version 2.0 of the MIT Tensiometer.

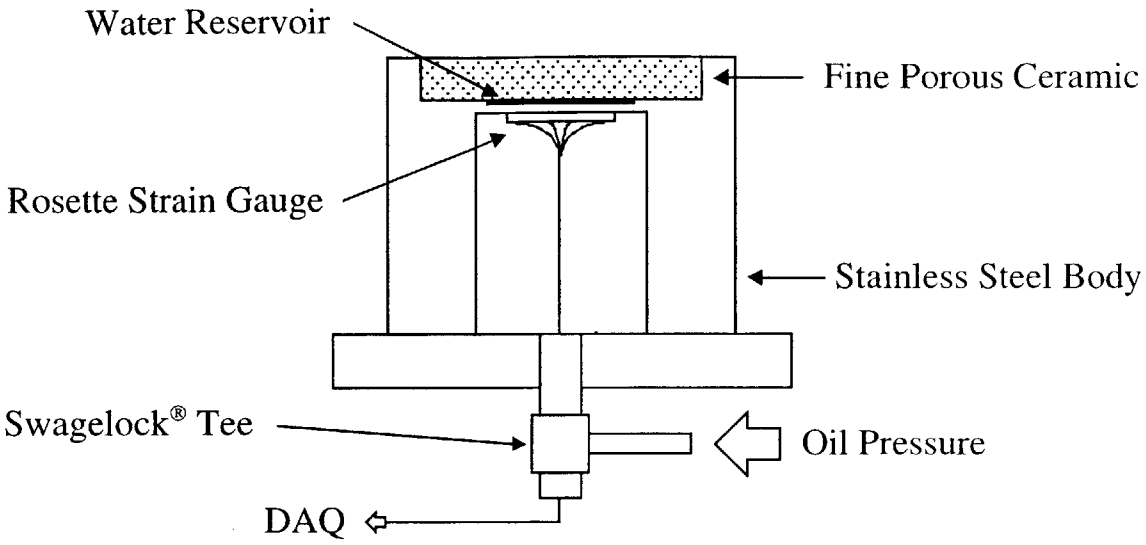

Figure 4-3. Version 3.0 of the MIT Tensiometer.

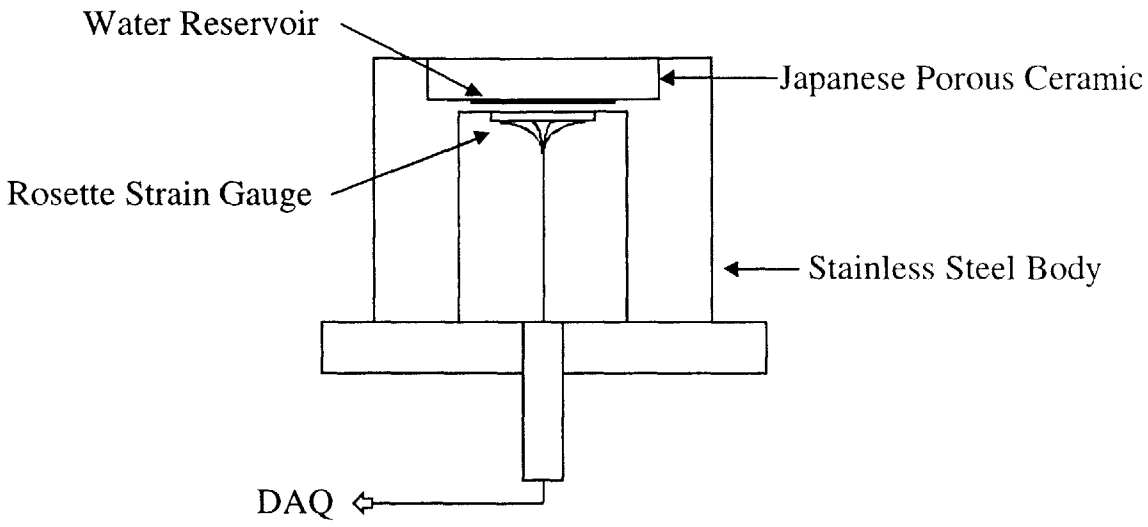

Figure 4-4. Version 3.1 of the MIT Tensiometer.

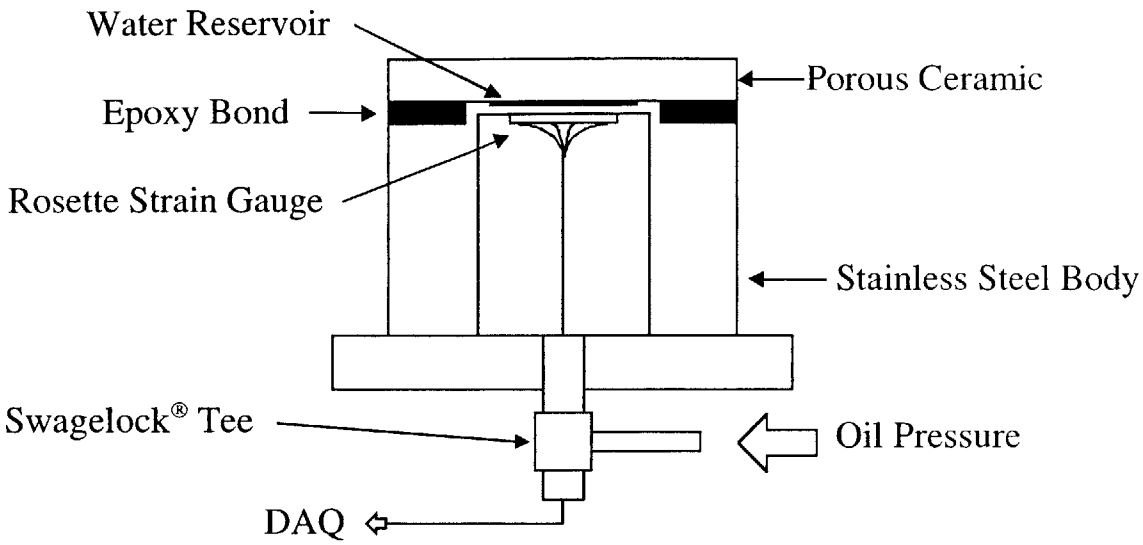

Figure 4-5. Version 4.0 of the MIT Tensiometer.

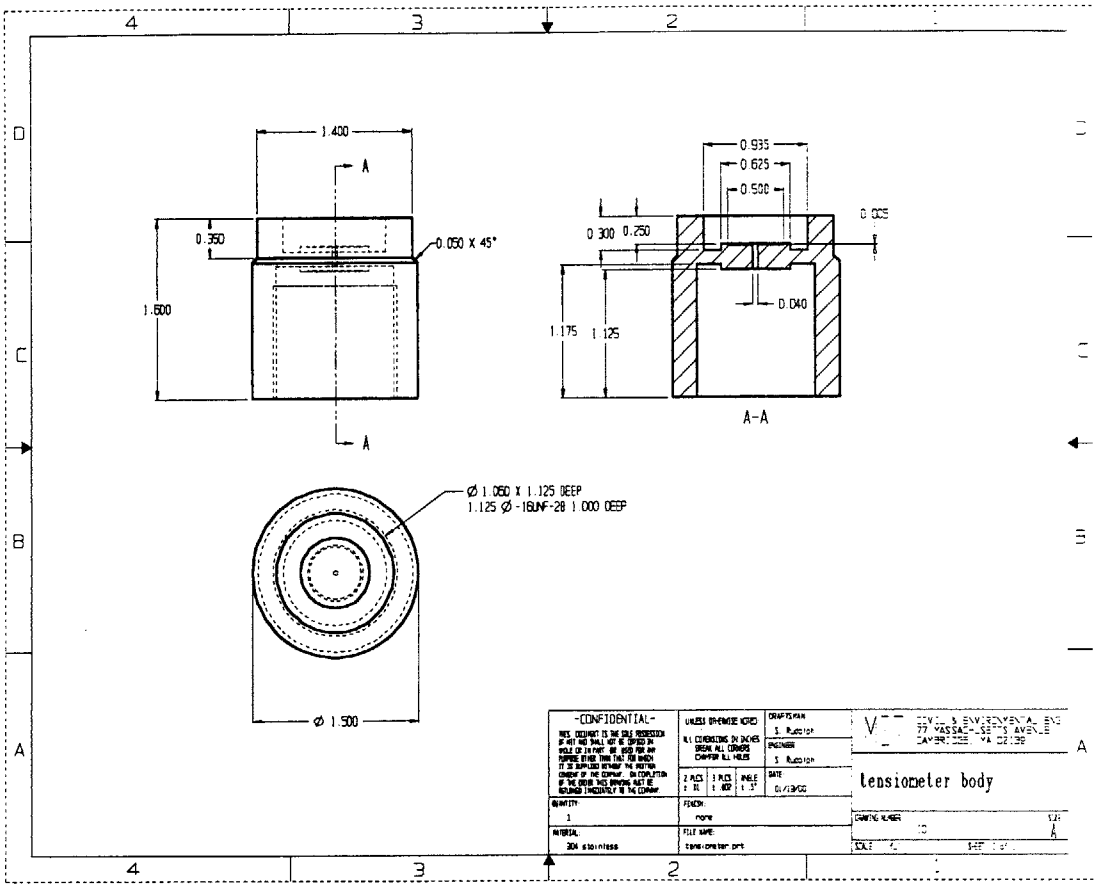

Figure 4-6. CAD Drawing of version 5.0 of the MIT Tensiometer.

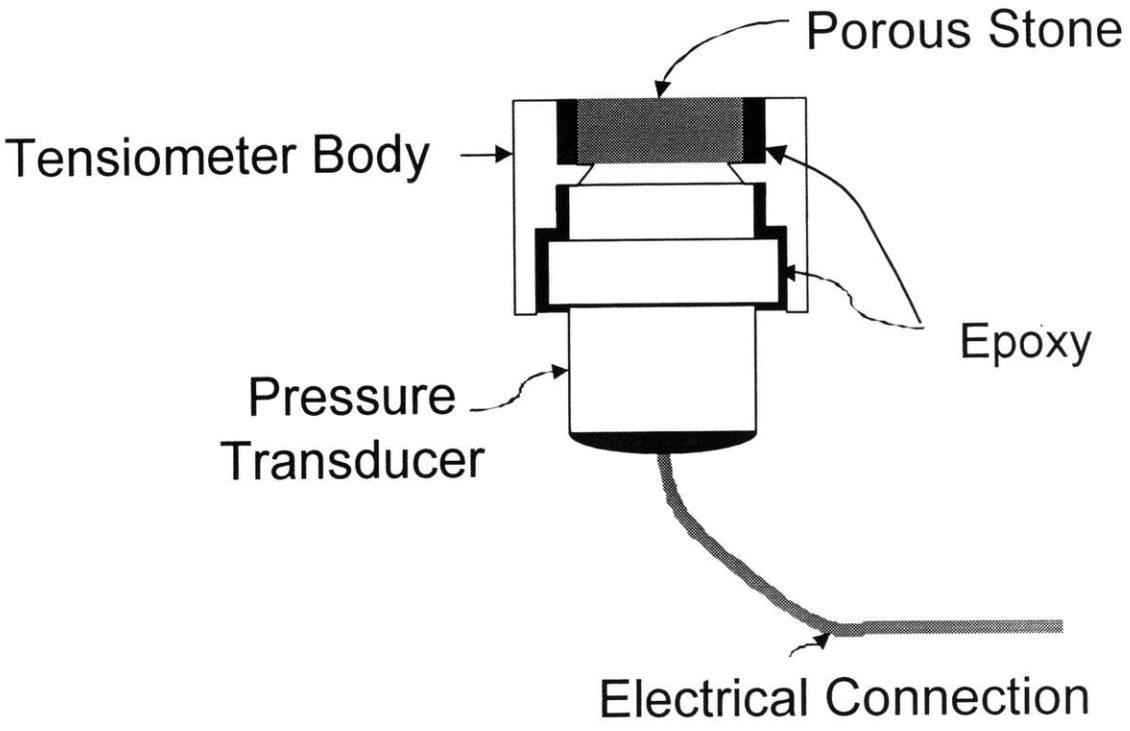

Figure 4-7. Version 5.0 of the MIT Tensiometer.

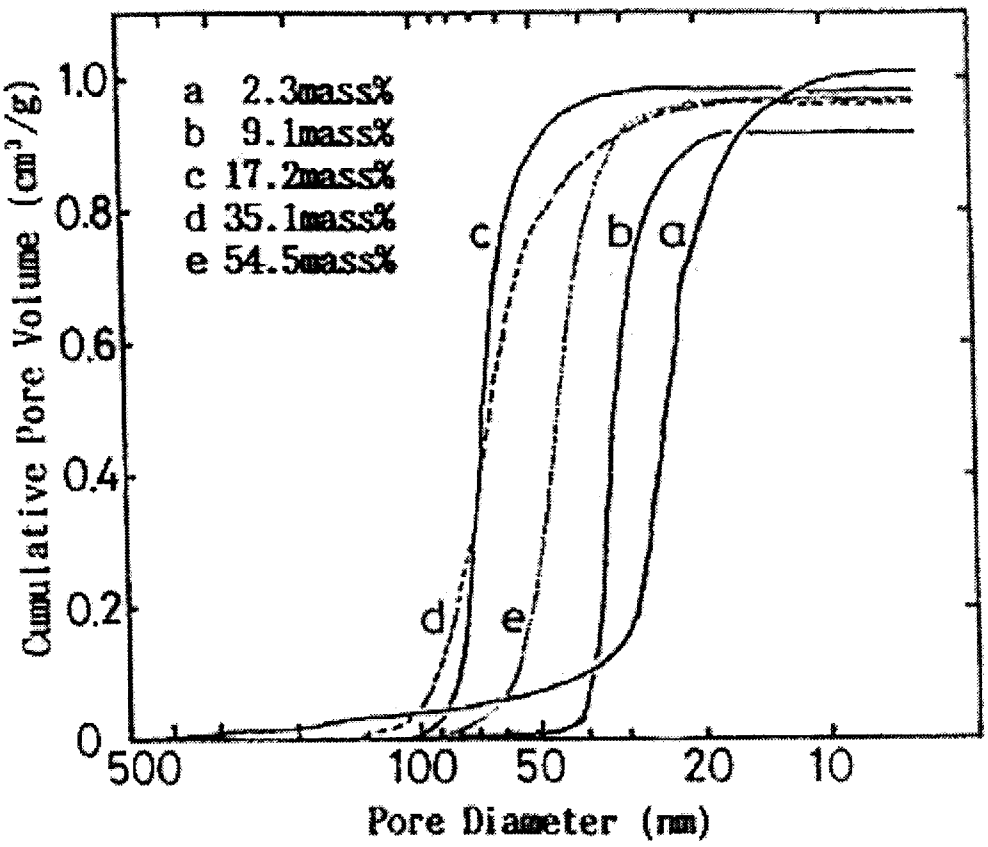

Figure 4-8. Pore distribution for Kochi Universities ceramics (after Yanagisawa et al. 1994).

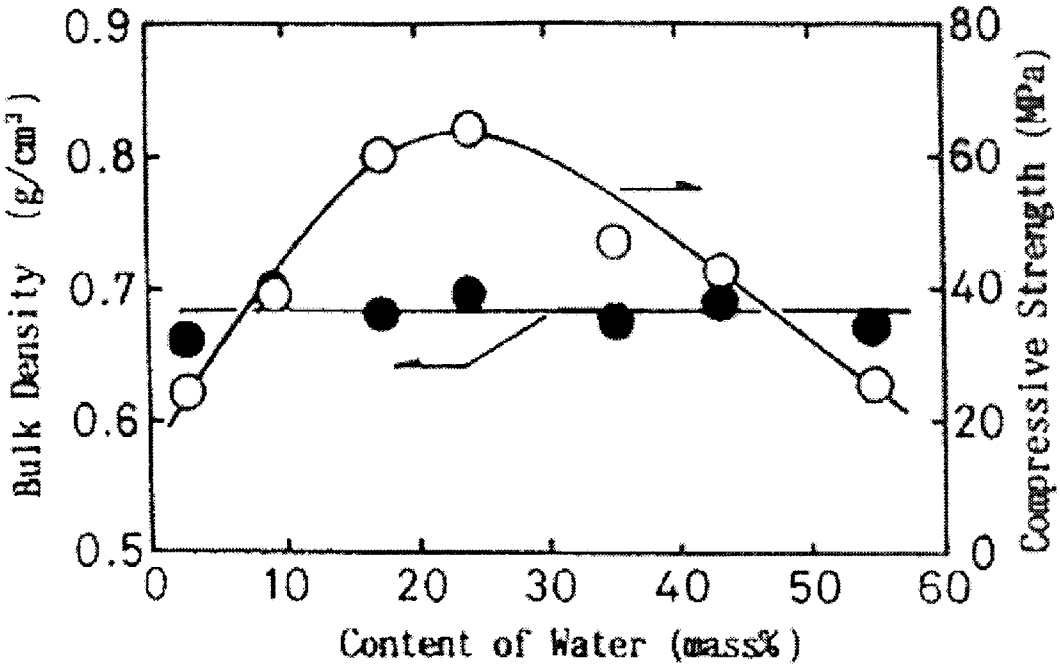

Figure 4-9. Physical properties of the Kochi University ceramics (after Yanagisawa et al. 1994).

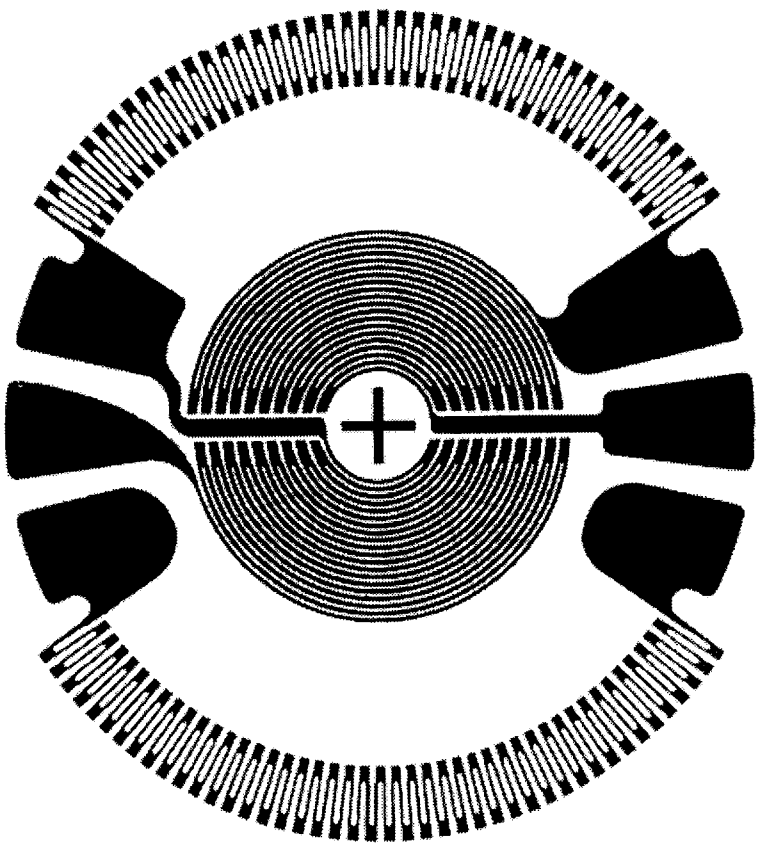

Figure 4-10. BLH Full bridge strain gage configuration.

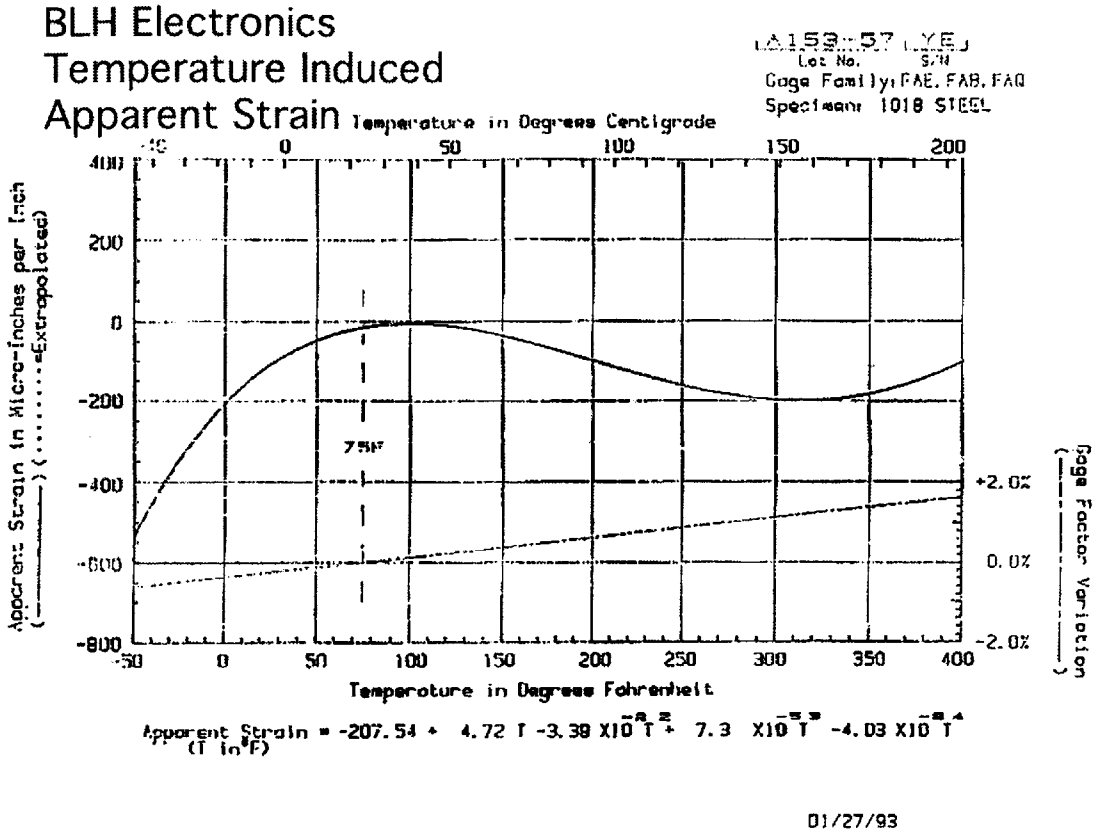

Figure 4-11. Thermal drift of BLH strain gage.

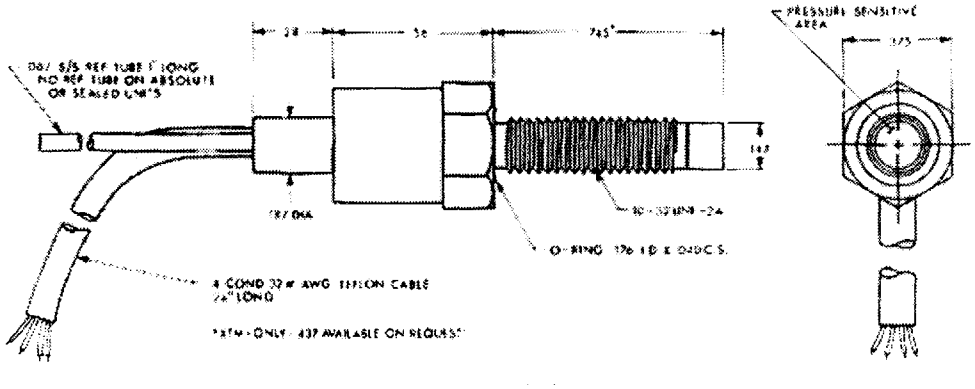

Figure 4-12. Kulite miniature pressure transducer.

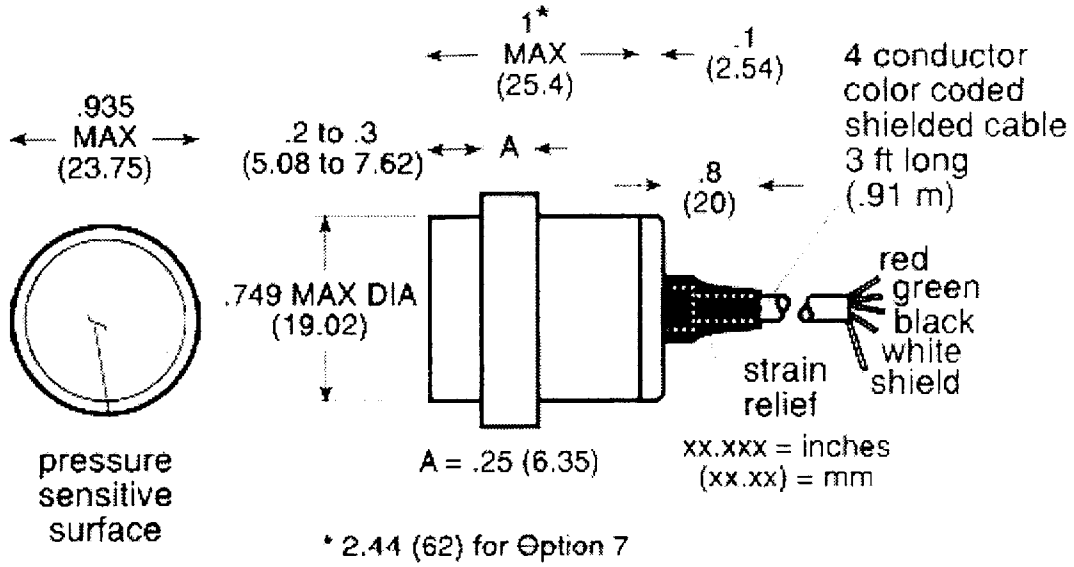

Figure 4-13. Data Instruments pressure transducer.

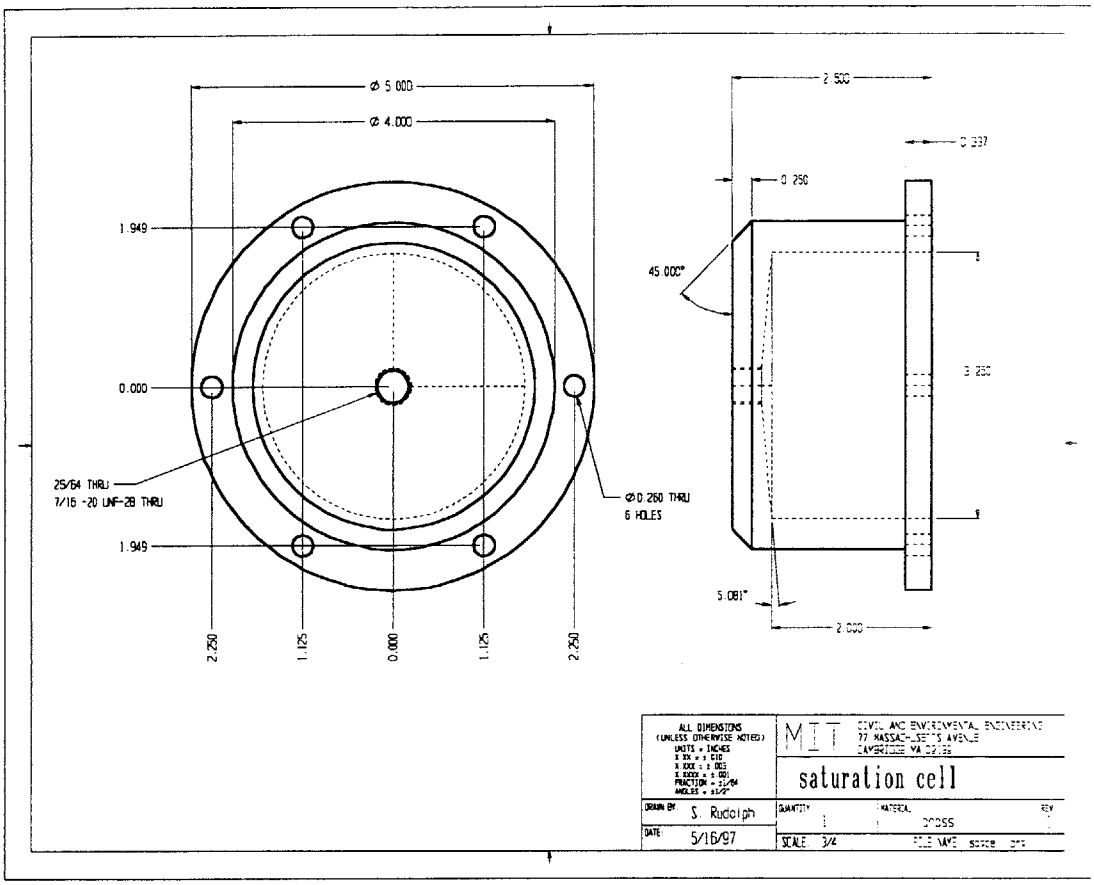

Figure 4-14. Mechanical drawing of saturation chamber (from Rudolph).

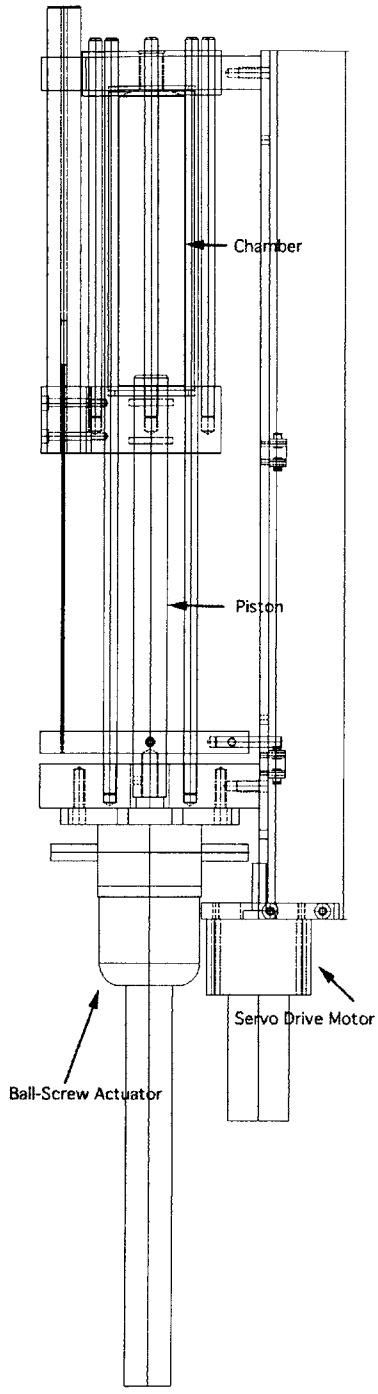

Figure 4-15. Pressure volume device setup.

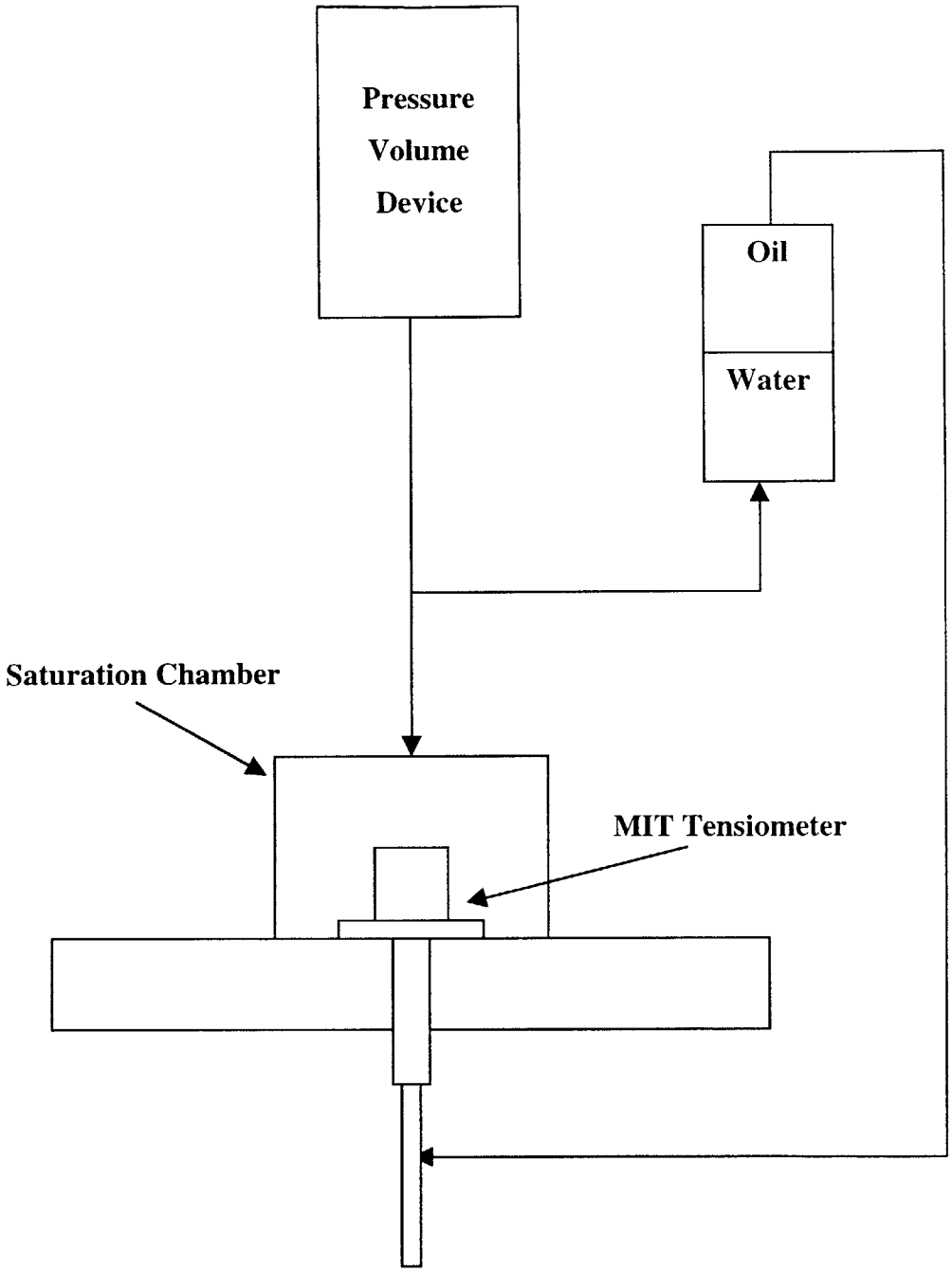

Figure 4-16. Schematic of saturation setup.

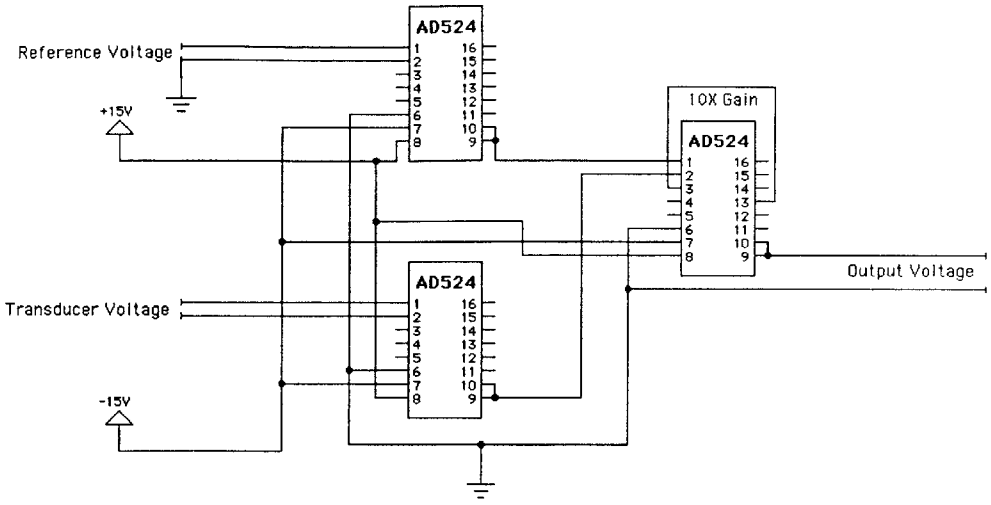

Figure 4-17. Analog-analog feedback circuit.

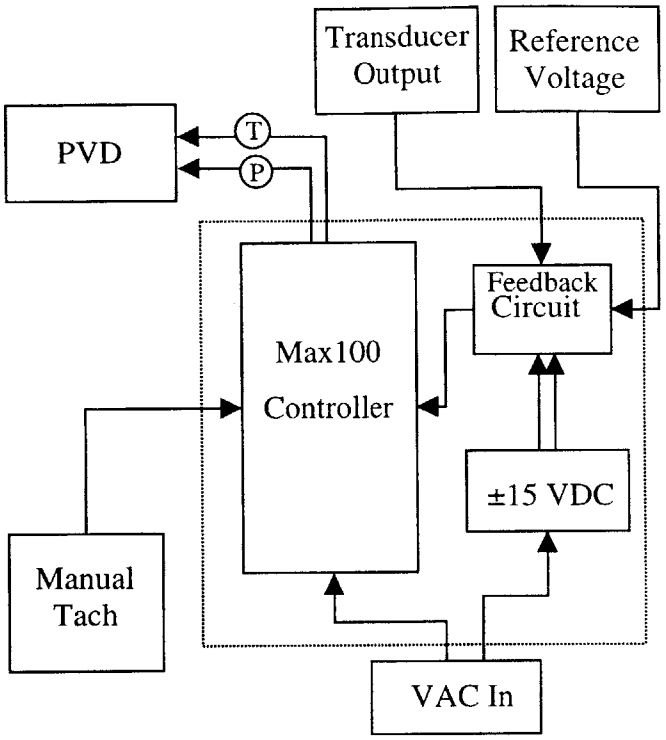

Figure 4-18. Block diagram of saturation control system.

Chapter 5 Equipment Evaluation

5.1 Introduction

This Chapter discusses the performance of the MIT Tensiometer and the supporting equipment to measure the drying curve of porous materials. The various versions of the Tensiometer were constructed in order to improve the performance of previous versions. These improvements are described in two sections. Section 5.2 evaluates the two stones used in the research and discusses the relative advantages of each. The Tensiometer performance is discussed in Section 5.3, and finally the balance used to measure the moisture loss of the system is reviewed in Section 5.4.

5.2 Porous Ceramic Stones

The porous ceramics used as the interface material of the Tensiometer had several functions. The ceramic supported the matrix of the material to be tested while allowing the pore water to migrate freely between the pores and the Tensiometer reservoir. The stone also provided the ability of the Tensiometer to sustain a tension measurement by acting as a capillary barrier between the material to be measured and the reservoir. These functions made the stones a key component in the performance of the Tensiometer. Therefore, a significant effort was put into evaluation of the ceramics.

5.2.1 Saturation Curves

During the saturation process, the Tensiometer was monitored to assure a complete saturation. It was observed that the rate in which the water permeated through the stone was far in excess of what was to be expected. As discussed in the previous Chapter, the saturation process consisted of several steps. First the Tensiometer was placed in the

saturation chamber and a vacuum was applied for 0.5 hour. Then the chamber and Tensiometer were flooded with water while still under vacuum. Once filled, the pressure in the water was raised to the required overpressure value. A typical response of the Tensiometer during this process is shown in Figure 5-1.

Figure 5-1 shows several 'zones' of the saturation process. The first portion of the curve is flat, this is prior to application of a vacuum to the system. Once the vacuum is applied, the transducers measure a drop in pressure as shown in the figure by a decreasing slope. At the point of the first arrow in the figure, this is the time when the vacuum is stopped and water is flooded into the chamber. Once water fills the chamber a jump in pressure is measured by the transducers as the pressure in the system goes from a negative pressure to a positive pressure. The positive pressure is a result of the hydrostatic head from the height of the water supply above the chamber. The second arrow in the figure gives an indication of the time when the MIT Tensiometer registers a positive pressure. The lag time between the arrows indicates the time that water must travel through the ceramic stone and into the water reservoir of the Tensiometer in order for the correct pressure to be read. After this point, the analog-analog feedback system is activated. The transducers measure an increase in pressure until the target pressure is reached. From there the feedback control systems maintains the pressure on the saturation system.

The lag time discussed above is to be expected as the hydraulic conductivity of the ceramic stone is quite low. Using a reasonable estimate of the hydraulic conductivity of the porous stone, it is possible to calculate the expected time of the lag. From Soil Moisture Corporation, a 15 bar stone has a hydraulic conductivity of 2.59×10^{-9} cm/sec. The driving head across the stone is approximately one atmosphere, and the thickness of the ceramic stone is 0.6 cm. Using the Darcy Equation for flow:

$$q = ki \qquad [5.1]$$

where;

q is the Darcy velocity [L/T]
k is the hydraulic conductivity [L/T]
i is the hydraulic gradient [L/L]

Inserting the above values into Equation [5.1] gives a Darcy velocity of 4.32×10^{-6} cm/sec. Using the 0.6 cm thickness of the stone, a travel time of 38 hours is obtained. However, the measured lag time is much less at 3-5 minutes. Clearly the transport of the water through the stone is not occurring as liquid advective transport. A more realistic model would be a vapor transport model since the negative pressure of the saturation chamber would certainly cause some water to be in the vapor state.

5.2.2 Maximum Tension Developed

To maximize the efficiency of the saturation process, it was desired to determine the lowest over-pressure needed to achieve the highest sustained tension. Therefore, a series of tests were conducted to develop a relationship between overpressure and sustained tension in the MIT Tensiometer. The tests were conducted on Versions 3.0 and 3.1 of the Tensiometer.

For either version, the test followed the same procedure. A standard saturation procedure consisted of evacuation of the MIT Tensiometer and saturation chamber followed by flooding the system with de-aired water. The pressure in the water was then raised to a prescribed level and held overnight. The system was then relieved of the pressure and drained. The MIT Tensiometer was then allowed to dry in ambient laboratory air. The drying of the stone causes an increase of tension in the reservoir and stone pore water. The tension was allowed to increase to a maximum value until the system would break, i.e. loss of tension would occur. A plot of the tension obtained versus over-pressure is shown in Figure 5-2. A typical drying test is shown in Figure 5-3.

From Figure 5-2, it is clearly seen that the Kochi University stones required much less overpressure to obtain the maximum value as opposed to the Soil Moisture stones. From this evaluation, the saturation procedure of the MIT Tensiometer was modified to sufficiently saturate the stone.

5.2.3 Fatigue

It was observed with the Kochi University stones that over time the maximum sustained tension decreased. Upon changing the stones in the Tensiometer, the stones showed a great deal of fracturing. It is not known if the fracturing started as a micro-crack in the stone and then, once machined to be removed, expanded. In any case, once out of the Tensiometer the stone would break into several pieces. Removal of stones that showed no decrease in sustained tension remained intact once machined out.

This behavior is assumed to be attributed to repeated cycles of high tension in the pore water suddenly being released to atmospheric due to breaking of the tension. Whether the break in the tension was a result of inadequate saturation or simply exceeding the bubbling pressure of the stone is not necessary important. In either case, the water underwent a sudden release of energy. The energy released was large enough that an audible metallic click was heard at the time of the tension loss. From reviewing laboratory notes, a very rough estimate was made of the number of cycles of tension losses needed to degrade the stone. This appeared to approach 50 cycles before a noticeable decrease in tension was observed. No degradation was observed for the Soil Moisture stones, however, Guan and Fredlund (1997) reports this phenomenon for a porous ceramic used in their study (the ceramic was not identified).

5.2.4 Ion Effects

To determine if the MIT Tensiometer was acting as a semi-permeable membrane, several tests were done with salt solutions placed in contact with the ceramic stone. If the porous ceramic stone were in fact acting to prohibit salt ion migration, then the Tensiometer would measure some type of osmotic pressure. It has been argued that the porous ceramic stones could possibly create an osmotic pressure between the material being measured and the water reservoir in the measuring system (Ridley and Burland 1993). However, Ridley (1993) concluded that the stones were not acting to inhibit ion migration. This fact becomes important when measuring unsaturated soils as all soils release some ions in the pore fluid. If the stones act to set up an osmotic potential then

the Tensiometer would be measuring the total suction and not the matric suction as desired.

To check the compliance of the MIT Tensiometer with ions in a pore fluid three concentrations of sodium chloride were prepared at concentrations of 0.01, 0.1, and 1.0 molar solutions. Each solution was placed in a cup upon the MIT Tensiometer and left to sit in a temperature controlled environment (at 25°C) for 24 hours. None of the solutions produced any change in the output of the Tensiometer indicating that the MIT Tensiometer was not measuring any type of osmotic potential.

5.3 Base

The base of the MIT Tensiometer consisted of the metal body, diaphragm, reservoir, and any associated electronics. The following sections discuss the performance of these components in the various versions of the Tensiometer.

5.3.1 Measurement Range

The most critical driving force for the evolution of the MIT Tensiometer was the measurement range of the device. Each subsequent version was constructed to either extend the range of the prior version or increase the consistency of the measurements.

The first version of the MIT Tensiometer showed very poor measurement range. The device's maximum tension measured was nearly 0.9 bar. Since this version was never subjected to positive saturation pressures, it is not clear as to if the range of the device could have been extended with overpressure.

Version 2.0 was built to overcome the low tensions sustained by Version 1.0. At the time of construction, it was felt that the first version had too great a volume of water in the measuring system. Version 2.0 would overcome this by bringing the sensing diaphragm

of the Kulite pressure transducer close to the ceramic stone. The seal used to cut off the transducer from the outside was made with a compressed Buna-n o-ring. This version also incorporated the positive pressure saturation procedure. Positive pressures of 50 bar were used to saturate the device. With these two primary differences from the prior version, maximum sustained tensions approached 10 bar. However, consistency between maximum tension measurements varied greatly. With the same procedure and setup, the device would give tensions from slightly greater than 1 bar to 10 bar. After careful consideration of the design, it was theorized that the o-ring seal was the most probable the cause of the inconsistencies. Another device found in the literature utilized similar sealing configurations and experienced the same problem (Guan and Fredlund 1997), although the authors attributed some of the failures to the ceramic stones and not to the seal.

Version 3.0 was designed to eliminate the o-ring seal. The device used an integral diaphragm as part of the pedestal itself. As a result of eliminating the seals, Version 3.0 showed excellent ability to sustain tensions. This version consistently reached tensions equal to the rated bubbling pressure of the stone at 15 bar, thus confirming the hyppthesis.

To extend the range of Version 3.0, a new ceramic stone was incorporated into the design. The Kochi University stones were substituted into the design and proved to show immediate improvements in both maximum tension attained and ability to saturate. The saturation lag time discussed in Section 5.2.1 was reduced in half. This indicated to some extent the excellent interconnectivity of the pores in the ceramic. This feature was discussed by Professor Yanagisawa (1994). Lower saturation pressures were also required as discussed in Section 5.2.1. The maximum tension attained also was increased to a value of 22 bar. The long-term ability to sustain large tensions is discussed in Section 5.2.3.

An attempt was made to develop a device with a ceramic stone covering the entire cross sectional area. This was MIT Tensiometer Version 4.0. As discussed in the previous

Chapter, only slight modifications were needed to Version 3.0 to produce Version 4.0. However, all attempts at maintaining any tensions were not successful. Substantial effort was put into determining the reason for the failure of this version. At this point no conclusive reasons are known as to the cause of the device's inability to maintain a tension. Further work on this version was halted as it was deemed of lessor importance to the overall progression of the project.

Version 5.0 was constructed to overcome the electronic sensitivity and stability problems of Version 3.1. Since the same ceramic stones were used in this version as in Version 3.1, the maximum sustained tensions were similar at 20 bar.

5.3.2 Sensitivity

The absolute sensitivity of the Tensiometer is limited only by the data acquisition unit making the readings of the output signal. Currently the MIT Geotechnical laboratory utilizes a Hewlett Packard data acquisition unit (DAQ). The model number of the DAQ is *HP3497A*. The analog to digital conversion of the DAQ is given in a digit resolution. The maximum number of digits that the DAQ can resolve is 6.5. For the range of the Tensiometer output, this translates into a resolution of $1x10^{-6}$ volts for voltages up to 100mV.

The calibration factor for the MIT Tensiometer is 689.887 bar/V/V. Using an excitation voltage of 5.5 volts, this yields a minimum pressure that the Tensiometer can resolve as $1.25x10^{-4}$ bar ($1.82x10^{-3}$ psi). This is the 'best case' scenario without the effects of electronic noise and drift.

To provide an estimate of the amount of electronic noise associated with the DAQ, a simple monitoring test was conducted on the MIT Tensiometer. A reading was taken every second over a 2-minute interval with the DAQ (Figure 5-4). The range of the signals obtained was $\pm 8x10^{-6}$ volts. This translates into $\pm 1x10^{-3}$ bar ($1.5x10^{-2}$ psi) of

pressure. Therefore, for any given reading a maximum Tensiometer resolution based on electronic noise can be given to the nearest $1x10^{-3}$ bar.

5.3.3 Stability Over Time

Determination of the long-term stability of the MIT Tensiometer over time was evaluated. The MIT Tensiometer was placed in a temperature-controlled environment at 25°C with a 1 cm head of water above the stone. The electronic output of the Tensiometer was then monitored for 24 hours. The result of this monitoring is shown in Figure 5-5. Analysis of the monitoring revealed that the standard deviation of the electronic output was 0.12mV. This corresponds to a pressure fluctuation of 0.015 bar.

5.3.4 Response Time

Figure 5-6 shows the MIT Tensiometer's response when exposed to soils of various matric potentials. As can be seen in the figure, the Tensiometer responds very quickly to the imposed potential. Generally, the Tensiometer attains the equilibrium maximum suction within 2 minutes. As also shown in the figure, the long term stability of a suction measurement is very good and varies less than 2% of the maximum suction as measured over 1 day.

5.4 Balance

The electronic laboratory balance used to measure the mass loss of a drying test was the Mettler-Toledo BB2400. The following sections discuss the performance of the balance.

5.4.1 Stability

Monitoring the output made an approximation of the stability of the balance over a typical testing time of 24 hours. With a mass of 625 grams (an approximate mass of the MIT Tensiometer and specimen) on the balance, the re-zeroing stability was checked. Figure 5-7 displays the output of the balance over time with the mass re-zeroed. The

standard deviation of the output was less than 0.01 grams at 0.008 grams. The maximum drift of the output ranges from 0.01 to -0.02 grams with an average reading (mode) of -0.01 grams.

5.4.2 Sensitivity

The BB2400 has a resolution of 0.01 grams. The balance has a maximum capacity of 2400 grams and the resolution remains at 0.01 grams throughout. The repeatability and linearity of the balance are given by the manufacturer at 0.01 and ±0.02 grams respectively. These values are reported over the full-scale output.

5.4.3 Zero Drift

To estimate the zero shift of the balance, a 625 gram mass (approximate mass of the MIT Tensiometer and specimen) was put on the balance and zeroed. The mass was then removed after 24 hours and the balance returned to a reading of 0.00 grams. This indicates that for the measurements range and testing times expected, that the balance has negligible zero drift.

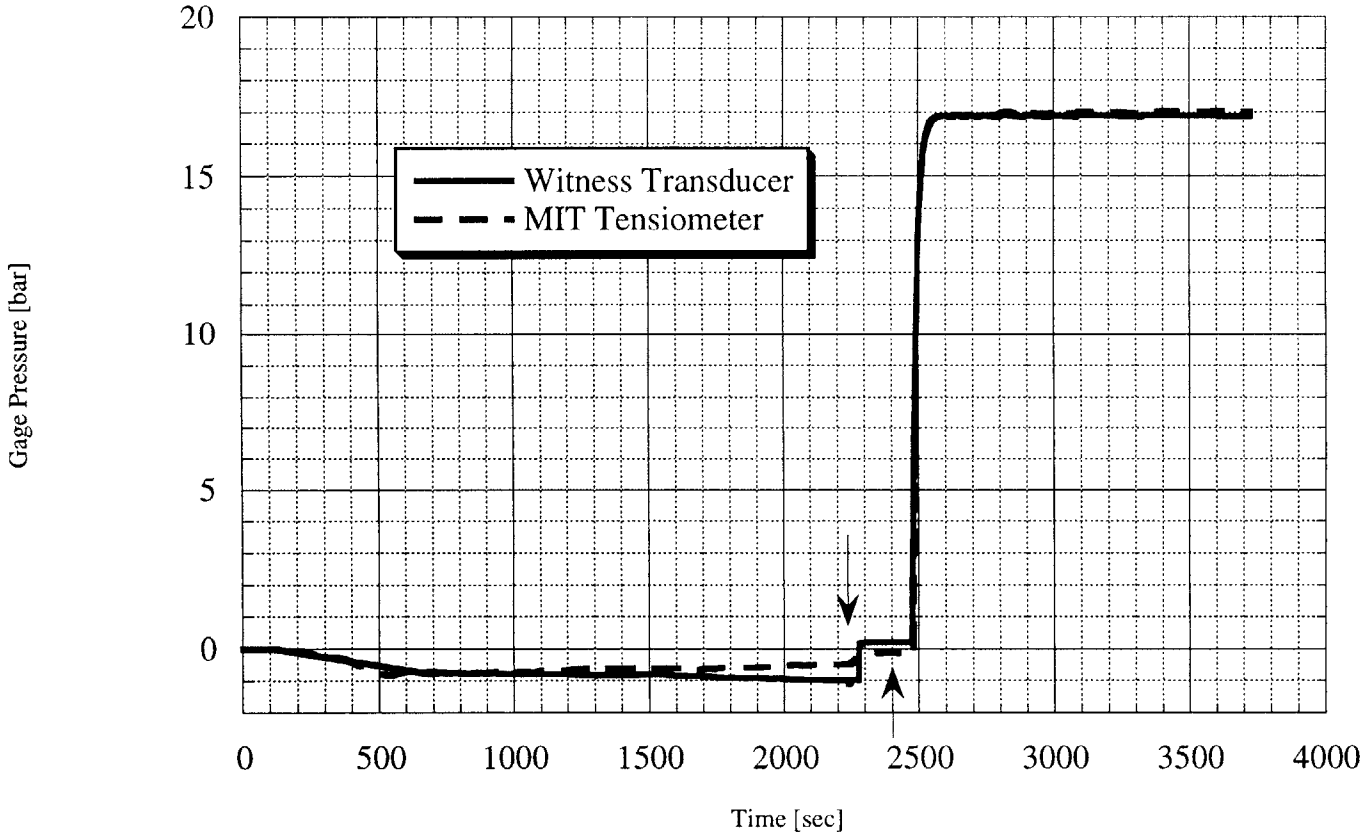

Figure 5-1. MIT Tensiometer response during saturation.

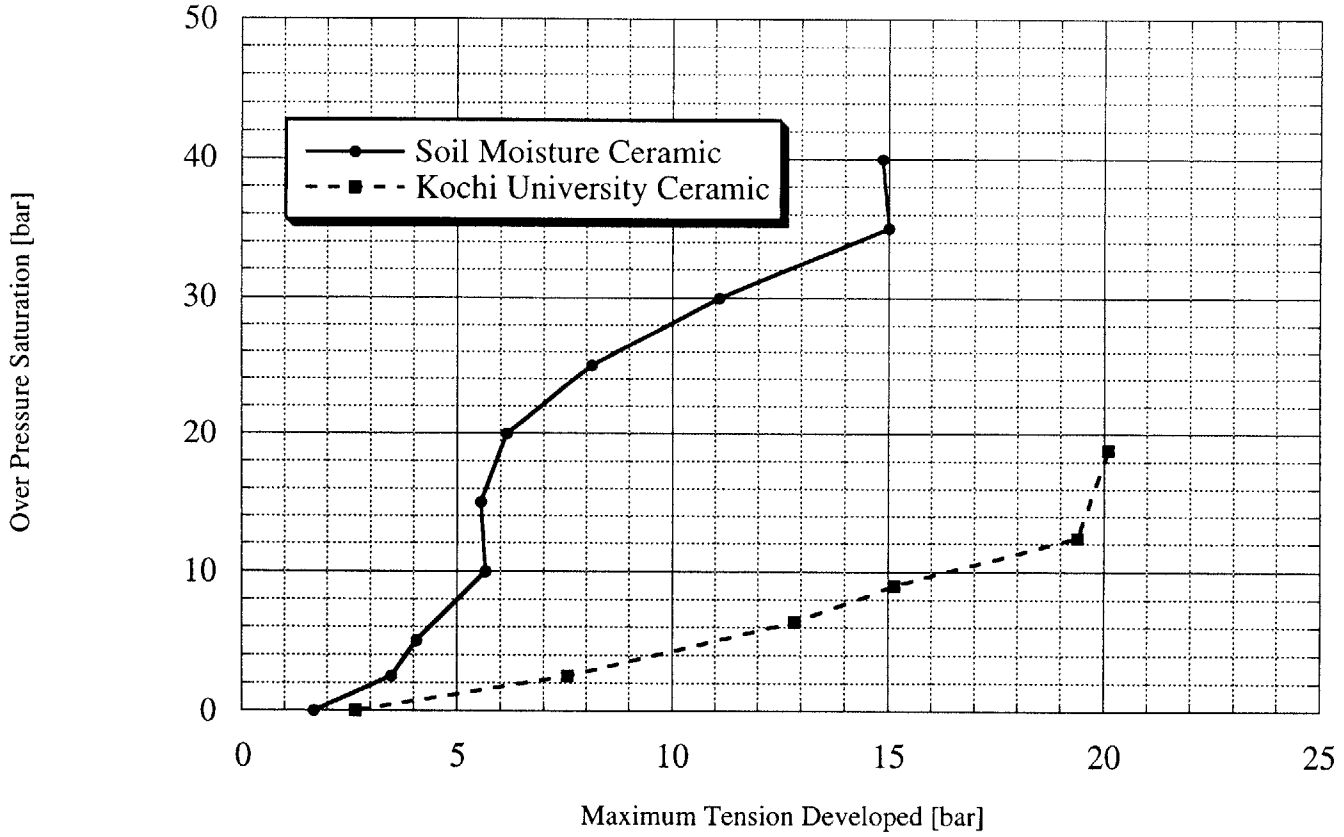

Figure 5-2. Maximum tension versus over-pressure for two types of stones.

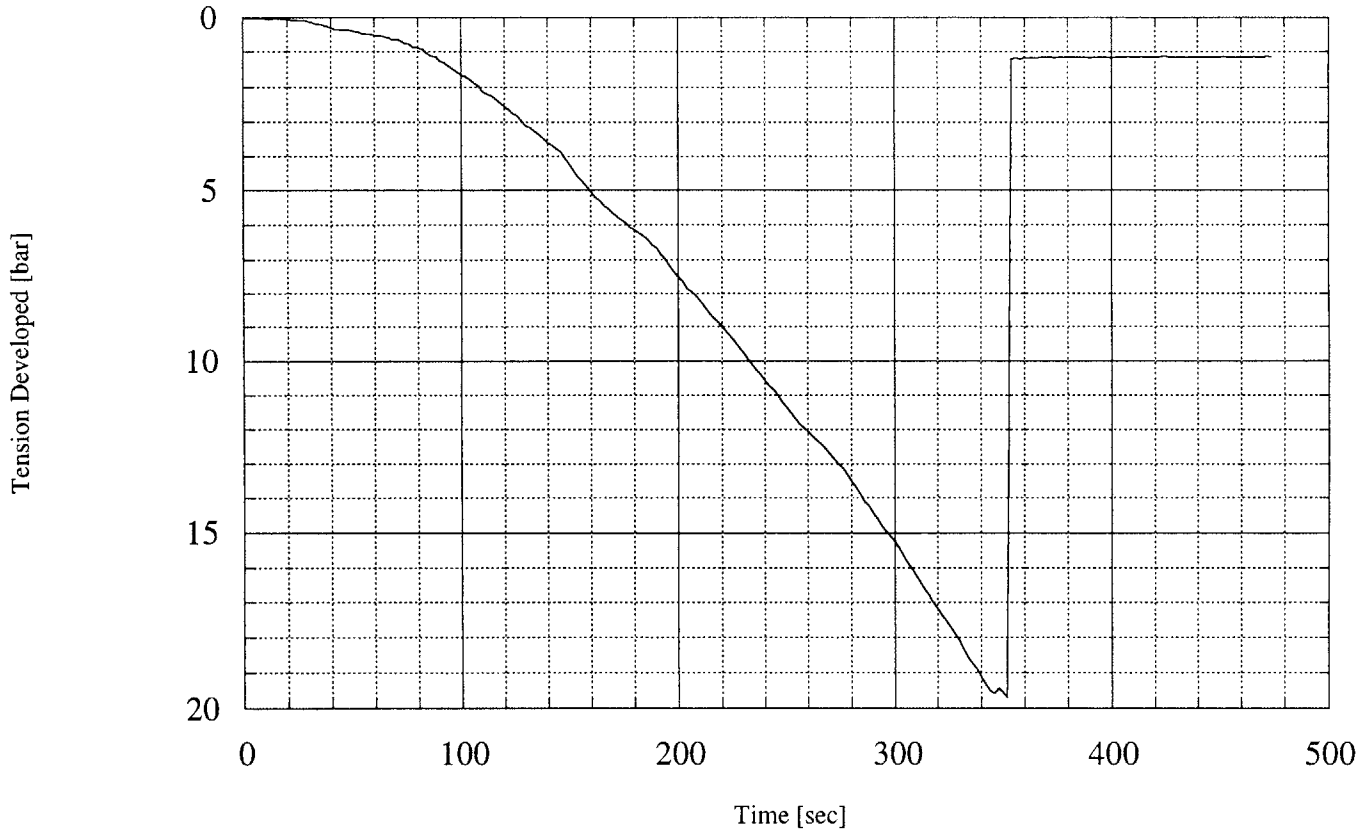

Figure 5-3. Typical drying response of MIT Tensiometer Version 3.1.

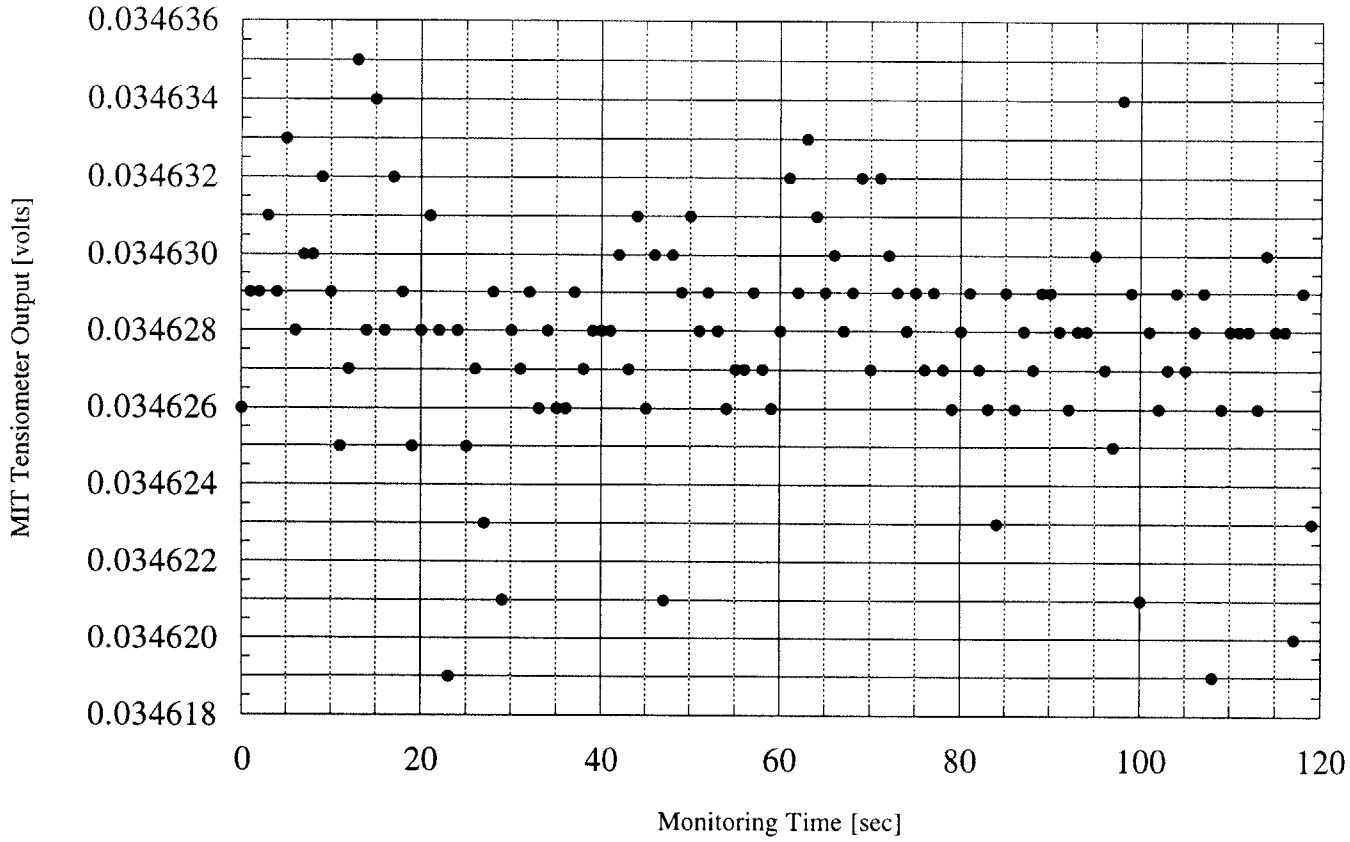

Figure 5-4. Monitoring of the MIT Tensiometer Version 5.0.

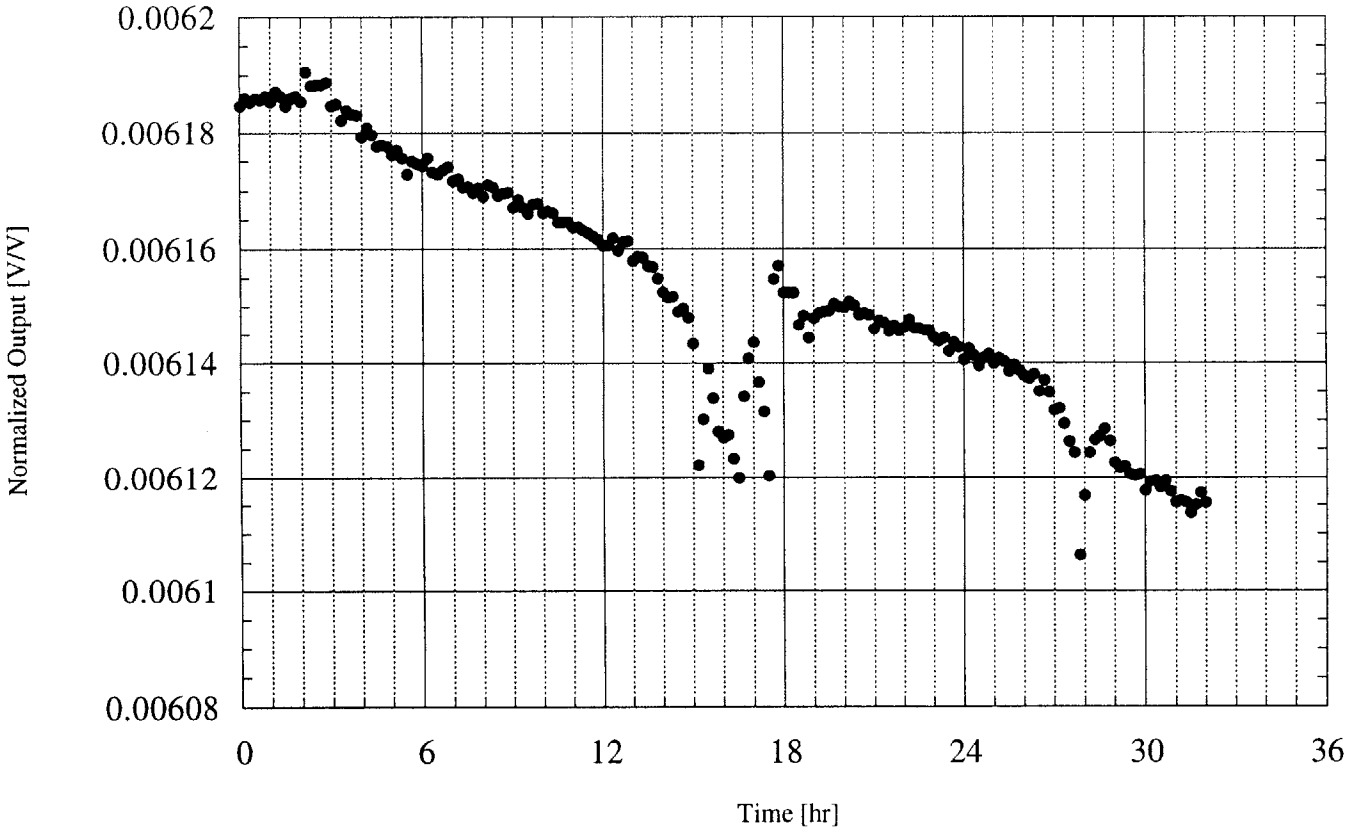

Figure 5-5. MIT Tensiometer Version 5.0 normalized output over time.

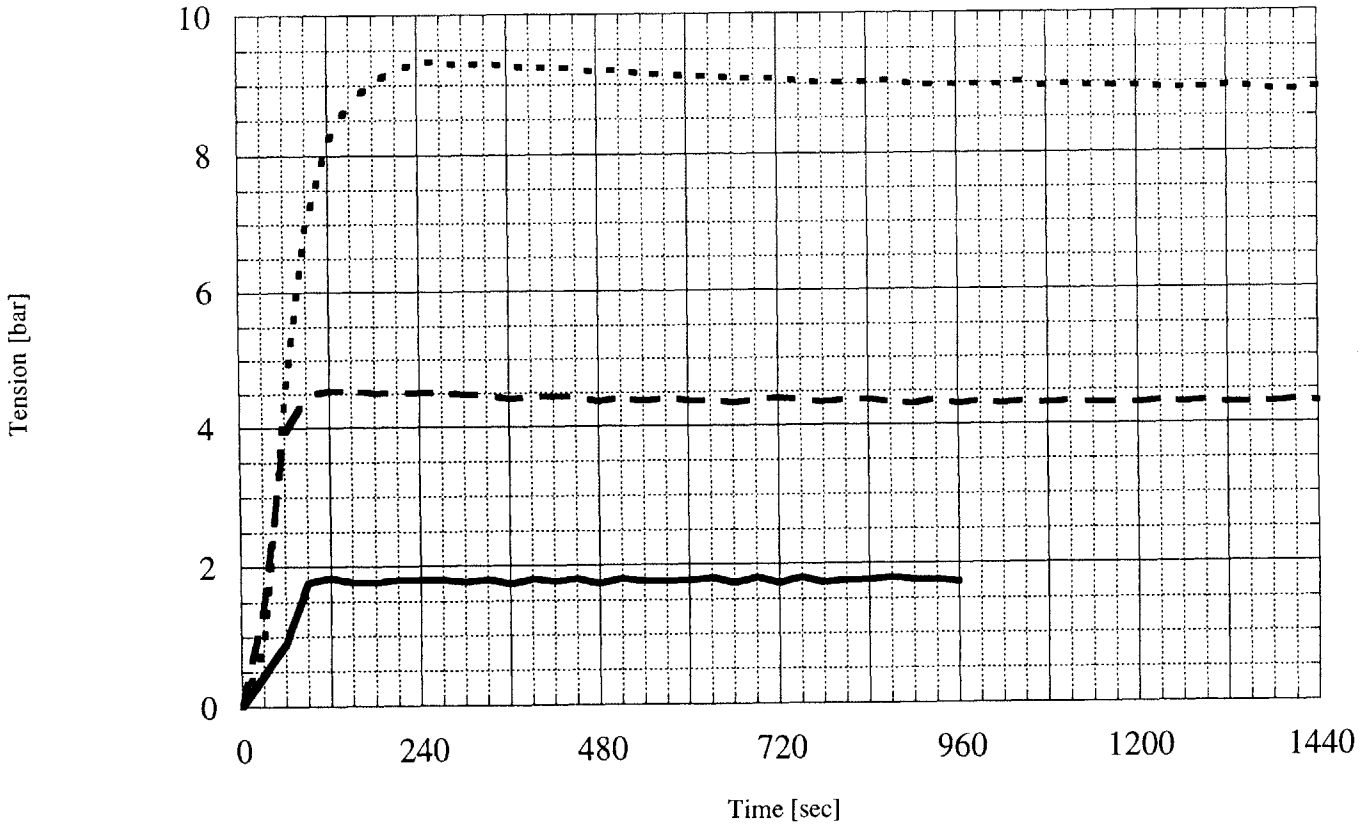

Figure 5-6. Typical MIT Tensiometer Version 3.0 response.

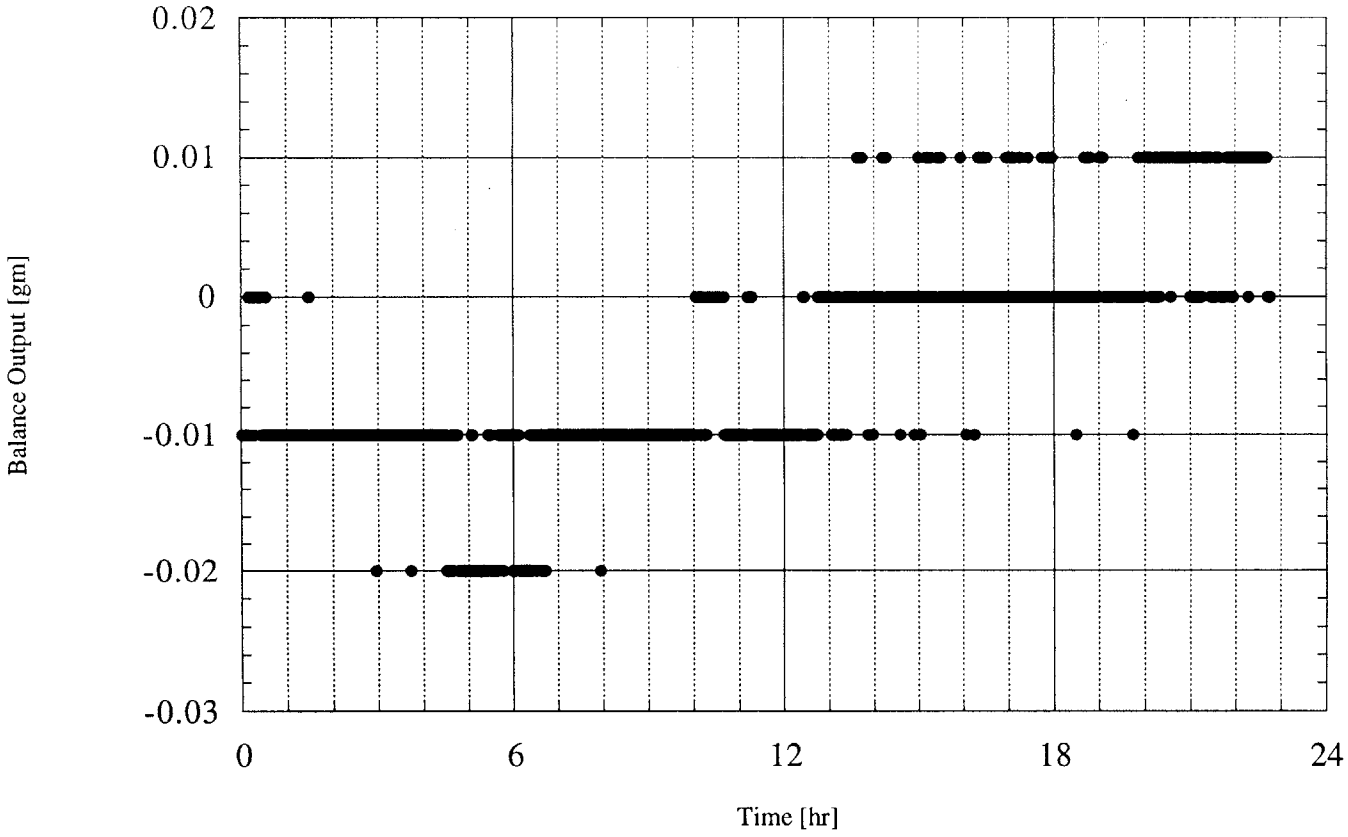

Figure 5-7. Balance output over time

Chapter 6 Materials and Procedures

6.1 Introduction.

This Chapter presents the materials and preparation procedures used throughout this research. Several soils were used along with glass beads. The soils chosen were two clays, one CL and one CH, two ML silts and a fine sand. These materials are described in Section 6.2. The method of preparation of the materials is described in Section 6.3. Finally, in Section 6.4, the testing procedures are described and explained.

6.2 Materials

Both natural and synthetic materials were tested in order to provide insight into the drying behavior of a porous matrix. These materials are discussed in the following sections and physical properties are listed in Table 6-1.

6.2.1 Glass Beads

A material with simple uniform geometry would need to be tested to better understand the drying process. The model of Chapter 3 simplifies a soil to a matrix of regularly packed spheres. By controlling the size and shape of the material, the proposed model could be verified. Thus glass beads were chosen as a primary material to examine. With glass beads, surface effects would be minimized and the material would have only one composition.

The glass beads were obtained in the lab from a previous research project. The beads were found in one large container and not fractionated. To separate the beads, a series of sieves were used. Based upon the available sieves in the laboratory, the following

fractions were separated; 75-90 μm, 125-150 μm, 250-300 μm, and 500+ μm. The specific gravity of the beads was measured to be 2.43. This corresponds to a Borosilicate composition.

6.2.2 Soils

Five soils were chosen to give a generalized behavioral trend over a wide range of soil types. Two clays were used, Resedimented Boston Blue Clay and a Vicksburg Buckshot Clay. These two clays cover a range of plasticity as RBBC has a USCS classification of CL and VCB is a CH type clay. Two types of silt were also tested to examine the behavior of non-plastic material. Both silts are classified by USCS as ML. Finally, fine sand was also tested. Manchester Fine Sand was chosen, as the grain size distribution of the material is very narrow. The five soils are described in the following sections.

6.2.2.1 Resedimented Boston Blue Clay (RBBC)

Resedimented Boston Blue Clay (RBBC) has been used in the MIT Geotechnical laboratory for forty years and its' properties are well documented (Cauble 1996; Force 1998). Cauble gives the procedure and method to produce a batch of RBBC from dry Boston Blue Clay. The material was prepared to give a saturated block of clay with a slight overconsolidation. The material was consolidated to 1 ksc and then unloaded to 0.25 ksc. This gave the RBBC a structure similar to natural Boston Blue Clay. The two batches used in this research were 418 and 420. Force gives the following index properties of these batches as: w_p = 23.5±1.1%, w_l = 46.1±0.9%, and I_p = 22.7±1.4%. Force also gives a range of specific gravity of the solids as 2.78 to 2.785. The clay fraction reported was 58±1.2% with a salt content of 11.6±1.5 g/L based on KCl. Finally loss on ingnition (ASTM 2974) was determined to be 4.4%. A grain size distribution is given in Figure 6-1.

6.2.2.2 Vicksburg Buckshot Clay

A CH type clay was obtained to examine the drying effects of a high plasticity clay. The clay chosen was a Vicksburg Buckshot Clay (VBC) and was obtained from ASTM. VBC is one of ASTM's test soils for the *Interlaboratory Testing Program.* ASTM also supplied the physical properties of the clay. VBC is classified as a CH type of clay due to the clay plotting above the A-Line on the plasticity chart and liquid limit greater than 50%. The Atterberg limits for VBC were given as: w_p = 20.4%, w_l = 59.7%, and I_p = 39.3. A hydrometer analysis, given in Figure 6-2, reveals that nearly 50% of the material is clay size (<2 μm). The specific gravity of the clay was given as 2.726.

6.2.2.3 Tennessee Silt

A silty soil was obtained from Mr. Samuel Dennis at Tennessee State University (sdennis@picard.tnstate.edu). Mr. Dennis provided 7 samples contained in aluminum rings. The rings measured 7.63 cm in diameter and also in height. The samples were completely air dried when received at MIT, thus the natural water content was not known. A grain size analysis was done on the sample numbered #371 and is presented in Figure 6-3. Atterberg limits were also done on the fine fraction of the soil. The soil displayed no plasticity in the index testing and thus was classified as silty sand following USCS and ASTM. A specific gravity of the material was not available.

6.2.2.4 Manchester Fine Sand

The MIT Geotechnical laboratory has utilized Manchester Fine Sand for many years on various research projects and its' properties are well documented. Da Re (2000) gives an in depth treatment to this topic, however the soil is classified as a poorly graded sand with silt or a USCS of SP-SM. A grain size distribution is given in Figure 6-4. The material had a specific gravity of 2.688 (Da Re 2000). The particles can be described as sub-angular and ellipsoidal in shape.

6.2.2.5 Maine Silt

The Maine Silt was obtained through the private consulting of Dr. John T. Germaine of the Department of Civil and Environmental Engineering at MIT. The soil originated in southern Maine, however no specifics are provided for client confidentiality reasons. The soil was fractionated by repeatedly settling the material in a water column. This resulted in a material with a very poor gradation. The specific gravity of the material was assumed to be 2.78. The USCS classification of the material is ML or Silt. The material produced a grain size plot that is shown in Figure 6-5.

6.3 Specimen Preparation

The following sections describe the procedures used to prepare the test material used in this research.

6.3.1 Glass Beads

The granular nature of the glass beads required an external-supporting device to maintain the shape of any prepared specimens. A Lexan® retaining ring was created to provide this function. The ring had an inside diameter slightly smaller than the diameter of the MIT Tensiometer, thus the ring rested upon the top of the Tensiometer. Figure 6-6 shows schematically this configuration. As shown in the Figure, the ring was constructed of several sections. These sections could be stacked in order to provide different specimen heights while maintaining the same cross sectional area. Each segment of the retaining ring had a height of 1 inch. Therefore, a maximum specimen size of 3 inches was possible. An o-ring seal was located in the bottom section to provide a water tight joint between the ring and the MIT Tensiometer. The other sections fit together with a compression seal.

The specimens, regardless of bead diameter were prepared in a similar manner. The retaining ring was affixed to the MIT Tensiometer and then placed into the saturation chamber. The number of sections of retaining ring depended on the height of the

specimen required. The dry beads were then poured into the retaining ring by means of a plastic funnel. The plastic funnel was fashioned from a disposable 25 mL pipet. As the beads ran into the retaining ring, the funnel was moved and raised to fill the entire cross section. Once near the top of the retaining ring, the beads were piled slightly higher than the ring. The excess beads were then scraped flush with the top of the retaining ring with a metal knife. A porous ceramic stone was then placed on top of the beads and rested on the top edge of the ring. The stone served to keep the beads from spilling out into the saturation chamber for the remainder of the process. The saturation process then continued as described in Section 6.4.1.

Due to the small size of the beads, a controlled packing arrangement was not possible. However, since the specimens were all prepared with the same procedure, it was felt that the resulting packing was very similar. The dry densities obtained from all of the tests using this procedure ranged from 1.39 to 1.46 g/cm^3 with an average of 1.43 g/cm^3 and a standard deviation of 0.02 g/cm^3.

For the specimens tested using version 5.0 of the MIT Tensiometer, a variation of the procedure outlined above was used. The glass beads were initially saturated by being placed into a flask and covered with water. The flask was then evacuated until all evidence of air was removed. This generally took 10-15 minutes with a vacuum of 10 Torr. The mixture of beads and water was then poured into the retaining ring on the Tensiometer. This procedure produced the same dry densities as the dry preparation method.

6.3.2 Soils

6.3.2.1 RBBC

Specimens of RBBC were taken from two batch numbers, 418 and 420. The batch properties and procedures are discussed in Section 6.2.2.1 and given by Force (1998). The specimens were prepared by cutting a section of the batch cake away from the main cake. This section was slightly larger than the final diameter of the specimens (1.4

inches). The sections were then trimmed to the final diameter with a wire saw using the standard laboratory triaxial miter box. Once a column of soil was trimmed to the final size, the column was covered in wax paper. This cylinder of soil was then placed into a metal pipe of slightly larger inside diameter than the diameter of the soil. Disks of RBBC were cut by extruding the soil column out of the pipe and cross cutting with a wire saw. The thickness of the disks ranged from approximately 0.5 cm to 1 cm. Once the disks were cut, they were massed to the nearest 0.01 gm. Each disk was then placed upon the MIT Tensiometer for testing.

6.3.2.2 Vicksburg Buckshot Clay

The Vicksburg Buckshot Clay was prepared in a similar fashion as the RBBC. The dry clay was mixed with water and boiled. The slurry was then poured into the consolidometer and resedimented to a large cake as described by Gonzalez (2000). The procedure was then very similar to the procedure for RBBC as given by Cauble (1996).

The specimen preparation was identical to that as described in Section 6.3.2.1 for the RBBC. A section of soil was cut away from the larger cake and then trimmed to a final column with a diameter of 1.4 inches. The column of soil was then cut into disks with a thickness between 0.5 and 1.0 cm. The cut disks were then massed prior to testing.

6.3.2.3 Tennessee Silt

Due to the relatively small size of the MIT Tensiometer, it was felt that the Tennessee Silt should be screened for oversized particles. Therefore, any size fraction larger than 420 microns (#40 Sieve) was removed. This eliminated any large-particle effects on the drying tests.

The screened material was placed into an evaporating dish and mixed with water until a water content of approximately 30% was obtained. At this point the soil was more slurry

in nature than a cohesive[1] material. The evaporating dish was then placed into a vacuum chamber and evacuated to remove any entrapped air from the mixing process. The vacuum was maintained for approximately 5-10 minutes. The slurry was then carefully poured into the specimen-retaining ring (Figure 6-6) that was on top of the saturated MIT Tensiometer. Once the material filled the ring, the top of the slurry was troweled with a knife to smooth the surface of the specimen.

6.3.2.4 Manchester Fine Sand

The Manchester Fine Sand required no special set up procedures. The material was placed into a vacuum flask and covered with water. A vacuum was applied to the system until all visible air was removed from the soil (usually 10 minutes). The soil was then transferred to the retaining ring with a metal spoon. The retaining ring was filled with water to the top of the ring. The sand was then allowed to slide off of the spoon while submerged. This eliminated the chance for air to become entrapped in the soil once out of the vacuum flask. As the soil was placed into the ring, the displaced water was removed with a pipette or paper towel.

6.3.2.5 Maine Silt

The same procedure outlined above in Section 6.3.2.4 was used for the Maine silt. The silt was slightly smaller in particle size and thus required a longer evacuation (15 minutes) prior to placement. The procedure then followed as described above.

6.4 Testing Methods

The following sections outline the basic procedures used to test the materials described above. A detailed step-by-step procedure is presented in Appendix B.

---

[1] *cohesive* in this sense refers to the material's ability to remain as a solid, this does not infer that the material exhibits plasticity.

6.4.1 Tensiometer Saturation Procedure

The MIT Tensiometer required saturation prior to each use. The saturation procedure could generally be accomplished overnight. The procedure consisted of three basic phases; evacuation, flooding and overpressure.

The MIT Tensiometer was secured into the saturation chamber at the onset of the procedure. The chamber along with the Tensiometer was wiped dry to eliminate delays caused by water going into the vapor state. The elimination of the water also insured that the chamber would not undergo a large drop in temperature due to the endothermic nature of water when exposed to a vacuum. The chamber top was then secured and a vacuum was applied to the system. The vacuum was held for approximately 30 min and usually attained a magnitude of 1- 5 mTorr.

De-aired water was then flooded into the chamber as the vacuum valve was closed. The seals of the chamber maintained a vacuum while water filled the chamber. Once the chamber was filled, a valve at the top of the chamber was cracked open to allow water to drain out. The supply of de-aired water was above the chamber, thus allowing positive pressure throughout the chamber. By allowing water to flow out the top of the chamber, it was verified that no air was trapped in any of the pipefittings at the top of the chamber.

After the chamber was filled with water and checked for trapped air, a positive pressure was applied to the chamber water. This was done by the pressure volume device (PVD) described in Chapter 4. A target voltage was set on the analog-analog feedback system controlling the PVD. This target voltage corresponds to a required pressure needed to saturate the MIT Tensiometer. During this process, the output of the Tensiometer was monitored to assure proper functioning of the device. The pressure was maintained overnight and usually lasted 12 hours, although longer times up to one week were maintained with no observable change in the operation of the device.

After the pressure up phase, the water pressure was reduced by using the manual tachometer on the analog-analog feedback control system. The rate of decrease was

approximately 1 bar/min. The pressure was decreased until the transducer output was that of the initial reading after the flooding phase. At this point the chamber was drained and disassembled. The MIT Tensiometer was now ready for use. Since the ceramic stone was very susceptible to drying, the Tensiometer was covered with a prophylactic until testing was to commence. This time period was never greater than a few hours.

6.4.2 Drying Test Procedure

The drying test procedure utilized three basic pieces of equipment; the MIT Tensiometer, a laboratory balance and a data acquisition unit. The basic setup is shown in Figure 6-7.

Once the MIT Tensiometer was saturated, the specimen was placed on the device (in the case of the glass beads this was done in the saturation phase). The device and specimen were then set in a plastic holder to allow for the electronics to exit the bottom unencumbered. Care was taken to keep the wires from being twisted, as this would cause a slight disturbance in the mass measurements. The configuration was then set on top of the laboratory balance and monitored for 5 minutes to allow any relaxation of the wires. After this time the balance was zeroed and the Tensiometer zero was taken.

The balance and Tensiometer were enclosed in a Styrofoam® box that was open on the top and bottom. The purpose of this box was to eliminate any air currents from disrupting the output of the balance. Above the specimen, a container of desiccant was suspended (this is not shown in Figure 6-7). This desiccant was used when it was necessary to increase the rate of drying of the specimen. The entire setup was enclosed in a temperature-controlled enclosure. The temperature was kept at 25°C for the duration of the test.

Once the equipment was set up, the procedure continued by simply taking readings on the data acquisition unit of the output of the MIT Tensiometer and the laboratory balance. As water left the specimen, the tension in the specimen's pore water increased. This increase in tension was measured via change in voltage output of the MIT Tensiometer.

Simultaneous readings of the balance were also made. The reading rate of a typical test was set at 1 minute intervals.

The drying test continued until a predetermined limit of tension was reached or the MIT Tensiometer experienced a loss in tension. In either case, the data acquisition was stopped and the specimen was removed from the device. A final gravimetric moisture content was then taken. Since the mass loss was recorded throughout the test, the moisture content for the entire test could be back calculated. The calculated initial moisture content could then be compared to the measured initial moisture content of similar material. A final plot of tension versus moisture content was then prepared.

6.4.3 Photographic Documentation of Desaturation

It was desired to examine the drying process from a visual standpoint. However, due to the small grain sizes of the materials used in the research, high magnifications were required to visually observe any drying phenomenon. Therefore, a larger material was used for these purposes. 5 mm glass beads were chosen as they would provide a large enough pore space to view with the optics available in the laboratory.

The laboratory setup for viewing the drying behavior of the beads was a camera fitted with a zoom lens. The camera was an *Olympus® OM-10®* 35mm manual camera. The zoom lens provided an image magnification of nearly 10×.

A drying test composed of several beads epoxied to a plate in various configurations was the first technique performed. Beads were arranged on a glass plate in two ways, three beads along one axis and eight beads arranged in a cubic packing pattern. In either case, water was introduced to the beads with a hypodermic syringe. The wet beads were then allowed to air dry, while periodic photographs of the beads were taken from an above vantage point. The camera was held above the beads with a camera stand obtained from the Civil Engineering Department. This fixed the camera to eliminate any optical errors from different photographic angles.

A second type of drying test was run, again with an above view (Figure 6-8a). For this test, the beads were placed into a 500 mL beaker and filled with water. The camera was arranged such that the field of view was as near the center of the beaker as possible. The beaker was then filled with water to a point that the beads were submerged. The water was then allowed to evaporate and periodic photographs were taken. The drying continued until the water level was out of the depth of field of the camera. This took two days to complete.

The final type of drying test allowed for a horizontal view of the drying water surface (Figure 6-8b). A box was constructed of glass plates to hold the beads and water. The box was 8 inches wide by 6 inches high by 2 inches deep. The camera was mounted horizontally to provide a view of the water surface against the flat plate. Water was filled in the box until the beads were submerged. The water was allowed to evaporate in the laboratory air and was aided with silica desiccant placed near the box. Periodic photographs were taken to document the movement of the water surface down through the matrix of beads. The test was run until the drying front moved out of the field of view of the lens. Due to the small cross sectional area of the surface, the drying front migrated quite slowly and took several days to move out of view.

Table 6-1. Material physical properties and sources.

Material[1]	Source[2]	Plastic Limit w_p	Liquid Limit w_l	Fraction <2μm	Specific Gravity G_s
RBBC	M.I.T.	23.5	46.1	0.58	2.780
VBC	ASTM	20.4	59.7	0.50	2.726
TS	T.S.U.	-	-	0.04	-
MFS	M.I.T.	-	-	-	2.688
MS	JTG	-	-	-	2.78
Glass Beads	M.I.T.	-	-	-	2.43

1: RBBC: Resedimented Boston Blue Clay
VBC: Vicksburg Buckshot Clay
TS: Tennessee Silt
MFS: Manchester Fine Sand
MS: Maine Silt

2: M.I.T.: Massachusetts Institute of Technology
ASTM: American Society for Testing and Materials
T.S.U.: Tennessee State University
JTG: Dr. John T. Germaine

This value was assumed

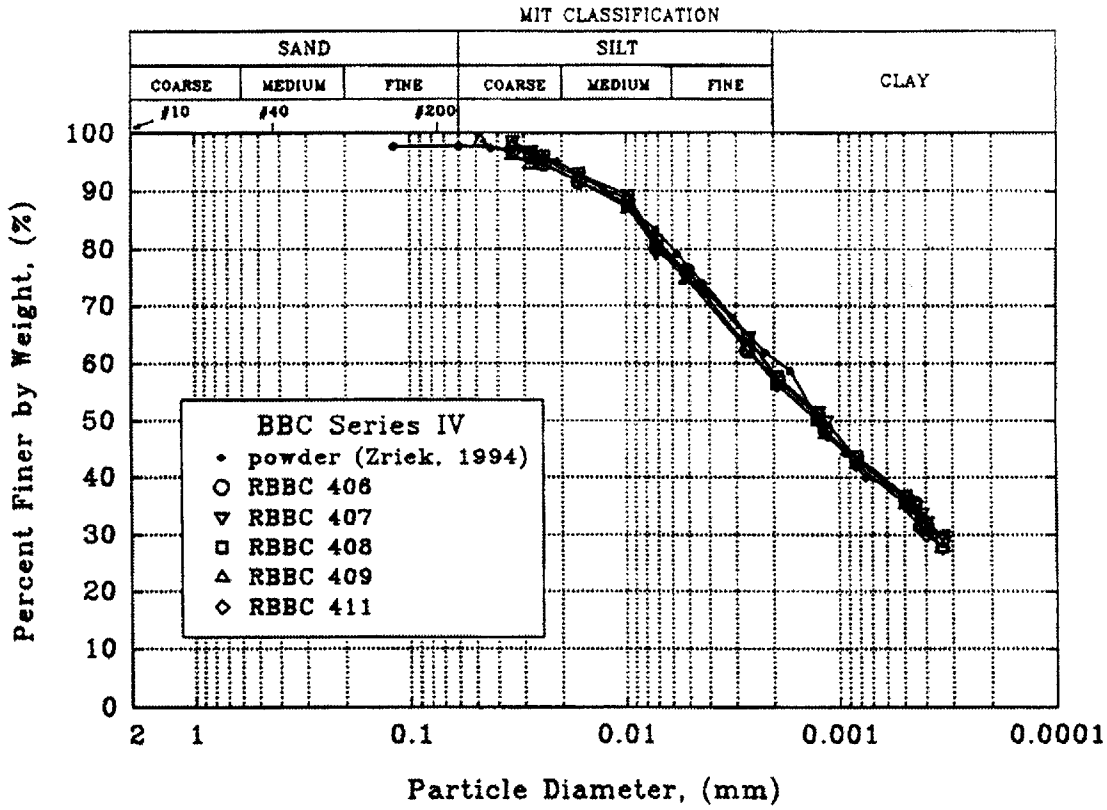

Figure 6-1. Grain size plot for RBBC (Cauble 1996).

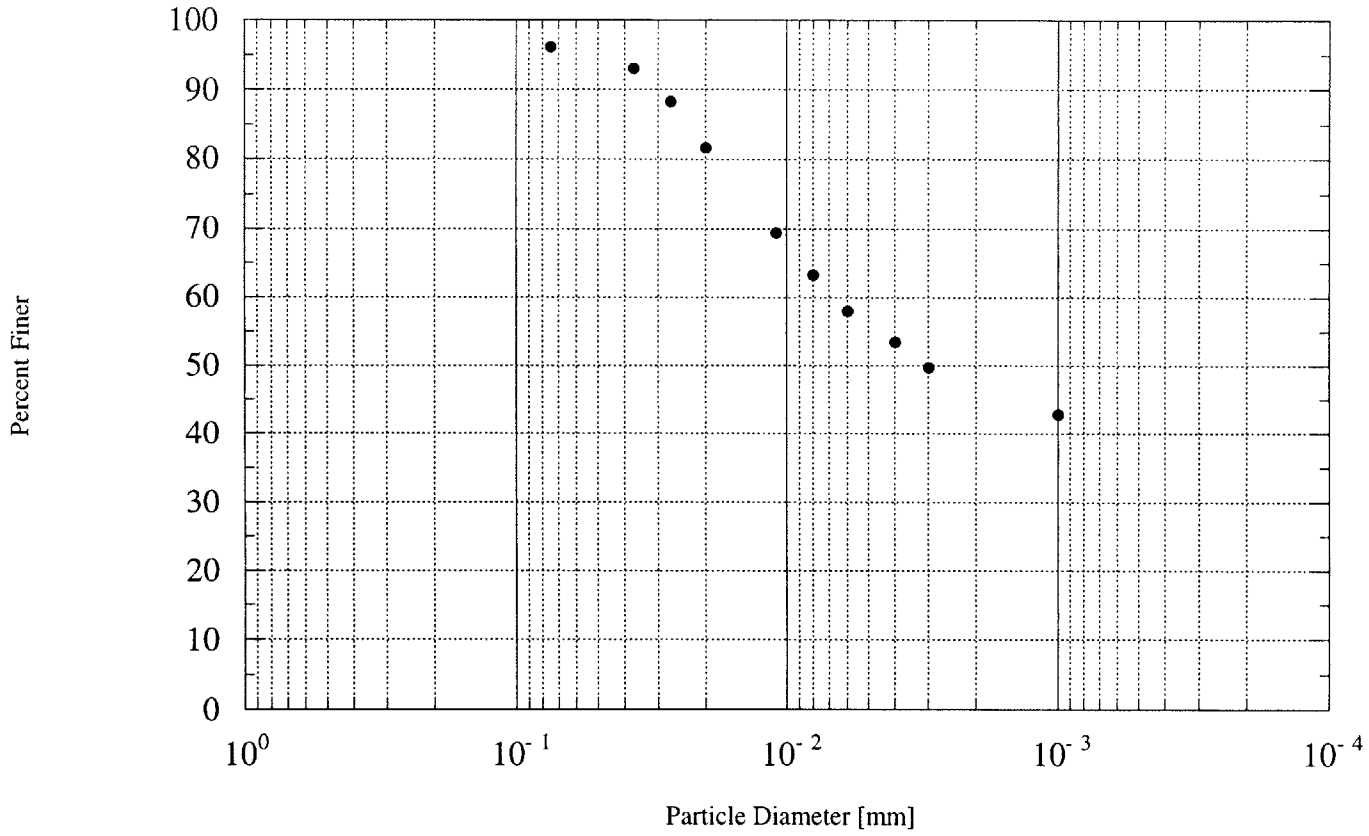

Figure 6-2. Hydrometer analysis of Vicksburg Buckshot Clay.

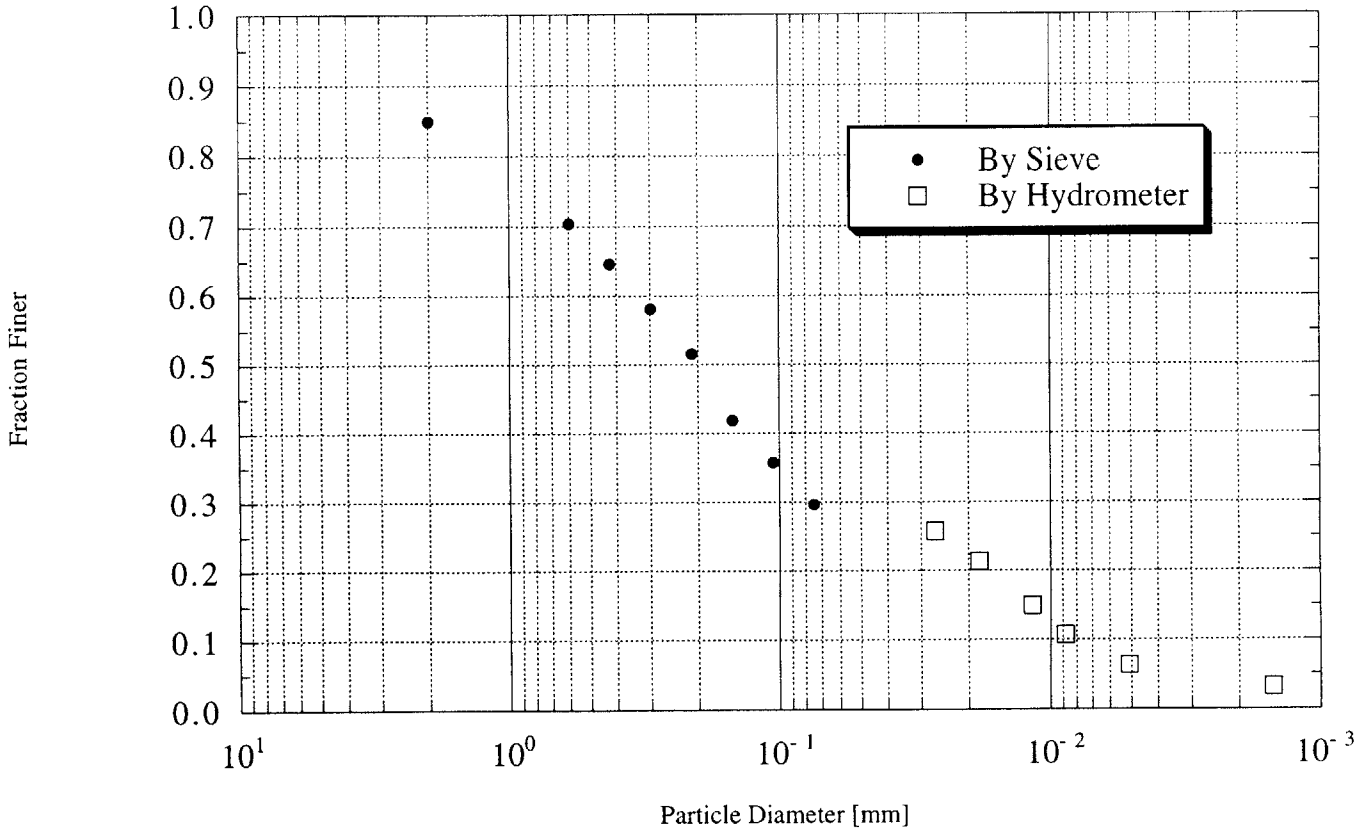

Figure 6-3. Grain size plot for Tennessee Silt.

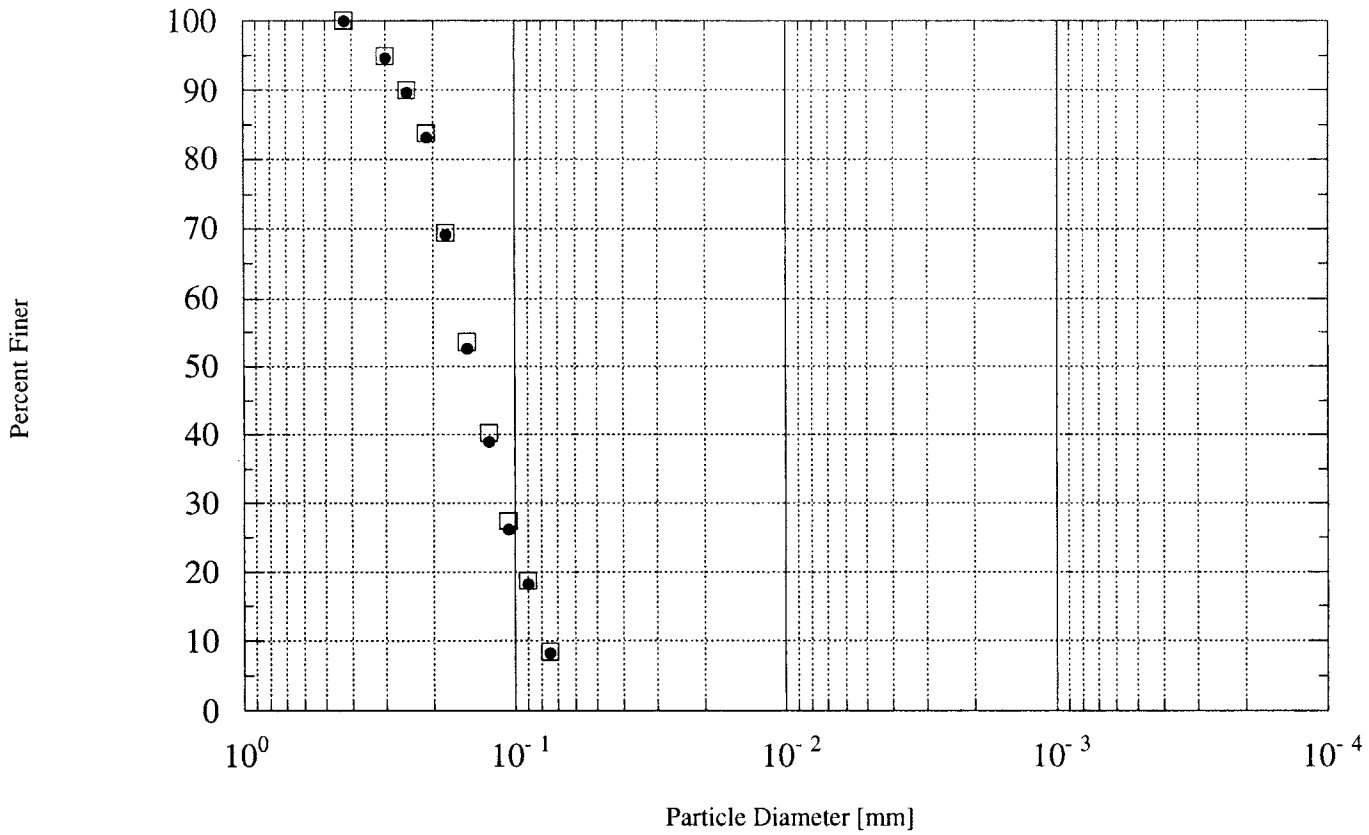

Figure 6-4. Grain size distribution for Manchester Fine Sand (data from Da Re 2000).

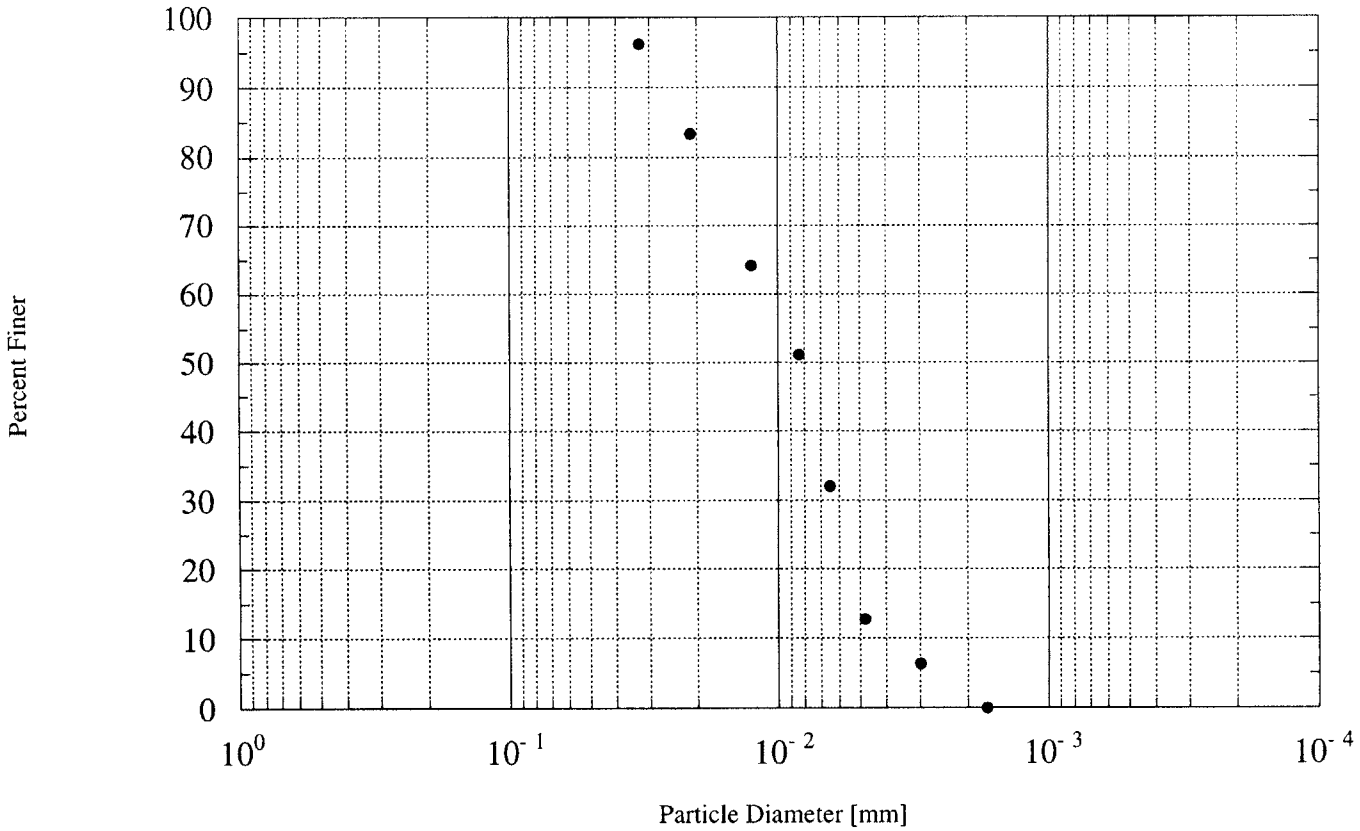

Figure 6-5. Grain size distribution for Maine Silt.

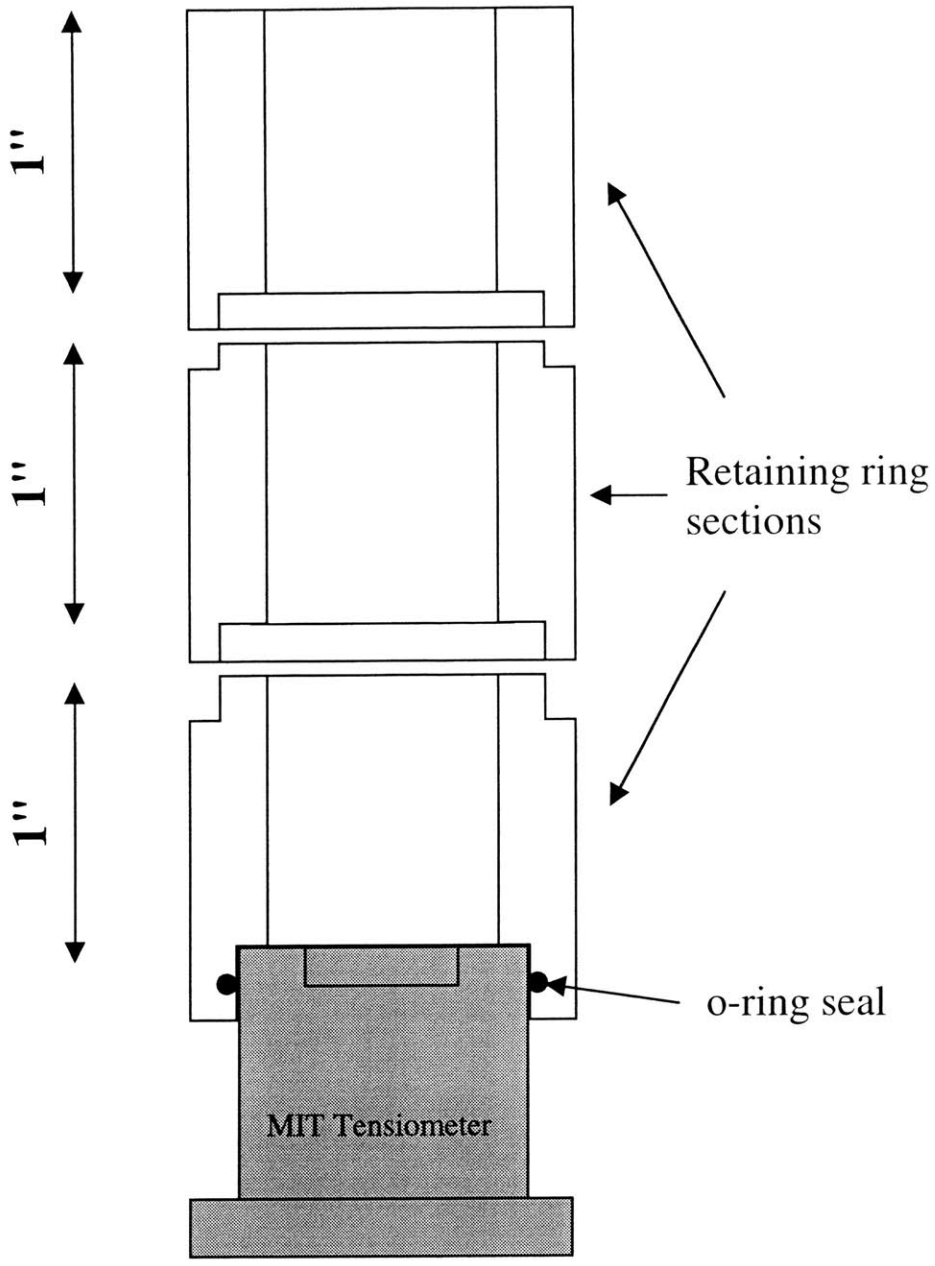

Figure 6-6. Sectional retaining ring for granular materials (N.T.S.).

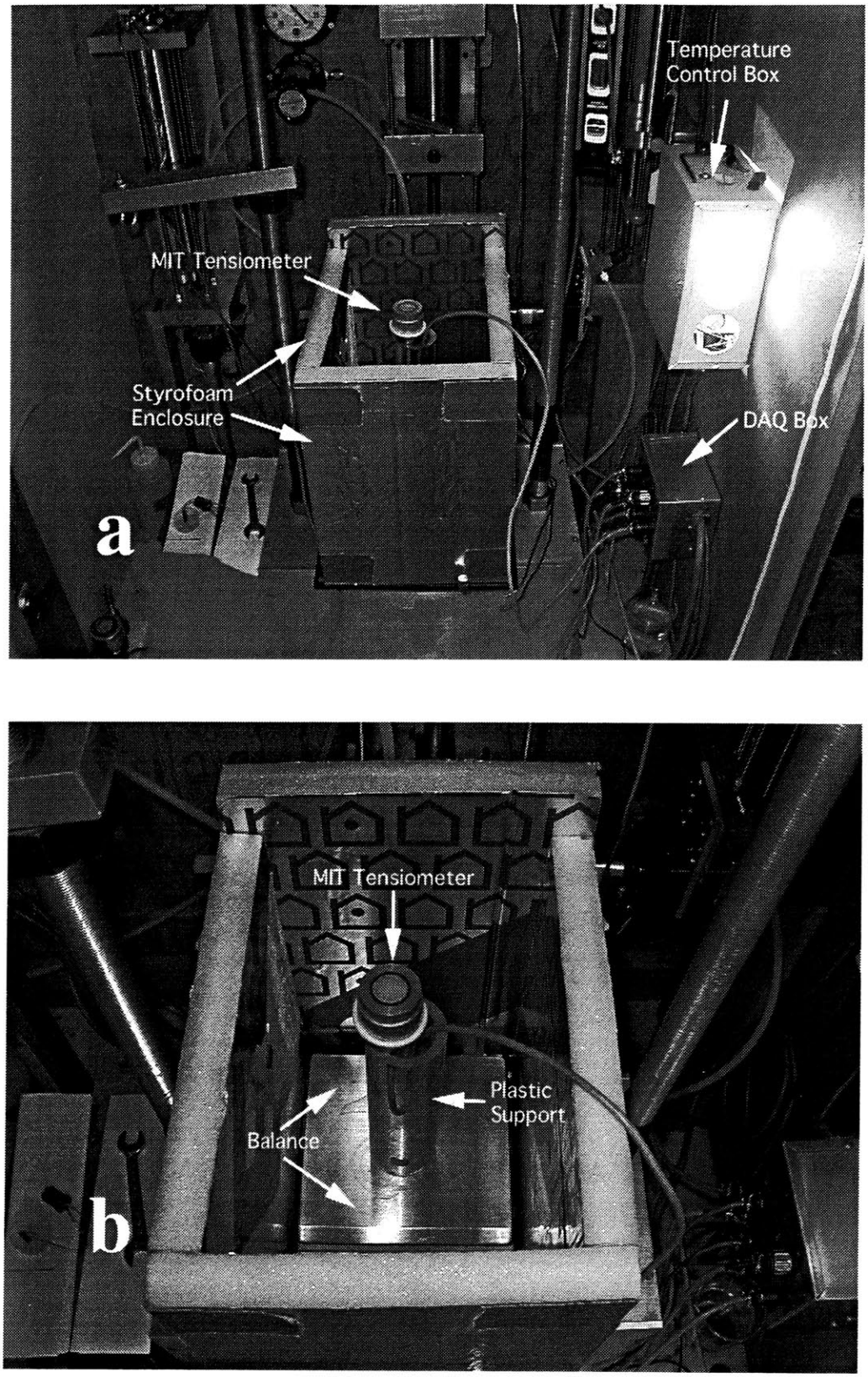

Figure 6-7. Photo of drying setup in full view (a) and close up (b).

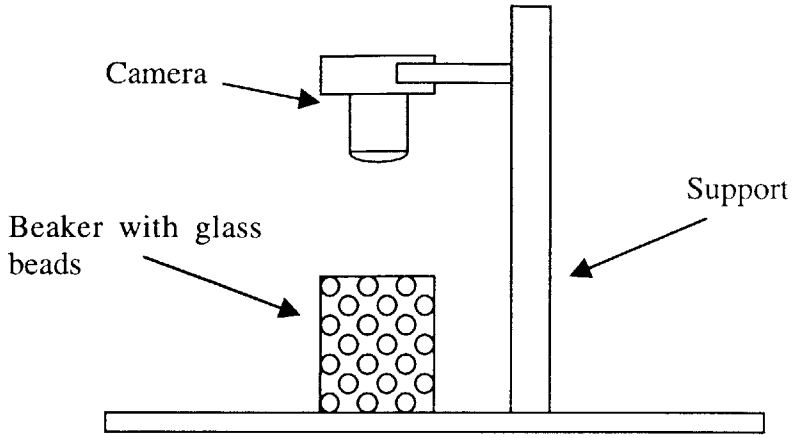

a

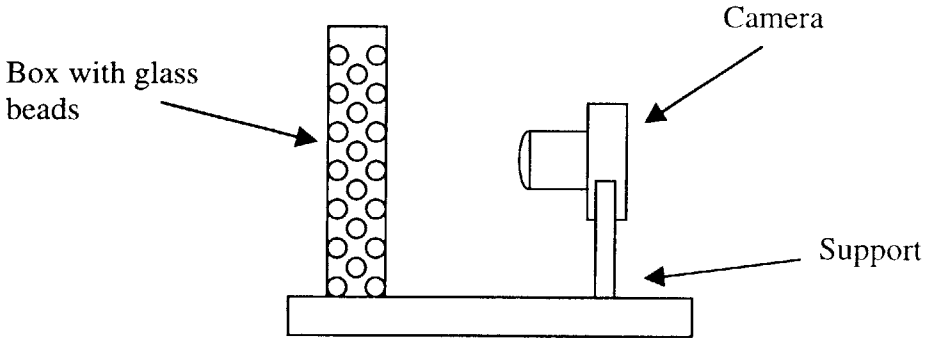

b

Figure 6-8. Schematic of photographic setup in vertical (a) and horizontal (b) positions.

Chapter 7 Experimental Results

7.1 Introduction

This Chapter presents the results of the experimental program. For purposes of clarity, this Chapter only presents the results of the experiments and not the interpretation of these results. The following Chapter is reserved for this purpose. This Chapter is divided into two sections, each covering a different aspect of the experimental program. Section 7.2 presents the results of the testing done with glass beads. This Section covers the effects of various glass bead sizes and the drying documentation. The results of the tests on soils are then given in Section 7.3.

7.2 Glass Beads

A total of fourteen separate drying tests were performed on five different size fractions of glass beads. The available sieves in the laboratory (as described in Chapter 6) governed the size fractions that were used. A temperature control of 25°C was maintained for the duration of all the tests.

The results of each of the drying tests are presented in Figures 7-1 through 7-5. Table 7-1 summarizes the measured values of the air entry pressures (AEP) and residual water contents (w_R). The following section groups the tests according to the individual size fractions used.

7.2.1 Effect Bead Size

7.2.1.1 500 μm Bead Size Fraction

Six drying tests (SM60 - SM65) were performed on the 500 μm size fraction. The results of the tests are shown in Figure 7-1. One of the tests, SM64, is only partially plotted due to excessive electronic noise in the first portion of the test. Each of the tests was performed similarly with the specimen being contained in a 1 inch support. All of the test specimens were allowed to dry in the ambient laboratory air without any use of desiccant to accelerate evaporation. The resulting average AEP for the tests was 0.072 bar with a standard deviation of ±0.026 bar. The residual water content averaged 0.008 ±0.002.

7.2.1.2 250 - 300 μm Bead Size Fraction

Figure 7-2 presents the results of the 250 - 300 μm bead size fraction. Two tests were performed on this material, SM66 and SM67. The specimens were 1 inch high and allowed to dry in the ambient laboratory air. Both tests gave the same AEP of 0.05 bar and a residual water content average of 0.018 ±0.004.

7.2.1.3 212 - 250 μm Bead Size Fraction

One test was conducted on this bead size, SM72. The test was performed without the aid of desiccant. The plot of the test is shown in Figure 7-3. During this test, a unique observation was made. At the beginning of the test, during the placing of the beads upon the MIT Tensiometer, the Tensiometer showed an immediate suction. This occurred in spite of the fact that the material was placed into a column of standing water. The output of the Tensiometer changed as soon as the material came in contact with the porous ceramic stone. This same observation was also made for other materials of this size and

smaller. As a result of this behavior, the plot shown in Figure 7-3 starts at a relatively high tension. The test yielded an AEP of 0.06 bar with a residual water content of 0.012.

7.2.1.4 125 - 150 μm Bead Size Fraction

A single test was done on the 125 - 150 μm bead size. SM68 is plotted in Figure 7-4. As with the larger bead sizes, the height of the specimen was 1 inch and no desiccant was used. The test yielded an AEP of 0.1 bar with a residual water content of 0.01.

7.2.1.5 75 - 90 μm Bead Size Fraction

Four tests were performed on the 75 - 90 μm bead size. SM69, SM70, SM71 and SM73 are plotted in Figure 7-5. Only SM69 was tested with desiccant in the testing chamber, the other three were allowed to dry in the ambient laboratory air. SM69 and SM70 were testing using the 1 inch specimen support. SM71 and SM73 were tested using a pan support. The dimensions of the support were 4.2 inches in diameter (three times the diameter of the Tensiometer) by 0.5 inches high. The effect of increasing surface area and specimen mass was to be examined by this support. The added mass would increase the sensitivity of the water content measurement and allow a better resolution of the residual water content zone. The resulting average AEP for the tests was 0.18 bar with a standard deviation of ±0.075 bar. The residual water content averaged 0.015 ±0.004. Each of the tests displayed an initial tension that occurred when the beads were in contact with the porous stone.

7.2.2 Drying Documentation

Four different types of drying sequences were documented using a standard 35 mm camera. Each of the sequences was photographed using an appropriate time between each succeeding photograph to allow enough change in the level of the water. This created a time-lapse drying sequence.

The first drying sequence is shown in Figures 7-6 and 7-7. Eight 5 mm glass beads were arranged on a glass slide in a cubic packing configuration. The beads were fixed to each other and the glass plate with a small amount of 5 minute epoxy at each of the contacts. This unit was then filled with water until the excess flowed out of the bottom and onto the glass plate.

From Figure 7-6a it can be seen that the water (the dark area in the photo) initially configures between the contacts in a manner that is geometrically stable in the pore. A dark line is drawn on the figure to indicate the starting point of the water between the beads. As the pore starts to desaturate (Figure 7-6b), this starting point remains unchanged and a pendular ring forms between the beads. The inclusive angle, α, is measured to be approximately 40°. Once the pore desatuates to the point of individual pendular rings (Figure 7-7c) this inclusive angle remains unchanged. With further time (Figure 7-7d) the pendular rings become smaller as water leaves the system. The non-uniform drying in the Figure is most likely caused by the uneven lighting scheme used to illuminate the beads. The light (heat) source was located in the lower right of the Figure, thus the right most ring dried the fastest.

The next drying sequences to be examined were on beads in a container with a large cross-sectional area and photographed from above. The photographs shown in Figure 7-8 were taken at the center of the container. It was felt that any edge effects would be negligible at this point. The top photograph in the Figure shows the beads completely submerged under water. The bottom photograph shows the same beads after substantial drying. As outlined in the Figure, the lines show half of a pendular ring starting to form. The angle of inclusion measured is again approximately 40°.

To better understand the drying front as the water surface moves down through a matrix of beads, a series of horizontal photographs were taken. Two of these photographs are shown in Figure 7-9a and Figure 7-9b. The first photo in the Figure shows the water

surface well above the top layer of beads. As the drying front progresses down into the matrix of beads, pendular rings start to form. Two rings are outlined in Figure 7-9b. The inclusive angles measured are approximately 45° and 40°. Although not marked in the Figure, other pendular rings start to develop with inclusive angles in the same range observed previously.

The final drying sequences to be examined were taken while a drying curve was being measured. The 500 μm bead fraction was tested in the drying curve series SM60 through SM65. During these tests several overhead vantage-point photographs were taken to document this process. Figure 7-10 locates on the drying curve where the photographs were taken. This Figure is a representative figure and not all the points correspond to an exact point of documentation. The Figure is meant to give a relative order and point on the curve where the photographs were taken since not all of the photographs were taken during one particular test. Unfortunately, the photographs taken of 500 μm beads do not reproduce well enough to include in this thesis. However, good conceptual information was obtained from the photographs.

Point A in the Figure indicates the starting point of a drying curve. At this point all of the pore spaces in the bead matrix are filled with water. As drying proceeds and tension increases in the matrix, air will start to enter the pores. At this point, pendular rings start to form at the contacts between the beads. The photograph at Point B confirms this. Point C located at much dryer (relatively) water content than Point B, indicates that the pendular rings do not change in geometry (and therefore tension) with respect to Point B. In fact, the photographs revealed that the pendular rings remain essentially the same geometrically until after Point D. The photograph at Point E showed that the pendular rings had shrunken in size as to be undetectable.

7.3 Soils

Three natural granular soils were tested in order to determine the effect of particle angularity on the resulting drying curve and two clays to examine the effect of large specific surface areas. The angularity of Manchester Fine Sand has been documented by Da Re (2000). The Tennessee Silty Sand and Maine Silt were not photographed under the Scanning Electron Microscope so the degree of angularity is not known. However, the materials are certainly more angular than the glass beads discussed in the previous section. The results for the granular soils are summarized in Table 7-2, and discussed in the following three sections. Two clays were also tested. The results of these soils are presented in Section 7.3.4.

7.3.1 Manchester Fine Sand

One test was conducted on Manchester Fine Sand, SM74. The material was confined in a 1-inch retaining ring and allowed to dry in ambient laboratory air. The drying curve for this test is shown in Figure 7-11. The MIT Tensiometer displayed the same behavior with this material as with some of the smaller glass bead fractions. As soon as the material came into contact with the Tensiometer, the output of the device recorded an initial suction that was slightly less than the air entry pressure. This is shown in the Figure at the beginning of the curve. The resulting AEP for the test was 0.12 bar and a residual water content of 0.01.

7.3.2 Tennessee Silty Sand

A single test was done on the Tennessee Silty Sand. The plot of SM76 is shown in Figure 7-12. The material was tested in the 1 inch retaining ring with no desiccant. The results from the test show no discernable AEP value. This was an expected result as the grain size distribution was very flat. However, the structure of the curve is somewhat unusual, indicating a complex pore structure. Two features of the curve stand out in the Figure. At the beginning of the curve there is somewhat of a draining zone occurring at 0.2 bar. This zone shows some fluctuation of tension as it drains. This is possibly due to

noise in the electronics and not a material behavior. The other interesting feature is the 'knee' bend in the curve occurring at 1 bar. This is certainly due to the pore size distribution and it is important to note that a standard pressure plate apparatus would need many points to pick out this feature. This attests to the power of the new measurement technique.

No residual water content can be determined from the plot as the Tensiometer lost tension before this could be determined. From the slope of the drying curve at this low water content, it can be reasonably assumed that the residual water content occurs at a tension in excess of the limits of the MIT Tensiometer.

7.3.3 Maine Silt

One test was done on the Maine Silt, SM77. As with the other soils, the Maine Silt was tested in a 1 inch retaining ring and allowed to dry in the laboratory air without the aid of desiccant. The result of this test is shown in Figure 7-13. This material had an air entry pressure of 0.70 and a residual water content of 0.01.

7.3.4 RBBC and RVBC

Several tests were done on cohesive soils in order to determine the applicability of the proposed drying technique to this type of soil. Figure 7-14 shows the resulting drying curves for RBBC and Figure 7-15 shows the result of RVBC. Also plotted on the Figures is a Constant Rate of Strain consolidation test (CRS) on the same material. The CRS data was then converted to an equivalent octahedral stress based on an assumed K_0 of 0.5. Figure 7-14 also plots the results of an Isotropic Triaxial consolidation test from Bensari (1984). The consolidation data shown with the figures is provided for a relative comparison only, no implied relation is inherent to the figures.

The testing of cohesive materials is beyond the scope of this thesis and the data results are not interpreted. The tests were done only to show the MIT Tensiometer's ability to

measure tensions in cohesive materials. Any data conclusions or interpretations are left for future work.

Table 7-1. Summary of glass bead drying tests.

Test Number	Bead Size Fraction [μm]	AEP [bar]	Residual water content w_R
SM60	500	0.10	0.007
SM61	500	0.056	0.008
SM62	500	0.10	0.008
SM63	500	0.06	0.007
SM64	500	-*	0.007
SM65	500	0.045	0.013
SM66	250-300	0.05	0.02
SM67	250-300	0.05	0.015
SM68	125-150	0.10	0.01
SM69	75-90	0.24	0.02
SM70	75-90	0.25	0.01
SM71	75-90	0.11	0.014
SM72	212-250	0.06	0.012
SM73	75-90	0.12	0.015

* Test SM64 provided no usable AEP information due to excessive electronic noise.

Table 7-2. Summary of results for soils tested.

Test Number	Material*	AEP [bar]	Residual water content w_R
SM74	MFS	0.12	0.01
SM76	TSS	-♠	-♠
SM77	MS	0.7	0.01

*Abbreviations for the soils follow;
MFS: Manchester Fine Sand
TSS: Tennessee Silty Sand
MS: Maine Silt

♠ The material displayed no distinct AEP. The residual water content was beyond the range of the device.

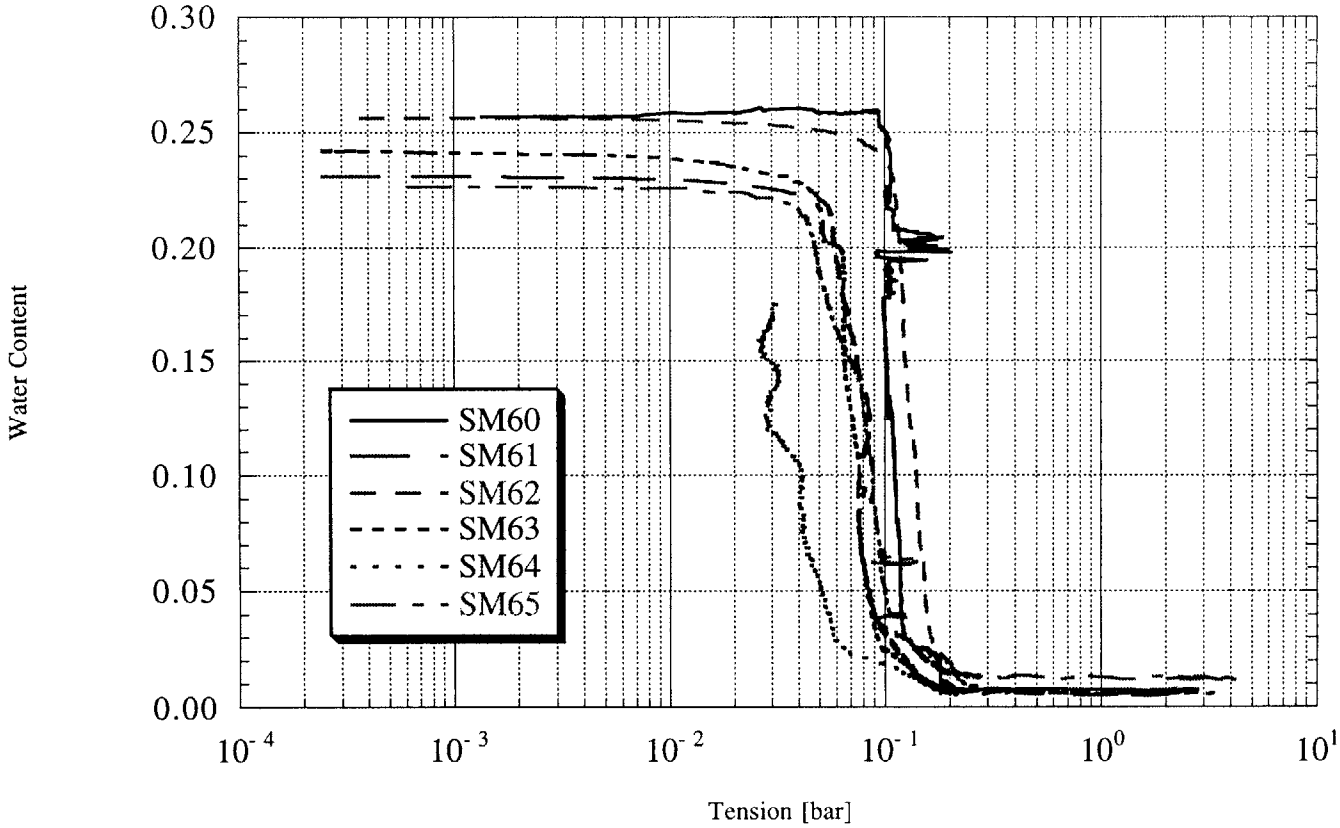

Figure 7-1. Results of the 500 µm glass bead drying tests.

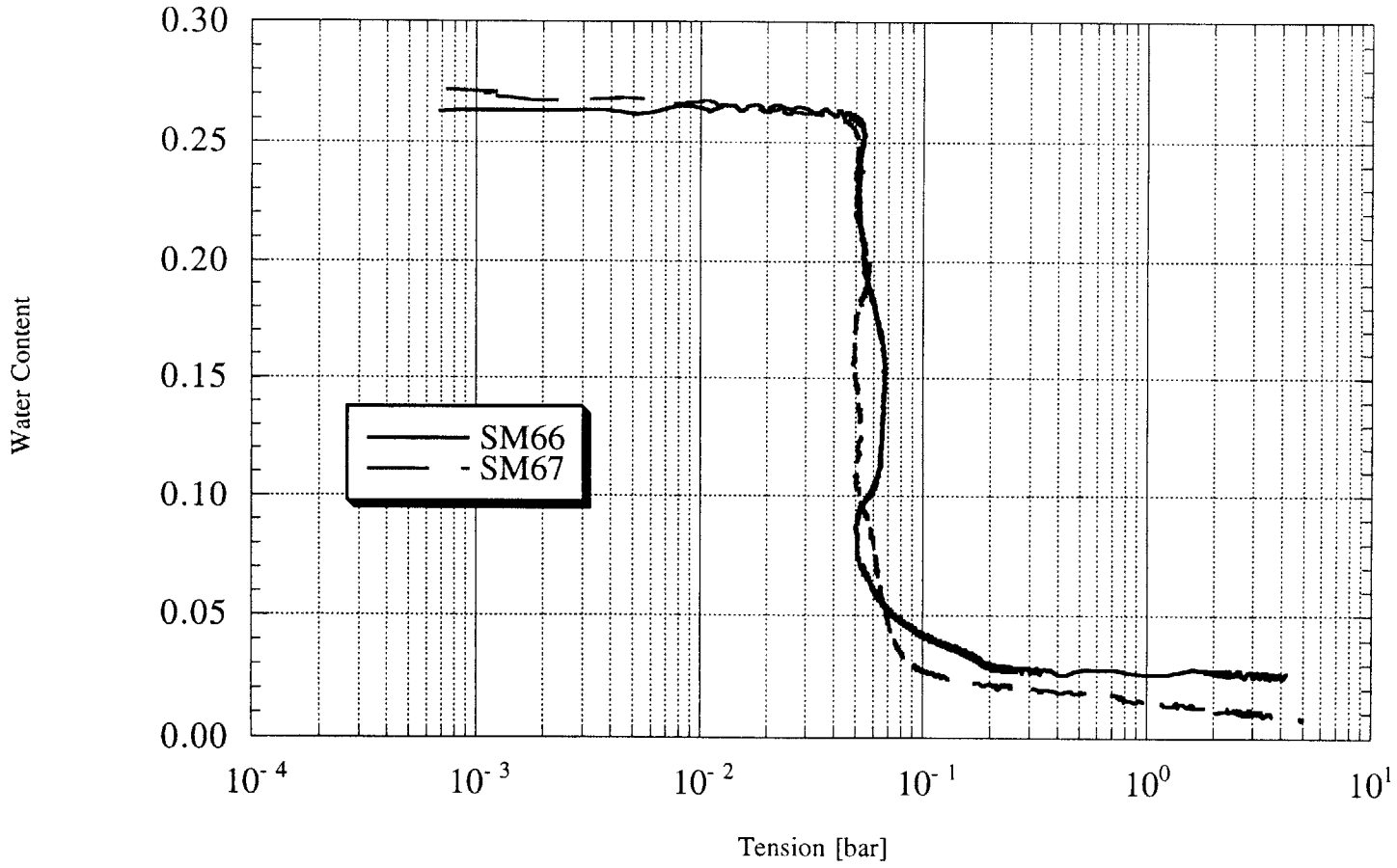

Figure 7-2. Results of the 250-300 μm glass bead drying tests.

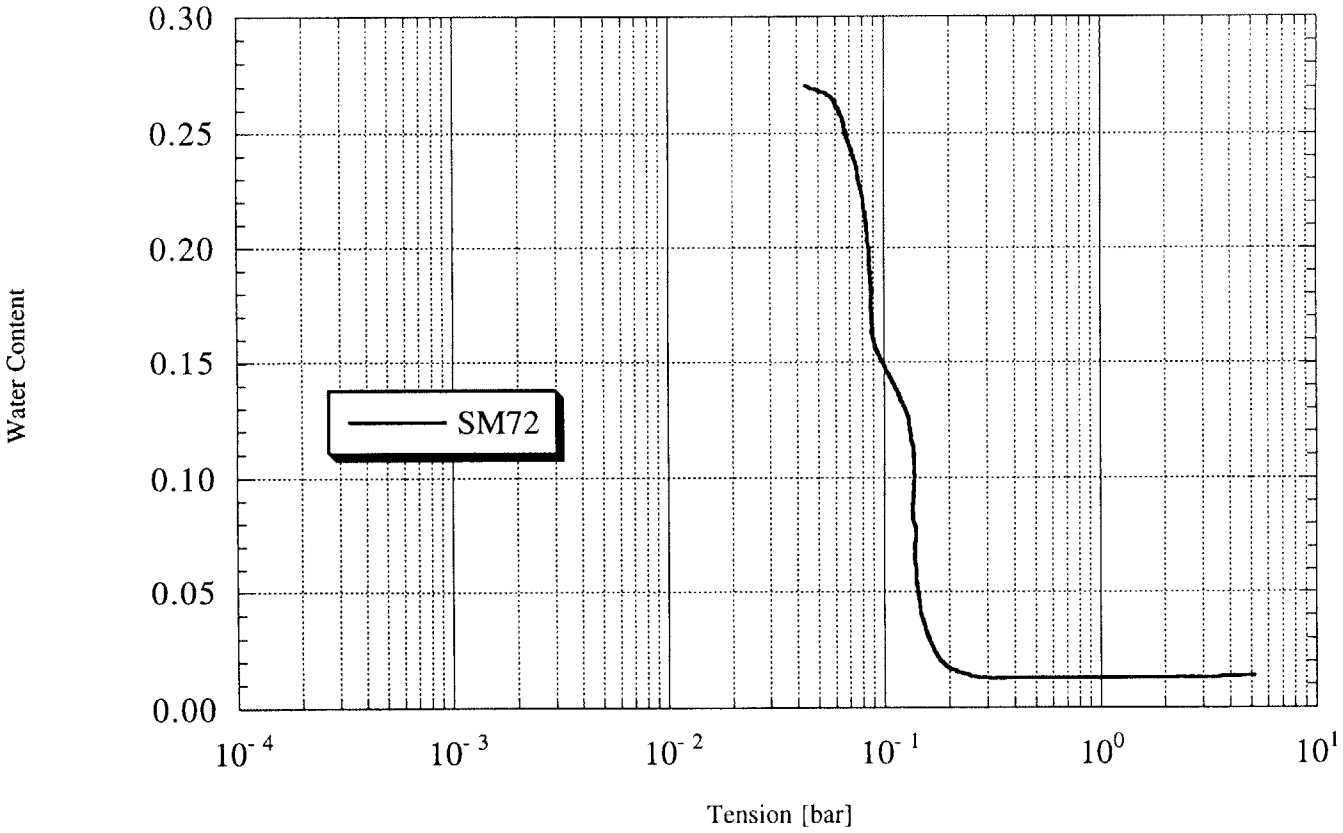

Figure 7-3. Result of the 212-250 μm glass bead drying test.

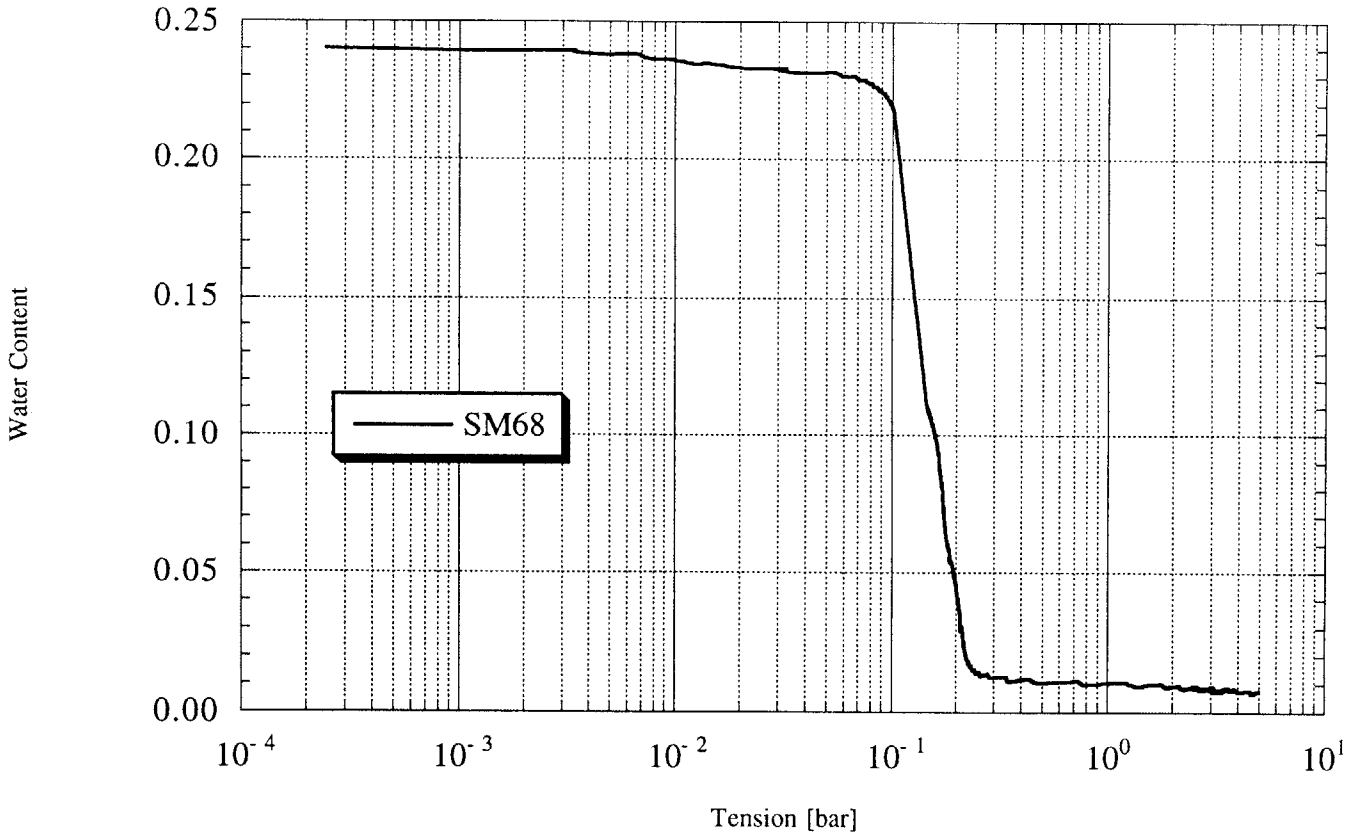

Figure 7-4. Result of the 125-150 μm glass bead drying test.

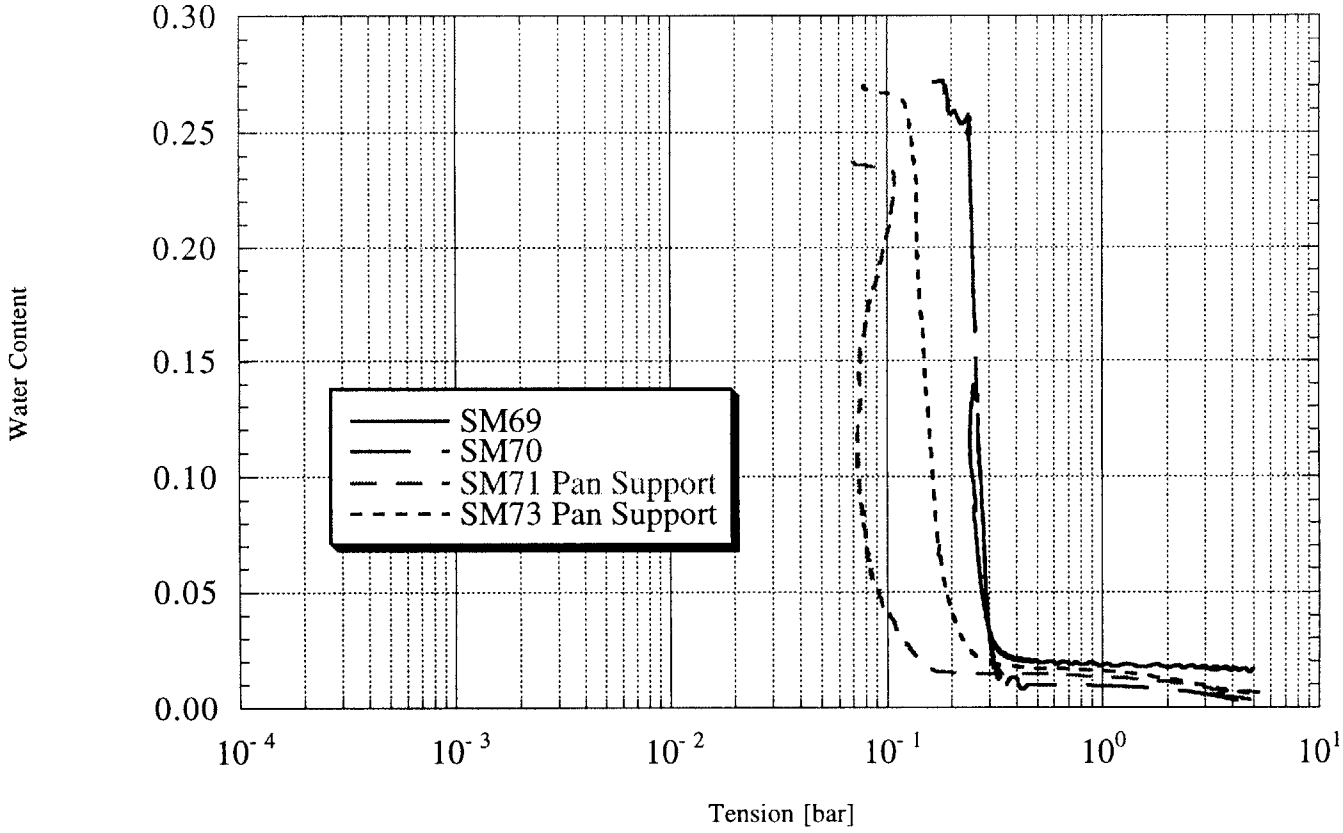

Figure 7-5. Results of the 75-90 µm glass bead drying tests.

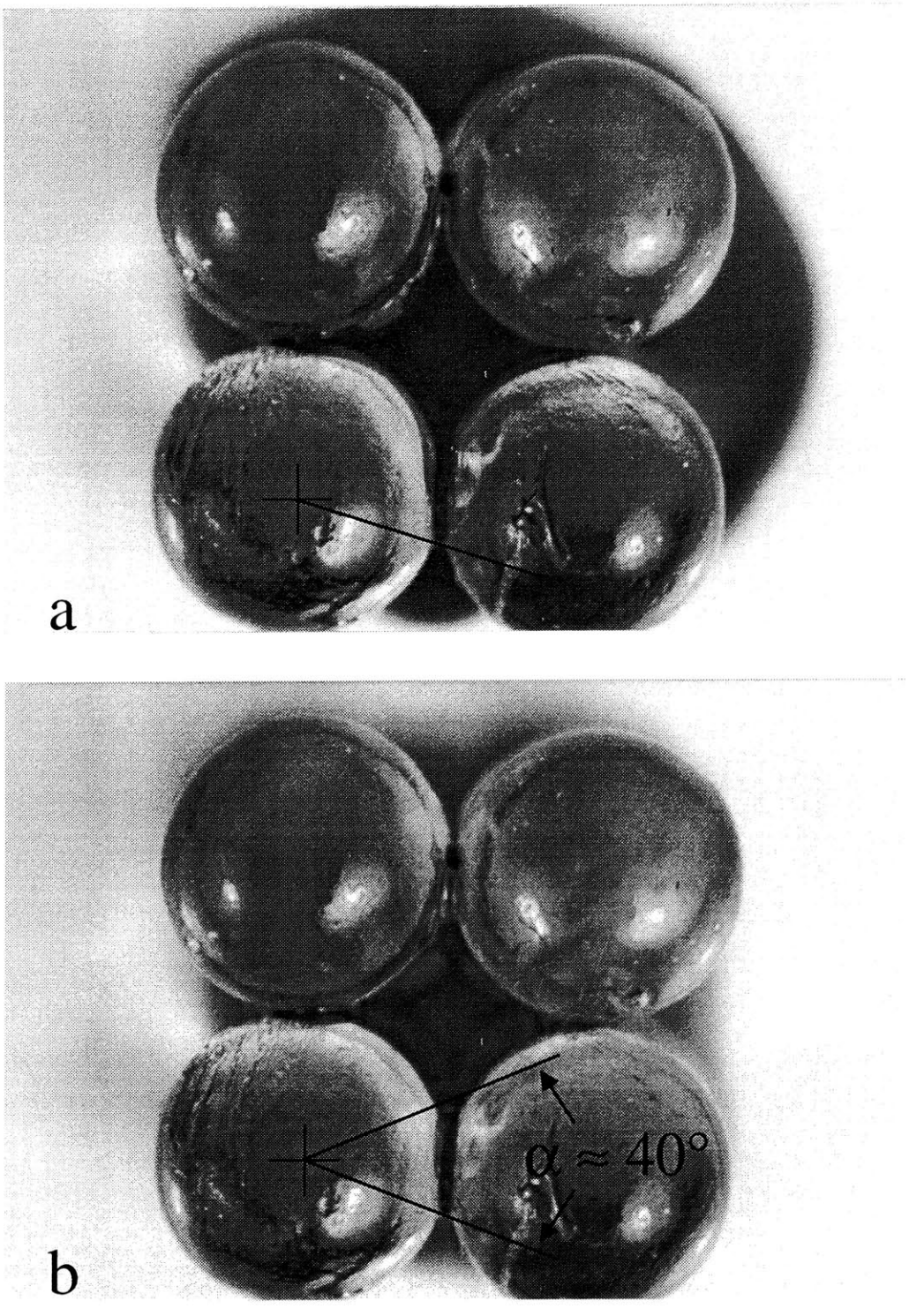

Figure 7-6. Drying sequence for cubic arrangement of beads (a,b).

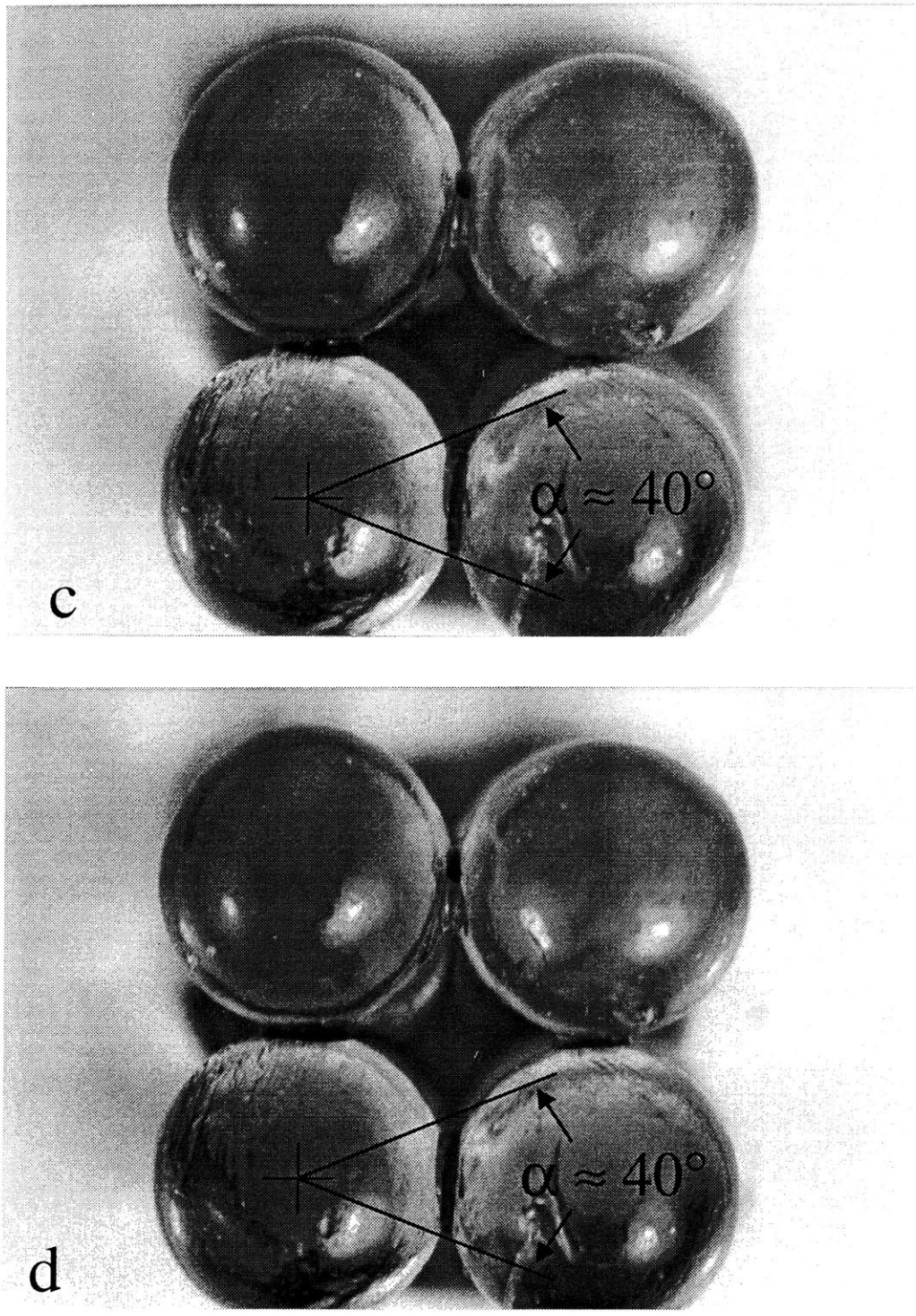

Figure 7-7. Drying sequence for cubic arrangement of beads (c,d).

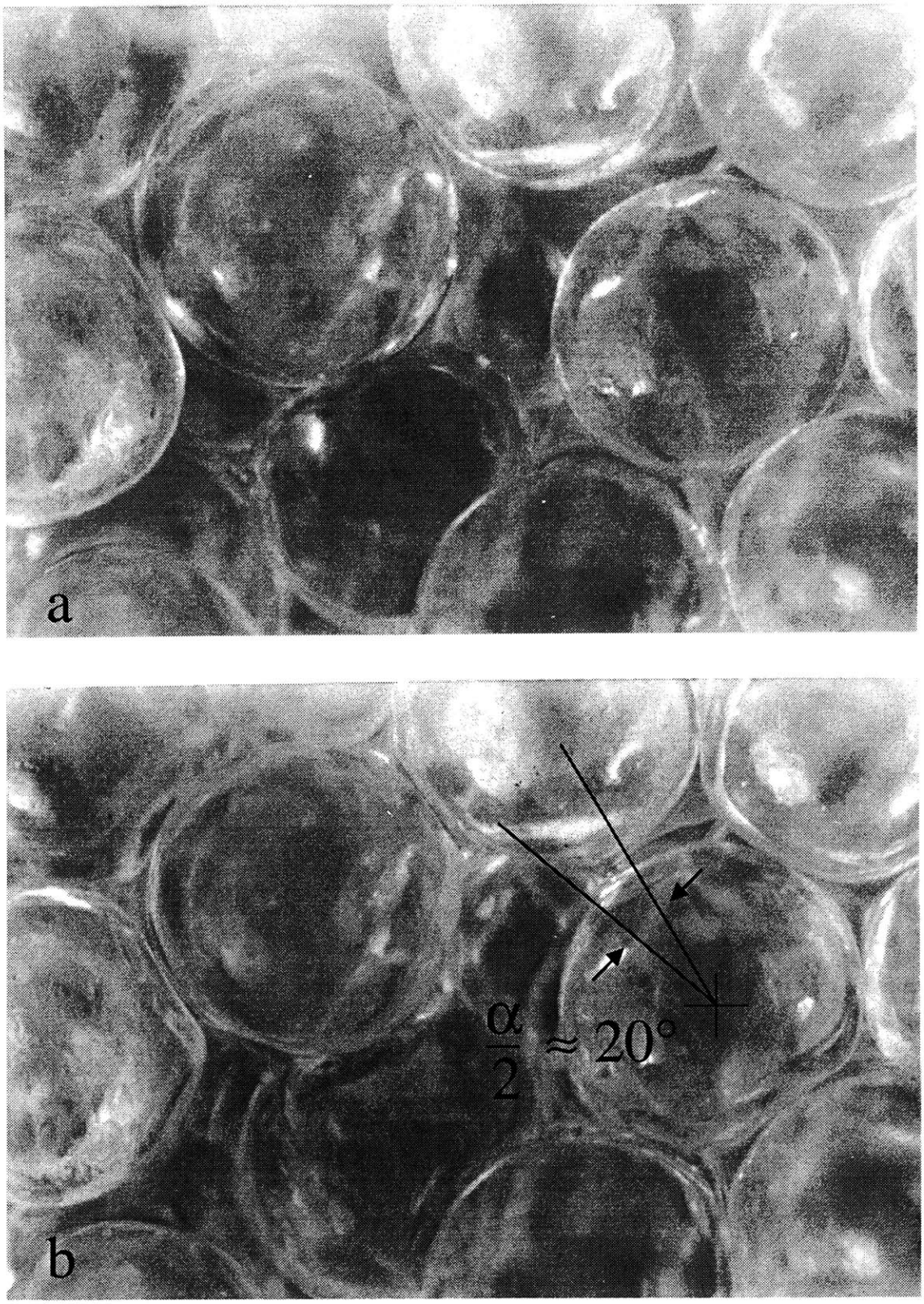

Figure 7-8. Drying sequence for top view of glass beads.

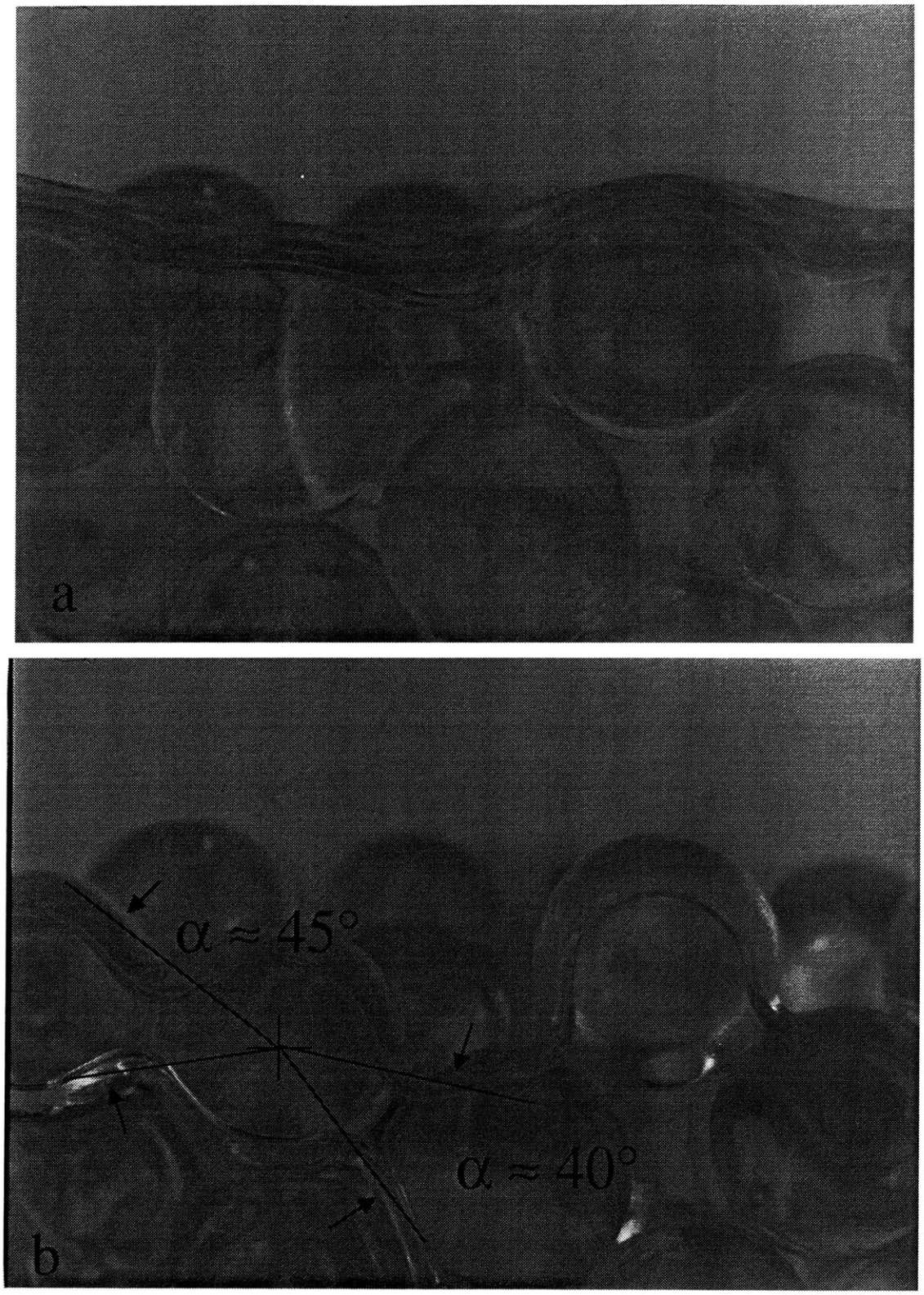

Figure 7-9. Horizontal drying sequence.

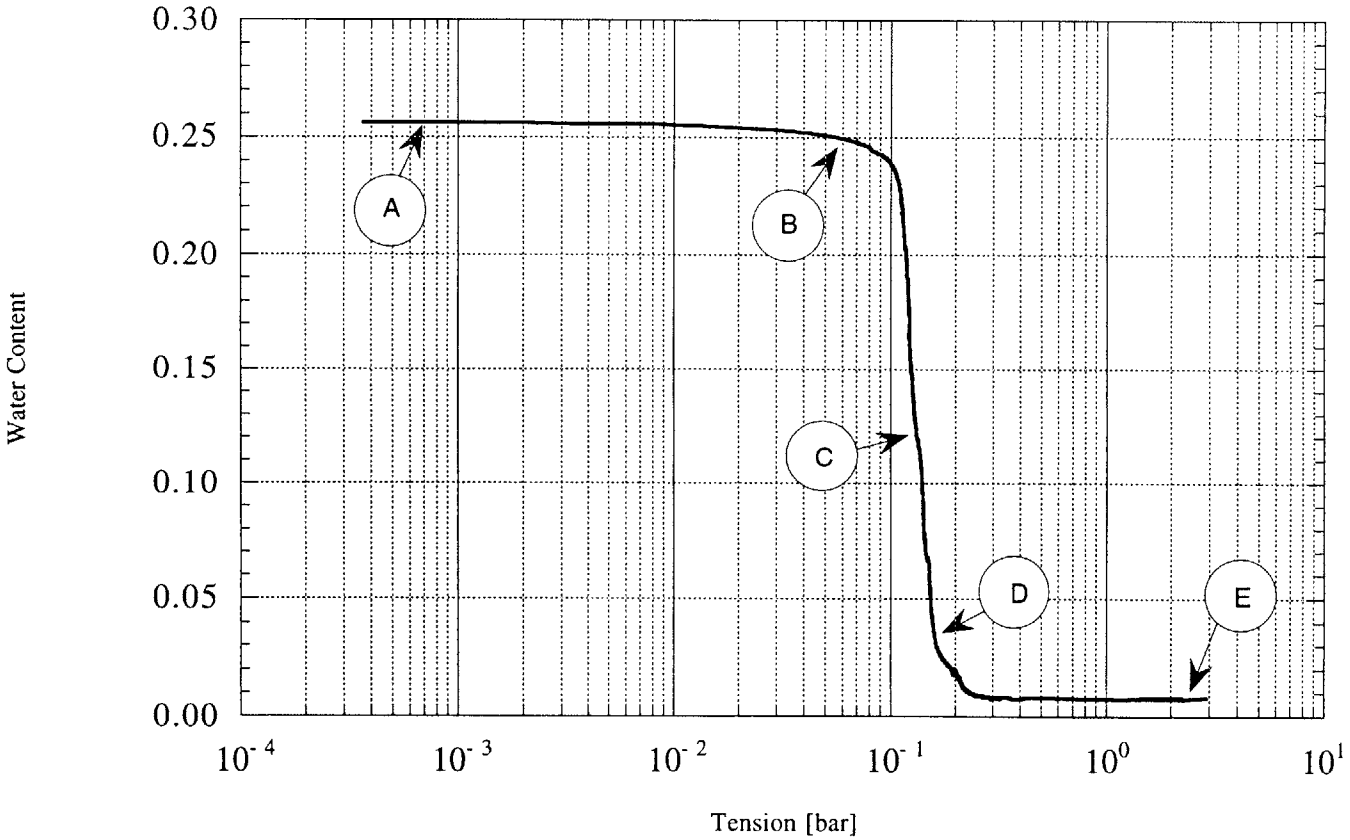

Figure 7-10. Sequential photographs during drying tests SM60-SM65.

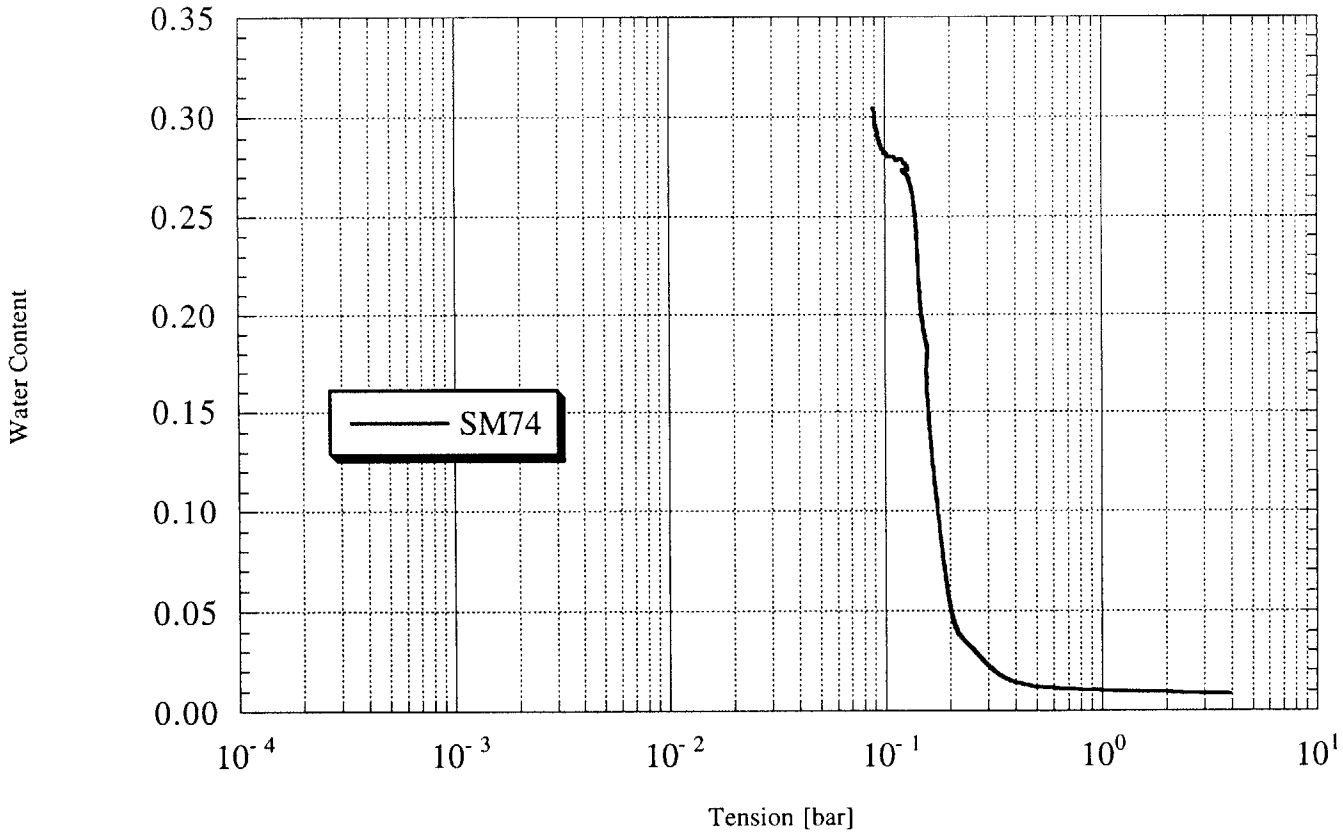

Figure 7-11. Manchester Fine Sand drying curve.

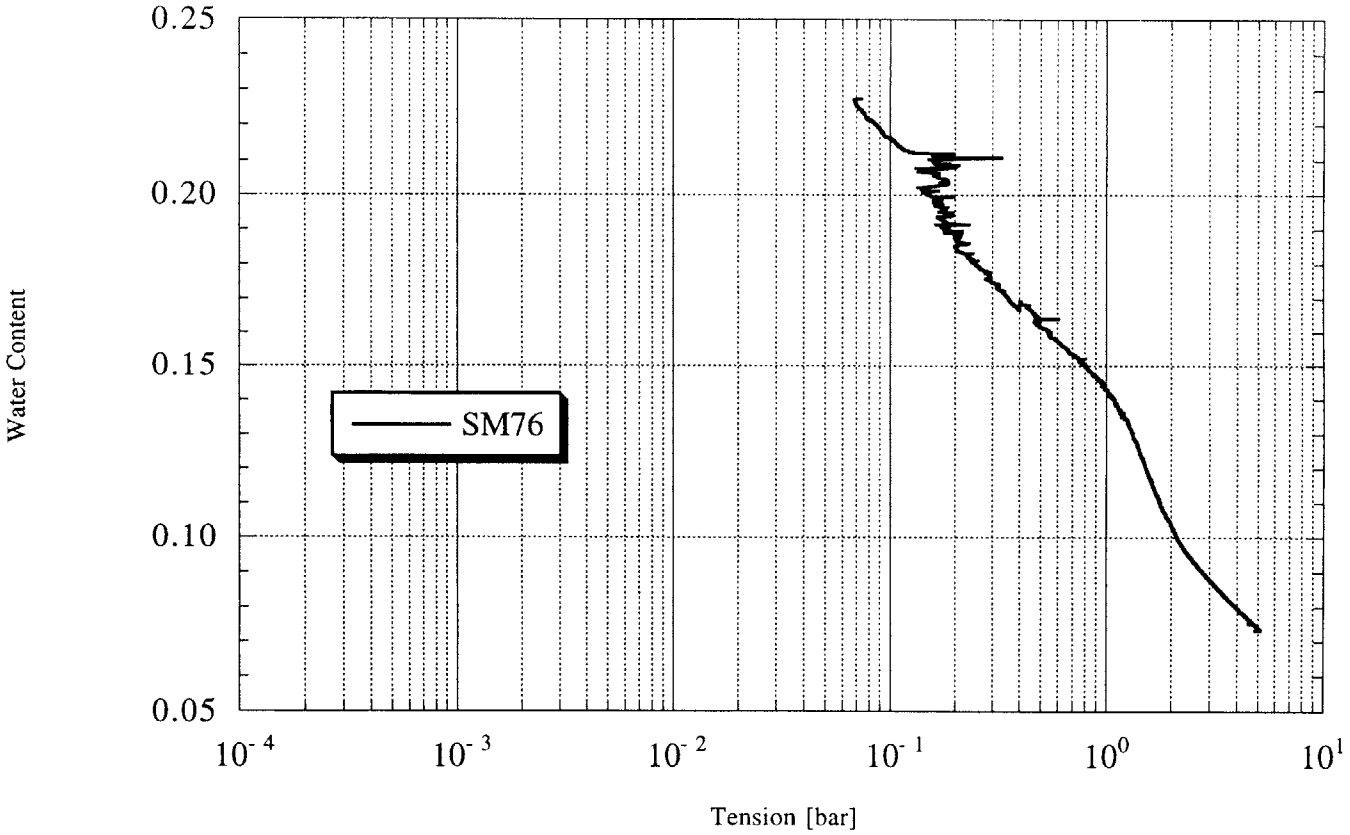

Figure 7-12. Tennessee Silty Sand drying curve.

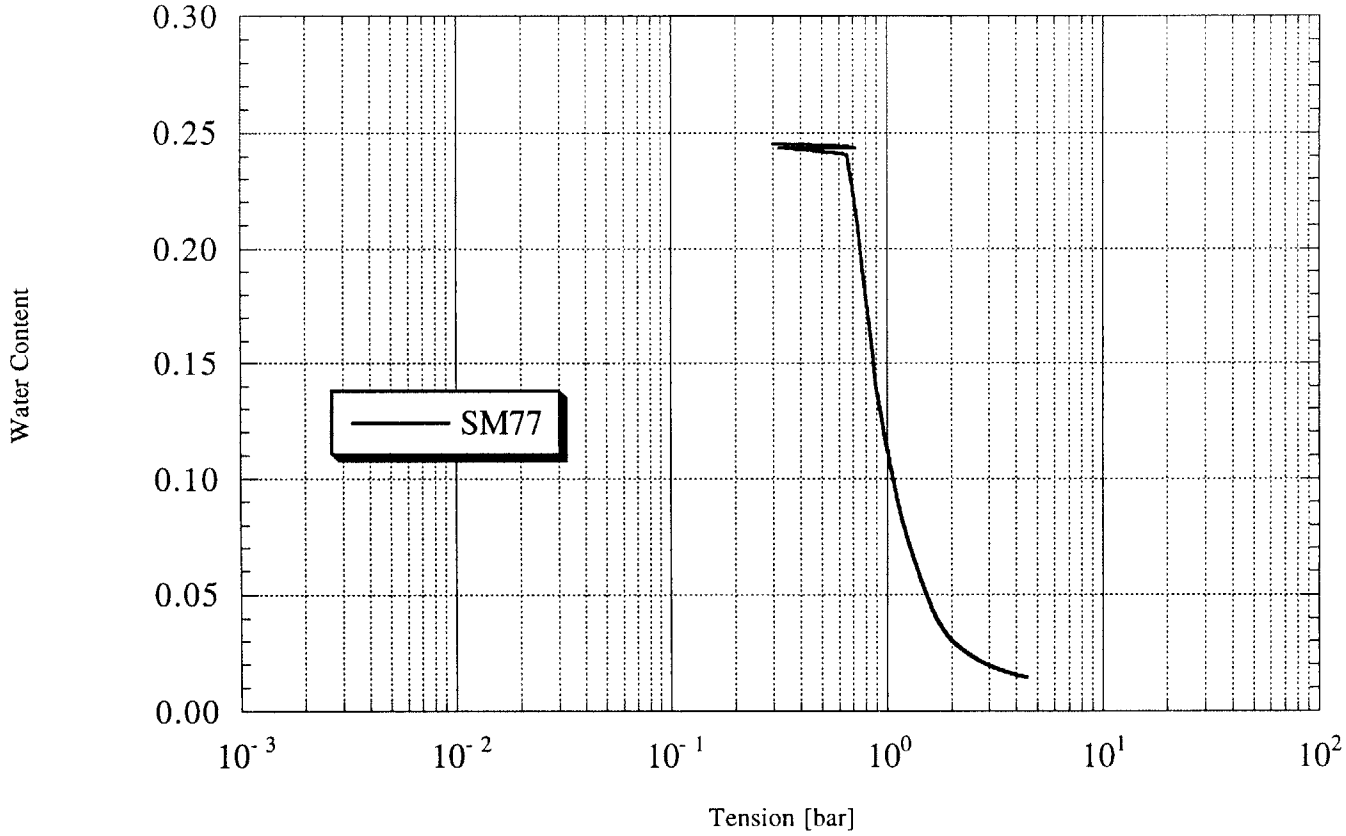

Figure 7-13. Drying test result for the Maine Silt.

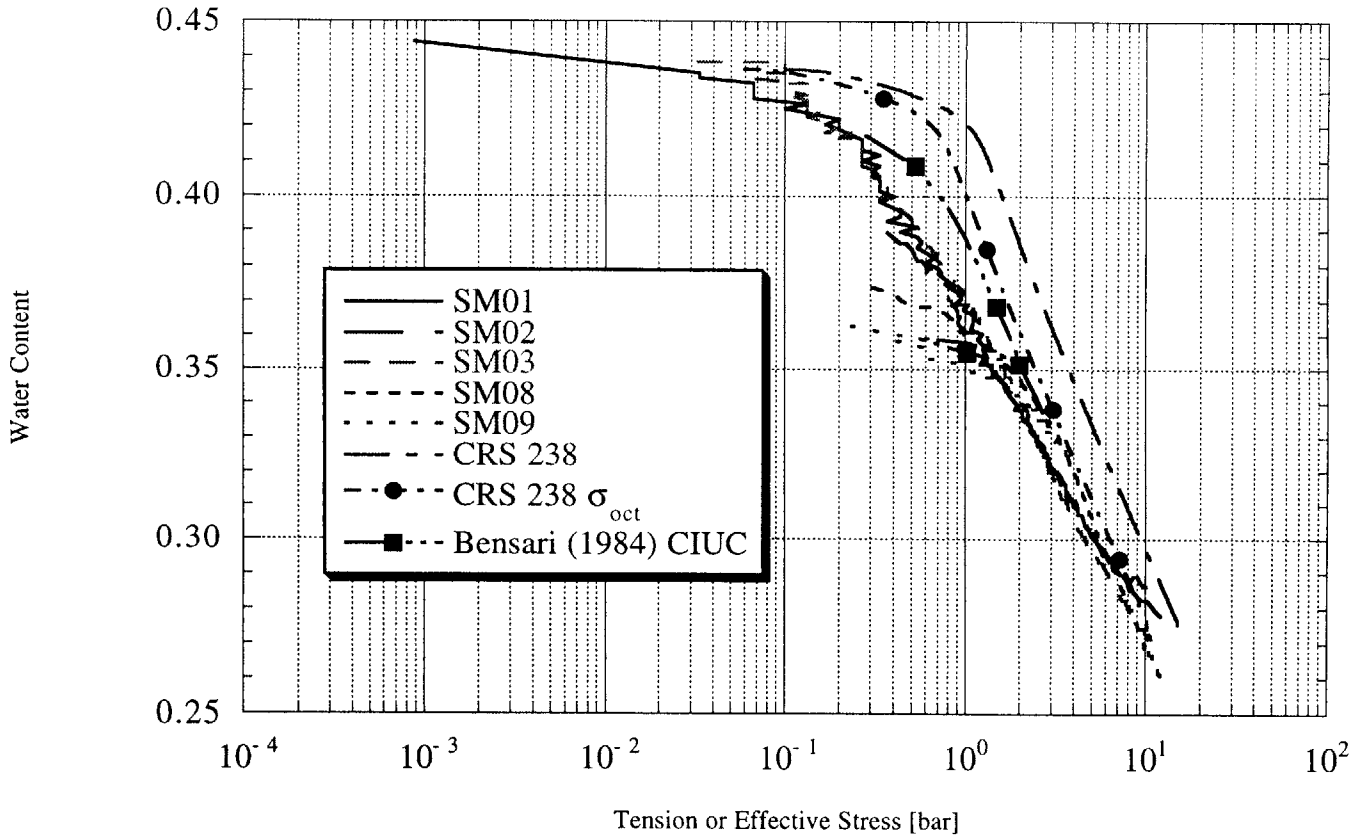

Figure 7-14. Characteristic curve for RBBC with CRS and CIUC data.

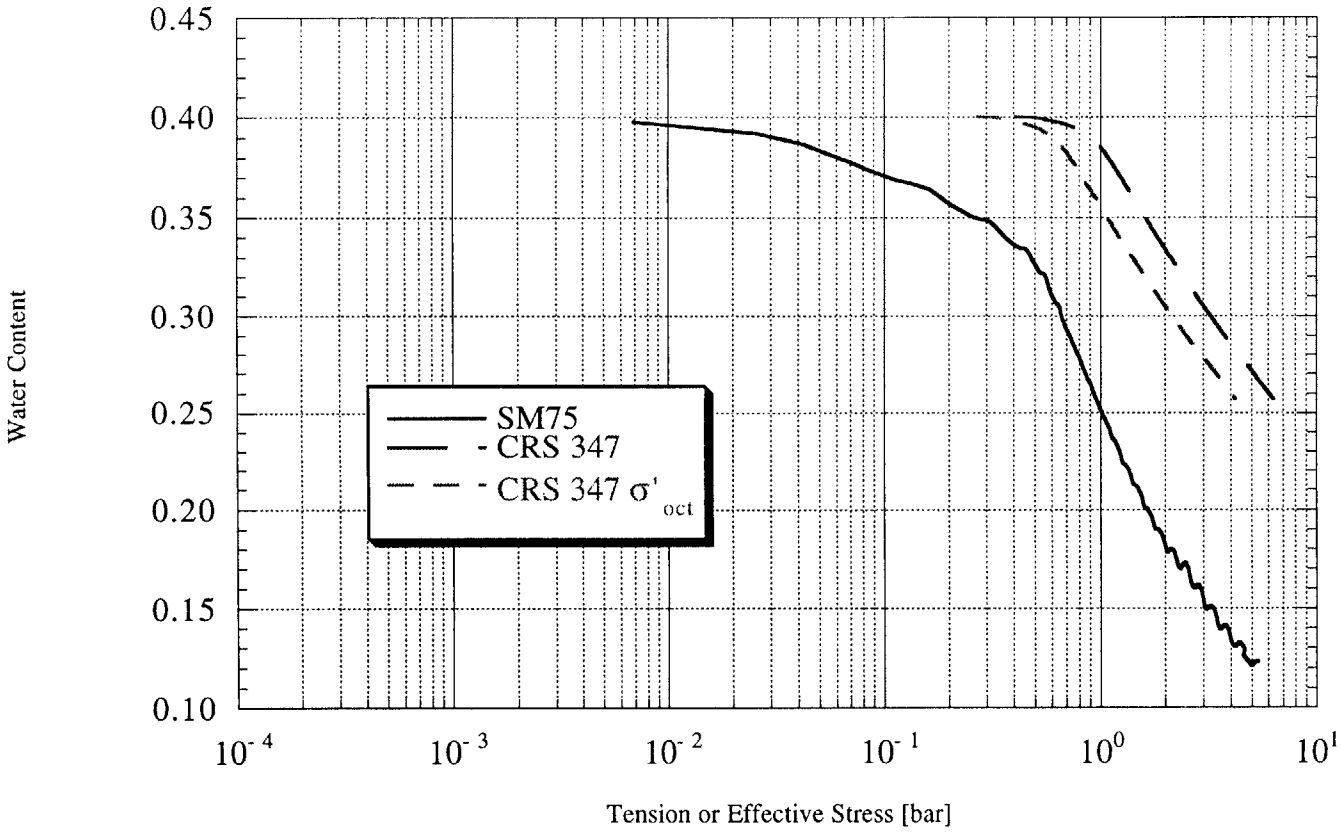

Figure 7-15. Characteristic curve for RVBC with CRS data

Chapter 8 Conclusions and Recommendations

8.1 Introduction

The purpose of this research was to better define the desaturation process of a porous matrix. First, a conceptual model of a draining material was developed. This was then formulated into an analytical model. The model was then tested using an unique measurement technique to determine a continuous drying curve of a porous material. The technique required the development of a tensiometer capable of directly measuring the high negative pressures.

The drying material was modeled by a regular packed matrix of spheres. Configuring the water into the geometric shape of pendular rings simulated the water held in the matrix. The analytical model related the water content of the matrix to the associated tension in the water. This Chapter presents the conclusions drawn from this research.

The conclusions are separated into several sections each of that focuses on specific portions of the work. Section 8.2 concludes the equipment performance of both the MIT Tensiometers and of the stones. The next section, Section 8.3, discusses the drying curves. Section 8.4 discusses the model predictions and includes some empirical relations for natural soils. Finally, Section 8.5 gives some recommendations for future research.

8.2 Equipment Development

8.2.1 New Measurement Technique

A new measurement technique to determine the drying curve of a porous material was developed. This new technique provided a continuous measurement of tension and water content from a fully saturated state to a point of residual saturation. This technique thus allowed a more accurate determination of the drying behavior of a material to that of the standard pressure plate technique. Another added benefit of the new technique is the rapid determination of the curve. The entire drying curve of a granular material could be determined within two days as opposed to only a single point with the pressure plate in nearly the same time.

8.2.2 MIT Tensiometer Designs

Several iterations of Tensiometer designs were investigated over the course of this research. The goal of each of the designs was to overcome the problems associated with the previous designs and to investigate aspects of behavior associated with the designs. From the discussion in Chapter 5, three designs were the culmination of the work presented. Versions 3.0, 3.1 and 5.0 were the final designs used to measure all the data given in this thesis. Version 3.0 and 3.1 provided the data on the stone saturation capabilities. Since this device was capable of undergoing any amount of overpressure, this was a perfect design to investigate the stone behavior. However, due to the poor electronic stability, this device was not a good choice for measuring drying curves of porous materials.

Version 5.0 was created with a commercial pressure transducer built in. This design essentially 'bought' the electronic stability and allowed very good resolution for measuring drying curves. All of the drying curves presented in this thesis were tested with Version 5.0. A few of the drying tests did encounter an excessive amount of electronic noise. This was most likely due to wiring and electrical connections to the data acquisition system in the laboratory and not from the device itself.

8.2.3 Stones

The two types of stones used in this research both proved to be adequate for their intended purpose. The Soil Moisture stones were rated at a bubbling pressure of 15 bars. This stone when saturated properly provided maximum sustained tensions in this range. However, as discussed in Chapter 5, in order to achieve this rated pressure, an overpressure of over twice this value was required during saturation. The saturation curve for this stone also gave an indication of the distribution of pores in the stone. The high degree of non-linearity of the saturation curve indicates that the pores are distributed over a relatively large range. Also, the long lag time in water transport across the stone discussed in Chapter 5, indicates that the pore connectivity is poor. Although reported in the literature, the Soil Moisture stone showed no apparent degradation over repeated use.

The Kochi University stones supplied by Professor Yanagisawa performed far superior to the Soil Moisture stones in terms of response and saturation capabilities. The relatively little lag time indicated that the Kochi stones had excellent pore interconnectivity. The linear saturation curve also indicated that the pore distribution was in fact very tightly centered on a single pore size. The Kochi stones also showed a better ability to sustain a higher tension at a maximum of 21 bars. However, the degradation of the stones appeared to be much greater than the Soil Moisture stones. Although no exact number was determined, approximately 50 cycles of saturation and tension loss was sufficient to degrade the Kochi stones. The degradation was such that only half of the original sustained tension could be maintained after this many cycles.

8.2.4 Design Considerations

From the performance of the various versions of the MIT Tensiometer, several important design requirements were determined. In order to maximize the efficiency of the Tensiometer, the following observations were made.

The Tensiometer diaphragm should be permanently sealed. This could be accomplished in two ways, either by making the diaphragm an integral part of the device as in Versions 3.0, 3.1, and 4.0 or seal the diaphragm with epoxy as in Version 5.0. In either case the resulting tensions could be sustained repeatedly with little or no variation in maximum tension. The o-ring seals used in Version 1.0 and 2.0 proved to be an unsatisfactory means to seal the diaphragm and resulted in inconsistent tension measurements.

The saturation of the device played a crucial role in the performance of the Tensiometer. An initial vacuum applied to the Tensiometer insured that the subsequent introduction of water would permeate the entire stone and reservoir. The final step of overpressure was absolutely necessary to maintain consistently high tensions. The omission of this step in Version 1.0 was probably the primary cause for the lack of tensions beyond 1 bar.

8.3 Drying Curves

The results of the drying tests were presented in Chapter 7. The following sections present an interpretation of the curves.

8.3.1 Glass Beads

The drying tests performed on the glass beads produced very significant insight into the behavior of a porous material upon desaturating. All of the beads tested were actually a distribution of beads within a given size fraction.

The 500 μm size fraction showed the most variability with respect to the air entry pressure (AEP). Three of the tests (SM61, SM63, and SM65) showed good reproducibility and yielded similar results. Two of the tests (SM60 and SM62) plotted at larger tensions and the other test (SM64) plotted at a lower tension. All of the curves ended with essentially the same residual water content. The reason for the variability of the AEP in the tests is not well understood. Each of the tests was performed identically

and electronic noise was not a factor in most of the tests (with the exception of the early part of SM64).

The other size fraction to show some variability in AEP was the 75-90 μm fraction. The four tests performed on this size displayed some variation, however the two tests that resulted in lower AEP (SM71 and SM73) were tested in the pan support. The effect of a larger surface area on the resulting curve is not known and warrants further investigation.

The remaining drying curves showed little noise and produced exceptionally good results. Nearly all the curves displayed some type of fluctuation (i.e., deviation from the vertical) during the draining phase. This fluctuation is most likely a result of the packing of the material. As the drying front moved down through the system, variations in pore sizes would certainly cause fluctuations in tension. Since the packing of the system could not be controlled, these variations are inevitable.

The residual water content of all of the tests resulted in an average value of 0.012 with a standard deviation of 0.005. At this point on the drying curve, all the water is held in pendular rings, thus for a regularly packed material this value is not governed by particle size. Therefore, this observation is expected.

The flattening of the drying curves after the residual water content has been reached, is not believed to be material behavior but the slow (relatively) drying of the porous ceramic stone. Once the material has reached this point, all pendular rings become independent of each other and contact is lost with the stone. Therefore, the stone will not measure any further increase in tension due to shrinking of the pendular rings. This conclusion was confirmed by attempting to rewet the material once the residual water content was reached. The re-wetted material did not display any reduction in tension. This indicates that the pendular rings in the material were not connected to the stone by a continuous film of water around the particles. This is an extremely important conclusion, especially with respect to the use of the axis translation technique. Since the pendular

rings are individual, no increase in air pressure would result in a reduction of pendular ring size (i.e. no draining of the material).

8.3.2 Soils

The results of the soil tests provided an interesting conclusion. The first material tested was the Manchester Fine Sand. Da Re (2000) documented the high degree of angularity of this material. Thus, it was not clear how this would effect the resulting drying curves. The material has a very steep grain size distribution and this would make for a good comparison with the steeply graded glass beads. The one test performed on this material (SM74) produced a well defined AEP and residual water content. Therefore, the high degree of angularity of the grains does not seem to be an important factor when measuring for the AEP and residual water content. The more important parameters are those associated with the grain size distribution.

A similar result was obtained from the finer grained Maine Silt. The Maine Silt was a finer fraction than the Manchester Fine Sand, but similar in Coefficients of Curvature and Uniformity. The amount of angularity of the particles was not determined at the time of writing of this thesis. The resulting drying curve was similar in shape to that of the Manchester Fine Sand and those of the glass beads. A well defined AEP and residual water content could be determined from the curve.

The other silty soil tested was the Tennessee Silty Sand. The drying curve from this material was substantially different from the other two silts and that of the glass beads. The curve was much flatter than that of the other materials tested. No discrete AEP could be determined from the curve, however there is some evidence to suggest that a large pore fraction drains between 0.1 and 0.2 bar. This is shown as the initial steep portion in the curve. Another unique feature of the curve is the 'knee' feature occurring between 1 and 2 bar. Although this type of feature would be very difficult to predict, it does illustrate the advantage of the continuous technique developed in this thesis. The standard pressure plate technique would most likely miss this feature unless an unusually

high number of specimens were to be tested. Even with a large number of specimens, the variability between each one could mask any unusual feature present. This test (SM76) failed to give a residual water content value for the soil, however from the slope of the curve (at low water contents) it is clear that this value would have exceeded the limit of the MIT Tensiometer.

The results of the two clay specimens indicate that this technique provides a fast means to determine the drying curve of cohesive materials. The equivalent drying test done on a conventional pressure plate would have taken well over two weeks assuming 5-8 points were evaluated. This in contrast with the new technique (which only took 4-6 hours for each of the tests) clearly shows another advantage of determining the drying curve in this fashion. A detailed analysis of the results of the clay specimens is beyond the scope of this thesis and is left for future work.

8.4 Desaturation Model Evaluation

A detailed account of the proposed desaturation mechanism was given in Chapter 3. The following is a brief recap.

For a regularly packed matrix of spheres, the relationship between the amount of water held in the pore spaces can be defined as the ratio of volume of water held to the volume of the matrix. This ratio was defined as the *Volume Water Content*, W_v. It was shown that this value is a function only of the inclusive angle, α and not the matrix radius. The expression is given by:

$$W_v = \frac{3}{4}\frac{\left[\cos\left(\frac{\alpha}{2}\right)-1\right]^2\left[2\cos\left(\frac{\alpha}{2}\right)-\sin\left(\frac{\alpha}{2}\right)\pi+\sin\left(\frac{\alpha}{2}\right)\alpha\right]}{\cos^3\left(\frac{\alpha}{2}\right)} \qquad [8.1]$$

The Volume Water Content can be converted easily to gravimetric water content by dividing by the specific gravity of the matrix material. Equation [8.1] was derived for a complete pendular ring, i.e. two spheres in contact with a pendular ring between them. Formulating the relationship in this manner allows for easy manipulation into any packing arrangement required.

For purposes of extremes, if two packing arrangements are considered one giving the largest pore space (Cubic) and the other giving the smallest (Tetrahedral), it is possible to evaluate the limits of real packing during the drying tests. The Cubic arrangement was discussed in Chapter 3 in detail, however for review the arrangement is characterized by the centers of the spheres being orthogonal to all other neighbors. The Tetrahedral packing does not yield a *unit void* arrangement, i.e. this unit does not repeat infinitely to create a uniform regularly packed material. However, for a single pore, it does represent the tightest arrangement and thus the smallest pore space.

The Tetrahedral packing is characterized by the centers of the spheres being at 60° in plane to each other when any three of the four spheres are considered. The four planes intersecting the centers of the spheres will define the unit pore for this packing. A schematic of the packing arrangements is presented in Figure 8-1. The physical properties of the packings are given in Table 8-1. In order to determine the Volume Water Content for the packing, the number of complete rings in the pore space must be known. This value is given as the last entry in the Table. Therefore, for the Volume Water Content for the Cubic and Tetrahedral packings will be the result of Equation [8.1] multiplied by 3 or 1.175 respectively.

The tension developed in the pendular ring was derived in Chapter 3, and in terms of the inclusive angle α, particle radius R, and surface tension σ is:

$$u_m = \frac{\sigma}{2}\frac{\left[1+\sin\left(\frac{\alpha}{2}\right)-3\cos\left(\frac{\alpha}{2}\right)\right]}{R\left[\cos\left(\frac{\alpha}{2}\right)-1\right]} \qquad [8.2]$$

Therefore, for a given particle radius, the relation between Volume Water Content and tension are known for a range of inclusive angle α. For uniform spheres, the only uncertainty in the model is at what α defines the upper limit of the model. This upper limit will correspond to the AEP that is physically measured. A first approximation of the upper limit would logically be the point at which a pendular ring first develops. In Figure 8-1 there is an inscribed circle in both the Cubic and Tetrahedral drawings. These circles represent the cross section of a sphere that would fit inside the packing normal to that face. The radius of this inscribed sphere is termed the *rooting radius.* The corresponding α for the packings at this rooting radius is $\pi/2$ and $\pi/3$ for the Cubic and Tetrahedral arrangements respectively.

Incorporating the observations made in the drying tests indicates that the initial inclusive angle at which a pendular ring forms is smaller than previously described. From the photographic evidence, an α of $2\pi/9$ (40°) is the starting value to be used. Using this as a basis for predictions of the AEP of uniform spheres, Equation [8.2] reduces to:

$$u_m = \frac{0.891\times10^{-5}}{R} \qquad [8.3]$$

where;

u_m is given in bar
R is expressed in meters

Equation [8.3] gives the tension in the pendular ring in units of bar so long as R is specified in meters. Using this as a prediction, a plot can be generated with the measured AEP of the glass beads versus the prediction of Equation [8.3]. This is shown in Figure 8-2. The predicted values are based on an average radius of the bead fraction (i.e., the median of the distribution). The predicted results are tabulated in Table 8-2. As can be

clearly seen, the model using an α of 40° does a very good job of predicting the AEP for the beads. The 500 μm bead fraction's measured AEP is higher than the predicted value, however this can be explained easily.

The 500 μm beads were tested in the 1 inch high specimen retaining ring described in Chapter 6. As a simple means to determine if gravity becomes important in the draining of this size material, a basic calculation can be checked. If it is assumed that the tension in the system is described correctly by Equation [8.2], then an equivalent height of water head can be formulated on the right side of the Equation. The Equation can then be rearranged to give the relation explicitly for the particle radius:

$$R = \frac{\sigma}{2} \frac{\left[1 + \sin\left(\frac{\alpha}{2}\right) - 3\cos\left(\frac{\alpha}{2}\right)\right]}{\gamma h \left[\cos\left(\frac{\alpha}{2}\right) - 1\right]} \qquad [8.4]$$

Where the substitution of $u_m = \gamma h$ was made. To determine what inclusive angle to use, Mao et al (1993) indicates that the largest stable pendular ring for an air-water interface will be on the order of 80° for α[2]. This was determined using a thermodynamic consideration of a draining bed of spheres. Therefore making the appropriate substitutions in Equation [8.4], gives a radius of particle for a 1 inch high specimen that gravity forces equal tension forces. The result yields a particle radius of 409 μm.

This analysis suggests that gravity forces become important at the radius of the 500 μm bead fraction. The exact fraction distribution was not know and may have contained particles with diameters as large as 625 μm. It is therefore postulated that the

[2] Mao et al (1993) provides drawings of the outlines of the stable pendular rings. To determine the equivalent inclusive angle, the drawings were measured directly.

measurements on the 500 μm bead fraction were not measuring the true AEP. The effects of gravity might cause the water to evaporate freely without a significantly increasing the tension of the pore water. Then, as the system continues to lose water, the tension would eventually increase to a point that was within the measuring range of the MIT Tensiometer.

The two soils that provided AEP data were the Manchester Fine Sand and the Maine Silt. The results of the tests are given in Table 8-3. A characteristic radius for the soils is required to compare the measured AEP to the model. Since the soils have a more complex grain size distribution than the glass beads, a simple median of size would not apply here. The radius of 80% finer from the grain size distribution was chosen as the characteristic radius. The reasoning behind this is explained in the next section, Section 8.4.1. Figure 8-3 plots the AEP of the soils versus the characteristic radius along with the model predictions (using $\alpha = 40°$). The model does a very good job of predicting the AEP of the two soils. This is regardless of the angularity of the particles. The model was based on spheres while the soils (esp. the MFS) are quite angular. The model also assumes that the matrix is a regularly packed material of uniform size, however the model still predicts the AEP even while the soils are not.

After the AEP in the drying curve, the next important feature is the transition to pendular ring drying. This coincides with the residual water content. At this point, all of the water from the pore is removed except that water which is held in pendular rings. Therefore, the same inclusive angle α is used as a predictor. Since the Volume Water Content is only a function of α and not of particle diameter, it is predicted by this model that all uniform packings will have the same residual water content. It should be recalled that the Volume Water Content is easily converted to gravimetric water content by dividing by the specific gravity of the solids. Table 8-4 gives the predicted gravimetric water content of residual moisture for a matrix of uniform spheres with a specific gravity of 2.43. The Table was calculated with use of Equation [8.1].

The resulting residual water contents for the specific bead fractions are given in Table 8-5. These data are plotted and shown in Figure 8-4. There is some scatter in the data, however the largest deviation from the prediction is within 1% water content. The two soil tests that gave residual water content information (SM74/Mancherster Fine Sand and SM77/Maine Silt) are also added to the figure. The data from the soil is presented in Table 8-3. These data for the soil are slightly lower in residual water content than most of the glass bead results. As will be described in the following section, the radius used was r_{80} from the grain size distribution. Both of the soils showed a residual water content of 1%.

The model using the tetrahedral packing does a very good job of predicting the residual water content. Although this packing is not a true packing, it does represent the smallest pore configuration for spheres of equal diameter. There is clearly some uncertainty in how the residual water content is determined and also some sensitivity to packing, however the model predicts this parameter to a reasonable scatter given this fact.

8.4.1 Predicting the AEP

After comparing the measured AEP of the soils tested to the model, it was determined that an empirical correlation might hold for granular materials. The model was determined for uniform spheres and the measured drying curves were for glass beads. The glass beads had a very small grain size distribution since they were fractionated. The soils tested as well had a very steep grain size distribution. Therefore, it was desirable to obtain data from soils with different types of grain size distributions.

A search was done in the literature for data containing measured drying curves and the associated grain size distributions. Surprisingly, this was not easy to find. The soil science literature contains many examples of drying curves however these data do not contain the associated grain size distributions. Eventually, four sources were located that provided data that were applicable for this purpose (Andersson and Wiklert 1972; Jonasson 1991; Oberg 1997; Rassam and Williams 2000). Table 8-6 summarizes all the

relevant information from the sources. The complete set of raw data is given in Appendix C.

Currently, the standard method to predict the AEP for a soil is to use the D_{10} correlation (Culligan 1999). This method uses the 10% finer fraction diameter from a grain size distribution. The diameter is then used to predict the AEP of the material by:

$$AEP = \frac{2\sigma}{r_{10}} \qquad [8.5]$$

where;

σ is the surface tension of water (72.75 mN/m)

This method makes no distinction between different types of grain size distributions and therefore does not provide any real insight into the AEP for granular materials. A plot of the data found in the literature and the predicted AEP using this method is shown in Figure 8-5. From the Figure it is clear that there is substantial scatter between the measured and predicted values.

An attempt was made to formulate an empirical model to describe the AEP by using the information from a grain size distribution. The data used for this new correlation resulted from soils having well defined AEP's. The soils that did not display defined AEP's had flat grain size distributions. Therefore, the data set was initially screened by selecting only the soils with steep (relatively) grain size distributions.

Several iterations were investigated to find the best fit for the data set, however only the best correlation will be discussed further. It was found that the Coefficient of Curvature, C_c provided a very good means to segregate the data. The Coefficient of Curvature is defined by:

$$C_c = \frac{D_{30}^{\ 2}}{D_{10}D_{60}} \qquad [8.6]$$

The diameters are taken from the grain size distribution that is plotted on semi-logarithmic axes. This tends to influence the Coefficient of Curvature in that a higher weight is put on the larger diameters. However as a general trend, as the material is more uniform, the smaller C_c becomes. Therefore, the first segregation of the data set uses C_c as a break. For any soil with a C_c less than unity, the AEP can be estimated by using Equation [8.3]. Since this Equation was developed from testing very uniform materials, the Equation serves as a natural predictor for materials with a low C_c. It was found that the best fit for data used a radius corresponding to the 80% percent passing fraction. Thus r_{80} was used to generate the plot in Figure 8-5. The Figure shows the performance of Equation [8.3] when predicting AEP for natural materials. As can be seen in the Figure, the predictions become better with increasing AEPs. This is somewhat expected as the lower AEPs correspond to a larger r_{80}. As the r_{80} size becomes larger, the effects of gravity draining increase. Although these effects are not quantified, they most certainly would cause a deviation of the measured AEP to the predicted.

For Coefficients of Curvature larger than unity, an interesting relation was found between the ratio of D_{60} to D_{30} and the inclusive angle, α. For each of the data with Cc >1, the measured AEP was compared with the α required to give the same result. Again r_{80} was used as the characteristic radius. A plot of the ratio of D_{60} to D_{30} versus the inclusive angle was created and shown in Figure 8-7. This plot is then used as the basis for the prediction. For a given D_{60}/D_{30} ratio, an α is determined using the regression parameters listed in Figure 8-7 and is given by:

$$\alpha = 103.18 - 28.988\frac{D_{60}}{D_{30}} \qquad [8.7]$$

and is valid when $D_{60}/D_{30} < 2.3$.

This α and r_{80} are then used in Equation [8.2] to give the predicted AEP. The resulting predicted versus measured AEP for the entire data set is given in Figure 8-8. The high goodness of fit is expected since this data set was used to derive the correlation.

The ratio of D_{60}/D_{30} was found to provide a better fit than the Coefficient of Uniformity to the data set. This indicates that the AEP is weighted more heavily towards the larger size pores. This is in contrast to the standard correlation that uses the characteristic pore size as the D_{10} size fraction. From Figure 8-5, it is seen that D_{10} does not provide a very reliable means to predict the AEP. This method also makes no distinction between different types of grain size distributions. Clearly, the grain size of a material should play an important role in determining what the dominant pore size will be.

The new proposed method not only considers this, but also provides a rationale to the parameters chosen. The new method also gives a simple and more accurate means to predict the AEP of a porous material based on grain size data than is currently available. The exact limitation of the method is not known, however the data set used to formulate the relation was limited to D_{60}/D_{30} to less than 2.3. Therefore, the new method should be applied to soils within this boundary.

8.5 Recommendations for Future Research

To better understand the physics of the desaturation process, the following recommendations are given for future research. These recommendations include suggestions to improve the equipment and also the drying technique.

- This work focused on only the drying behavior of the porous material. Studying the wetting curve of the material would provide a complete picture of the changes in soil suction with changes in seasonal wetting and drying.
- Particle shapes other than spherical or ellipsoidal should be incorporated into the testing program to provide a broader view of drying behavior in natural materials.
- Currently only poorly graded distributions of materials have been investigated. The effect of gap graded distributions on drying measurements should be considered.

- The addition of volume measurement to the drying technique would greatly extend the array of soils that could be examined. Soils that shrink upon drying could be examined and compared to consolidation behavior.
- Redesign the equipment to incorporate a replaceable seal such as the vacuum technology brass o-ring. This could potentially allow for a single device to have the ability to change pressure transducers of different capacities. This could greatly enhance the resolution of the tension measurements by maximizing the output of the transducer to that of the suction being recorded.
- Version 4.0 attempted to extend the geometry of the Soil Moisture stone without success. This was not explored any further as it was not necessary for the progress of the current work. However, this issue should be revisited, as it would allow for larger tensiometer configurations. This would allow for a larger cross sectional area of specimen to be tested.
- Explore the thermodynamics of gravity draining materials, as this would determine the limit of drying procedure in grain size and specimen height.
- An investigation of the physics of stone drying should give a better understanding of what materials or configuration of materials would give the desired tensions.
- During the course of this research a phenomenon was observed that has not been documented in the literature. A saturated cohesive soil was placed into a 100% relative humidity environment and over time the soil would lose moisture while the tension of the pore water would increase. This warrants further investigations.
- The observed lag time in the transport of the water through the porous stone during the saturation process was considerably faster than predicted using simple Darcy flow. A vapor transport model should be considered as it is probably more applicable to this situation.
- Near the end of this work, a pan support was created with dimensions that were 3 times the diameter of the MIT Tensiometer. Investigation of the effect of the larger surface area on the resulting drying curves needs to be quantified.
- The initial tension that was observed in the fine bead sizes while being poured onto the MIT Tensiometer should be further investigated. It is probable that the small size

of bead caused a turbulent flow of water above the stone. This flow could have driven water from the stone and thus appeared to cause a tension. The low hydraulic conductivity of the beads then restricted the water from returning to the stone and equilibrating the tension to a static head in a sufficient amount of time before the effects of evaporation induced tension began. Longer equilibration times before starting the tests could eliminate this phenomenon.

- A substantial amount of effort was placed into finding other materials to be used in place of the ceramic stone. This was done to try and extend the limitations of the commercially available stones. Several interesting alternative technologies were considered to modify or replace the ceramic stones. Some of these technologies included laser etching of silicon wafers, coating of surfaces with carbon based materials, and silicon nitride ceramics. Currently these technologies appear to be prohibitive to this application only due to the cost associated with creating a large enough stone/composite. However, this expense over time will surely reduce.
- The stones that were used in this study should be tested using mercury porosimetry. This would give a definitive pore size distribution of the stones and allow for a better criterion for selecting appropriate materials.
- The MIT Tensiometer could be easily adapted to a field application/instrumentation.
- Long term measurements of stability would need to be conducted if a field instrument was constructed.
- In evaluation of a field device, contact with a large volume of soil and monitoring could be conducted in the laboratory to evaluate the applicability to the field.

Table 8-1. Physical properties of two packing arrangements.

Packing	Cubic	Tetrahedral
Unit Void	8 - 1/8 Spheres	4 - 1/20 Spheres
Porosity, n	47.6%	11.1%
Voids Ratio♣, e	0.910	0.125
Pendular Ring angle of rotation	90°	70.5°
Number of Sphere Contacts	12	6
Number of Compete Rings	3	1.175

♣ The Volume Water Content is equal to voids ratio when $S = 1.00$

Table 8-2. Predicted AEP for various glass bead fractions.

Bead Size Fraction [μm]	Average Radius [μm]	Predicted AEP using Eq. [2.1] [bar]	Average Measured AEP [bar]
500	250	0.0356	0.072±0.026
250-300	138	0.0648	0.05
212-250	116	0.0771	0.06
125-150	69	0.130	0.10
75-90	41	0.216	0.18±0.075

Table 8-3. Parameter results of the soils tested.

Soil	Characteristic Radius, r_{80} [μm]	Measured AEP [bar]	Measured Residual Water Content, w_r
Manchester Fine Sand	100	0.12	0.01
Maine Silt	10	0.70	0.01

Table 8-4. Residual gravimetric water content predictions for uniform spheres.

Inclusive Angle, α [radians]	Tetrahedral Packing	Cubic Packing
$\pi/2$	-	0.0682
$\pi/3$	0.0343	0.0175
$2\pi/9$	0.0083	0.0042

Note: Specific gravity of solids used 2.43

Table 8-5. Measured residual water content for various glass bead fractions.

Bead Size Fraction [μm]	Average Radius [μm]	Measured Residual Water Content, w_r
500	250	0.008±0.002
250-300	138	0.018±0.004
212-250	116	0.012
125-150	69	0.010
75-90	41	0.015±0.004

Table 8-6. Grain size indices on data found in the literature.

Source	Test #	D_{10} [μm]	D_{30} [μm]	D_{60} [μm]	D_{80} [μm]	C_c	C_u	AEP [bar]
Andersson & Wiklert	6-1	530	610	760	880	0.924	1.434	0.008
	6-3	68	88	120	160	0.949	1.765	0.049
	6-4	68	88	120	160	0.949	1.765	0.088
	6-5	22	27	38	48	0.872	1.727	0.290
	6-7	6.8	8.8	12	16	0.949	1.765	0.980
	6-8	2.2	2.7	3.8	4.8	0.872	1.727	2.94
	8-8	63	82	120	160	0.889	1.905	0.069
	9-10	23	56	105	150	1.300	4.565	0.059
	12-13	5	16	32	52	1.600	6.400	0.390
	14-8	3	10	23	41	1.449	7.667	0.590
Jonasson	16006	75	170	310	460	1.243	4.133	0.018
	16007	90	205	320	470	1.459	3.556	0.012
Rassam & Williams	Med Sand	180	300	520	720	0.962	2.889	0.015
	50 m	60	160	300	420	1.422	5.000	0.028
	150 m	18	75	170	270	1.838	9.444	0.070
Öberg	S5.7	30	75	130	150	1.442	4.333	0.080
	S10.4	21	45	90	120	1.071	4.286	0.100
	S13.5	6	21	48	100	1.531	8.000	0.200
	S21	5	11	29	40	0.834	5.800	0.600
	G4.4	3.5	8.5	17	26	1.214	4.857	0.700
	G7.9	4.5	10	21	29	1.058	4.667	0.500
	G12	8	25	40	50	1.953	5.000	0.100
	G14.9	8	30	48	52	2.343	6.000	0.100
	G17	5	17	28	34	2.064	5.600	0.400
	R2.5	7	17	30	40	1.376	4.286	0.300
	R3.5	10	30	60	90	1.500	6.000	0.080
	R4.5	7	16	30	40	1.219	4.286	0.300
This Work	MFS	80	110	160	200	0.945	2.000	0.120
	MS	4	6	10	20	0.900	2.500	0.700

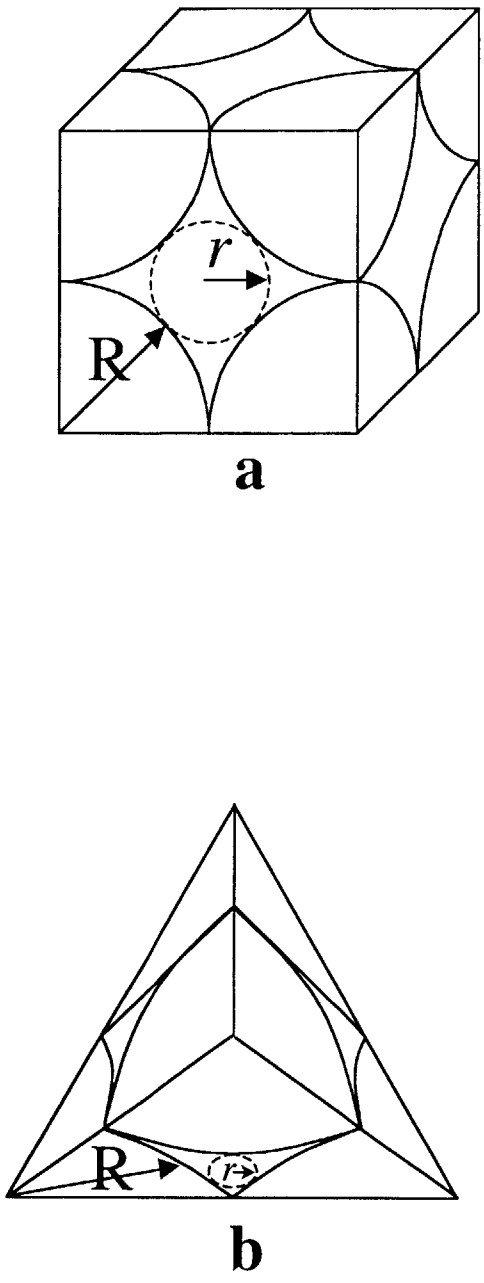

Figure 8-1. Unit Pore for (a) Cubic and (b) Tetrahedral packing schemes.

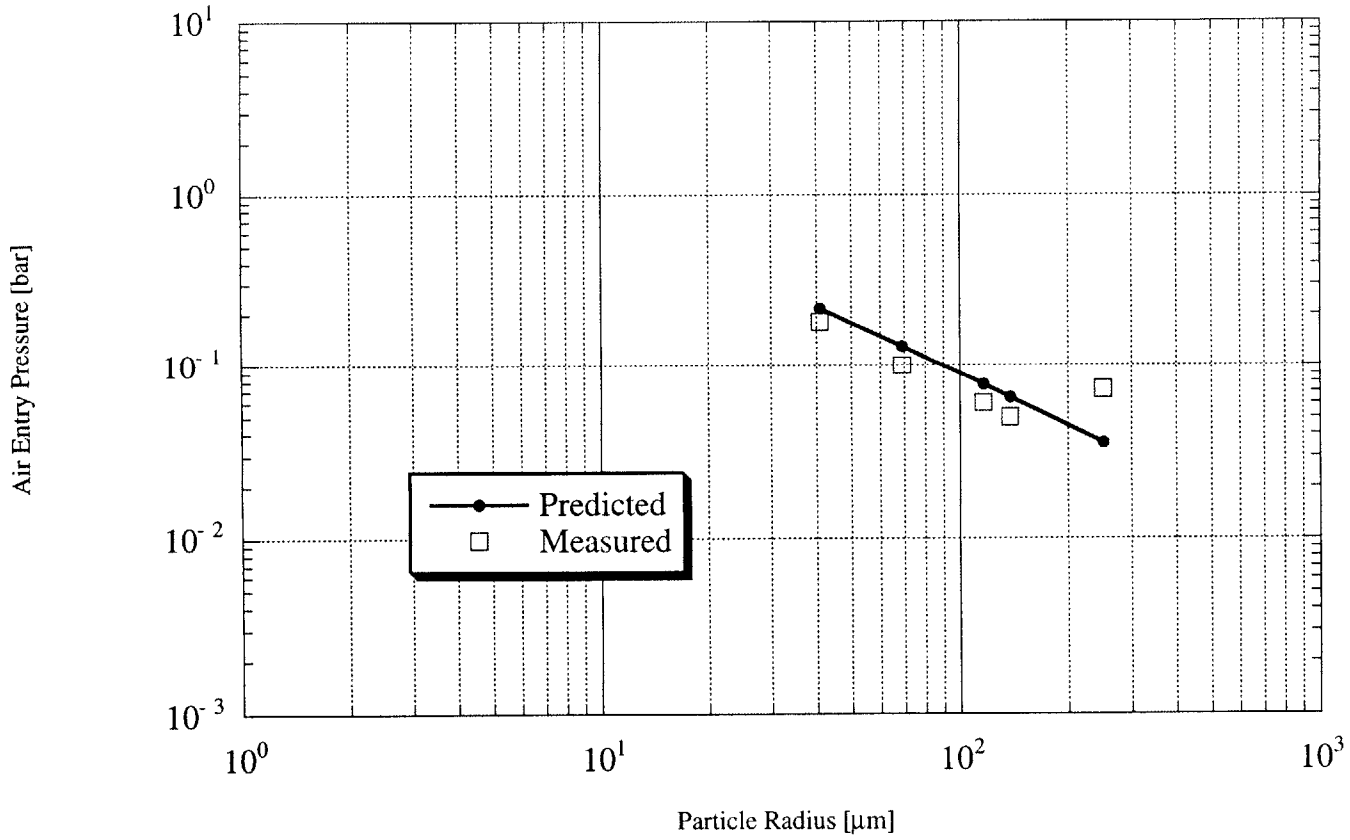

Figure 8-2. Predicted versus measured AEP for the glass bead drying tests.

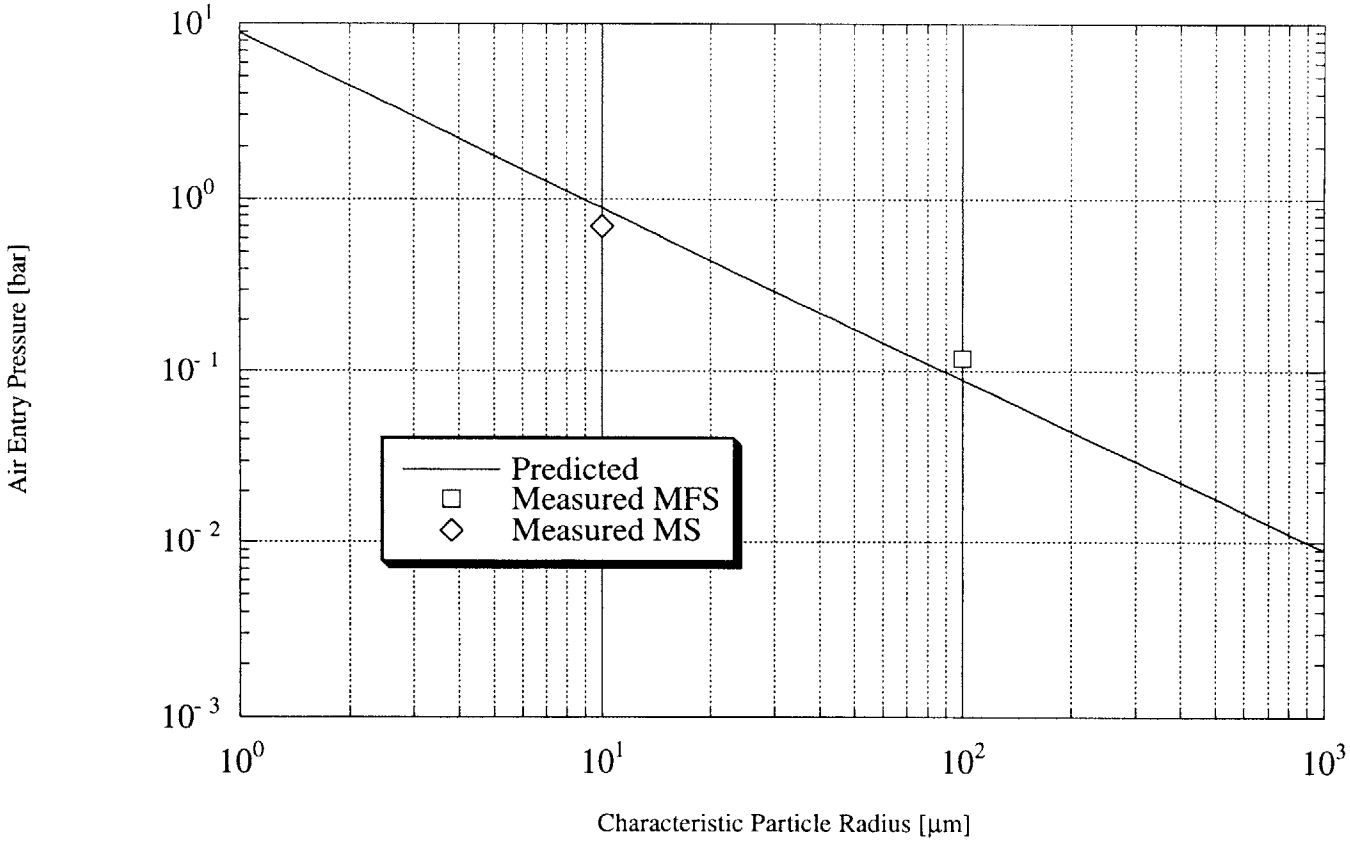

Figure 8-3. Measured AEP for soils tested.

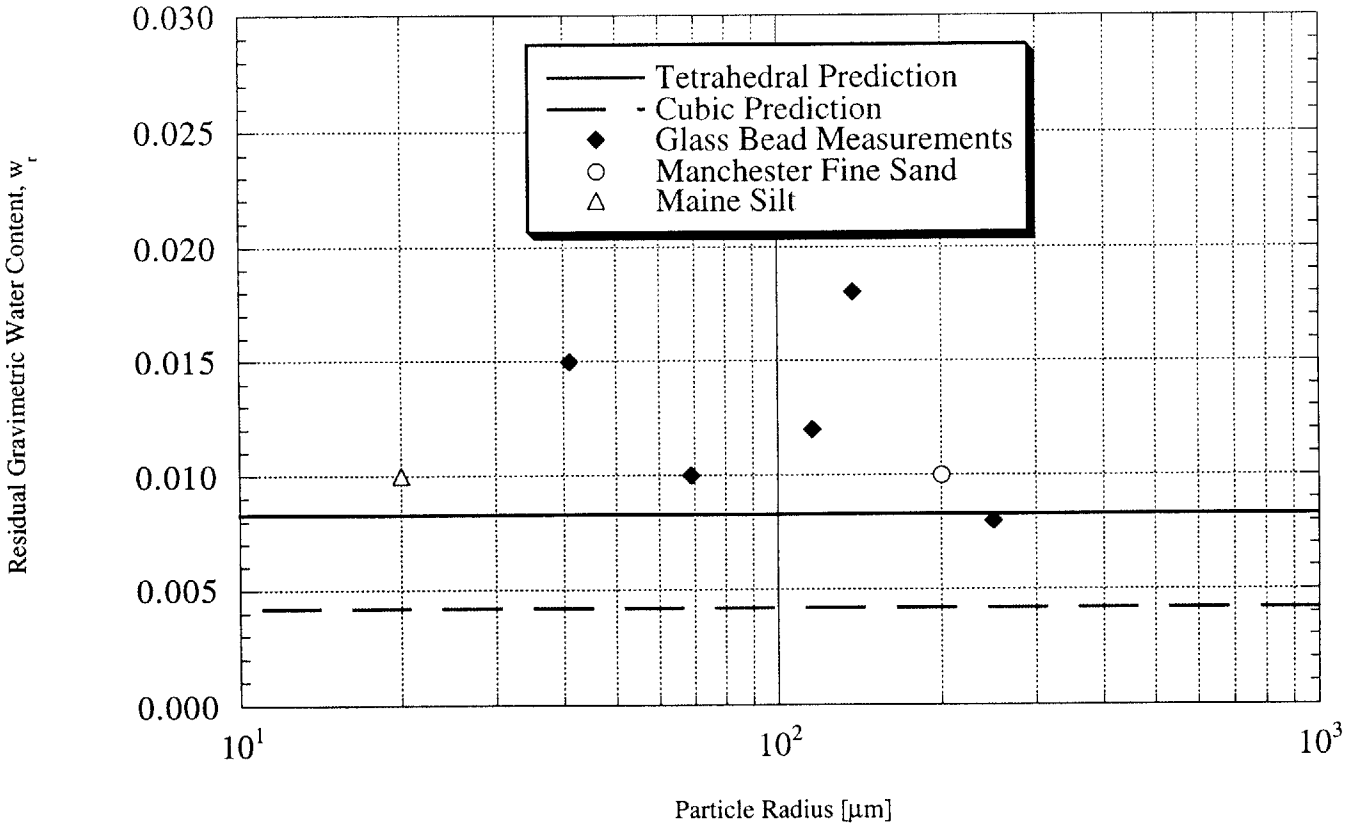

Figure 8-4. Predicted versus measured residual water contents for glass beads.

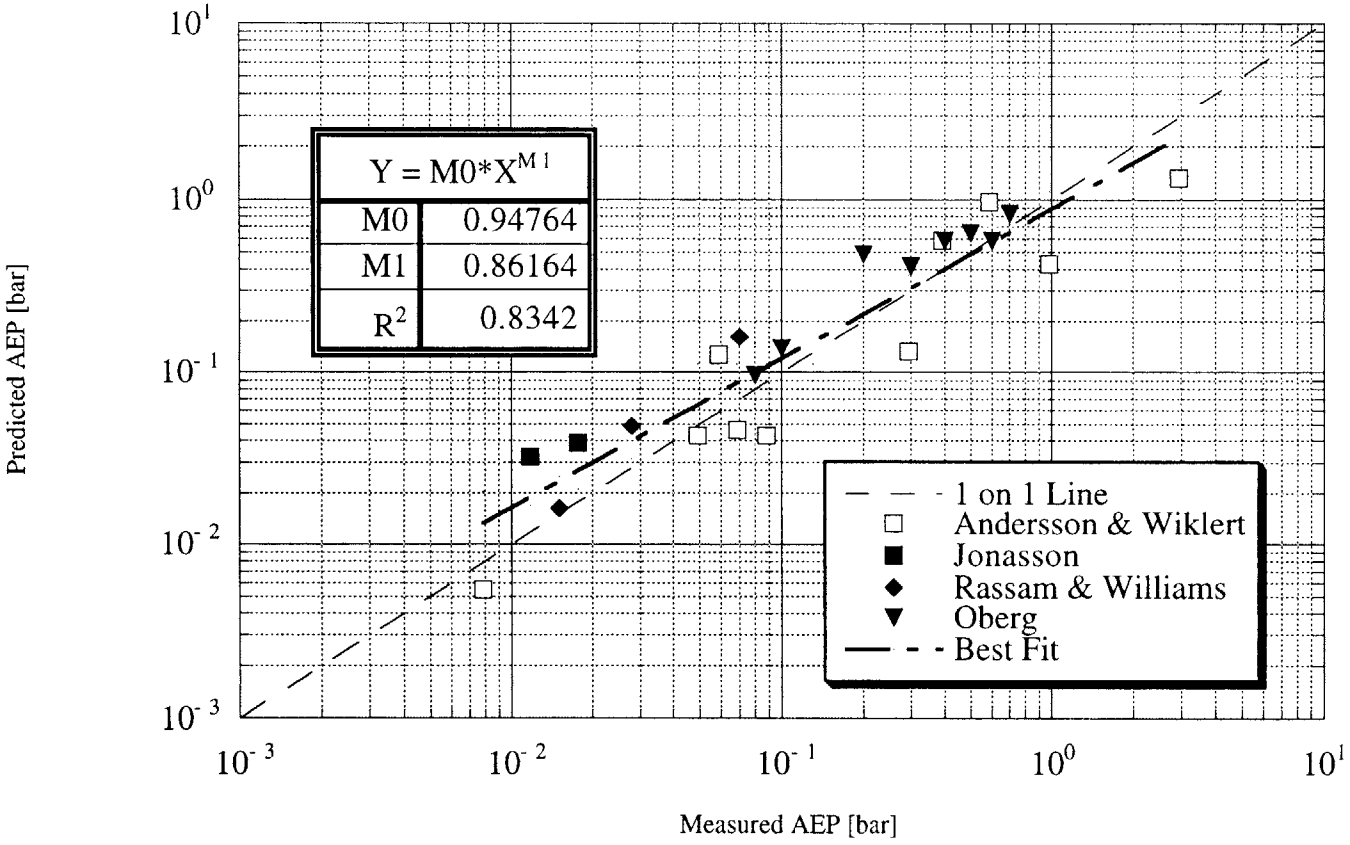

Figure 8-5. D_{10} method of predicting the AEP for the data set.

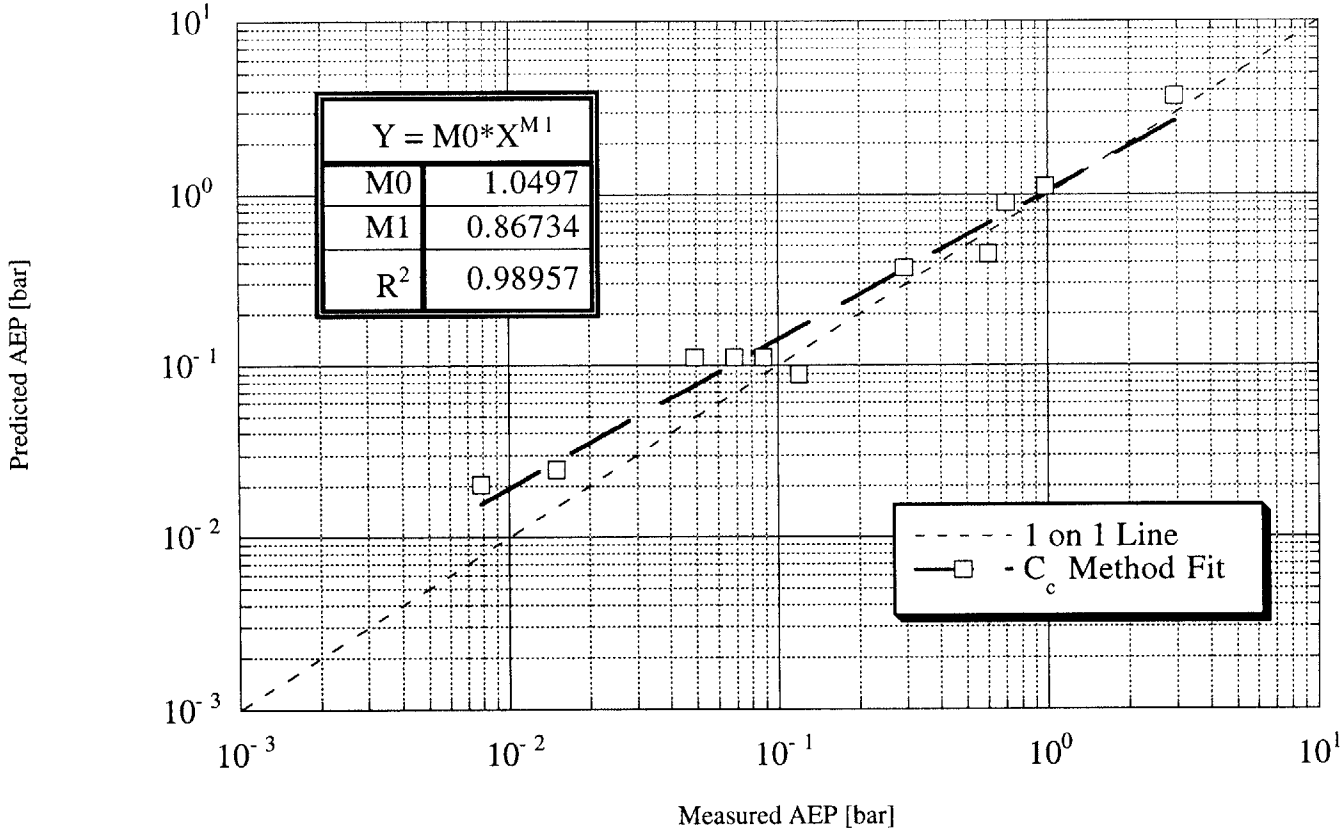

Figure 8-6. Model prediction of AEP for $C_c < 1$.

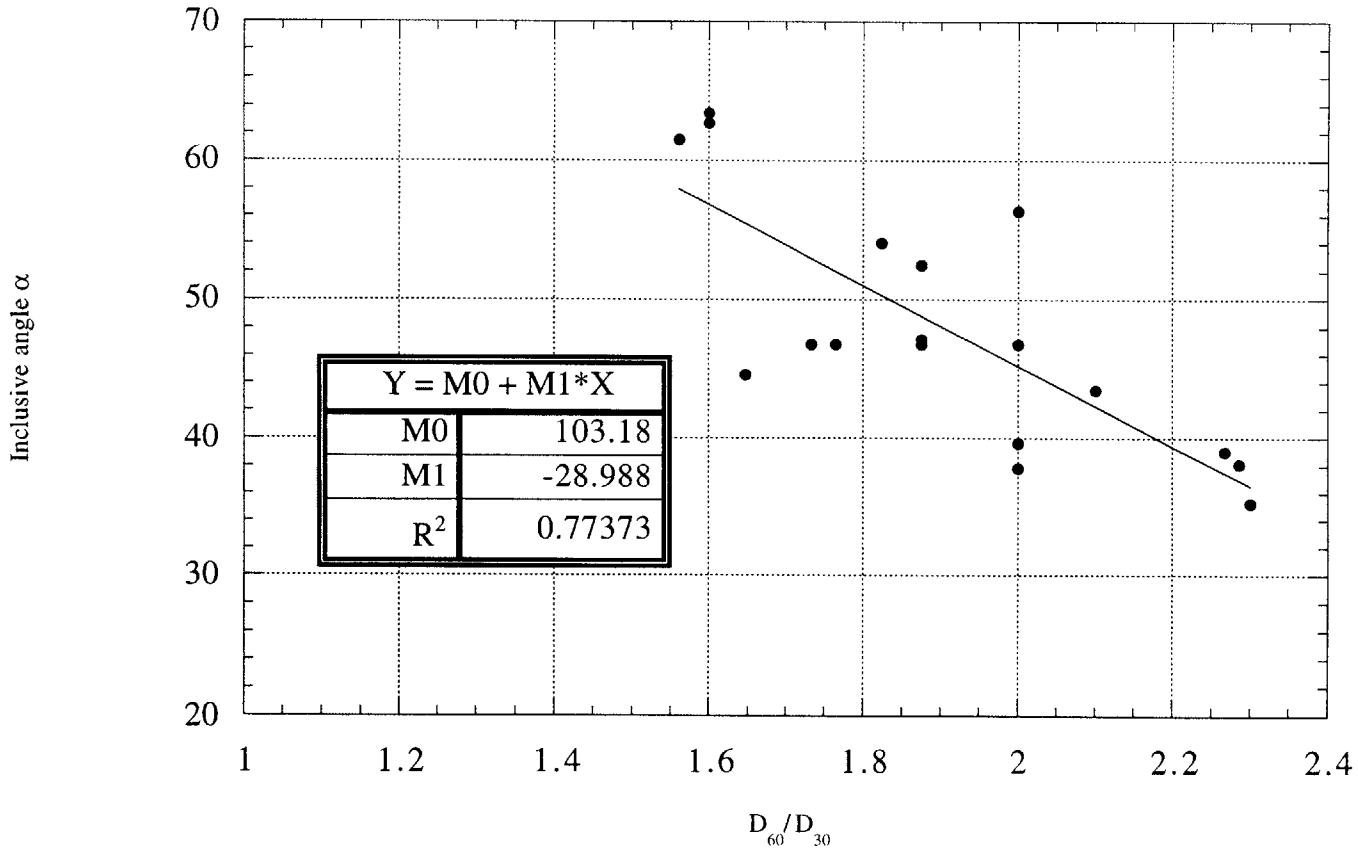

Figure 8-7. Relation between D_{60}/D_{30} and inclusive angle, α.

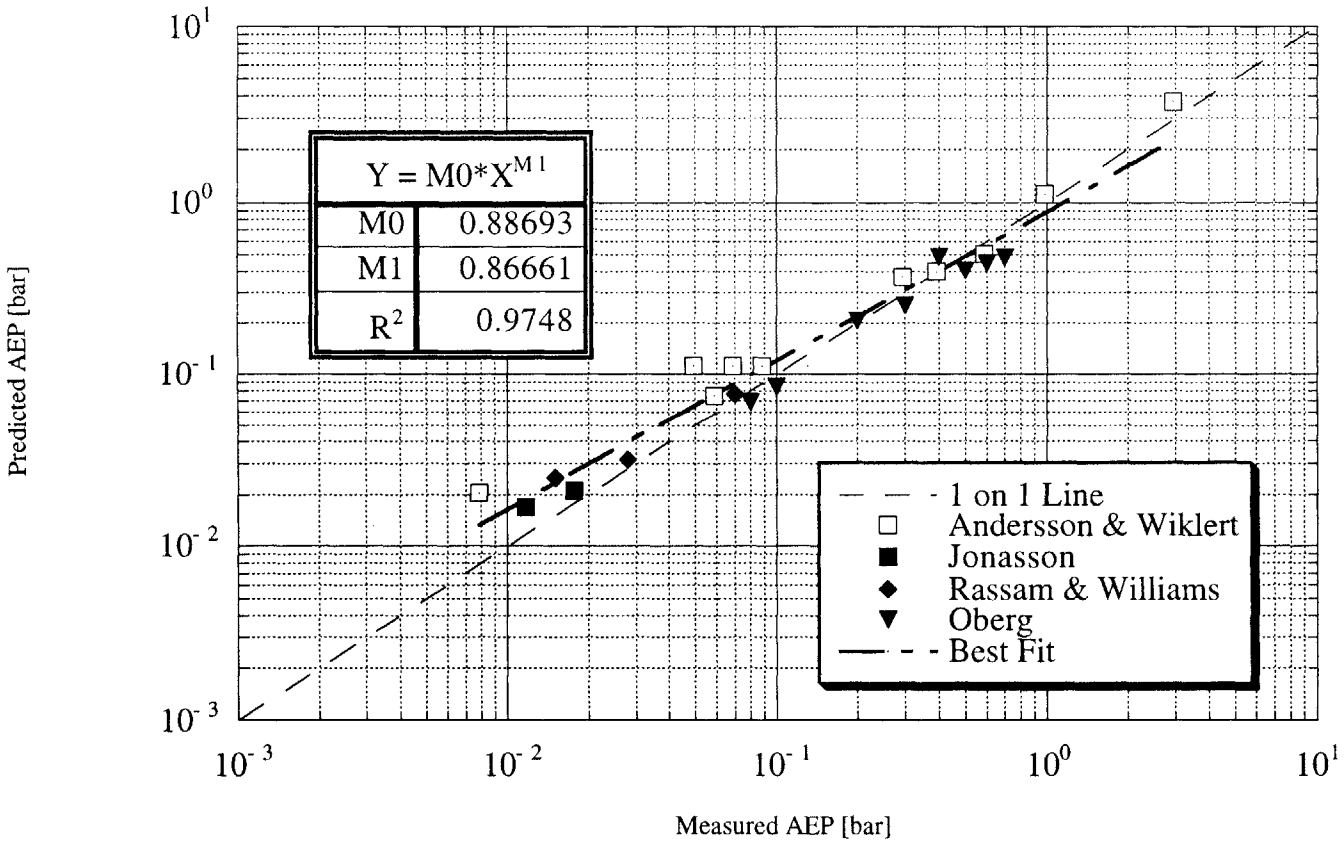

Figure 8-8. Summary of new prediction method for AEP.

Chapter 9 References

Adler, P. M., and Brenner, H. (1988). "Multiphase Flow in Porous Media." *Annual Review of Fluid Mechanics*, 20, 35-59.

Andersson, S., and Wiklert, P. (1972). "Markfysikaliska undersokningar i odlad jord. XXIII. Om de vattenhallande egenskaperna hos svenska jordarter." *Grundforbattring*, 25, 53-143.

Aslyng, H. C. (1963). "Soil physics terminology." *International Society of Soil Science Bulletin*, 23, 7-10.

ASTM. (1993a). "D422-63: Standard Test Method for Particle-Size Analysis of Soils." Soil and Rock; Dimension Stone; Geosynthetics, R. A. Storer, Director, ed., American Society for Testing and Materials, Philadelphia, PA, 93-99.

ASTM. (1993b). "D2325-68: Standard Test Method for Capillary-Moisture Relationships for Coarse- and Medium-Textured Soils by Porous-Plate Apparatus." Soil and Rock; Dimension Stone; Geosynthetics, R. A. Storer, Director, ed., American Society for Testing and Materials, Philadelphia, PA, 301-307.

ASTM. (1993c). "D3152-72: Standard Test Method for Capillary-Moisture Relationships for Fine-Textured Soils by Pressure-Membrane Apparatus." Soil and Rock; Dimension Stone; Geosynthetics, R. A. Storer, Director, ed., American Society for Testing and Materials, Philadelphia, PA, 430-435.

Bear, J., and Verruijt, A. (1992). *Modeling groundwater flow and pollution*, D. Reidel Publishing Company, Dordrecht.

Bennett, R., and Wilson, S. (1999). "Unsaturated soils come home." Ground Engineering, 26-28.

Bensari, J. E. (1984). "Stress-Strain Characteristics from Undrained and Drained Triaxial Tests on Resedimented Boston Blue Clay," Master of Science in Civil Engineering, Massachusetts Institute of Technology.

Bocking, K. A., and Fredlund, D. G. "Limitations of the axis translation technique." *Fourth International Conference on Expansive Soils*, Denver, CO, 117-135.

Bolt, G. H. (1976). "Soil physics terminology." *International Society of Soil Science Bulletin*, 49, 16-22.

Brooks, R. H., and Corey, A. T. (1966). "Properties of Porous Media Affecting Fluid Flow." *Journal of the Irrigation and Drainage Division, Proceedings of the American Society of Civil Engineers*, 92(IR2), 61-88.

Cauble, D. F. (1996). "An Experimental Investigation of the Behavior of a Model Suction Caisson in a Cohesive Soil," Doctor of Philosophy in Geotechnical Engineering, Massachusetts Institute of Technology.

Clark, W. C., Haynes, J. M., and Mason, G. (1968). "Liquid bridges between a sphere and a plane." *Chemical Engineering Science*, 23, 810-812.

Da Re, G. (2000). "Physical Mechanisms Controlling the Pre-failure Stress-Strain Behavior of Frozen Sand," Doctor of Philosophy, Massachusetts Institute of Technology.

Daniel, D. E. (1983). "Permeability test for unsaturated soil." *Geotechnical Testing Journal*, 6(2), 81-86.

Demond, A. H., and Roberts, P. V. (1991). "Effect of Interfacial Forces on Two-Phase Capillary Pressure-Saturation Relationships." *Water Resources Research*, 27(3), 423-437.

Dullien, F. A. L. (1992). *Porous Media : Fluid Transport and Pore Structure*, Academic Press, San Diego.

Edwards, C. H., and Penney, D. E. (1990). *Calculus and Analytic Geometry*, Prentice Hall, Englewood Cliffs, NJ.

Fisher, R. A. (1926). "On The Capillary Forces In An Ideal Soil." *The Journal of Agricultural Science*, 16, 492-505.

Force, E. A. (1998). "Factors Controlling Pore Pressure Generation During K_0 Consolidation of Laboratory Tests," Master of Science in Civil and Environmental Engineering, Massachusetts Institute of Technology.

Fourie, A. B., Papageorgiou, G., and Blight, G. E. (1995). "The rapid determination of the moisture-retention characteristics of soil." *Geotechnical Testing Journal*, 18(2), 276-285.

Fredlund, D. G. (1996). "The emergence of unsaturated soil mechanics." Fourth Spencer J. Buchanan Lecture, Texas A & M University, College Station, Texas, 39.

Fredlund, D. G., and Rahardjo, H. (1993). "Soil mechanics for unsaturated soils." , 507.

Fredlund, D. G., and Xing, A. (1994). "Equations for the soil-water characteristic curve." *Canadian Geotechnical Journal*, 31, 521-532.

Gardner, R. (1937). "A method of measuring the capillary tension of soil moisture over a wide moisture range." *Soil Science*, 43(4), 277-283.

Gardner, W. R. (1958). "Some steady state solutions of the unsaturated moisture flow equation with application to evaporation from a water table." *Soil Science*, 85(4), 228-232.

Gonzalez, J. (2000). "Experimental and Theoretical Ivestigation of Constant Rate of Strain Consolidation," Master of Science in Civil and Environmental Engineering, Massachusetts Institute of Technology.

Guan, Y., and Fredlund, D. G. (1997). "Use of the tensile strength of water for the direct measurement of high soil suction." *Canadian Geotechnical Journal*, 34(4), 604-614.

Gvirtzman, H., and Roberts, P. V. (1991). "Pore Scale Spacial Analysis of Two Immiscible Fluids in Porous Media." *Water Resources Research*, 27(6), 1165-1176.

Haines, W. B. (1925). "Studies in the Physical Properties of Soils." *Journal of Agricultural Science*, 15, 529-535.

Haines, W. B. (1927). "A further contribution to the theory of capillary phenomena in soils." *The Journal of Agricultural Science*, 17, 264-290.

Henderson, S. J., and Speedy, R. J. (1980). "A Berthelot-Bourdon tube method for studying water under tension." *Journal of Physics e - Scientific Instruments*, 13(no.7), 778-82.

Henderson, S. J., and Speedy, R. J. (1987). "Temperature maximum density in water at negative pressure." *Journal of Physical Chemistry*, 91(11), 3062-8.

Hilf, J. W. (1956). "An investigation of pore-water pressure in compacted cohesive soils." *654*, United States Department of the Interior.

Holden, J. C., and Truong, H. V. P. "Soil suction in embankments of expansive clay." *1st International Conference on Unsaturated Soils*, Paris, France, 609-614.

Houston, S. L., Houston, W. L., and Wagner, A. M. (1994). "Laboratory Filter Paper Suction Measurements." *Geotechnical Testing Journal*, 17(2), 185-194.

Jonasson, S. A. (1991). "Estimation of soil water retention for natural sediments from grain size distribution and bulk density," PhD, Chalmers University of Technology and University of Gotenborg.

Jones, W. M., Overton, G. D. N., and Trevena, D. H. (1981). "Tensile Strength Experiments With Water Using a New Type of Berthelot Tube." *Journal of Physics D-Applied Physics*, 14(7), 1283-1291.

Kaye, G. W. C., and Laby, T. H. (1973). *Tables of Physical and Chemical Constants*, Longman.

Kim, M., and Change, S. (1979). "Effect of the curvature dependency of surface tension on pendular ring condensation calculations." *Journal of Colloid & Interface Science*, 69(no.1), 34-44.

Krahn, J., and Fredlund, D. G. (1972). "On Total Matric and Osmotic Suction." *Journal of Soil Science*, 114(5), 339-348.

Lambe, T. W., and Whitman, R. V. (1969). *Soil Mechanics*, John Wiley & Sons, New York.

Lang, A. R. G. (1967). "Osmotic coefficients and water potentials of sodium chloride solutions from 0 to 40 degrees C." *Australian Journal of Chemistry*, 20, 2017-2023.

Leong, E. C., and Rahardjo, H. (1997). "Review of soil-water characteristic curve equations." *Journal of Geotechnical and Geoenvironmental Engineering*, 123(12), 1106-1117.

Levine, S., and Neale, G. H. (1974). "Theory of the rate of wetting of a porous medium." *Journal of the Chemical Society. Faraday transactions II*, 71, 12-21.

Levine, S., Reed, P., Shutts, G., and Neale, G. (1977). "Some aspects of wetting/dewetting of a porous medium." *Powder Technology*, 17, 163-181.

Lian, G., Thornton, C., and Adams, M. J. (1993). "A Theoretical Study of the Liquid Bridge Forces between Two Rigid Spherical Bodies." *Journal of Colloid and Interface Science*, 161, 138-147.

Manheim, F. T. (1966). "A Hydraulic Squeezer for Obtaining Interstitial Water from Consolidated and Unconsolidated Sediments." *550-e*, United States Geological Survey.

Mao, Z.-S., Xiong, T.-Y., and Chen, J.-Y. (1993). "Theoretical Predictions of static liquid holdup in trickle bed reactors and comparison with experimental results." *Chemical Engineering Science*, 48(15), 2697-2703.

Mao, Z.-S., Xiong, T.-Y., Wang, R., and Chen, J.-Y. (1994). "Note on the thermodynamic stability of pendular rings between solid particles." *Chemical Engineering Science*, 49(20), 3519-3521.

Marmur, A. (1992). "Penetration and displacement in capillary systems." Modern Approaches to Wettability: Theory and Applications, M. E. Schrader and G. I. Loeb, eds., Plenum Press, New York, 327-358.

Marshall, T. J., Holmes, J. W., and Rose, C. W. (1996). *Soil Physics*, Cambridge University Press, New York.

Mason, G. (1972). "Desaturation of porous media. I. Unconsolidated materials." *Journal of Colloid & Interface Science*, 41(2), 208-27.

Mayer, A. S., and Miller, C. T. (1992). "The influence of porous medium characteristics and measurement scale on pore-scale distributions of residual nonaqueous-phase liquids." *Journal of Contaminant Hydrology*, 11, 189-213.

Morrow, N. R. (1970). "Irreducible wetting-phase saturations in porous media." *Chemical Engineering Science*, 25(11), 1799-1815.

Oberg, A.-L. (1997). "Matrix Suction in Silt and Sand Slopes," Doctor of Philosophy, Chalmers University of Technology.

Ohde, Y., Hiro, K., Ouchi, T., Takeshita, T., and Hayasi, N. (1991). "Pre- and post-treatment conditioning approach for a metal Berthelot tube system." *Journal of Physics D-Applied Physics*, 24(6), 859-864.

Ohde, Y., Ikemizu, M., Okamoto, H., Hosokawa, W., and Ando, T. (1988). "Two-stage increase in negative pressure with repeated cavitation for water in a metal Berthelot tube." *Journal of Physics D-Applied Physics*, 21(10), 1540-1542.

Ohde, Y., Ikemizu, M., Okamoto, H., Yokoyama, T., and Shibata, S. (1989). "Cavitation history effect of a water-metal Berthelot tube system interpreted by an elaborated gas-trapping crevice model." *Journal of Physics D-Applied Physics*, 22(11), 1721-1727.

Ohde, Y., Wantanabe, H., Hiro, K., Motoshita, K., and Tanzawa, Y. (1993). "Raising of negative pressure to around -200 bar for some organic liquids in a metal berthelot tube." *Journal of Physics D-Applied Physics*, 26(8), 1188-1191.

Olson, R. E., and Langfelder, L. J. (1965). "Pore water pressure in unsaturated soils." *Journal of the Soil Mechanics and Foundations Division, Proceedings of the American Society of Civil Engineers*, 91(SM4), 127-150.

Petrucci, R. H. (1989). *General Chemistry: Principles and Modern Applications*, Macmillan Publishing Company, New York.

Rassam, D. W., and Williams, D. J. (2000). "A Dynamic Method for Determining the Soil Water Characteristic Curve for Coarse-Grained Soils." *Geotechnical Testing Journal*, 23(1), 67-71.

Richards, B. G., and Peter, P. (1987). "Measurement of negative pore pressures or soil water suction." Lecture, Geotechnical Instrumentation, Australian Geomechanics Society, Melbourne, Australia.

Richards, L. A., and Gardner, W. (1936). "Tensiometers for measuring the capillary tension of soil water." *Journal of the American Society of Agronomy*, 28, 352-358.

Richards, L. A., and Ogata, G. (1958). "A thermocouple for vapour pressure measurement in biological and soil systems at high humidity." *Science*, 128, 1089-1090.

Ridley, A. M., and Burland, J. B. (1993). "A new instrument for the measurement of soil moisture suction." *Geotechnique*, 43(2), 321-324.

Ridley, A. M., and Burland, J. B. (1995). "Measurement of suction in materials which swell." *Applied Mechanics Reviews*, 48(9), 727-732.

Ridley, A. M., and Wray, W. K. "Suction Measurement: A review of current theory and practices." *1st Internation Conference on Unsaturated Soils*, Paris, France, 1293-1322.

Soil Moisture Equipment Corp. (1995). "Soil Moisture Catalog." , Soil Moisture Equipment Corp, Santa Barbara, CA.

Spanner, D. C. (1951). "The peltier effect and it's use in the measurement of suction pressure." *Journal of Experimental Botany*, 11, 145-168.

Stannard, D. I. (1992). "Tensiometers - Theory, Construction, and Use." *Geotechnical Testing Journal*, 15(1), 48-58.

Tabor, D. (1979). *Gases, liquids, and solids*, Cambridge University Press, New York.

Taylor, D. W. (1965). *Fundamentals of Soil Mechanics*, John Wiley & Sons, New York.

Trevena, D. H. (1987). *Cavitation and tension in liquids*, IOP Publishing Ltd, Philadelphia.

Truong, H. V. P., and Holden, J. C. "Soil suction measurement with transistor psychrometer." *1st International Conference on Unsaturated Soils*, Paris, France, 659-665.

Turner, G. A., and Hewitt, G. F. (1959). "The amount of liquid held at the point of contact of spheres and the static liquid holdup in packed beds." *Transactions of the Institution of Chemical Engineers*, 37, 329-334.

van Brakel, J., and Heertjes, P. M. (1977). "Capillary rise in porous media. Part I: A problem." *Powder Technology*, 16, 75-81.

van Genuchten, M. T. (1980). "A closed-form equation for predicting the hydraulic conductivity of unsaturated soils." *Soil Science Society of America Journal*, 44, 892-898.

White, N. F., Sunada, D. K., Duke, H. R., and Corey, A. T. (1972). "Boundary effects in desaturation of porous media." *Soil Science*, 113(1), 7-12.

Woodburn, J. A., and Lucas, B. "New approaches to the laboratory and field measurement of soil suction." *1st Conference on Unsaturated Soils*, Paris, France, 667-671.

Yanagisawa, K., Ioku, K., and Yamasaki, N. (1994). "Pore size control of porous silica ceramics by hydrothermal hot-pressing." *Journal of the Ceramic Society of Japan, International Edition*, 102, 968-973.

Appendix A Computer Data Acquisition Code

```
DECLARE SUB SetUpDataFile ()
DECLARE SUB Plotter ()
DECLARE SUB WriteToFile ()
DECLARE SUB ConvertData ()
DECLARE SUB GetVoltage ()
DECLARE SUB PrintEngData ()
DECLARE SUB Pause ()
DECLARE SUB Zeroes ()
DECLARE SUB SetUpScreen ()
DECLARE SUB SetUpDAQ ()
DECLARE SUB IntroScreen ()
DECLARE SUB PrintMask (Row!, Column!, Number!, Places!)
DECLARE SUB CenterText (Column!, Text$)
DECLARE SUB PrintLabels (Row!, Column!, Text$)
DECLARE FUNCTION Voltage! (Channel!, Gain!, BaseAddress!, Boolean!)
DECLARE FUNCTION ConvertDate! (CurrentDate$, CurrentTime$)
DECLARE FUNCTION GetMass! ()


DIM SHARED AD1170
DIM SHARED AD11702
DIM SHARED MultiPlex
DIM SHARED MultiPlex2
DIM SHARED IntTime
DIM SHARED IntBit
DIM SHARED DAQFileName$
DIM SHARED PorePressChannel
DIM SHARED VoltageInChannel
DIM SHARED ReferenceChannel
DIM SHARED PorePressCalibration
```

```
DIM SHARED PorePressZero
DIM SHARED OldY
DIM SHARED OldX
DIM SHARED VinChannel
DIM SHARED GrndChannel
DIM SHARED PorePress
DIM SHARED PorePressVoltage
DIM SHARED VoltageIn
DIM SHARED counter
DIM SHARED ExecutionNumber
DIM SHARED InitialTime
DIM SHARED DAQTime
DIM SHARED DeltaTime
DIM SHARED StartTime$
DIM SHARED StartDate$
DIM SHARED Mass
DIM SHARED TimeInterval
DIM SHARED TempTime
DIM SHARED StartTime

CLS

IntroScreen
'SetUpDAQ
Zeroes
SetUpDataFile
Pause
SetUpScreen
'InitialTime = ConvertDate(DATE$, TIME$)
'TempTime = InitialTime
```

```
RANDOMIZE TIMER
StartTime = TIMER
TempTime = TIMER - StartTime

        DO

            GetVoltage
            Mass = GetMass
            ConvertData
            PrintEngData
            WriteToFile
            'Plotter

        LOOP WHILE INKEY$ <> CHR$(27)


SUB CenterText (Column, Text$)
    length = LEN(LTRIM$(RTRIM$(Text$)))
    start = (80 - length) / 2
    PrintLabels Column, start, Text$
END SUB


SUB ConvertData
PorePress = 1'(PorePressVoltage / VoltageIn - PorePressZero) * PorePressCalibration
'DeltaTime = DAQTime - InitialTime
END SUB
```

```
FUNCTION ConvertDate (CurrentDate$, CurrentTime$)
    Hour = VAL(CurrentTime$)
    Minutes = VAL(MID$(CurrentTime$, 4, 2))
    Seconds = VAL(RIGHT$(CurrentTime$, 2))
    TimeinDays = (Hour + Minutes / 60 + Seconds / 3600) / 24

    Month = VAL(CurrentDate$)
    Day = VAL(MID$(CurrentDate$, 4, 2))

    SELECT CASE Month
        CASE IS = 1
            DaystoDate = 0
        CASE IS = 2
            DaystoDate = 31
        CASE IS = 3
            DaystoDate = 59
        CASE IS = 4
            DaystoDate = 90
        CASE IS = 5
            DaystoDate = 120
        CASE IS = 6
            DaystoDate = 151
        CASE IS = 7
            DaystoDate = 181
        CASE IS = 8
            DaystoDate = 212
        CASE IS = 9
            DaystoDate = 243
        CASE IS = 10
            DaystoDate = 273
        CASE IS = 11
```

```
            DaystoDate = 304
        CASE IS = 12
            DaystoDate = 334
        END SELECT

        TotalDays = DaystoDate + (Day - 1)

        ConvertDate = TotalDays + TimeinDays
END FUNCTION


FUNCTION GetMass
OPEN "COM1:2400,E,7,1,ASC,CS,CD,DS,RS,LF" FOR RANDOM AS #1

  DO
    IF NOT EOF(1) THEN
        ' LOC(1) gives the number of characters waiting
        ScaleInput$ = INPUT$(LOC(1), #1)
        ScaleWord$ = ScaleWord$ + ScaleInput$
    END IF
  LOOP WHILE ScaleInput$ <> CHR$(10)  'Checks for the terminal LineFeed

  ScaleNumber = VAL(LTRIM$(MID$(ScaleWord$, 6, 7))) 'Extracts the Numeric Data

CLOSE #1

GetMass = ScaleNumber
END FUNCTION


SUB GetVoltage
```

```
PorePressVoltage = 1'Voltage(PorePressChannel, 1, AD1170, 0)
VoltageIn = 5.3 'Voltage(VoltageInChannel, 1, AD11702, 1)

PrintLabels 24, 1, STRING$(80, " ")

PrintMask 24, 9, PorePressVoltage, 5
PrintMask 24, 66, VoltageIn, 3

DAQTime = TIMER - StartTime'ConvertDate(DATE$, TIME$)
END SUB


SUB IntroScreen
    CLS
    CenterText 10, "Soil-Moisture Program"
    CenterText 11, "Version 1.0 - 7/3/97"
    CenterText 12, "Written by Kurt Sjoblom"
END SUB


SUB Pause
CenterText 24, "Press any key to continue..."
DO
LOOP UNTIL INKEY$ <> ""
END SUB


SUB Plotter
        'Graph #1 Suction-time
        NewY = -(110 * PorePress / (16))
```

```
        NewX = DAQTime / 3600 / 4 * 225
        LINE (OldX, OldY)-(NewX, NewY)
        OldX = NewX
        OldY = NewY
END SUB


SUB PrintEngData
PrintMask 5, 27, PorePress, 3
PrintMask 5, 55, Mass, 2
PrintMask 9, 65, DAQTime / 3600, 2
PrintLabels 10, 68, TIME$
' loops
counter = counter + 1

IF counter = 10 THEN
    PrintLabels 11, 9, STRING$(8, " ")
    PrintLabels 11, 28, STRING$(8, " ")
    PrintMask 10 + counter, 9, PorePress, 2
    PrintMask 10 + counter, 28, Mass, 2
    counter = 0
ELSE

    PrintMask 10 + counter, 9, PorePress, 2
    PrintMask 10 + counter, 28, Mass, 2

    PrintLabels 11 + counter, 9, STRING$(8, " ")
    PrintLabels 11 + counter, 28, STRING$(8, " ")

END IF
END SUB
```

```
SUB PrintLabels (Row, Column, Text$)
    LOCATE Row, Column
    PRINT Text$;
END SUB


SUB PrintMask (Row, Column, Number, Places)
    Mask$ = "####."
    FOR i = 1 TO Places
    Mask$ = Mask$ + LTRIM$("#")
    NEXT i

    LOCATE Row, Column

    PRINT USING Mask$; Number;
END SUB


SUB SetUpDataFile
    OPEN DAQFileName$ FOR OUTPUT AS #1
    PRINT #1, "'Soil - Moisture Program'"
    PRINT #1, "'Written by Kurt Sjoblom'"
    PRINT #1, "'Version 1.10, 3/24/98'"
    PRINT #1, DATE$, TIME$
    PRINT #1, "'Seconds'", "'Pore Voltage'", "'Voltage In'", "'Mass'"
    PRINT #1,
    CLOSE #1
END SUB
```

```
SUB SetUpDAQ
    'rountine to setup data aquisition card
    'routine to be run once
    ' 768 = decimal I/O address of AD1170 A/D converter
    ' 776(old), 772(new) = decimal I/O address of multiplexer channel selector
    ' 15 = multiplexer connection to ground
    '
    'StrawberryTree = 6928
    'Switch = StrawberryTree + 4

    MultiPlex = 776
    AD1170 = 768


    IntTime = 22                '300 msec integration time of A/D converter
    IntBit = 15                 'bit precision
    OUT AD1170, 70: WAIT AD1170, 1, 1  'set default calibration time
    OUT AD1170 + 1, IntBit          'load data format into 2nd byte
    OUT AD1170, 48: WAIT AD1170, 1, 1  'lock in the loaded data format
    OUT AD1170, 176: WAIT AD1170, 1, 1 'begin background calibration
    'OUT Switch, 1                 'Open relay to control box

   ' MultiPlex2 = 1796
   ' AD11702 = 1792

   ' IntTime = 22                '300 msec integration time of A/D converter
   ' IntBit = 15                 'bit precision
   ' OUT AD11702, 70: WAIT AD11702, 1, 1  'set default calibration time
   ' OUT AD11702 + 1, IntBit          'load data format into 2nd byte
   ' OUT AD11702, 48: WAIT AD11702, 1, 1  'lock in the loaded data format
```

```
    ' OUT AD11702, 176: WAIT AD11702, 1, 1 'begin background calibration
END SUB


SUB SetUpScreen
'SCREEN 10 '640x350 graphics
CLS

PrintLabels 3, 8, "          Current Suction        Current Mass"
PrintLabels 4, 8, "          ---------------        ------------"

PrintLabels 9, 8, "Pore Pressure       Mass"
PrintLabels 10, 8, "-------------       ------"
PrintLabels 9, 52, "Elapsed Time:"
PrintLabels 9, 73, "hrs"
'Graph#1-Suction-Time Curve

'VIEW (375, 150)-(600, 260)      'view port of graph
'LINE (0, 0)-(225, 110), , B     'Border of graph
'FOR j = 1 TO 3
'       x = 225 * (j / 4)
'       LINE (x, 110)-(x, 105)  'x ticks
'       LINE (x, 0)-(x, 5)
'NEXT j
'FOR j = 1 TO 7
'       y = 110 * (j / 8)
'       LINE (0, y)-(5, y)    'y ticks
'       LINE (225, y)-(220, y)
'NEXT j

'y axis labels
```

```
'PrintLabels 11, 44, "0"
'PrintLabels 15, 44, "-8"
'PrintLabels 19, 44, "-16"

'x axis labels
'PrintLabels 20, 47, "0"
'PrintLabels 20, 62, "2"
'PrintLabels 20, 76, "4"
END SUB


FUNCTION Voltage (Channel, Gain, BaseAddress, Boolean)
'IF Channel = VoltageInChannel THEN
IF Boolean = 1 THEN
'Get OffSetVoltage

    OUT BaseAddress + 4, ReferenceChannel'Point Mux to Reference Channel
    OUT BaseAddress, IntTime: WAIT BaseAddress, 1, 1  'Take a reading and wait

'Convert this data into the OffSetVoltage

LowByte = INP(BaseAddress + 1)
MidByte = INP(BaseAddress + 2)
HiByte = INP(BaseAddress + 3)
Counts = LowByte + 256 * MidByte + 65536 * HiByte
OffSetVoltage = (Counts * 10 / 2 ^ (IntBit + 7) - 5)

'Get Vin Voltage Using the Null feature of the AD1170
    OUT BaseAddress, 112: WAIT BaseAddress, 1, 1     'Null command
    OUT BaseAddress, 120: WAIT BaseAddress, 1, 1     'Null Enable command
    OUT BaseAddress + 4, Channel            'Point Mux to Vin Channel
```

```
    OUT BaseAddress, IntTime: WAIT BaseAddress, 1, 1 'Take a reading
    OUT BaseAddress, 128: WAIT BaseAddress, 1, 1     'Disable the Null feature
ELSE
    OUT BaseAddress + 8, Channel              'Take regular readings
    OUT BaseAddress, IntTime: WAIT BaseAddress, 1, 1
END IF

'IF Channel = VoltageInChannel THEN
IF Boolean = 1 THEN
'Convert to voltage
LowByte = INP(BaseAddress + 1)
MidByte = INP(BaseAddress + 2)
HiByte = INP(BaseAddress + 3)
Counts = LowByte + 256 * MidByte + 65536 * HiByte
OUT BaseAddress, 176: WAIT BaseAddress, 1, 1      'reenable background calibration
TempVoltage = (Counts * 10 / 2 ^ (IntBit + 7) - 5)

    TempVoltage = OffSetVoltage + TempVoltage
ELSE

'Convert to voltage
LowByte = INP(BaseAddress + 1)
MidByte = INP(BaseAddress + 2)
HiByte = INP(BaseAddress + 3)
Counts = LowByte + 256 * MidByte + 65536 * HiByte
OUT BaseAddress, 176: WAIT BaseAddress, 1, 1      'reenable background calibration
TempVoltage = (Counts * 10 / 2 ^ (IntBit + 7) - 5)

END IF

Voltage = TempVoltage / Gain
```

```
END FUNCTION


SUB WriteToFile
    'Temp = (DeltaTime * 86400) - INT(DeltaTime * 86400 / TimeInterval) *
TimeInterval
     'IF Temp < 3 THEN '3 second delay is needed for DAQ to occur
     IF DAQTime >= TempTime + TimeInterval THEN
         OPEN DAQFileName$ FOR APPEND AS #1
         PRINT #1, DAQTime, PorePressVoltage, VoltageIn, Mass
         CLOSE #1
         TempTime = TempTime + TimeInterval
     END IF
END SUB


SUB Zeroes
     DAQFileName$ = "C:\Suction\smdat78e.dat" 'xx-number of test
     TimeInterval = 60
     PorePressChannel = 3
     VoltageInChannel = 0
     ReferenceChannel = 14

     PorePressCalibration = -700.97615#'bar/v/v
     PorePressZero = .03765 / 5.3

     'OldY = 110
END SUB
```

Appendix B Drying Test Procedure

The following is a step by step procedure that was used to determine the drying curve for the materials presented in this thesis.

Saturation Procedure

1. To prepare the Tensiometer for saturation, the device was first cleaned with water and blotted dry if needed.
2. The saturation chamber was also blotted dry and the o-rings and o-ring grooves cleaned with a cotton applicator.
3. The Tensiometer was placed into the chamber and secured with the bolts.
4. The valves were arranged on the chamber to allow a vacuum to be applied to the chamber and device.
5. A vacuum was applied to the system for a minimum of twenty minutes. This was usually sufficient to obtain a vacuum of 1-5 Torr.
6. The system was then flooded with de-aired water. During this process, the device was monitored by observing the output Tensiometer on a voltmeter.
7. Once the Tensiometer responded to the introduction of the water, the pressure in the system was raised by turning the analog-analog feedback system on.
8. The elevated pressure was typically left on overnight, however if needed the device could be removed after several hours.
9. After the determined amount of pressurization, the pressure was removed by turning the analog-analog feedback system off and starting the manual tachometer. The rate of pressure release was set to approximately 1 bar/minute.
10. The device was then taken from the saturation chamber and prepared for testing.

Drying Test Procedure

1. After completing the saturation of the MIT Tensiometer, the Tensiometer was fitted with the appropriate retaining ring and filled with distilled water.

2. The Tensiometer was then placed into the temperature-controlled chamber and plugged into the Data Acquisition system. The Tensiometer was set into the Lexan® support and placed on top of the balance. The balance was re-zeroed at this point.
3. The Tensiometer was allowed to equilibrate in this system for 8-12 hours (overnight). A Data Acquisition file was started in order to monitor this process. Typically the reading rate at this point was every five minutes.
4. The material being tested was put into a vacuum flask and covered with distilled water. A vacuum was applied to the flask and kept on until all evidence of any entrapped air was removed. The flask was then placed inside the temperature-controlled chamber and allowed to equilibrate to the temperature for at least one hour.
5. After the equilibration process, the material to be tested was placed into the retaining ring. The water in the retaining ring was partially removed to account for the volume of the material.
6. The material was placed to the top of the retaining ring and leveled off with a metal knife.
7. The balance was again re-zeroed.
8. The reading rate of the central data acquisition file was then set to one-minute readings.
9. The local data acquisition was then started and by use of a timer, readings were taken that were coincident with the central file.
10. The tests were monitored frequently throughout the testing time to ensure that the Tensiometer had not lost tension.
11. The test was ended when either the tension was determined to be high enough or if the system lost tension. In either case, the data files were stopped and the Tensiometer was removed from the testing chamber.
12. The material was taken from the retaining ring and a water content determination was made.

Appendix C Literature Data for Correlation

Data from Jonasson (1991)

Table C-1. Percentage finer by mass.

	Sample Number						
Diameter [mm]	16001	16002	16005	16006	16007	16008	16009
0.002	13.9	11.9	3	0	0	18.9	8.5
0.006	17	16.6	3.5	0	0	26.8	12
0.02	25.8	22.8	6.1	0	0	40	20
0.06	53.6	47.7	13.1	4	1	66.3	28
0.2	87.6	92.2	53	35.4	28	78.9	55
0.6	95.9	97.4	94.9	94.4	95	93.7	96
2	100	100	100	100	100	100	100

Table C-2. Volumetric water content.

	Sample Number						
Tension [bar]	16001	16002	16005	16006	16007	16008	16009
0.588	24.2	20.9	14.8	3.4	2.5	23.5	20.5
0.392	27.6	23.3	16.1	3.8	2.6	26.3	21.1
0.196	33.1	28.3	19.1	4.5	3	30.5	22.1
0.098	35.9	32.1	21.8	4.8	3	37.2	26.2
0.078	36.3	34	23.3	4.8	3.2	40.7	27.6
0.054	38.2	37.6	29.8	7	6.6	44.1	31.6
0.029	40	40.1	38.7	22.3	19.4	48.3	44
0.015	41.6	42.4	45	37.9	33.1	50.9	47.8
0.0098	42.9	45.4	45.4	39.5	37.9	51.4	48.2
0.0049	43.9	46.5	46.3	41	39.5	51.9	48.9
0	48.3	48.9	50.5	44.1	42	57.4	52.2

Data from Andersson and Wiklert (1972)

Table C-3. Percent finer and AEP.

	Figure-Number						
Diameter [mm]	8-8	9-10	12-13	14-8	29-6	35-8	48-3
0.6	100	98.99	97.96	100	100	100	98.94
0.2	97	94.95	96.94	100	98.99	100	97.87
0.06	5	31.31	86.73	94.85	97.98	98.98	95.74
0.02	2	4.04	34.69	52.58	93.94	95.92	94.68
0.006	1	2.02	11.22	14.43	65.66	86.73	85.11
0.002	0	0	4.08	7.22	32.32	43.88	70.21
AEP [bar]	0.069	0.059	0.391	0.588	1.47	1.76	5.38

Data from Öberg (1997)

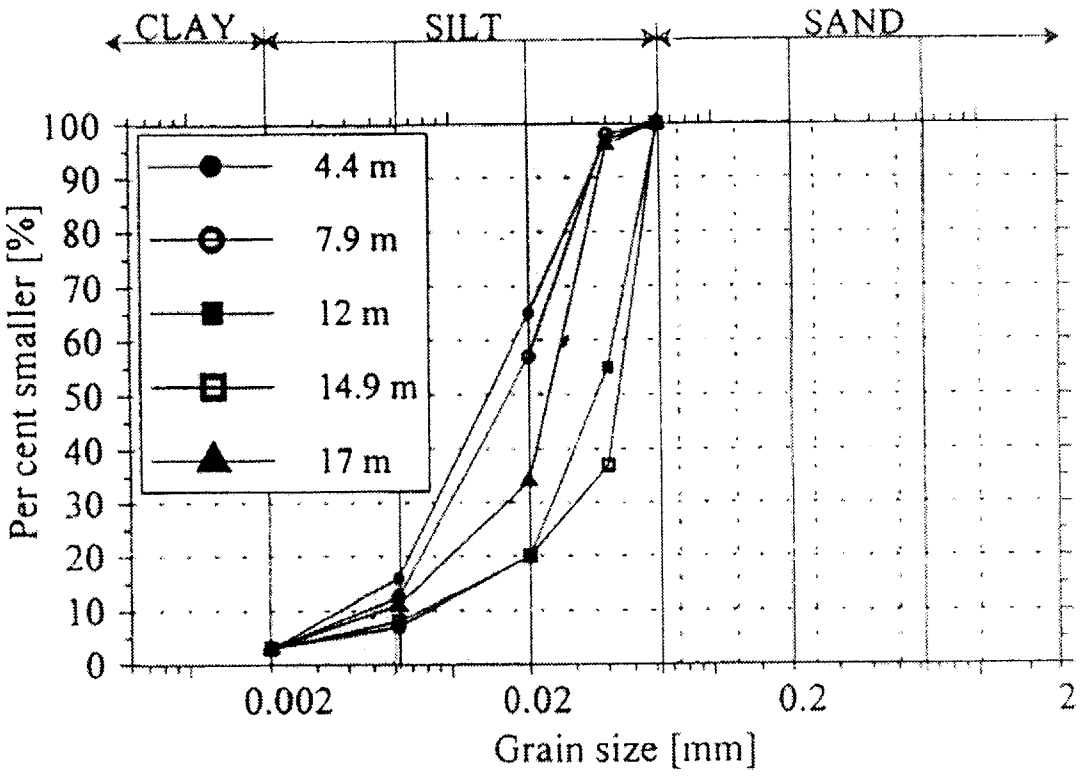

Figure C-1. Grain size from Gagnefs Kyrkby test site.

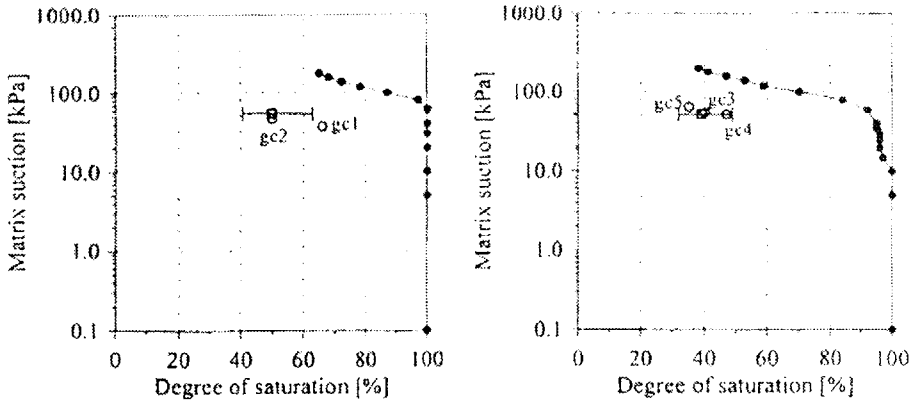

a) Water retention curve 4.4 m

b) Water retention curve 7.9 m

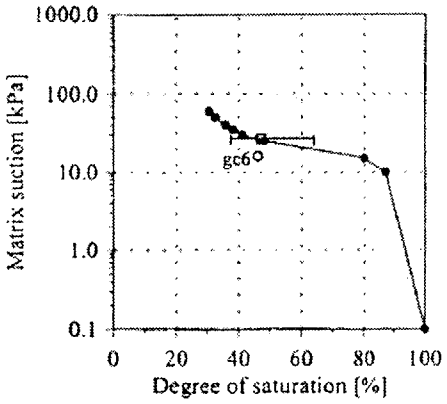

c) Water retention curve 12 m

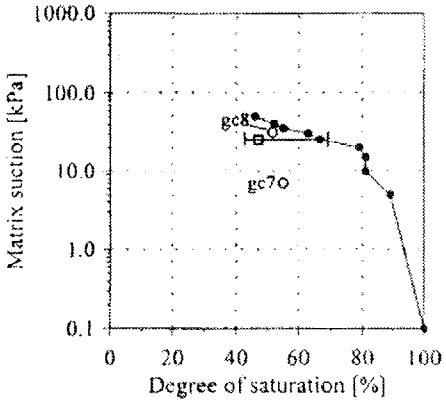

d) Water retention curve 14.9 m

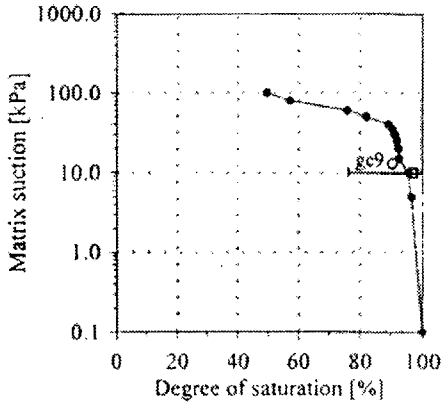

e) Water retention curve 17 m

Figure C-2. Retention curves from Gagnefs Kyrkby test site.

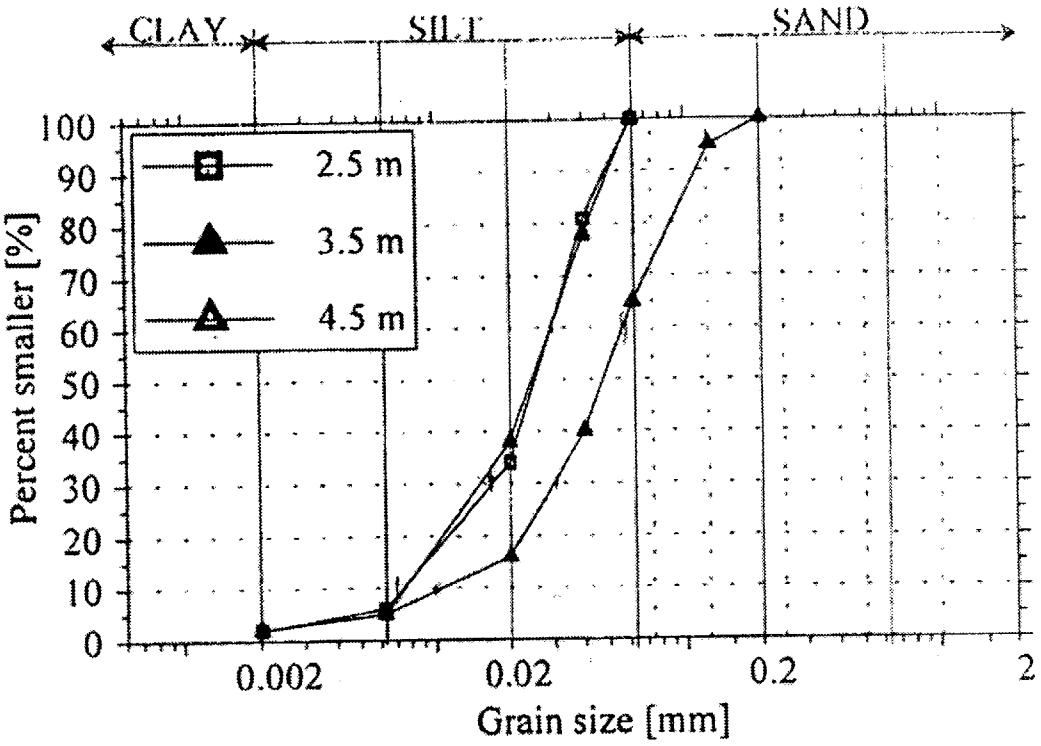

Figure C-3. Grain size for the Ransäter test site.

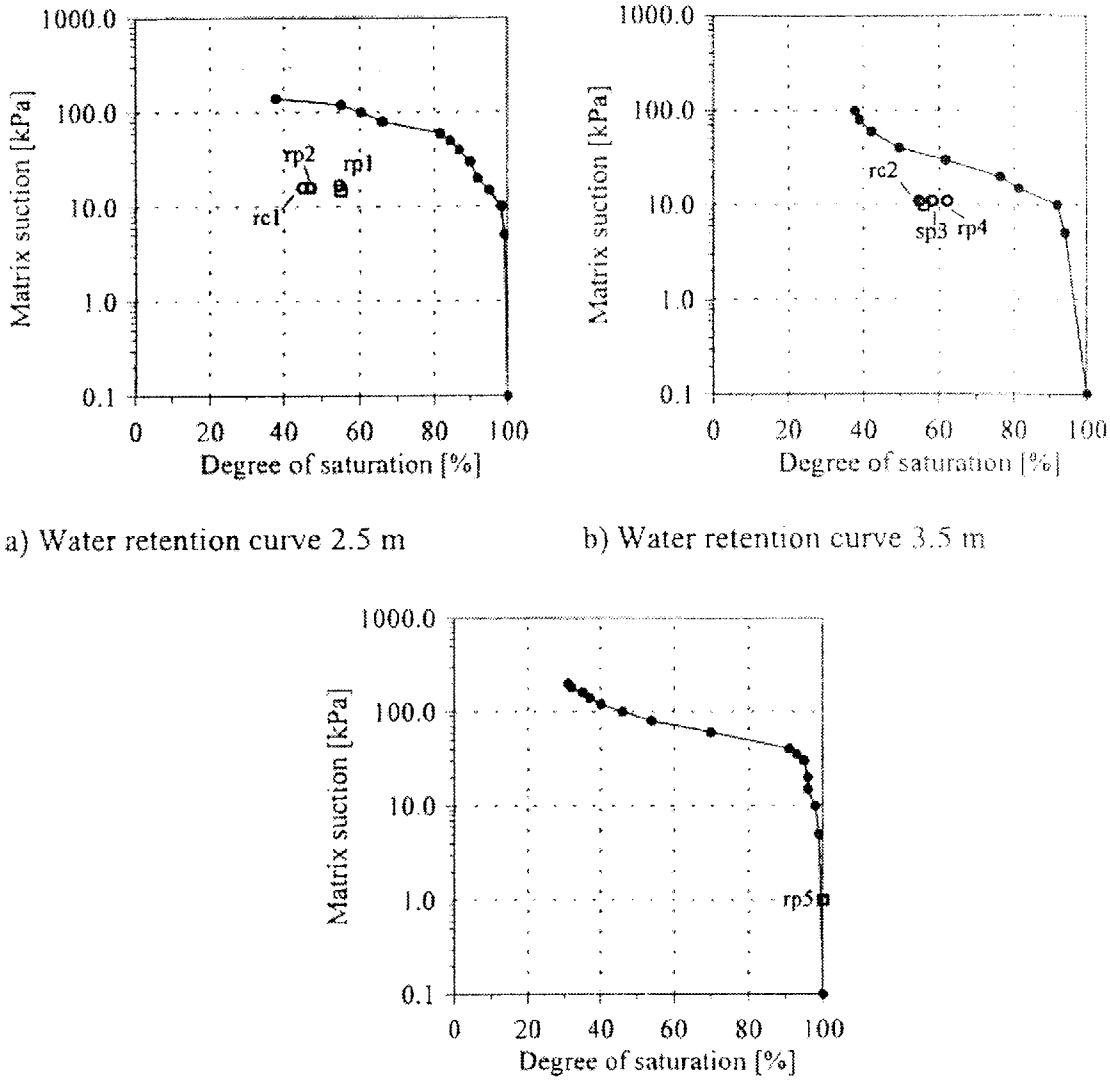

a) Water retention curve 2.5 m

b) Water retention curve 3.5 m

c) Water retention curve 4.5 m

Figure C-4. Retention curves for the Ransäter test site.

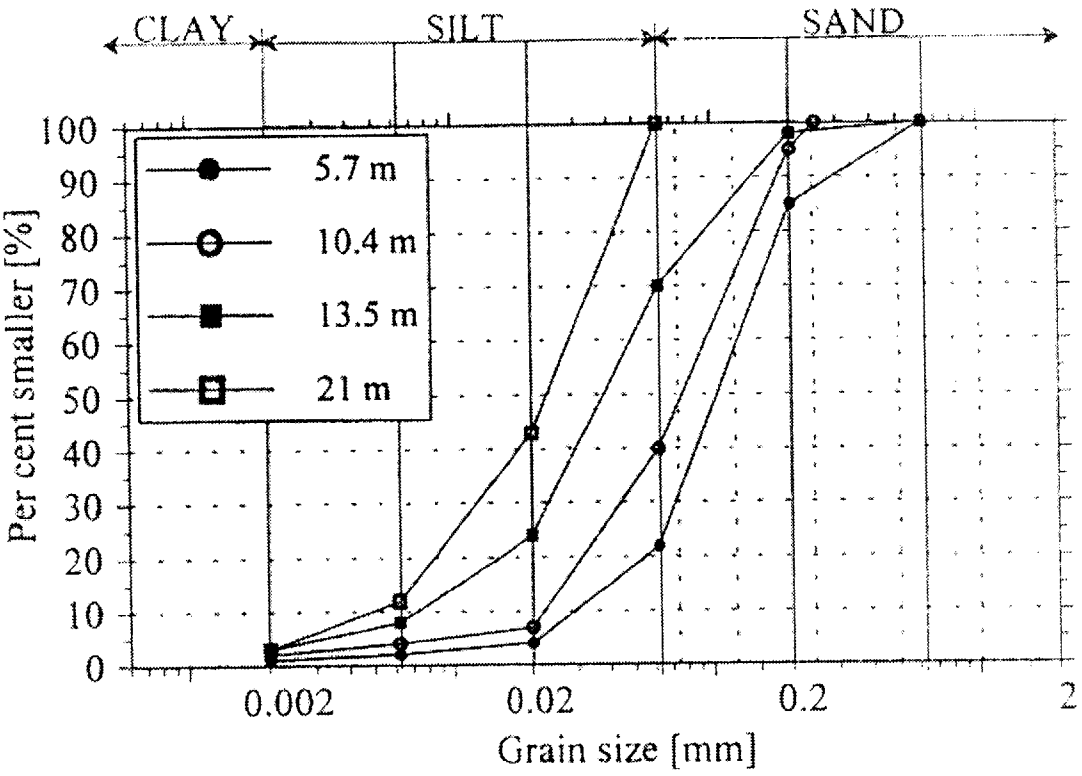

Figure C-5. Grain size for Skedomsravinen test site.

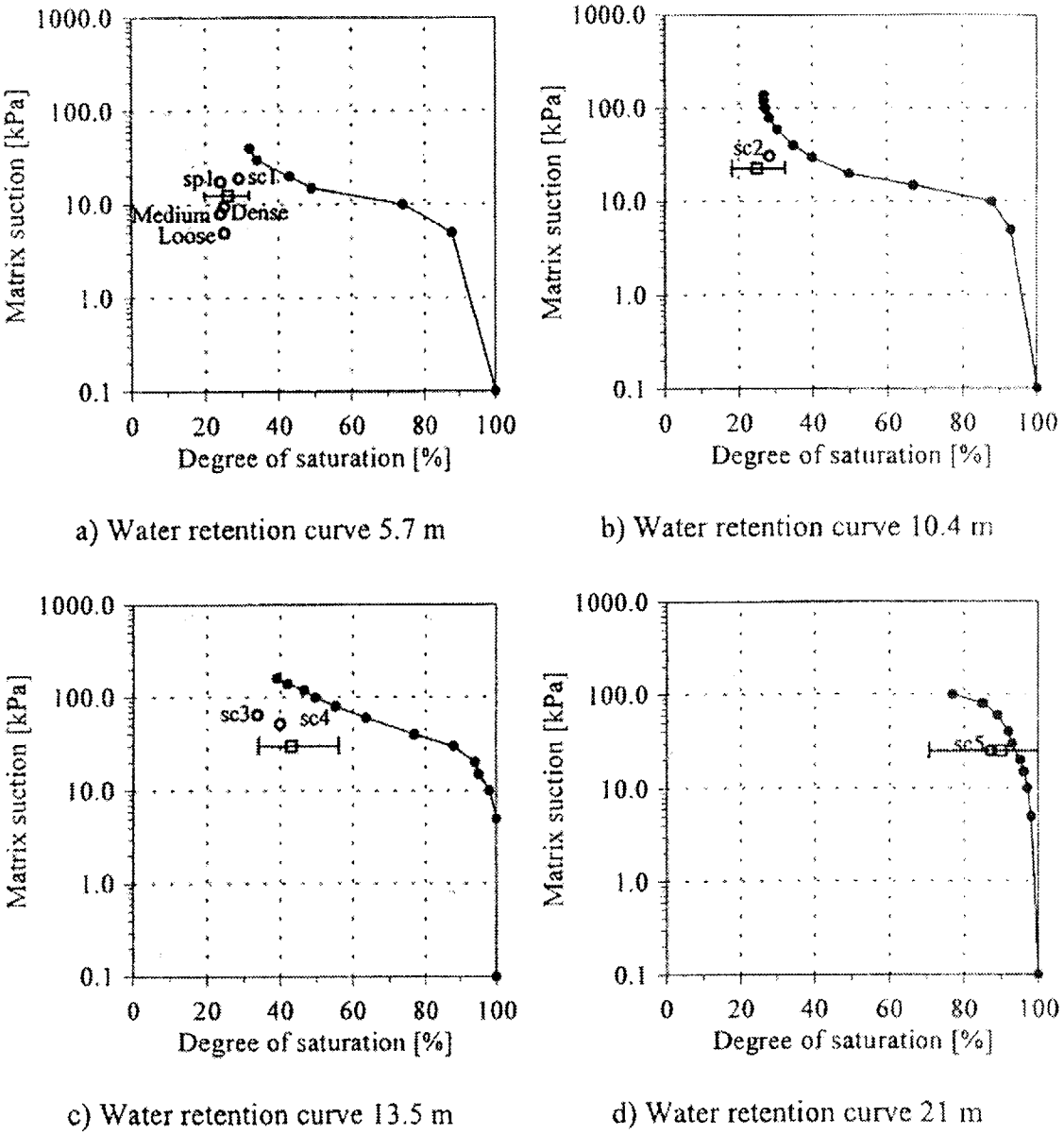

a) Water retention curve 5.7 m

b) Water retention curve 10.4 m

c) Water retention curve 13.5 m

d) Water retention curve 21 m

Figure C-6. Retention curves for the Skedomsravinen test site.

Data from Rassam and Williams (2000)

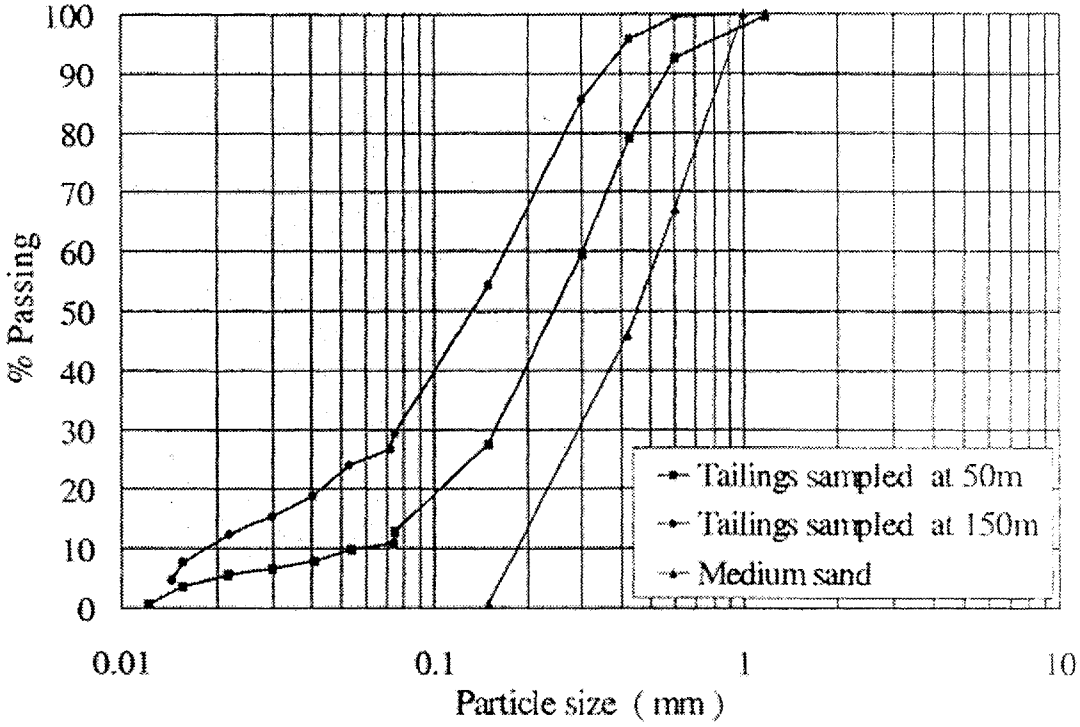

Figure C-7. Grain size for the tailings.

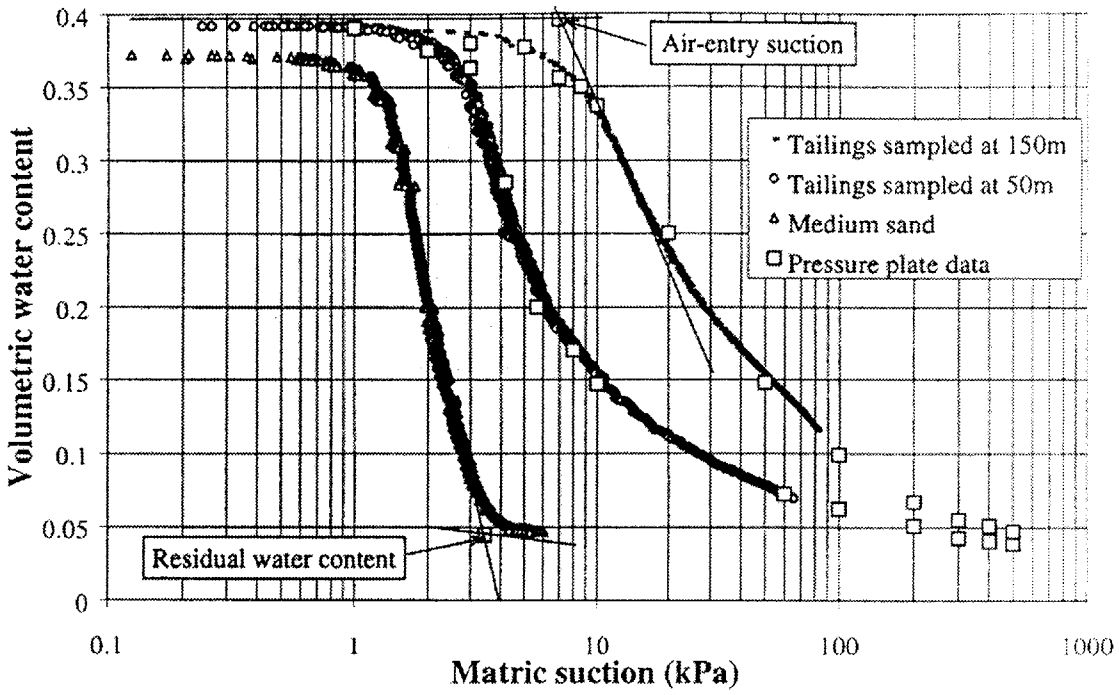

Figure C-8. Retention curves for the tailings.

Appendix D Testing Data for All Tests

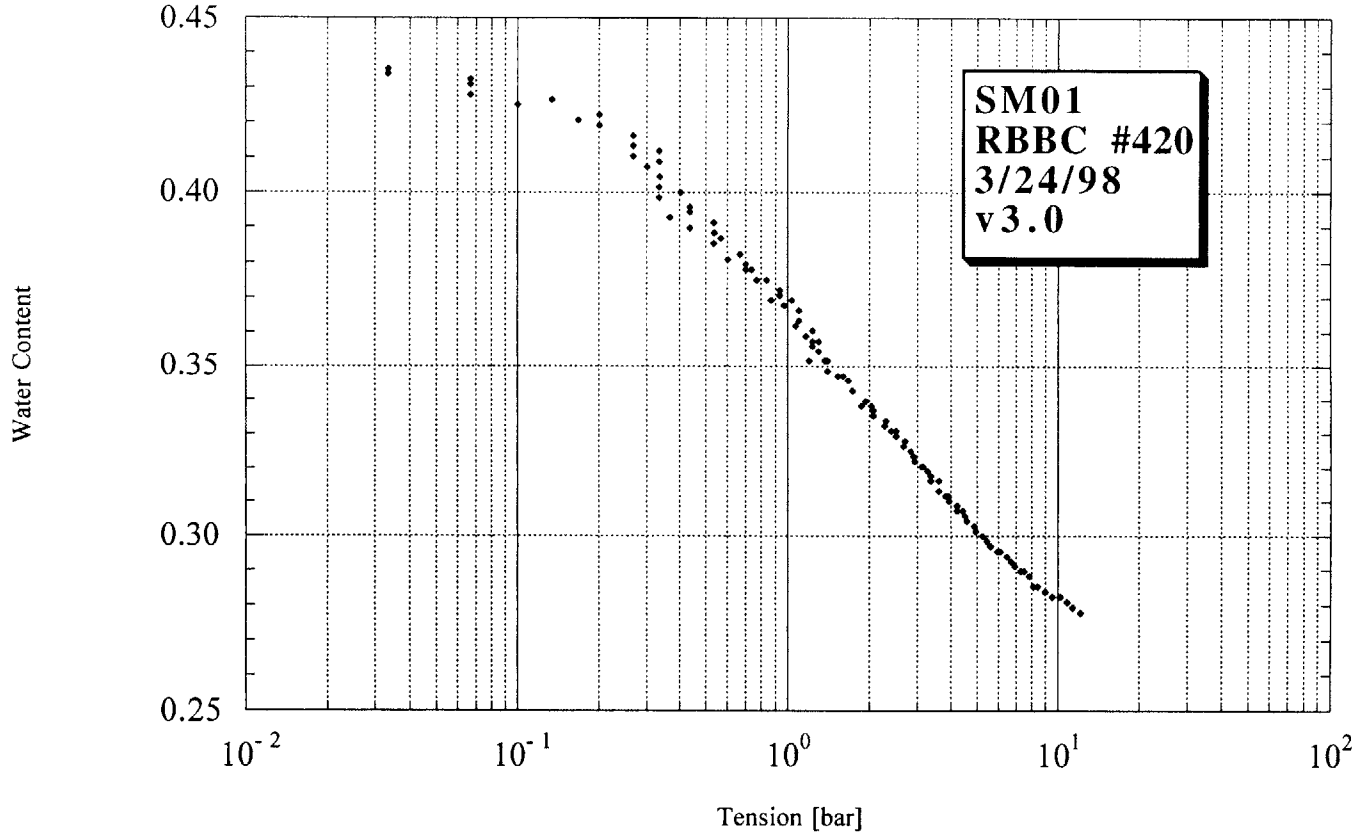

Figure D-1. SM01 testing results.

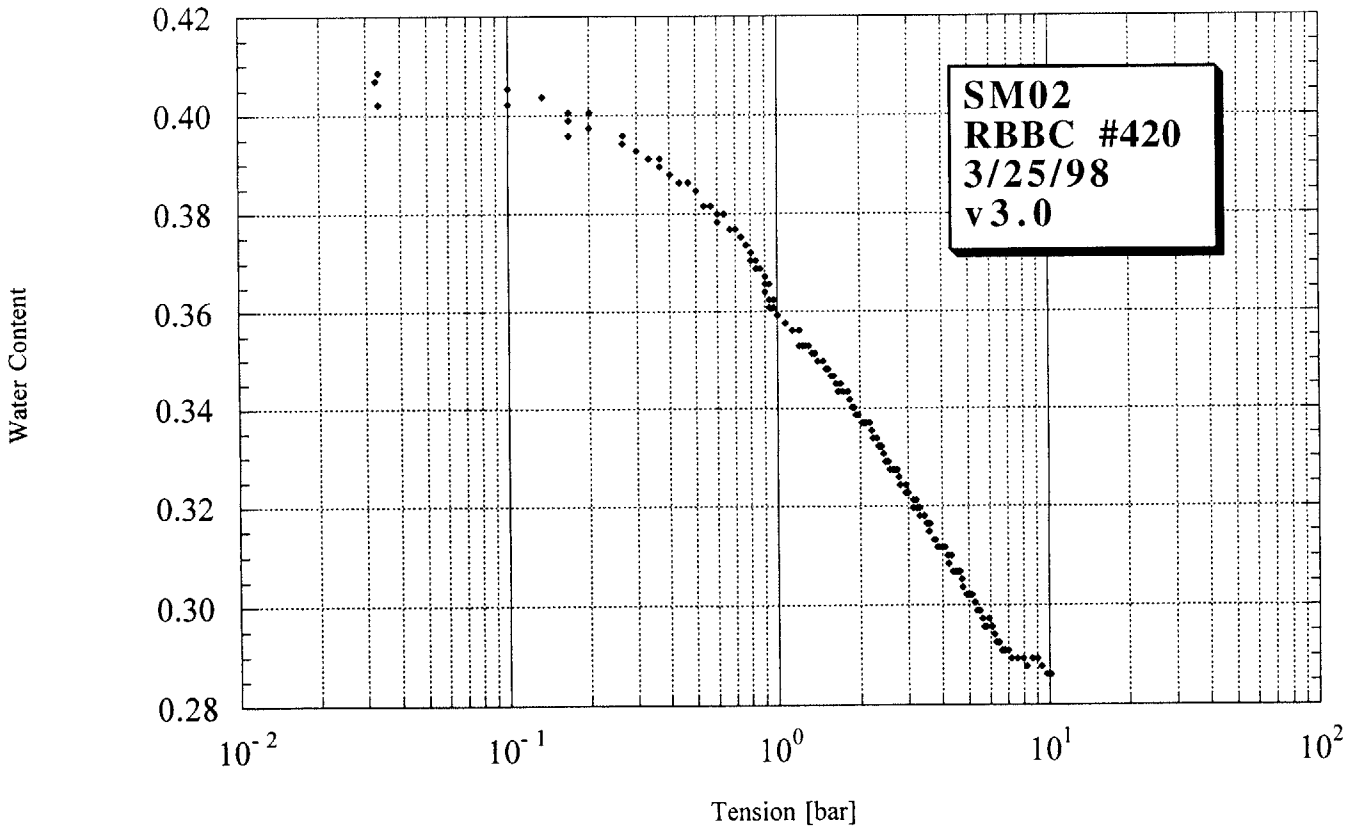

Figure D-2. SM02 testing results.

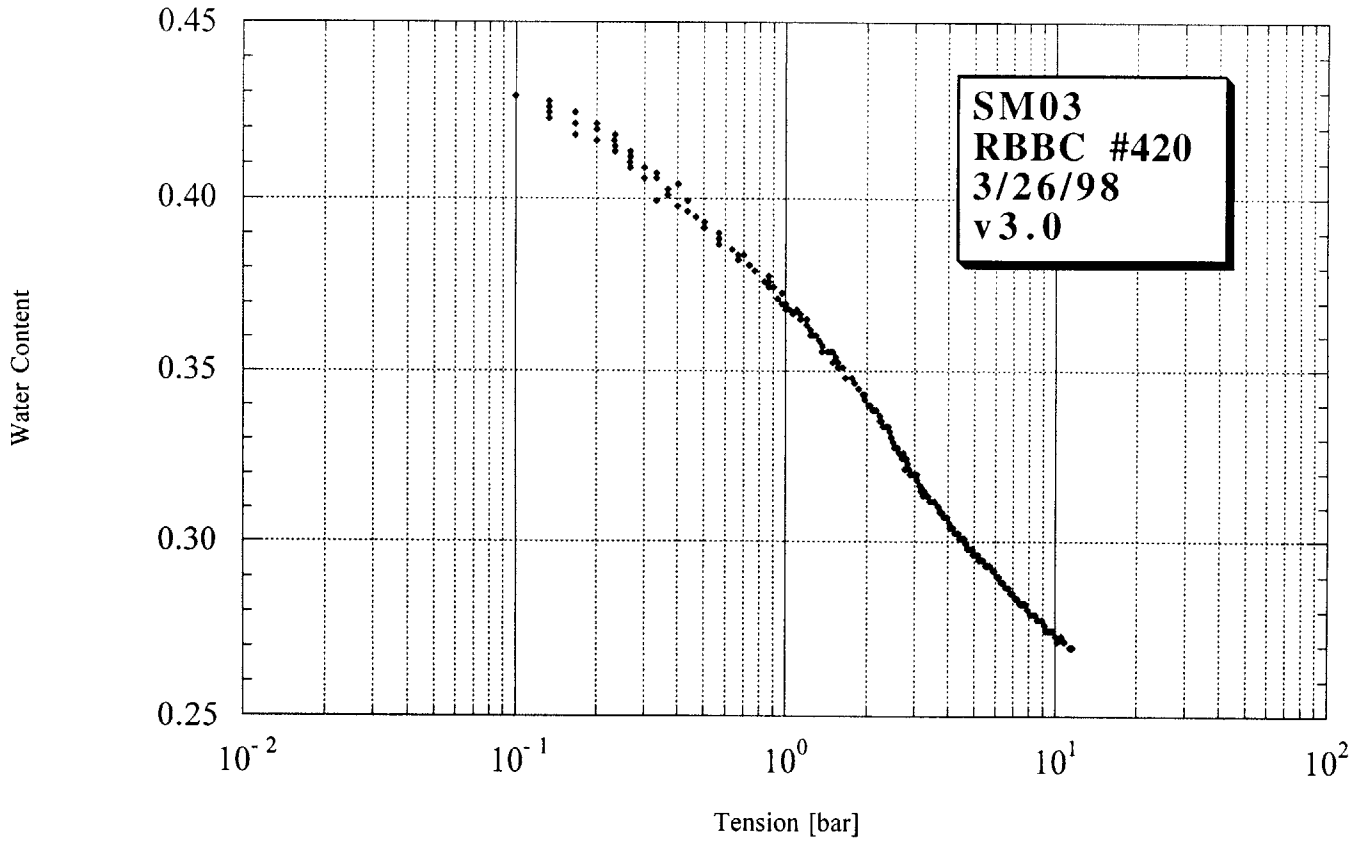

Figure D-3. SM03 testing results.

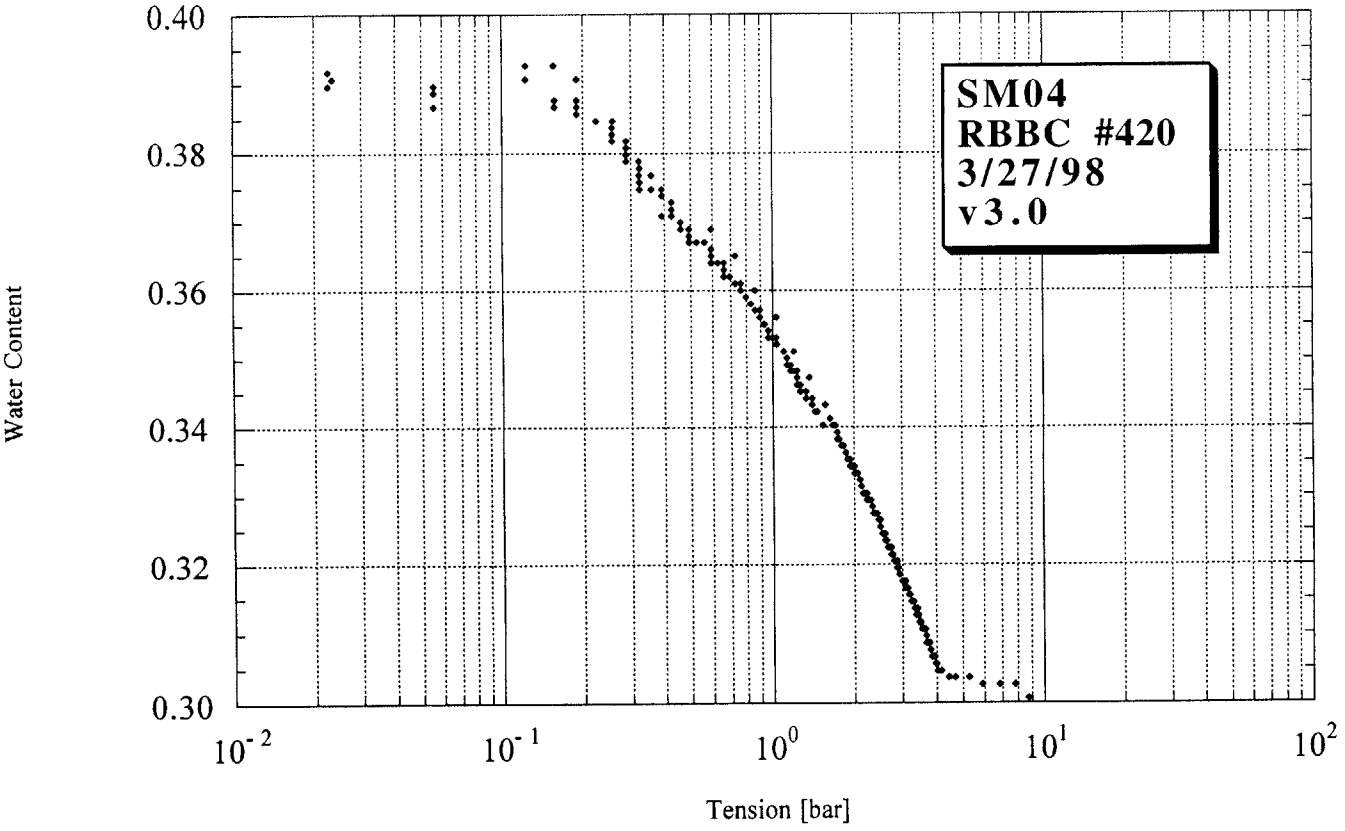

Figure D-4. SM04 testing results.

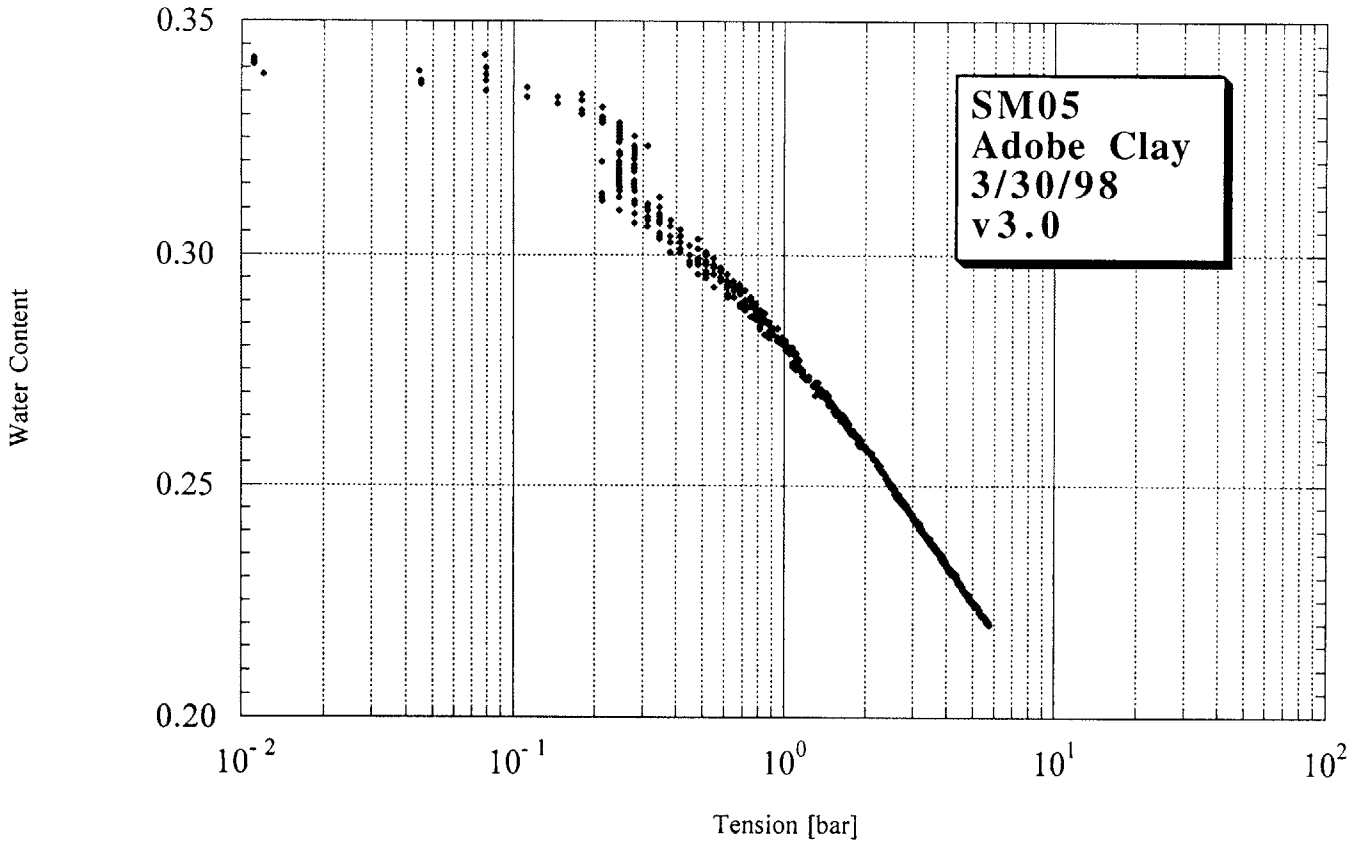

Figure D-5. SM05 testing results.

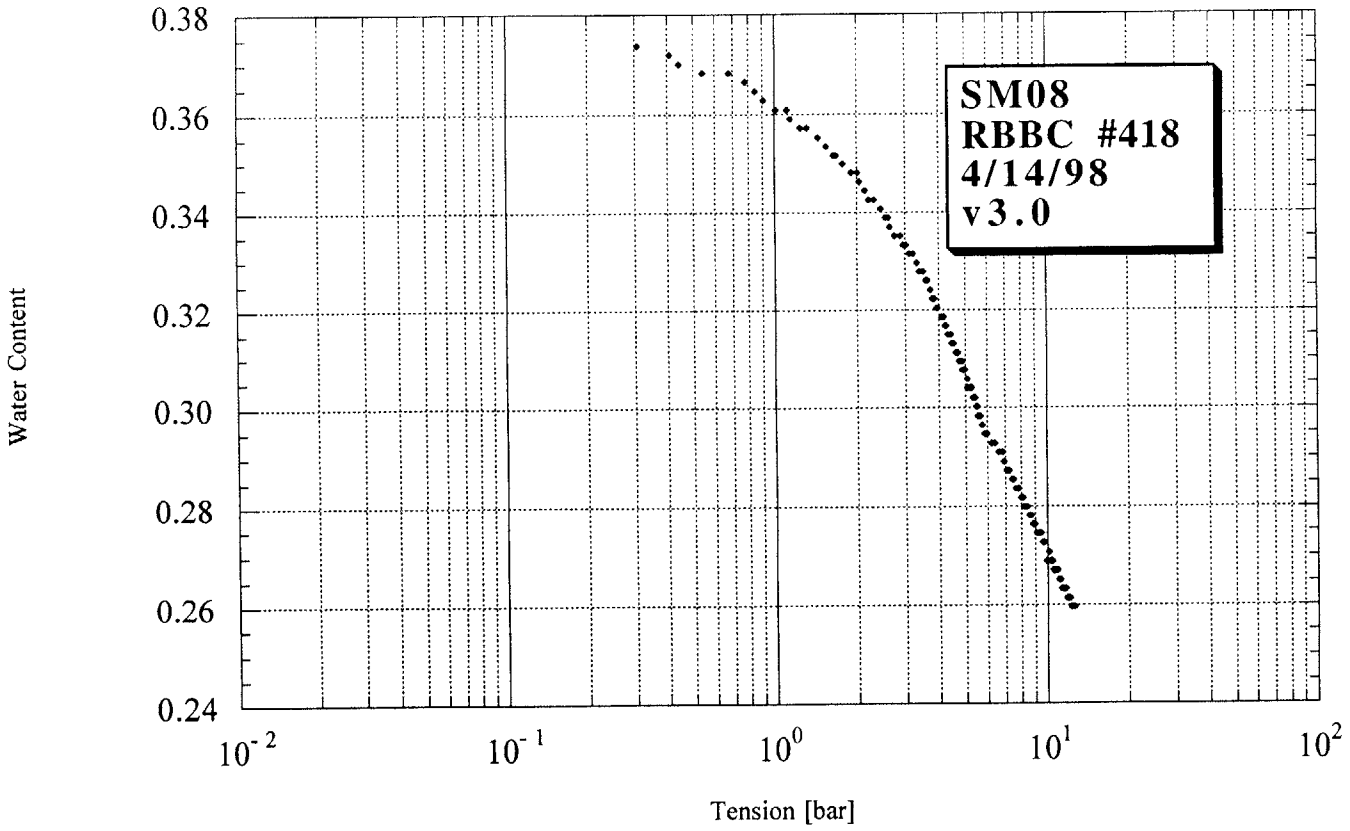

Figure D-6. SM08 testing results.

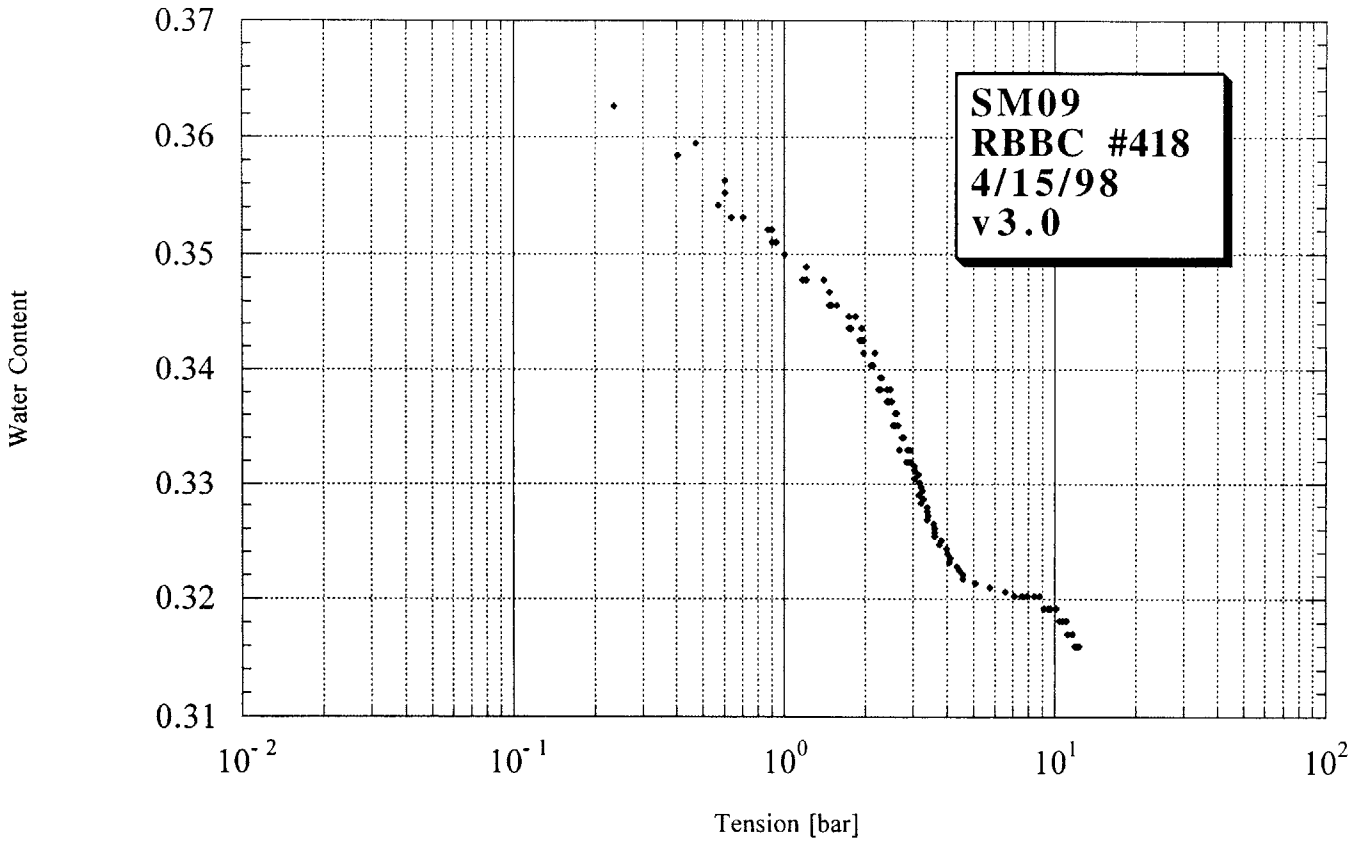

Figure D-7. SM09 testing results.

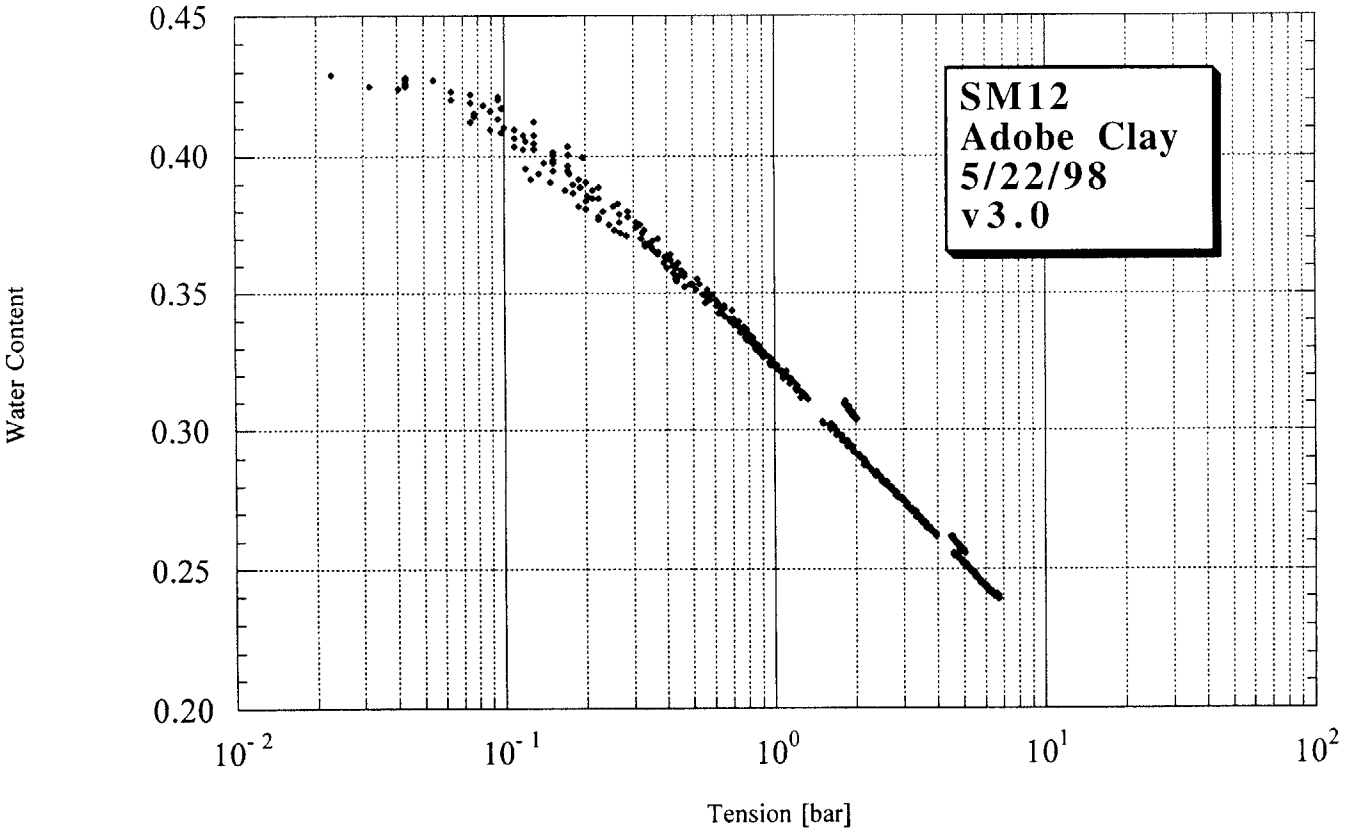

Figure D-8. SM12 testing results.

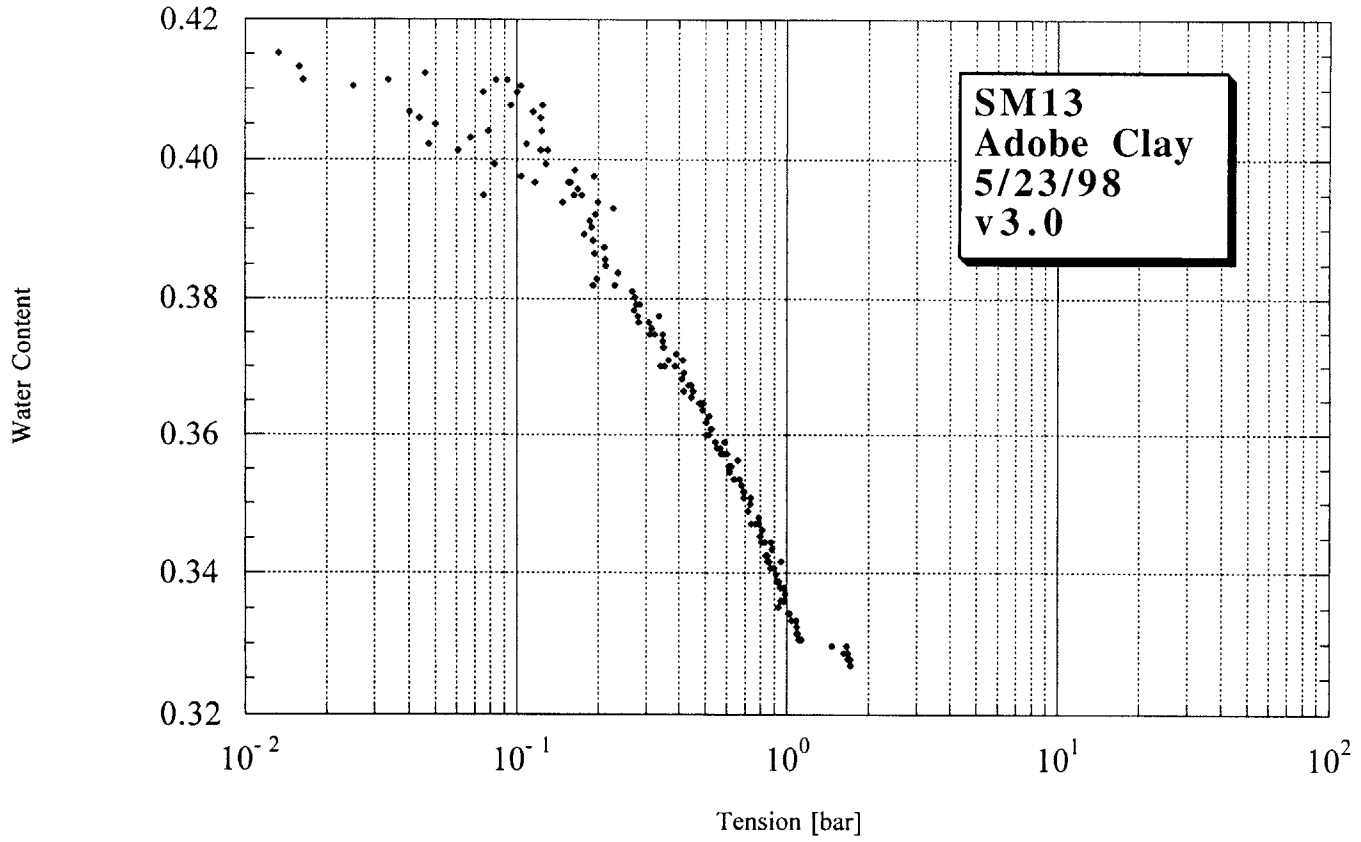

Figure D-9. SM13 testing results.

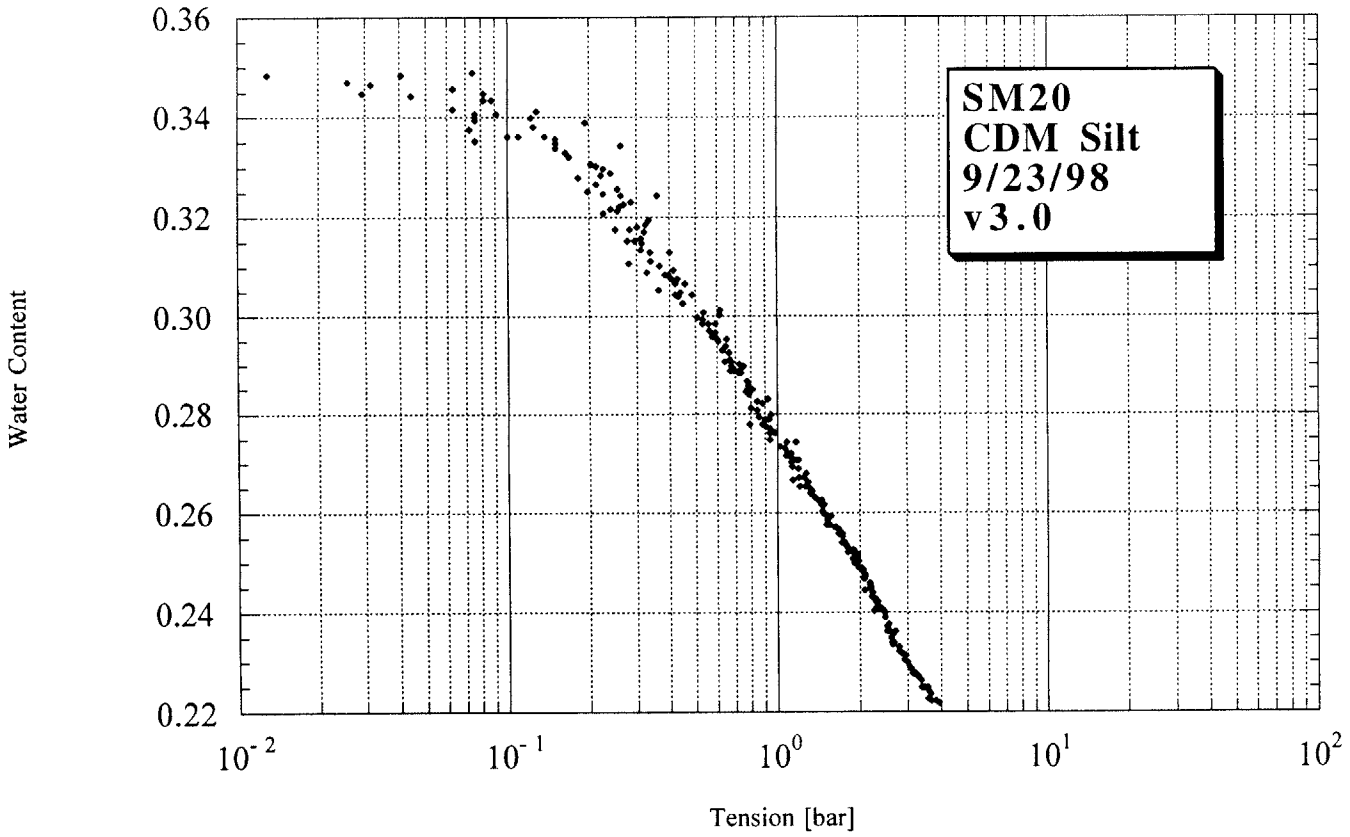

Figure D-10. SM20 testing results.

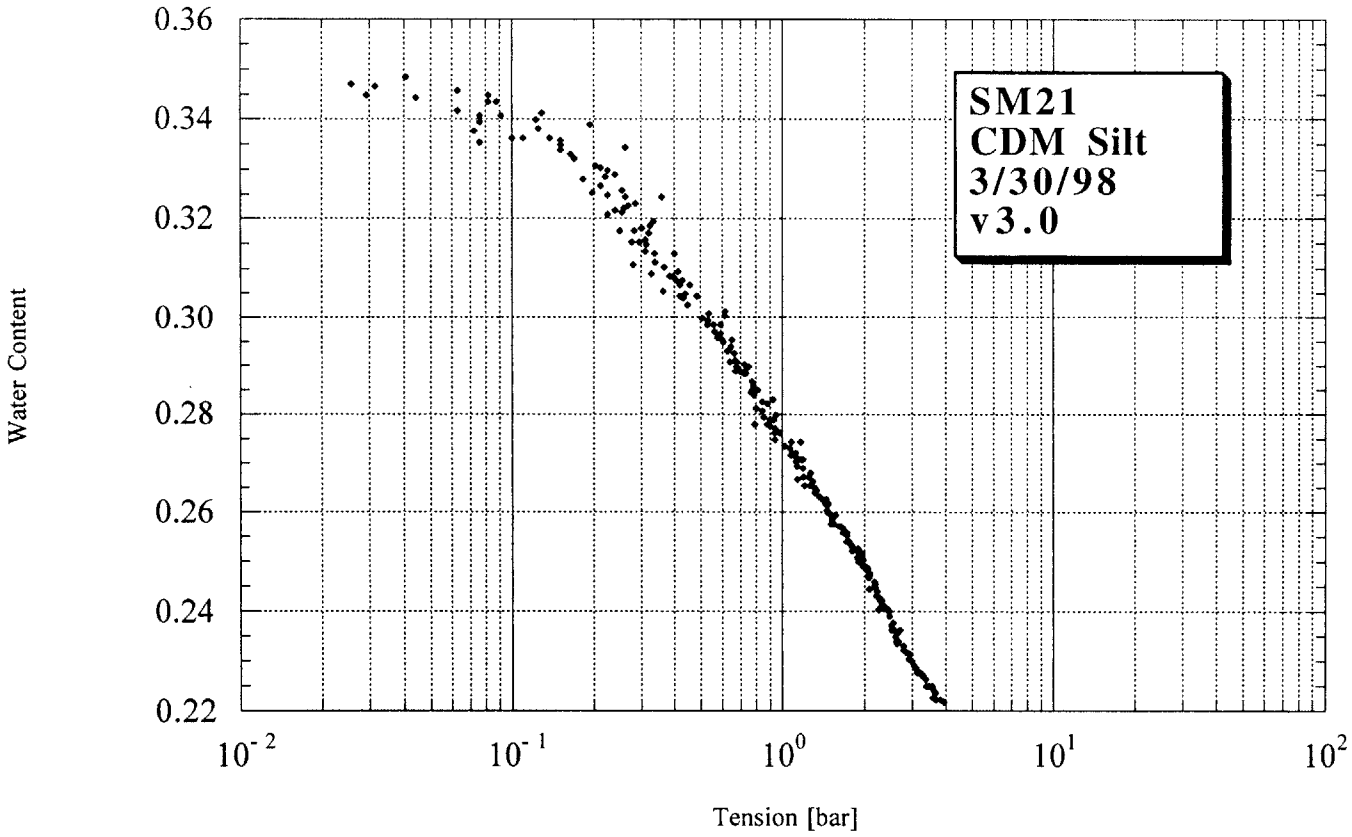

Figure D-11. SM21 testing results.

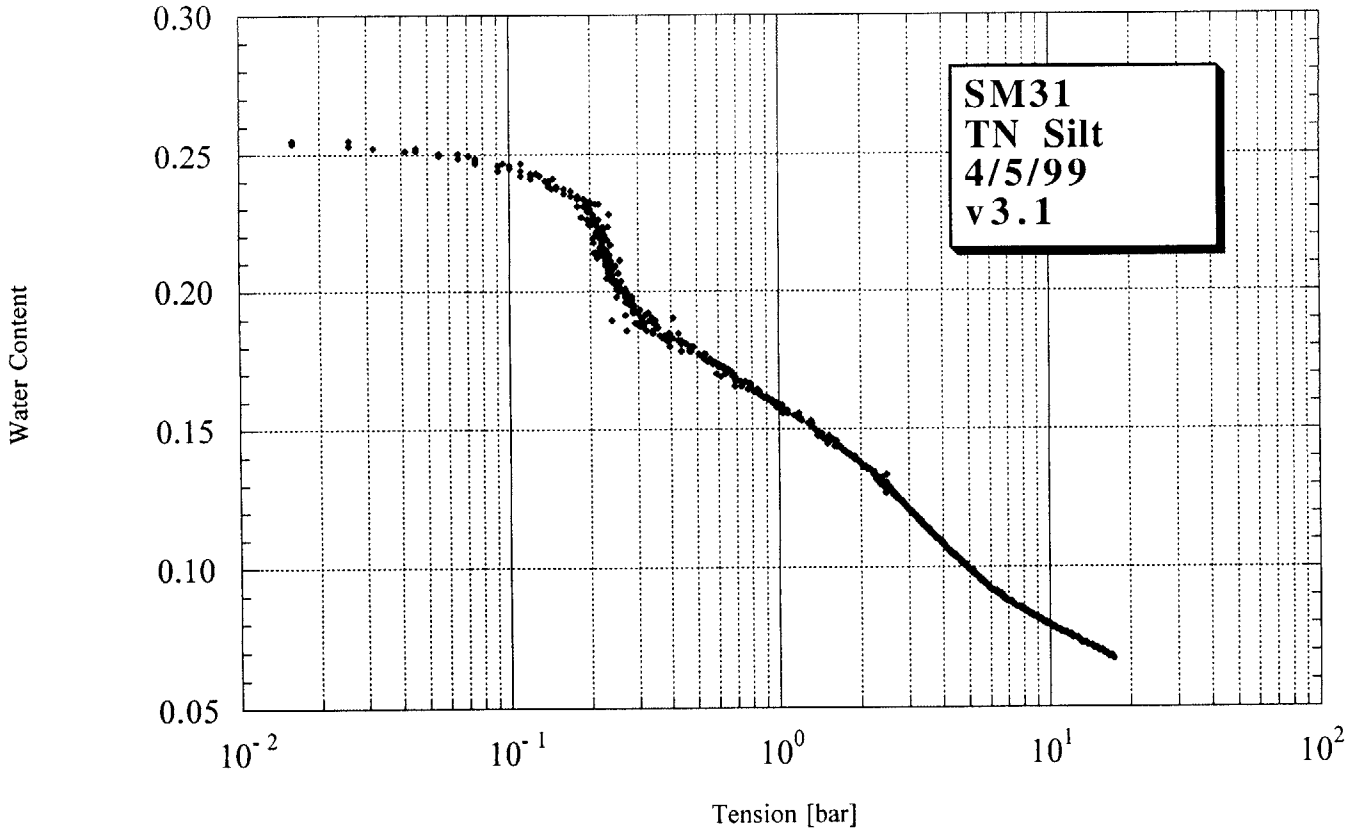

Figure D-12. SM31 testing results.

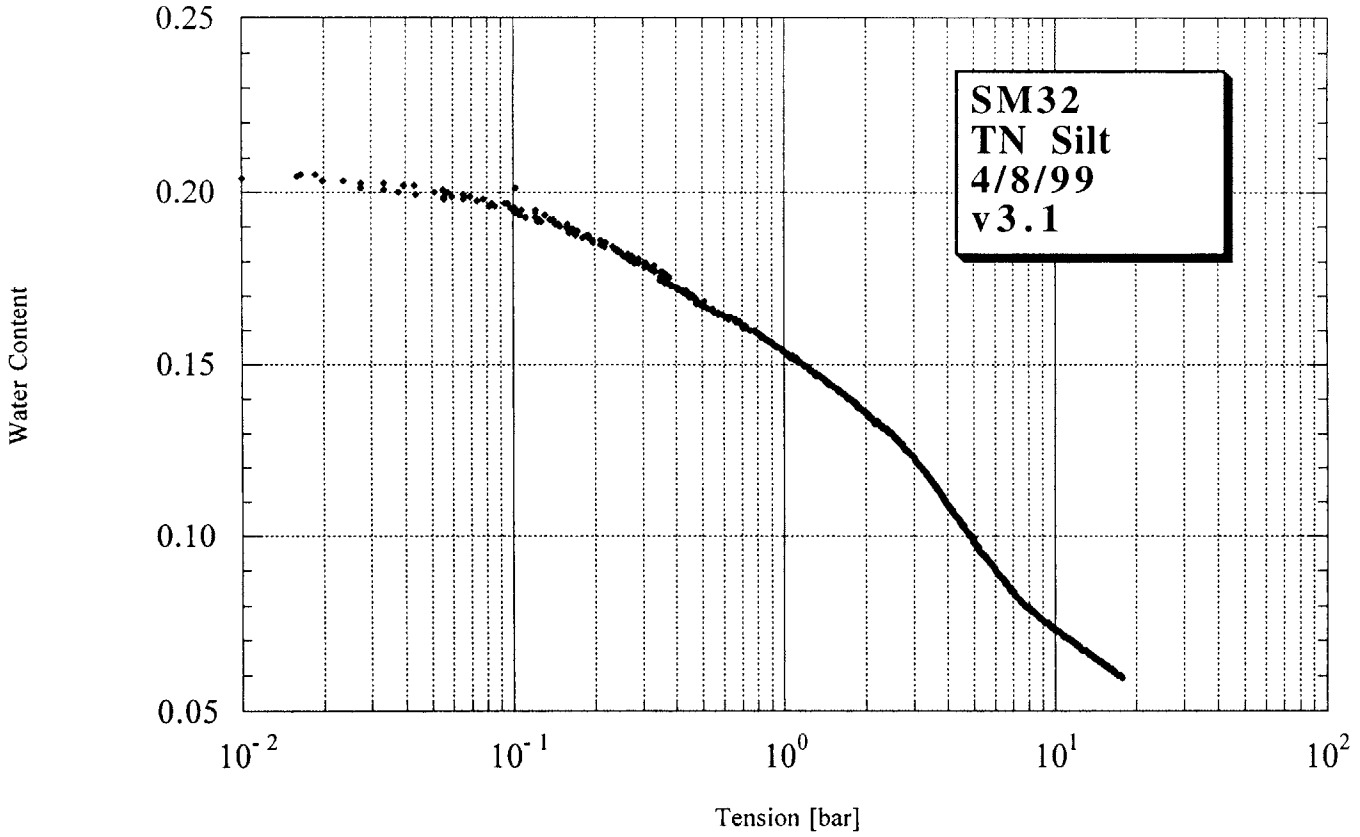

Figure D-13. SM32 testing results.

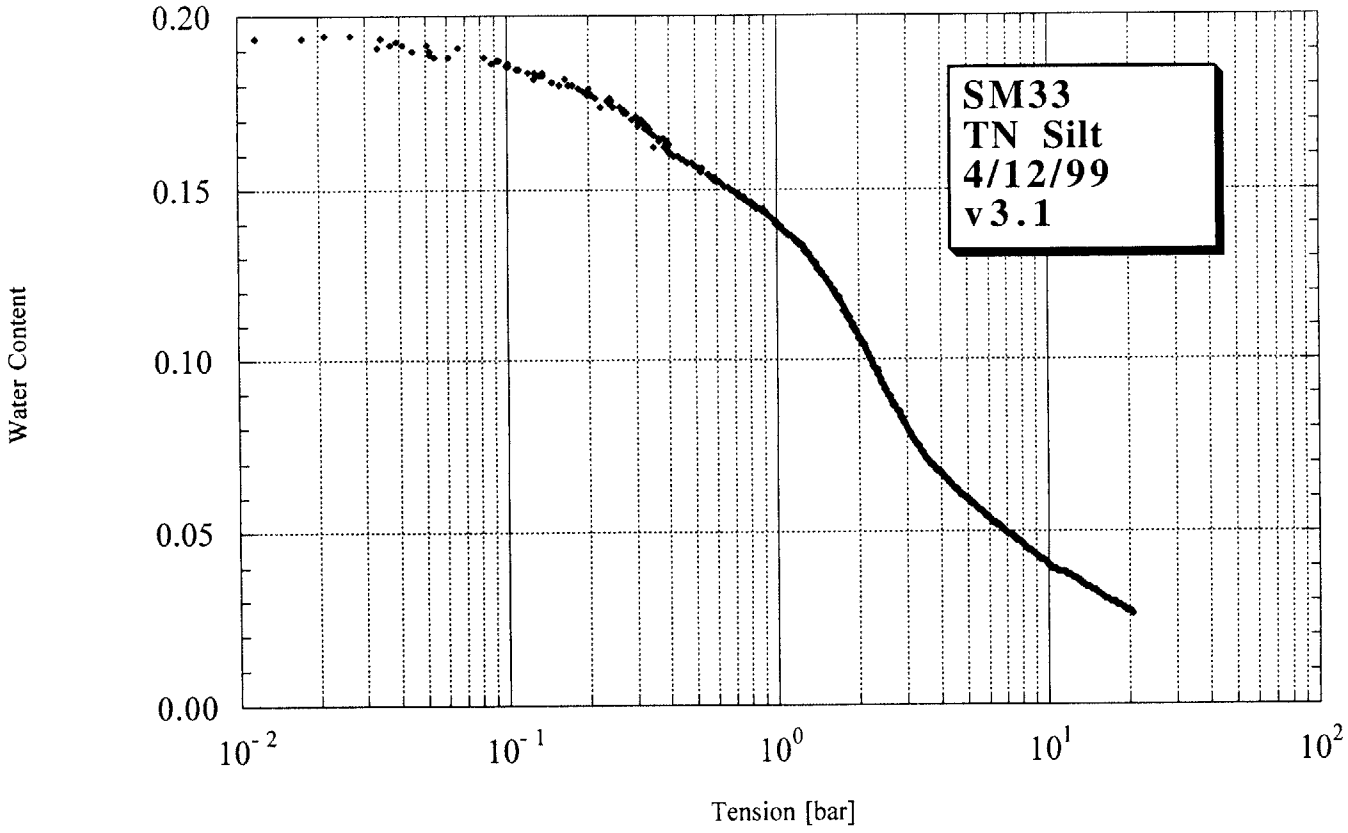

Figure D-14. SM33 testing results.

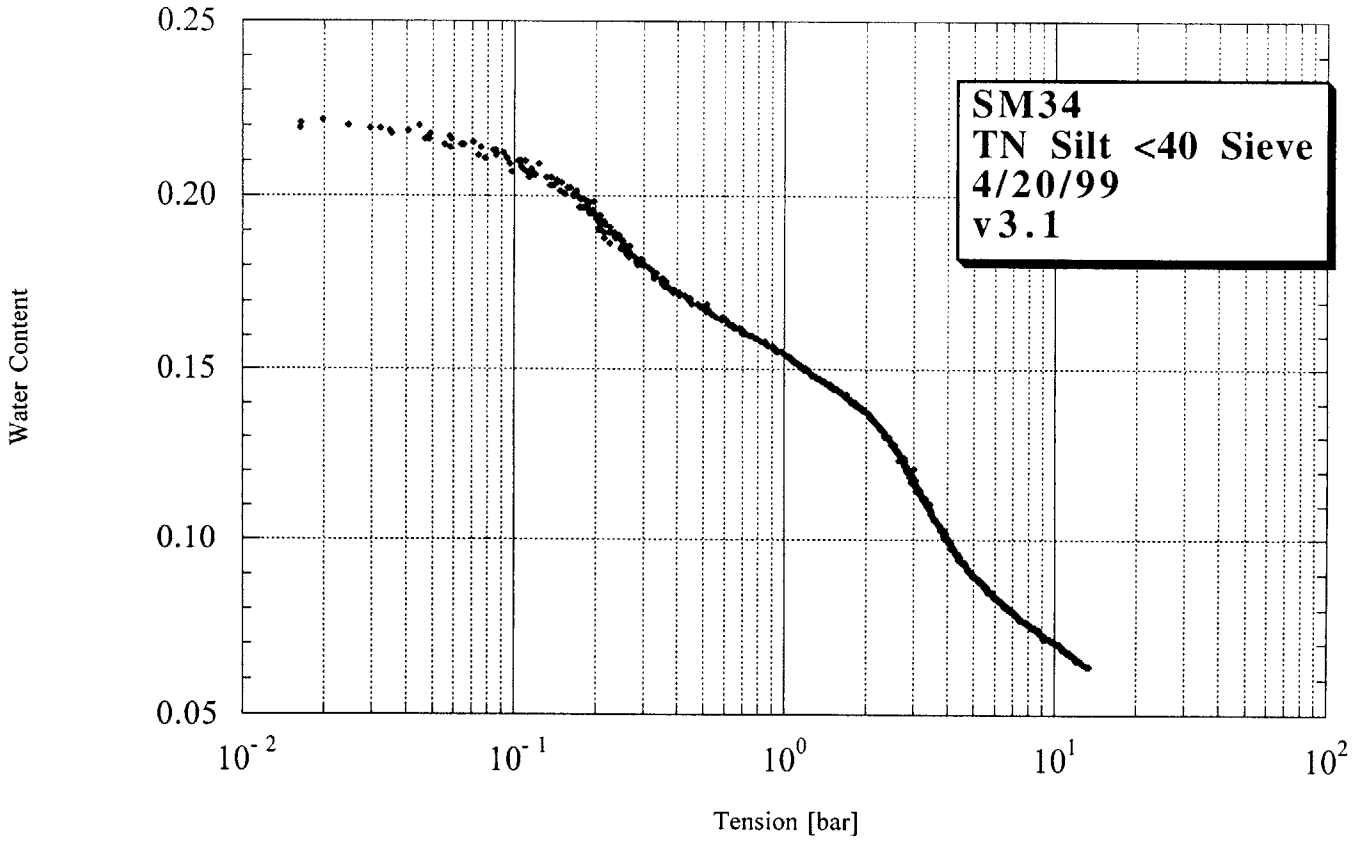

Figure D-15. SM34 testing results.

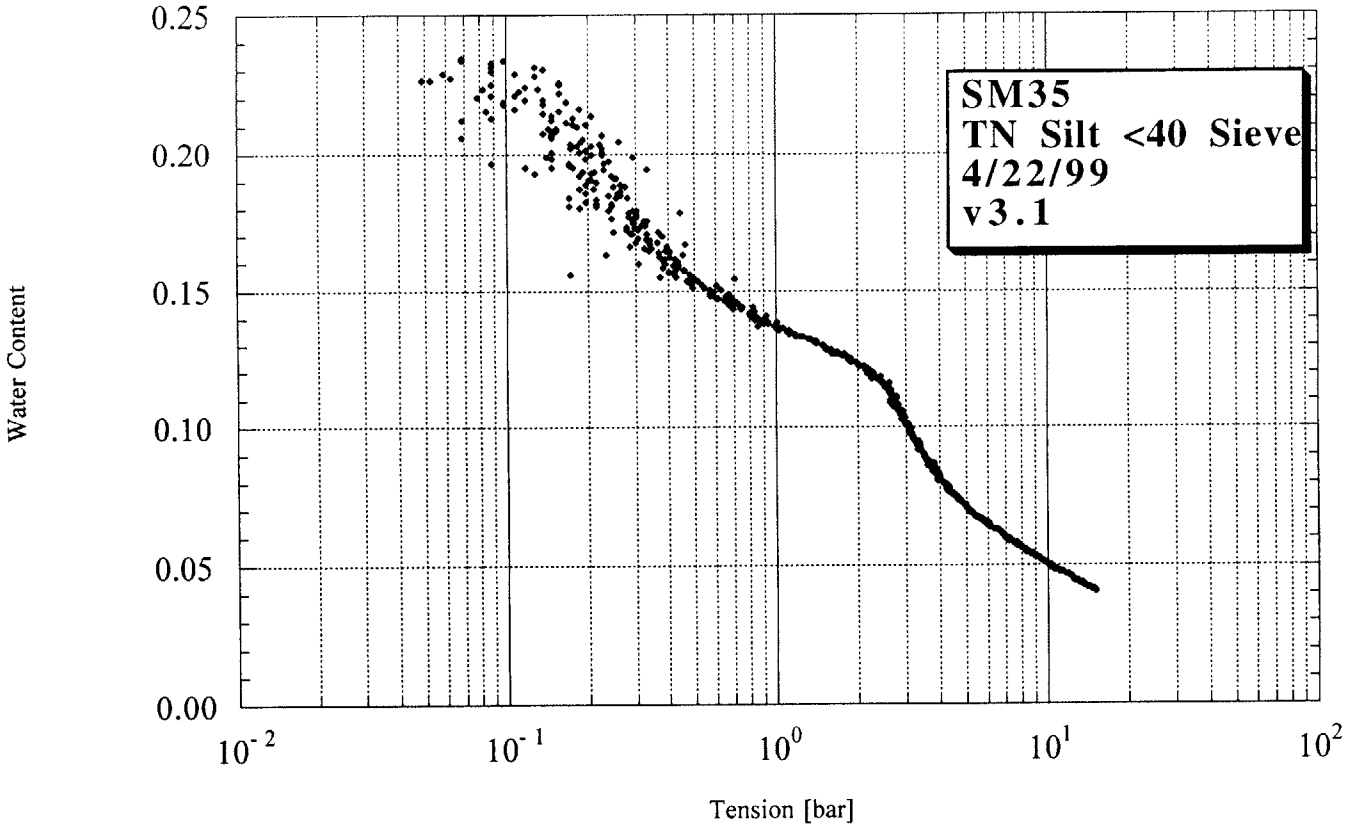

Figure D-16. SM35 testing results.

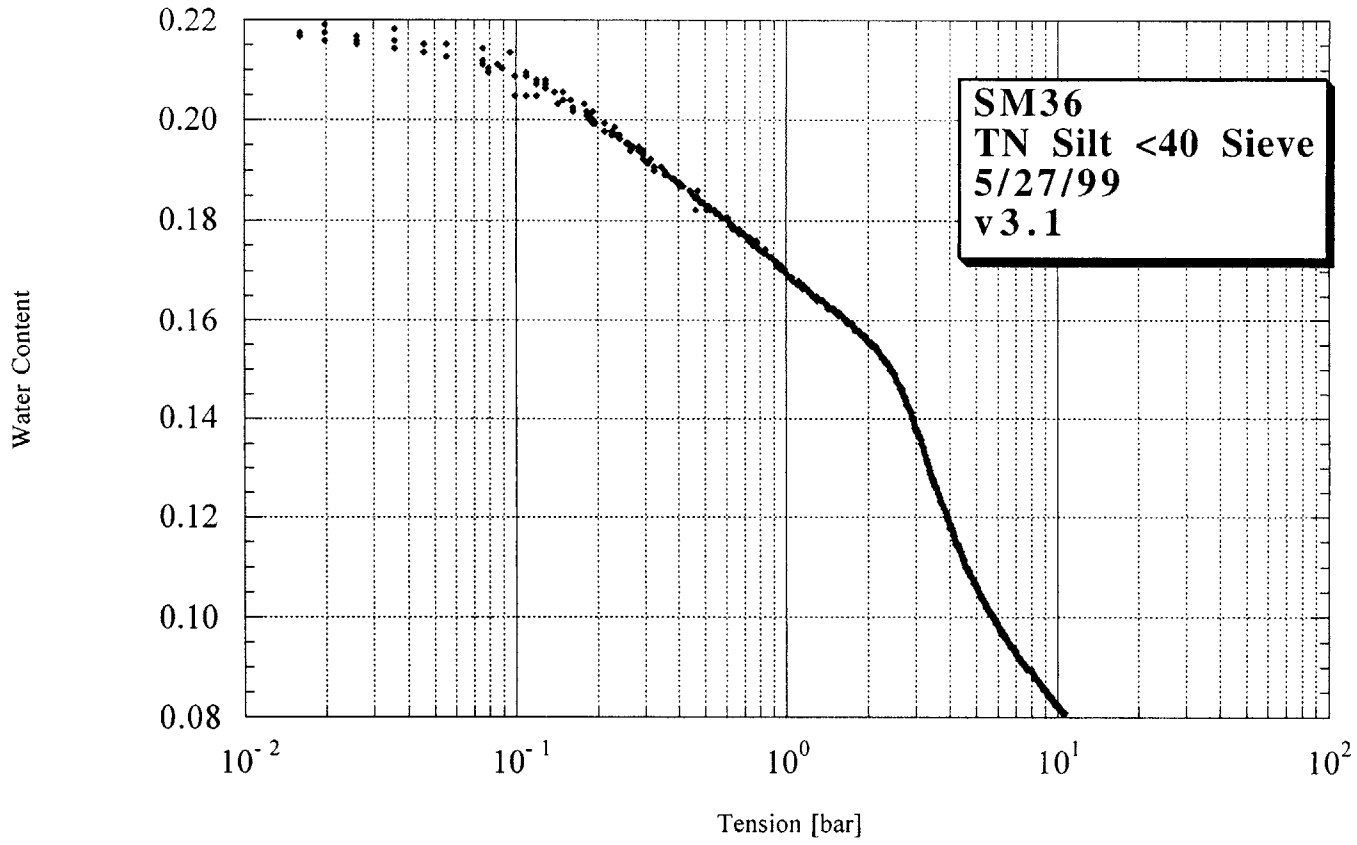

Figure D-17. SM36 testing results.

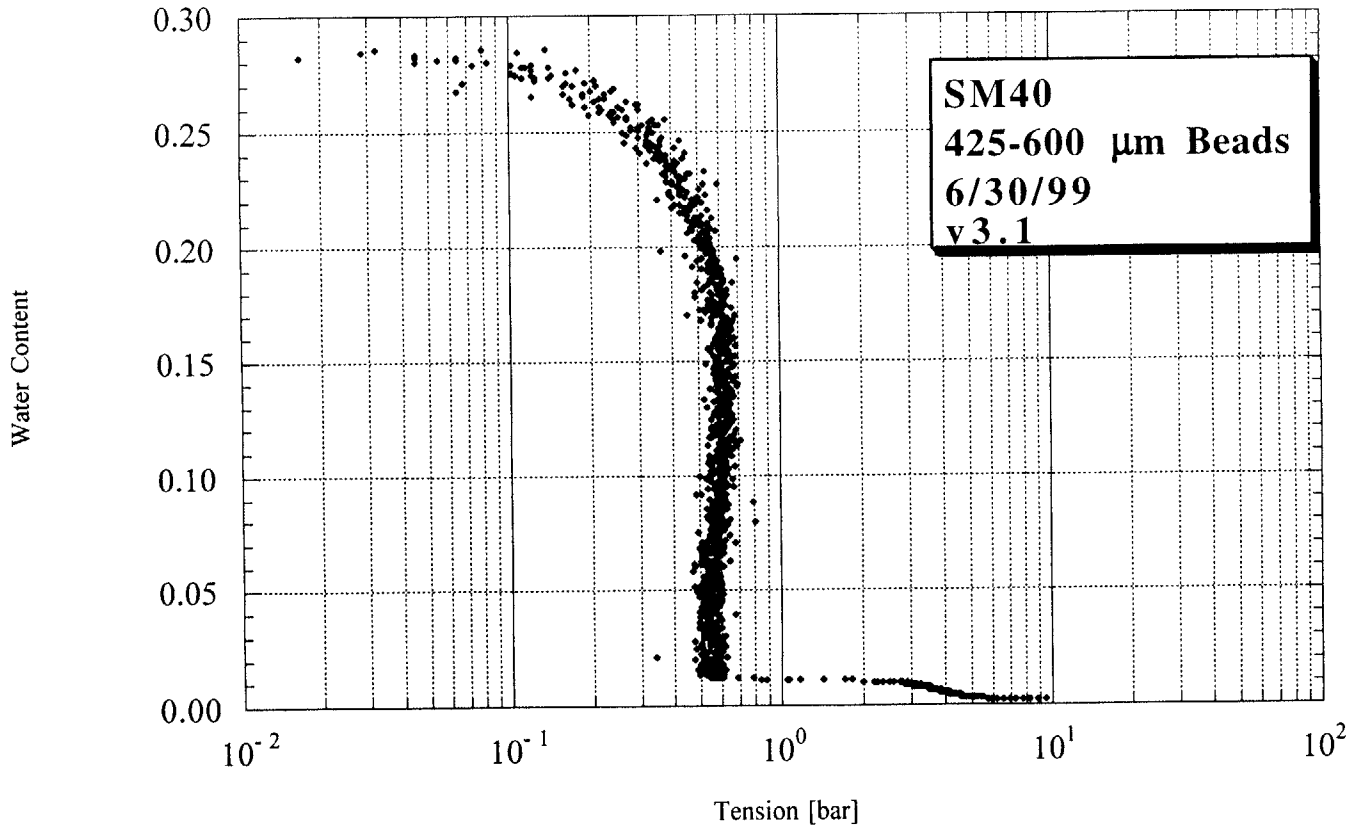

Figure D-18. SM40 testing results.

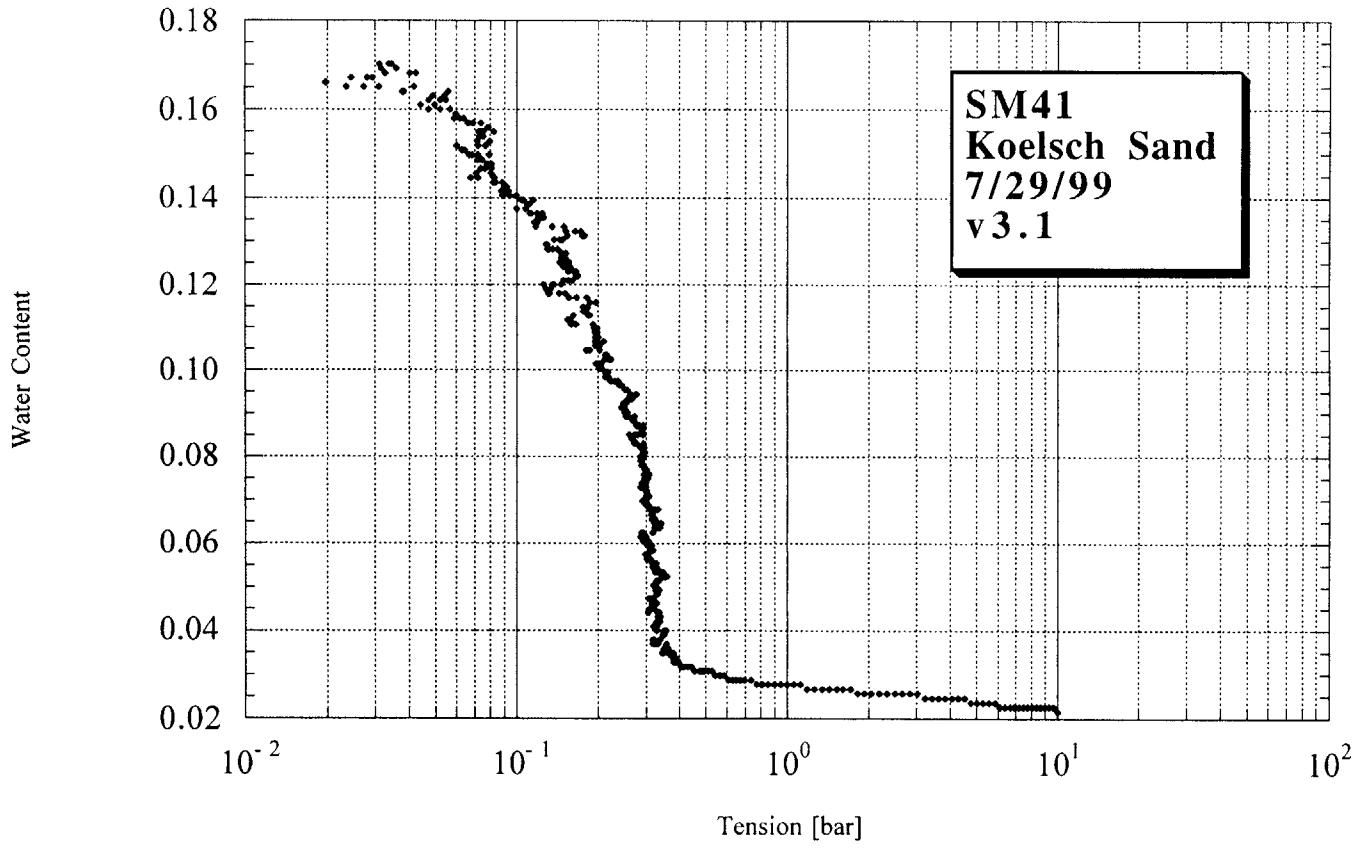

Figure D-19. SM41 testing results.

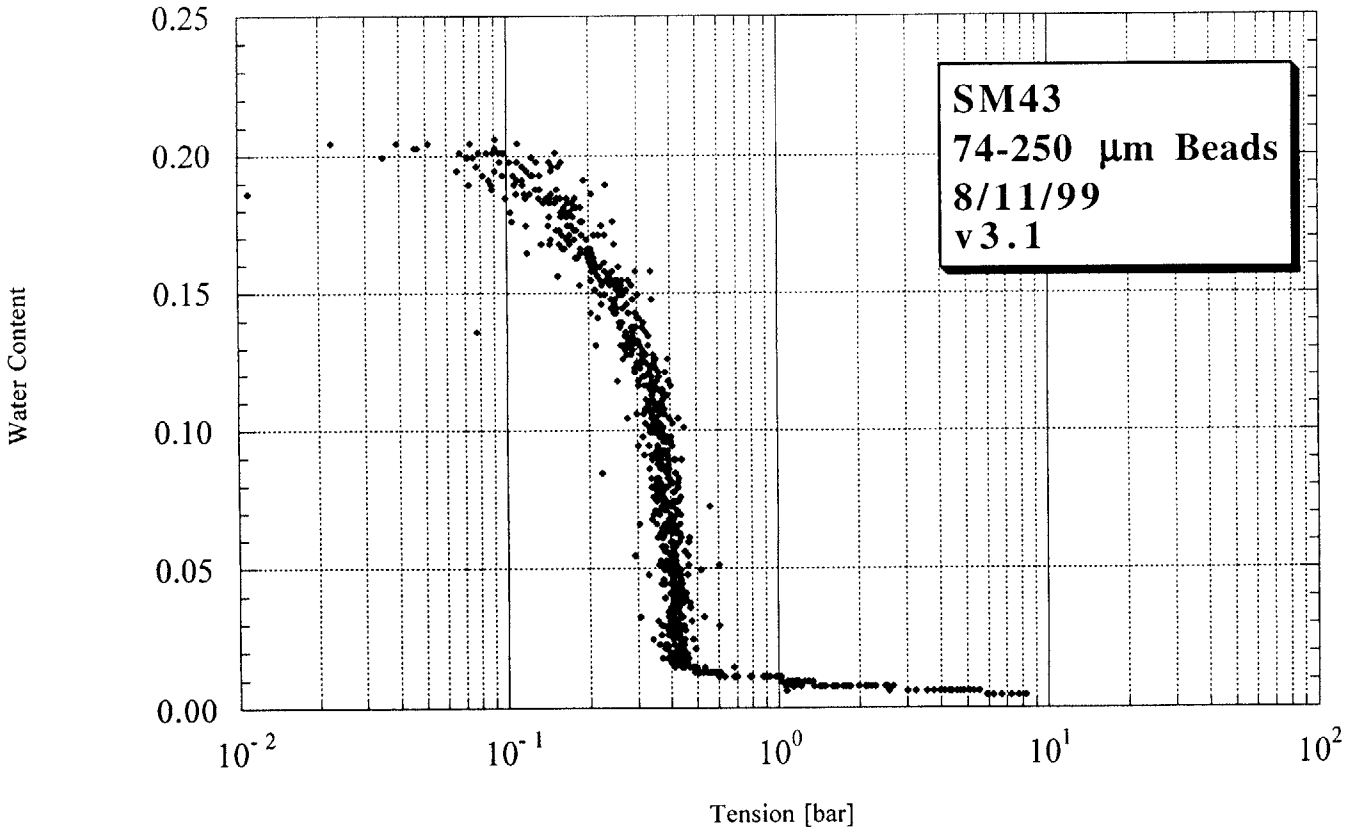

Figure D-20. SM43 testing results.

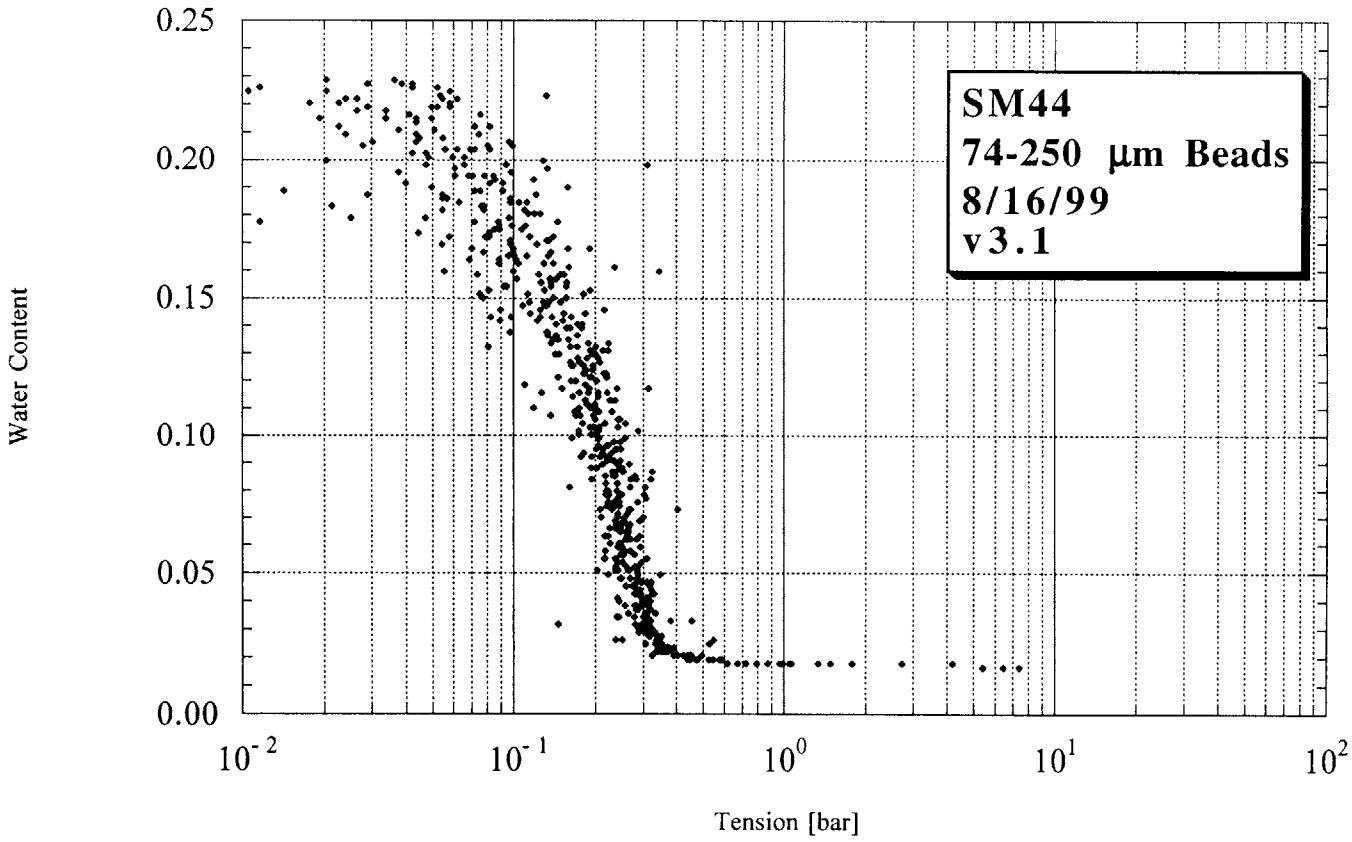

Figure D-21. SM44 testing results.

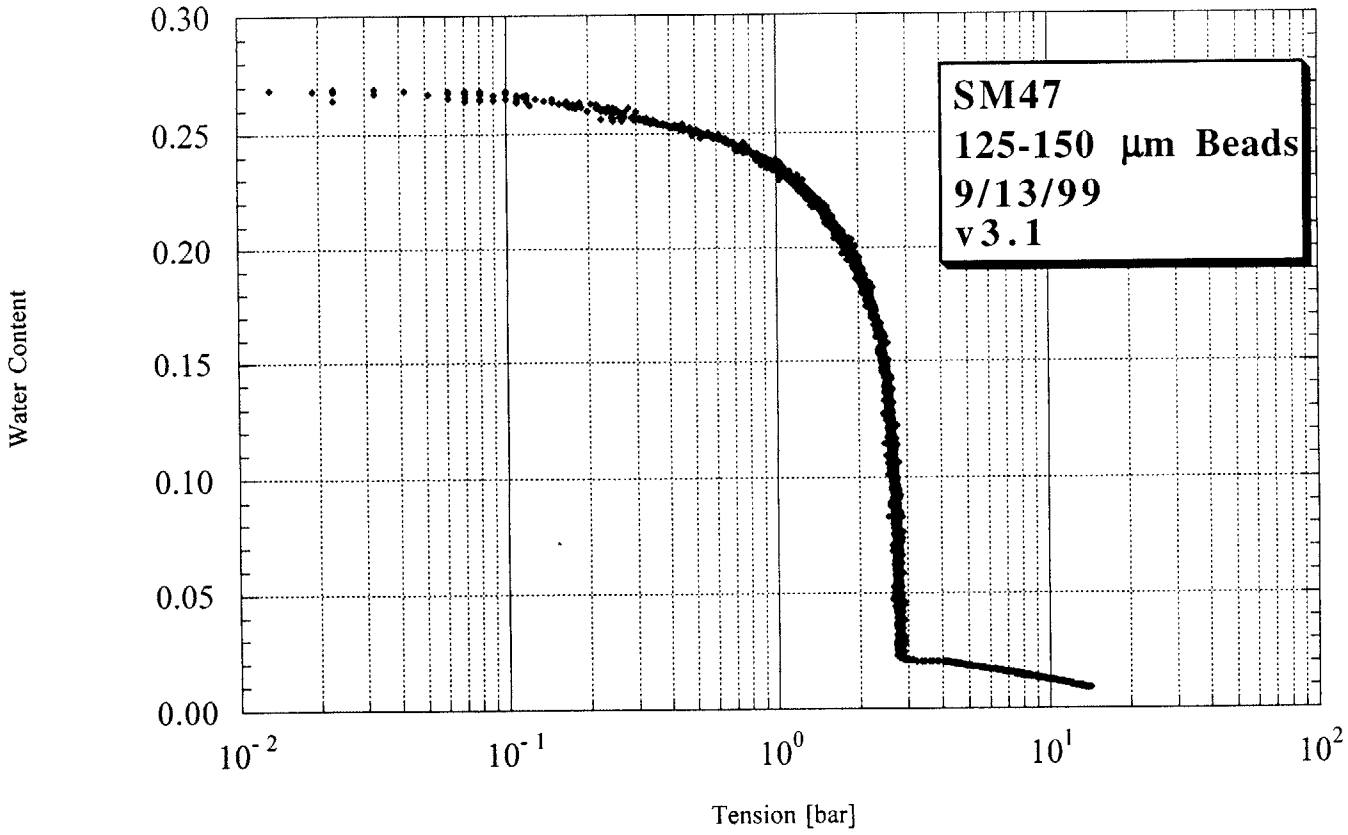

Figure D-22. SM47 testing results.

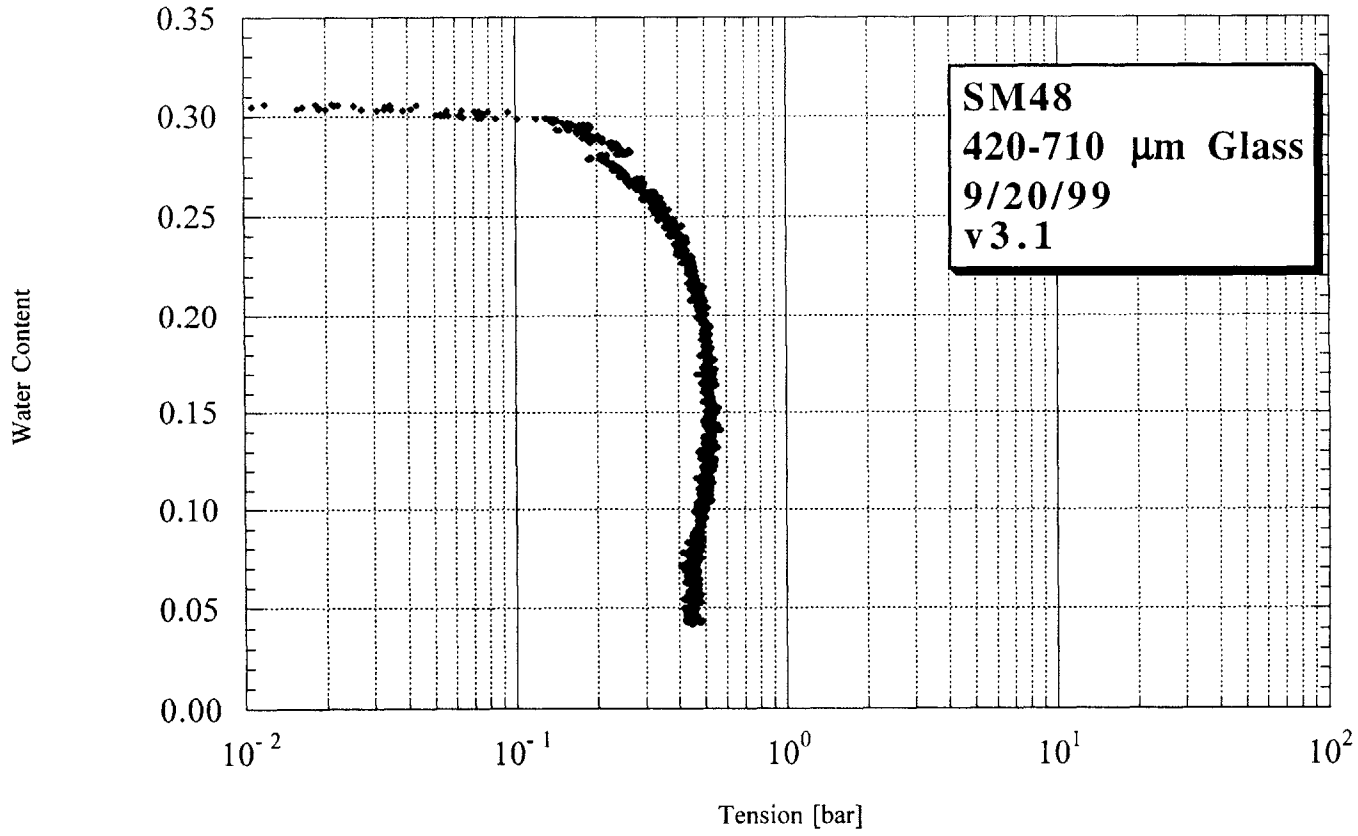

Figure D-23. SM48 testing results.

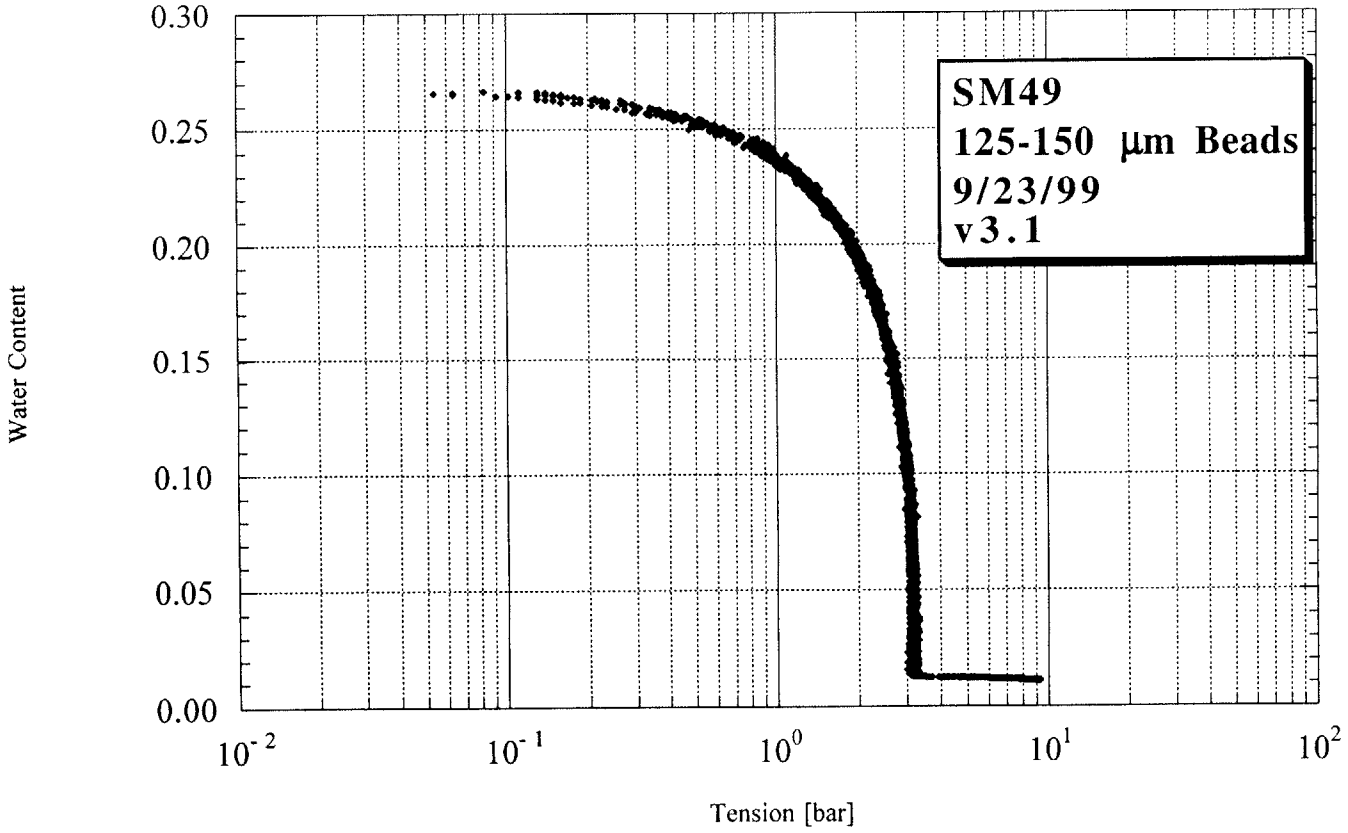

Figure D-24. SM49 testing results.

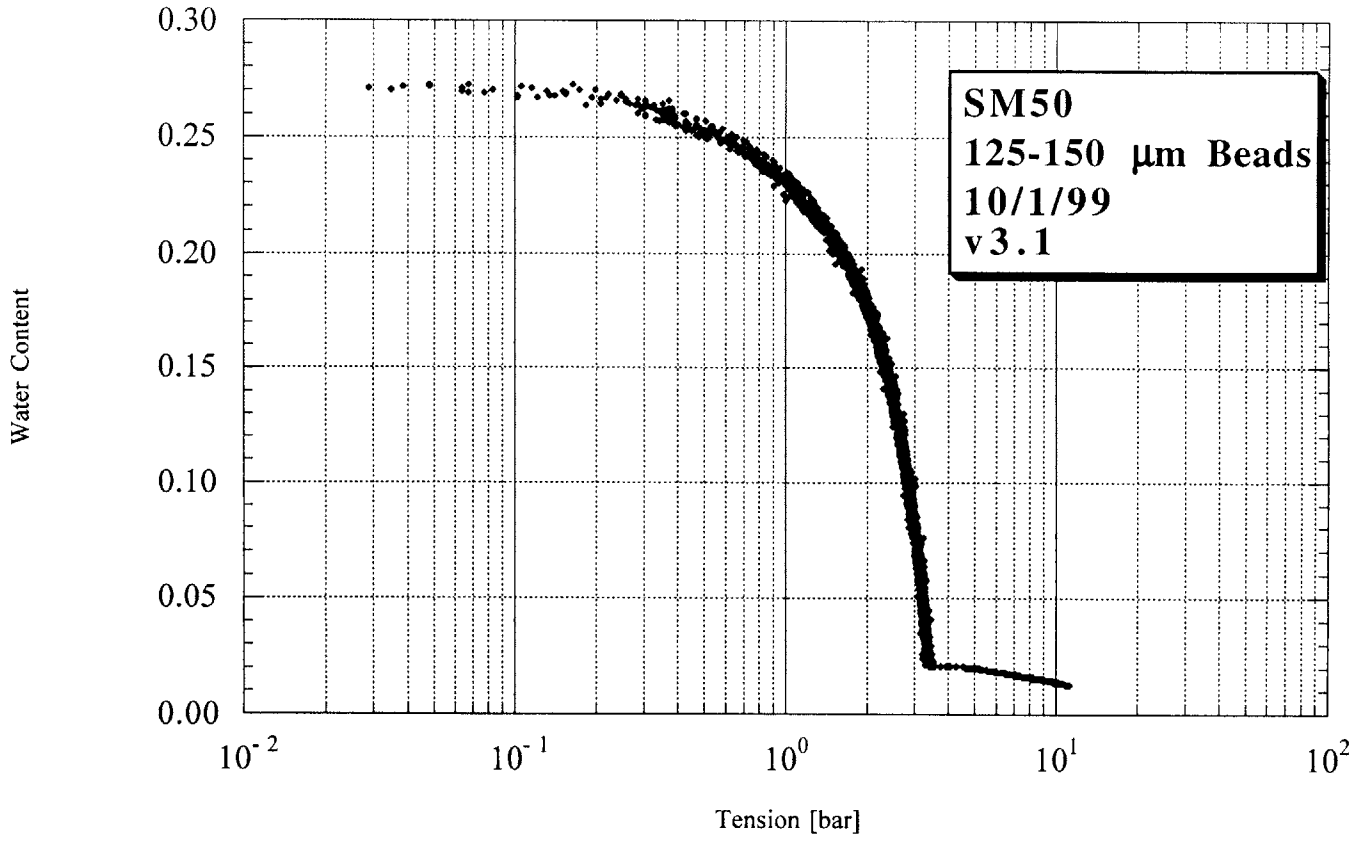

Figure D-25. SM50 testing results.

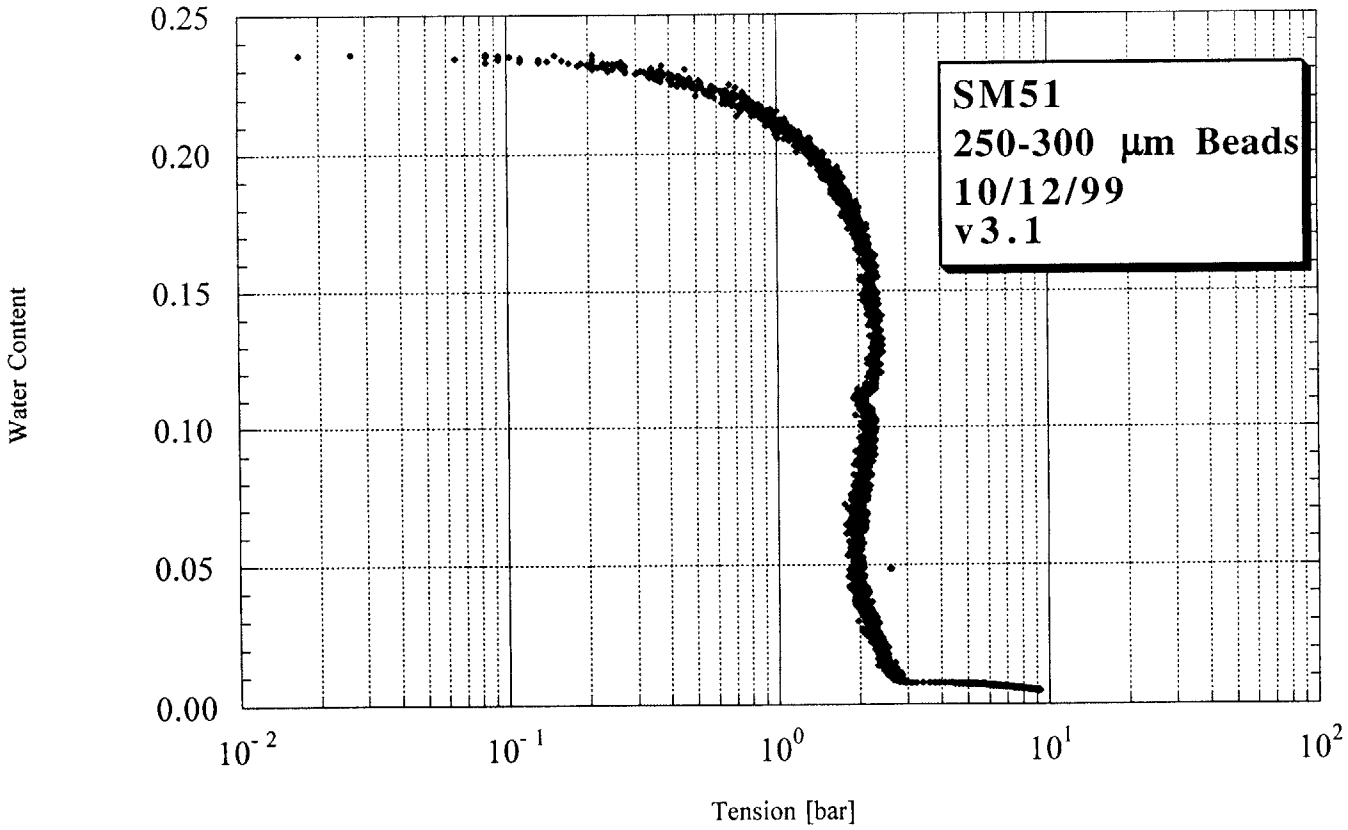

Figure D-26. SM51 testing results.

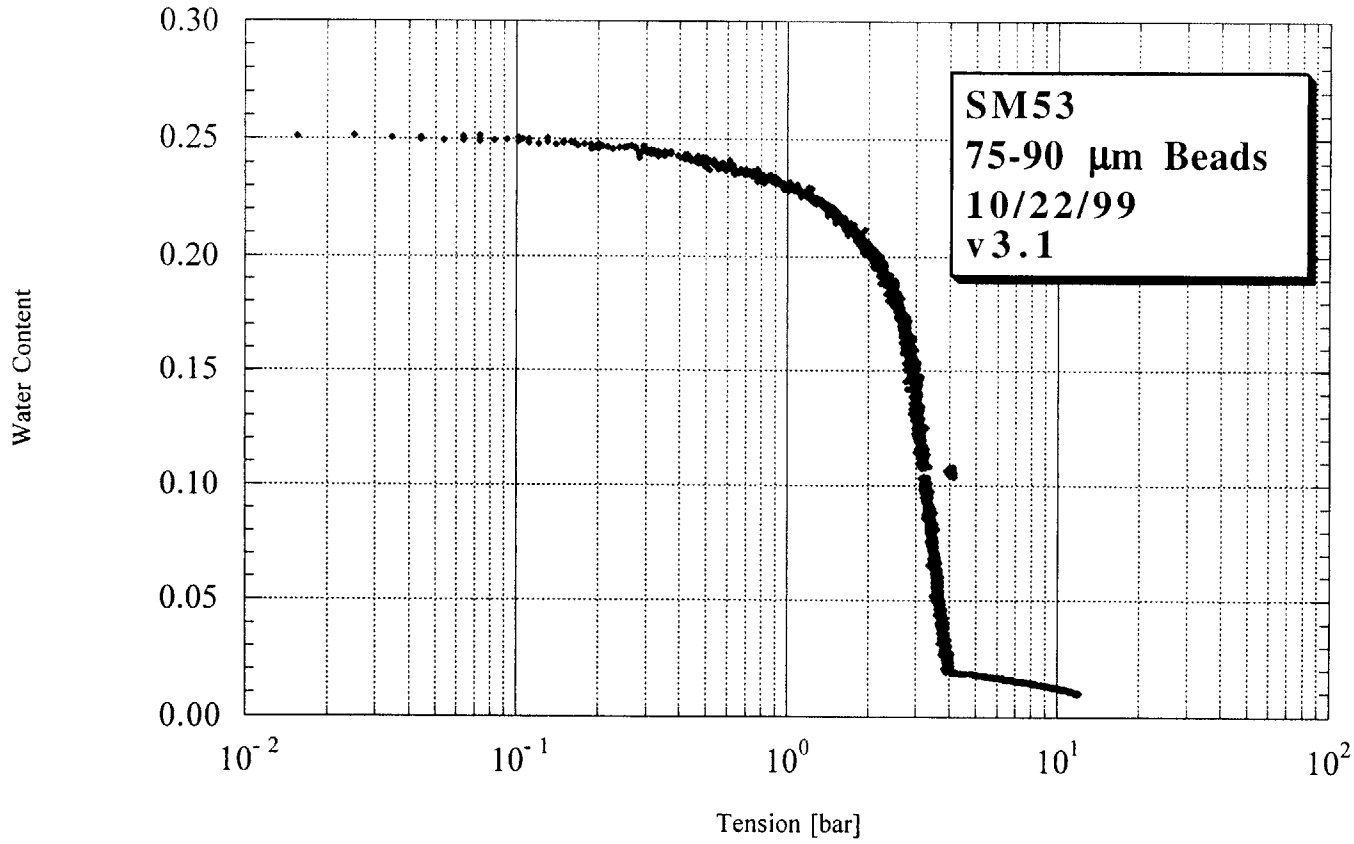

Figure D-27. SM53 testing results.

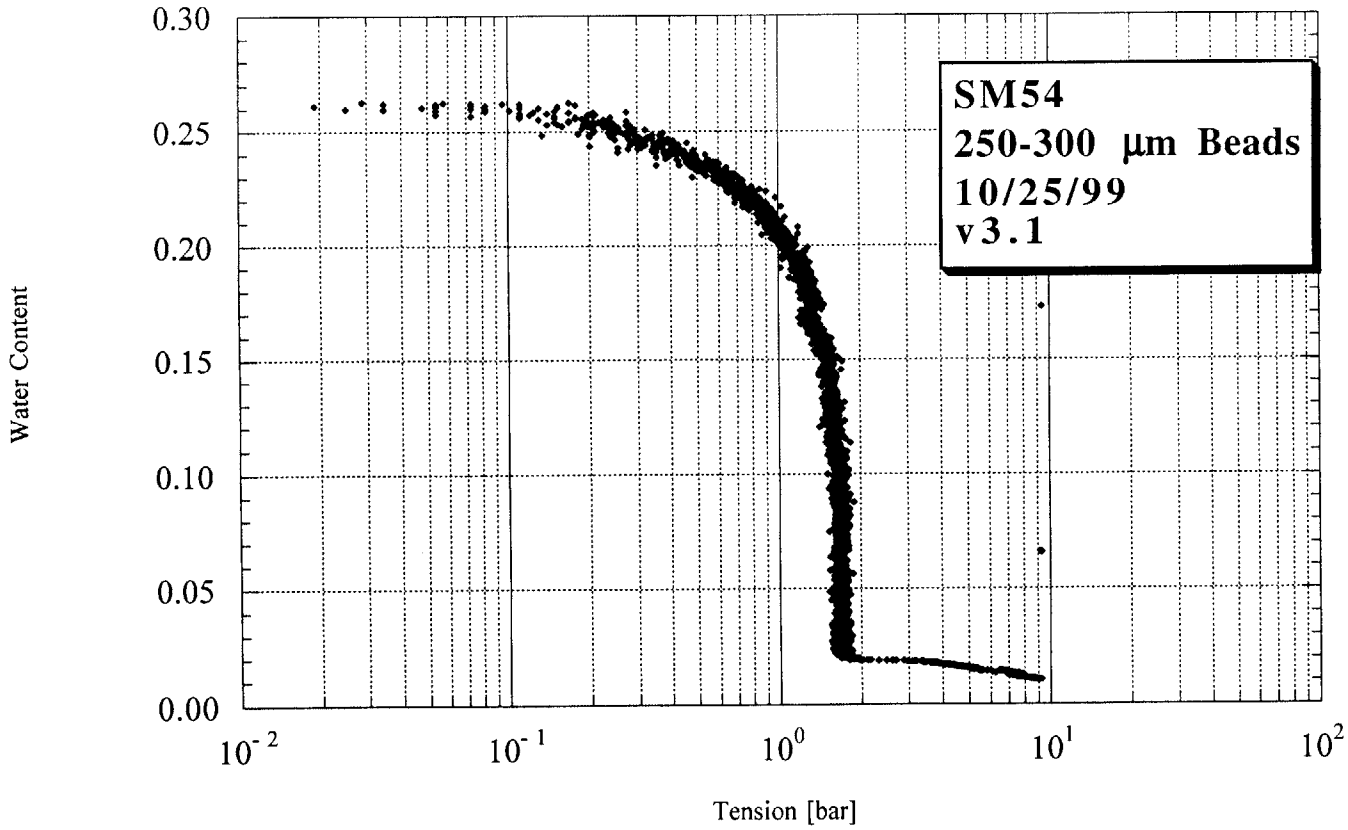

Figure D-28. SM54 testing results.

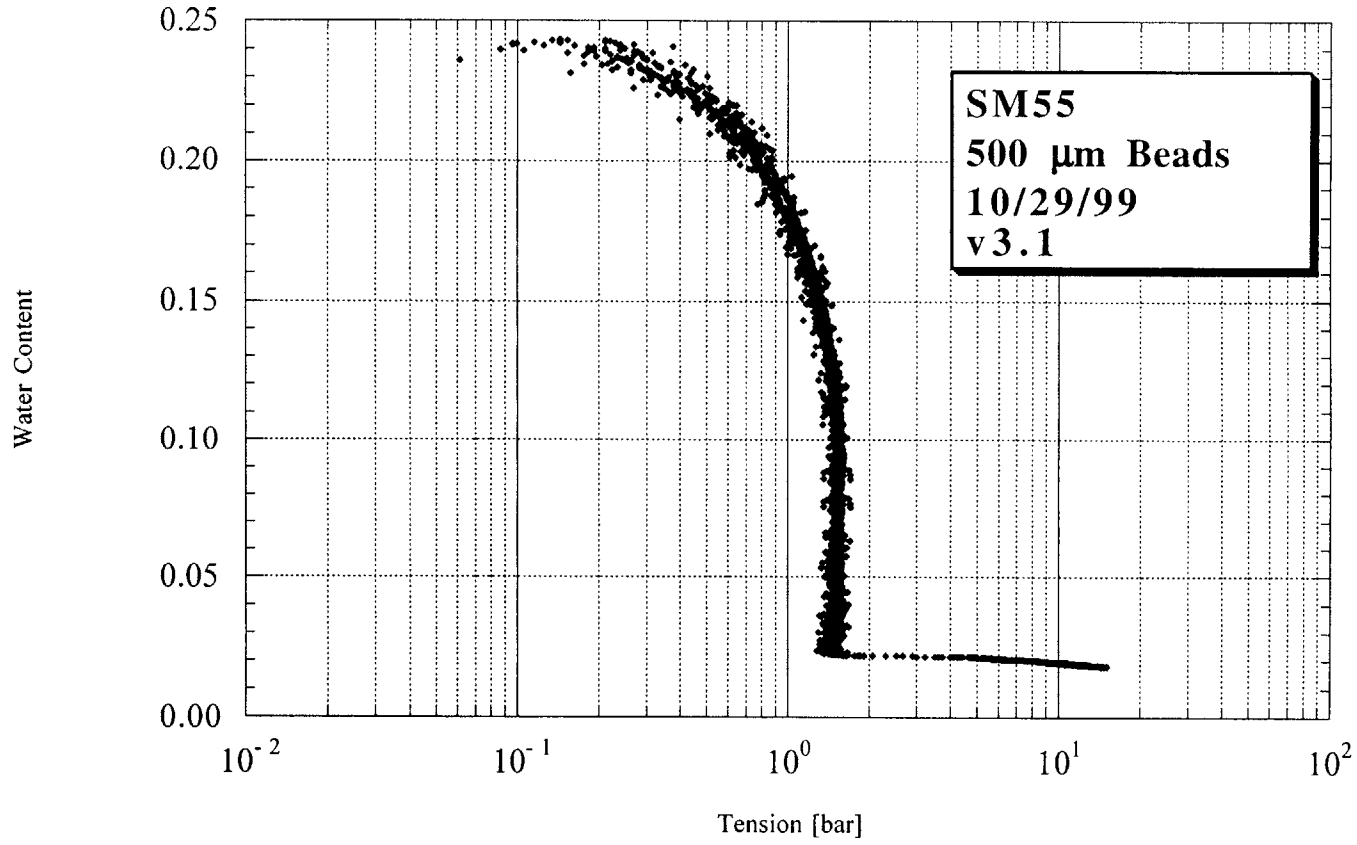

Figure D-29. SM55 testing results.

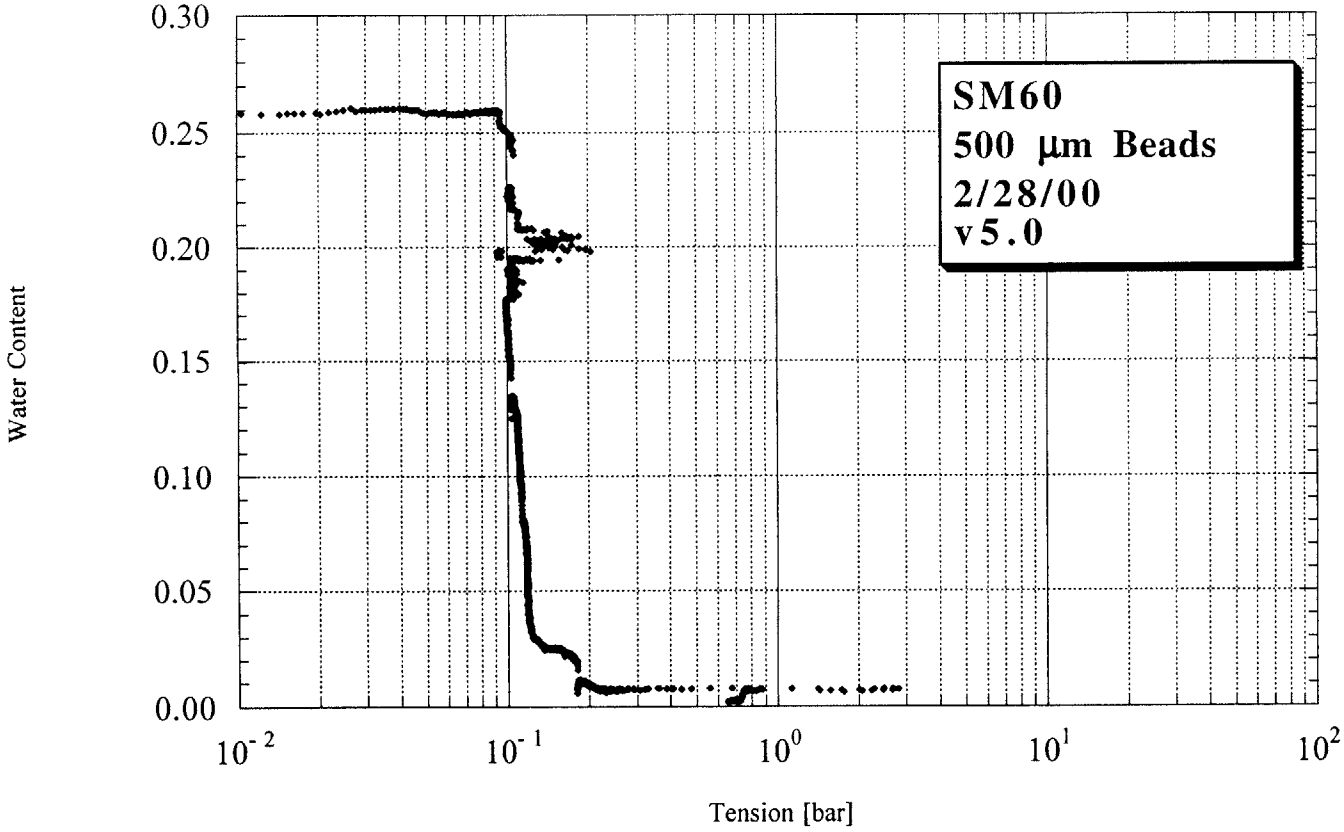

Figure D-30. SM60 testing results.

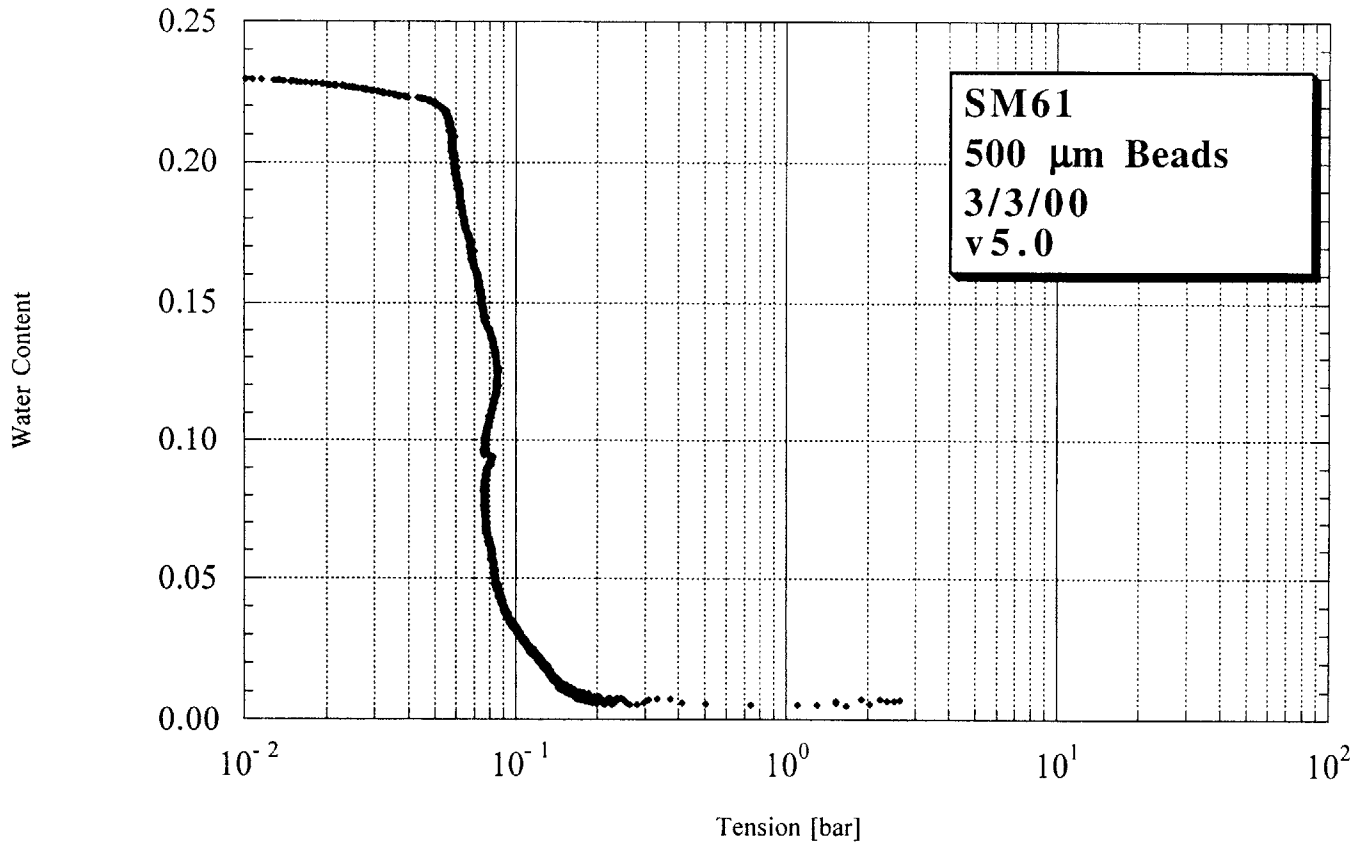

Figure D-31. SM61 testing result.

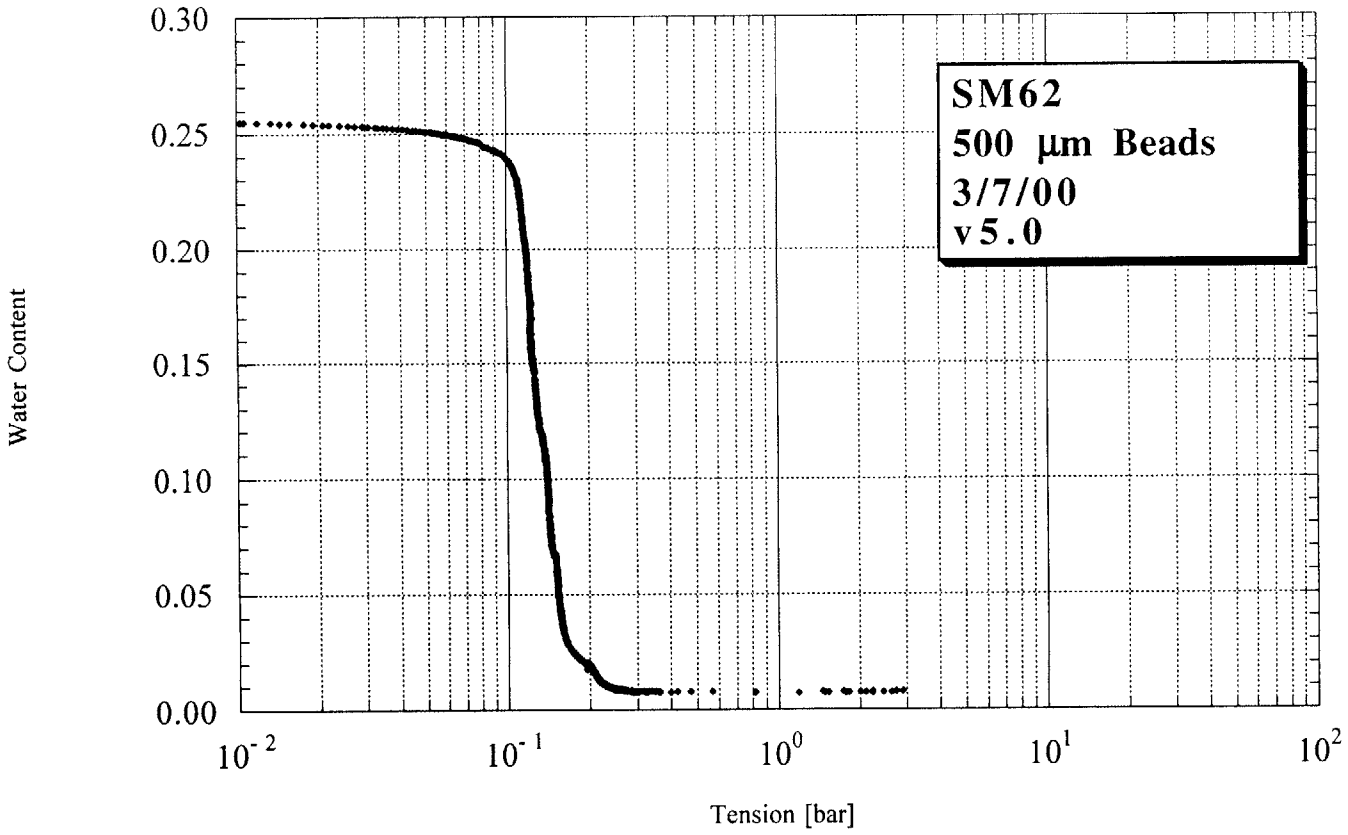

Figure D-32. SM62 testing results.

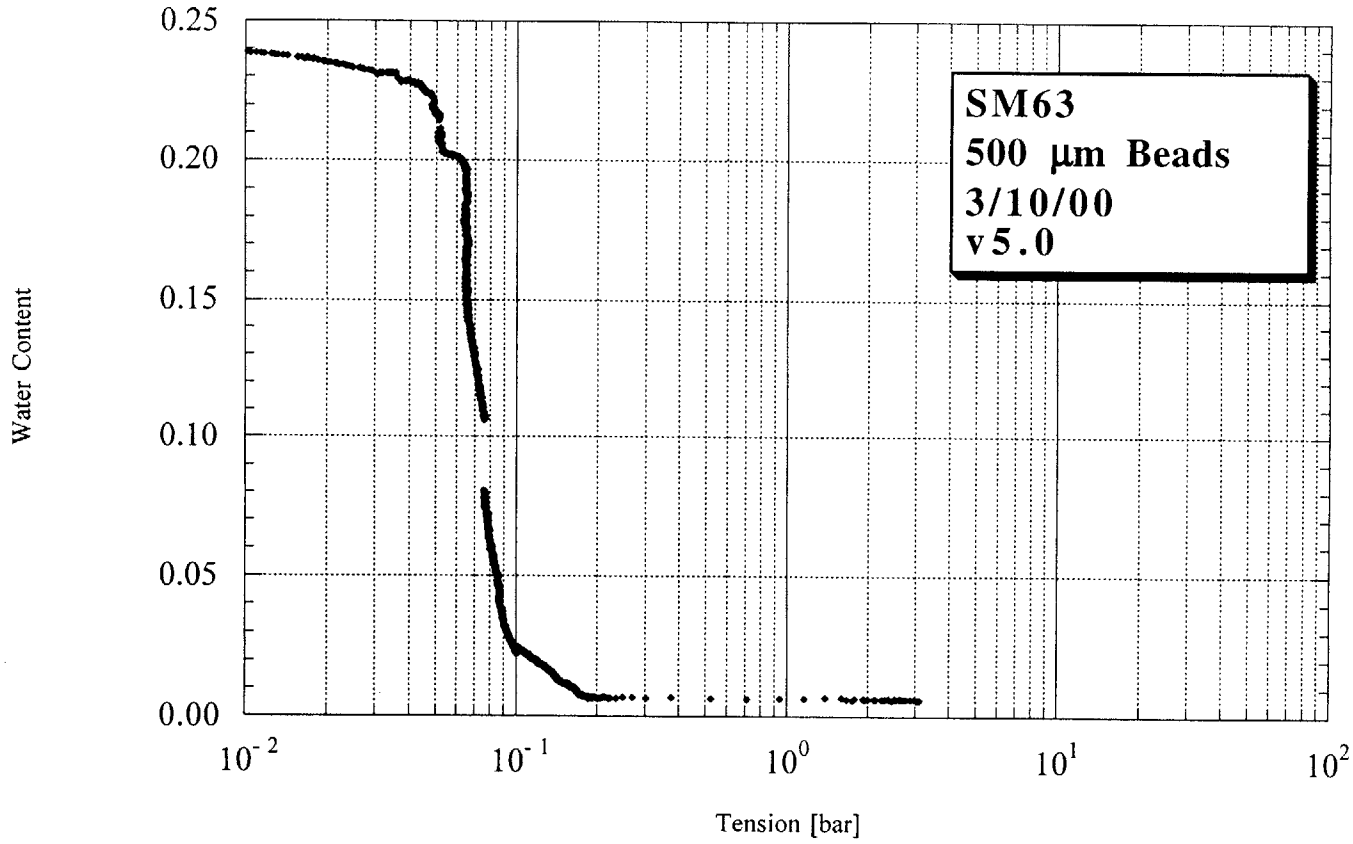

Figure D-33. SM63 testing results.

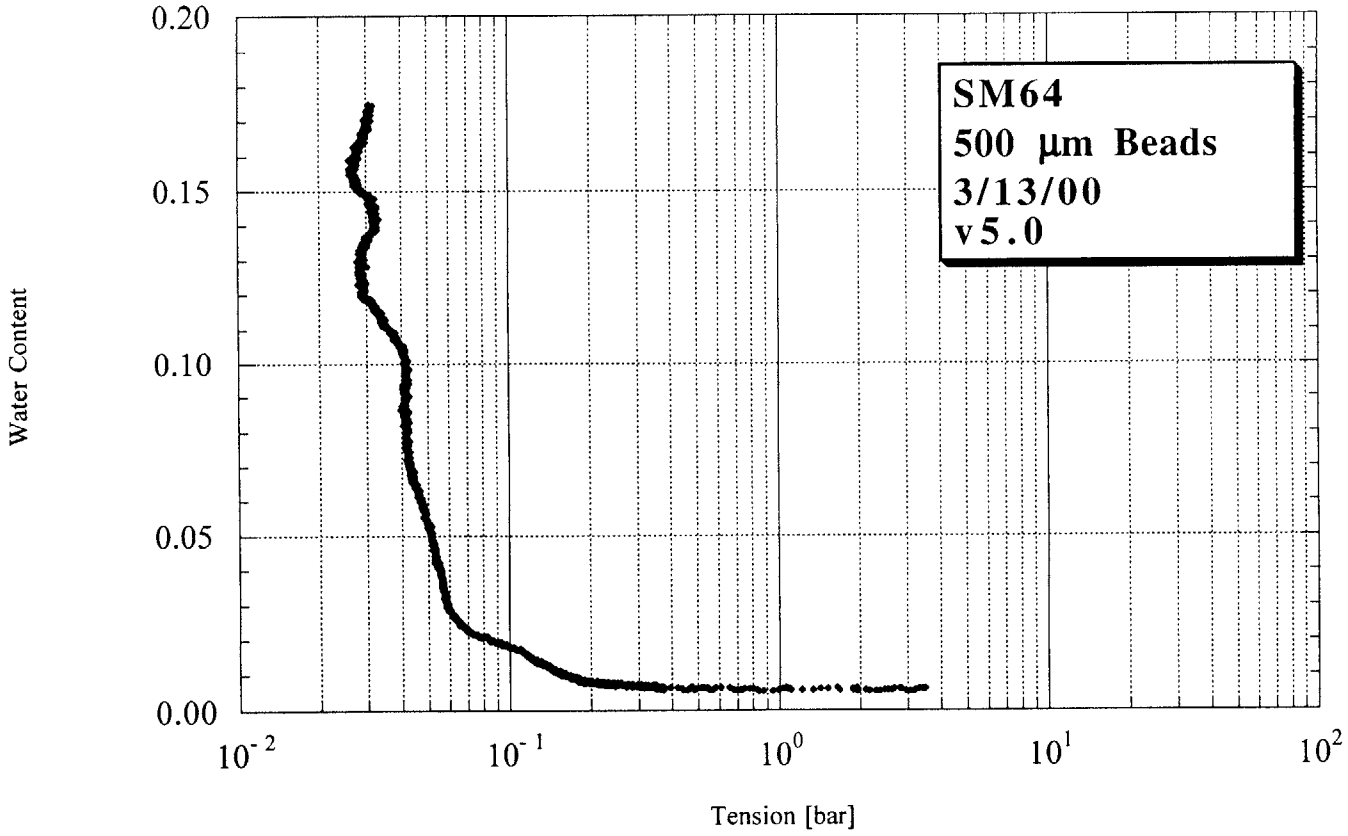

Figure D-34. SM64 testing results.

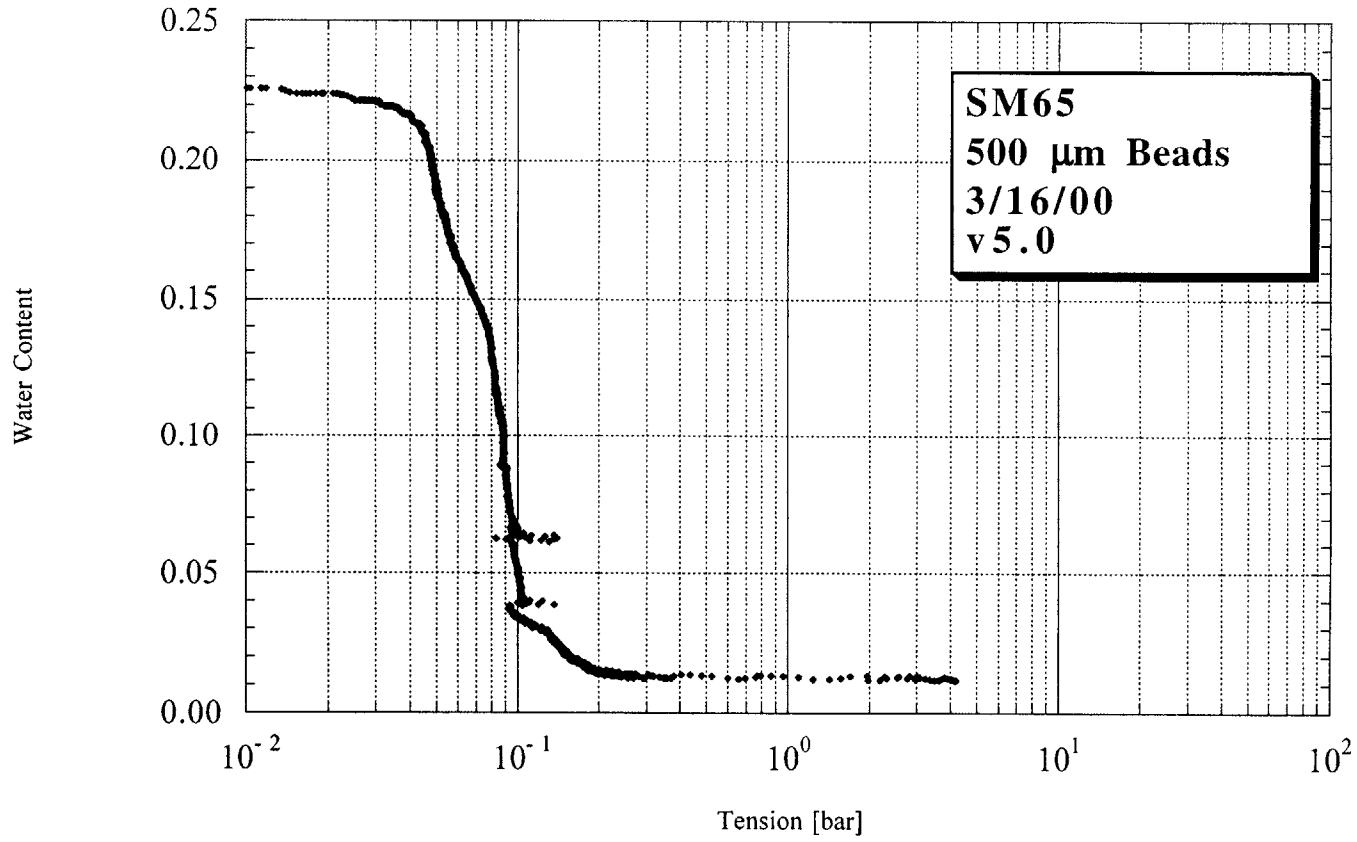

Figure D-35. SM65 testing results.

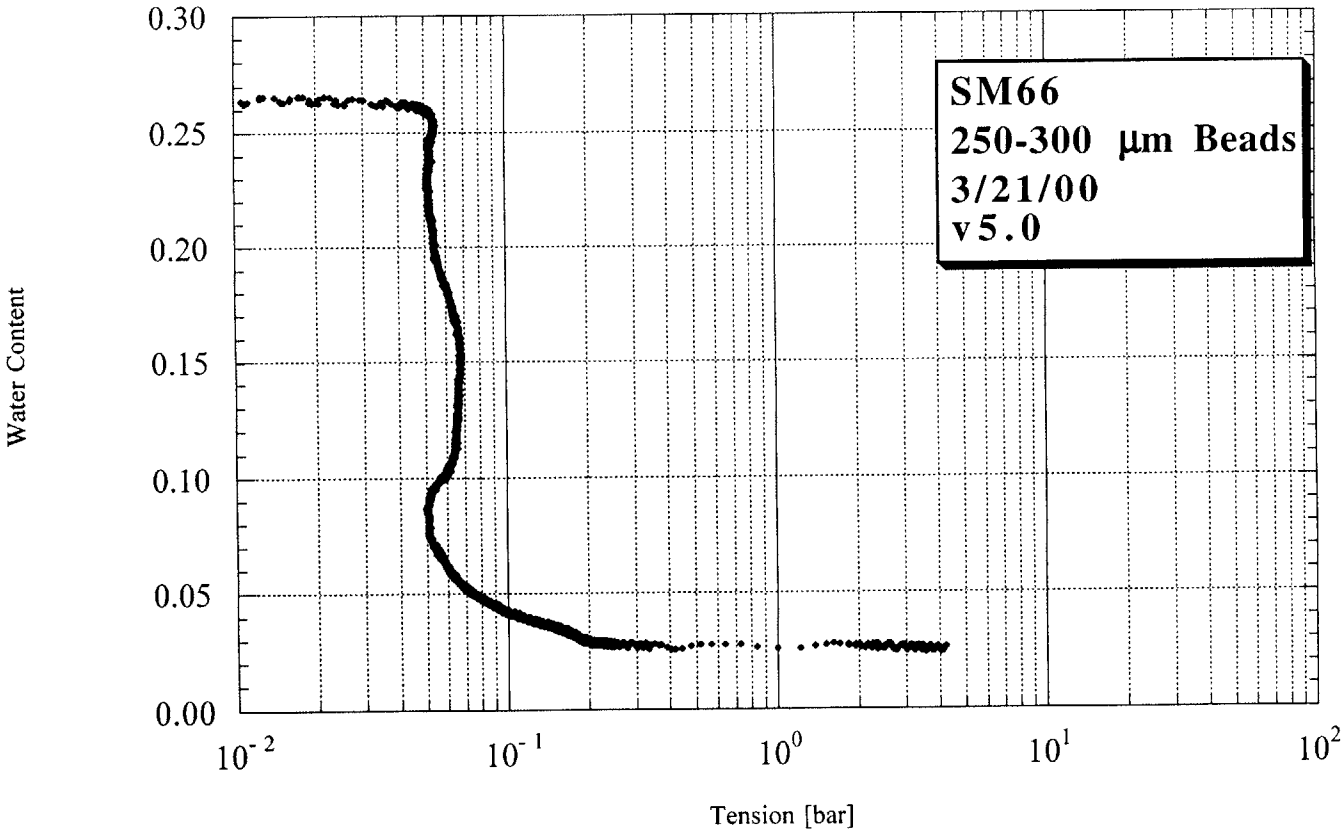

Figure D-36. SM66 testing results.

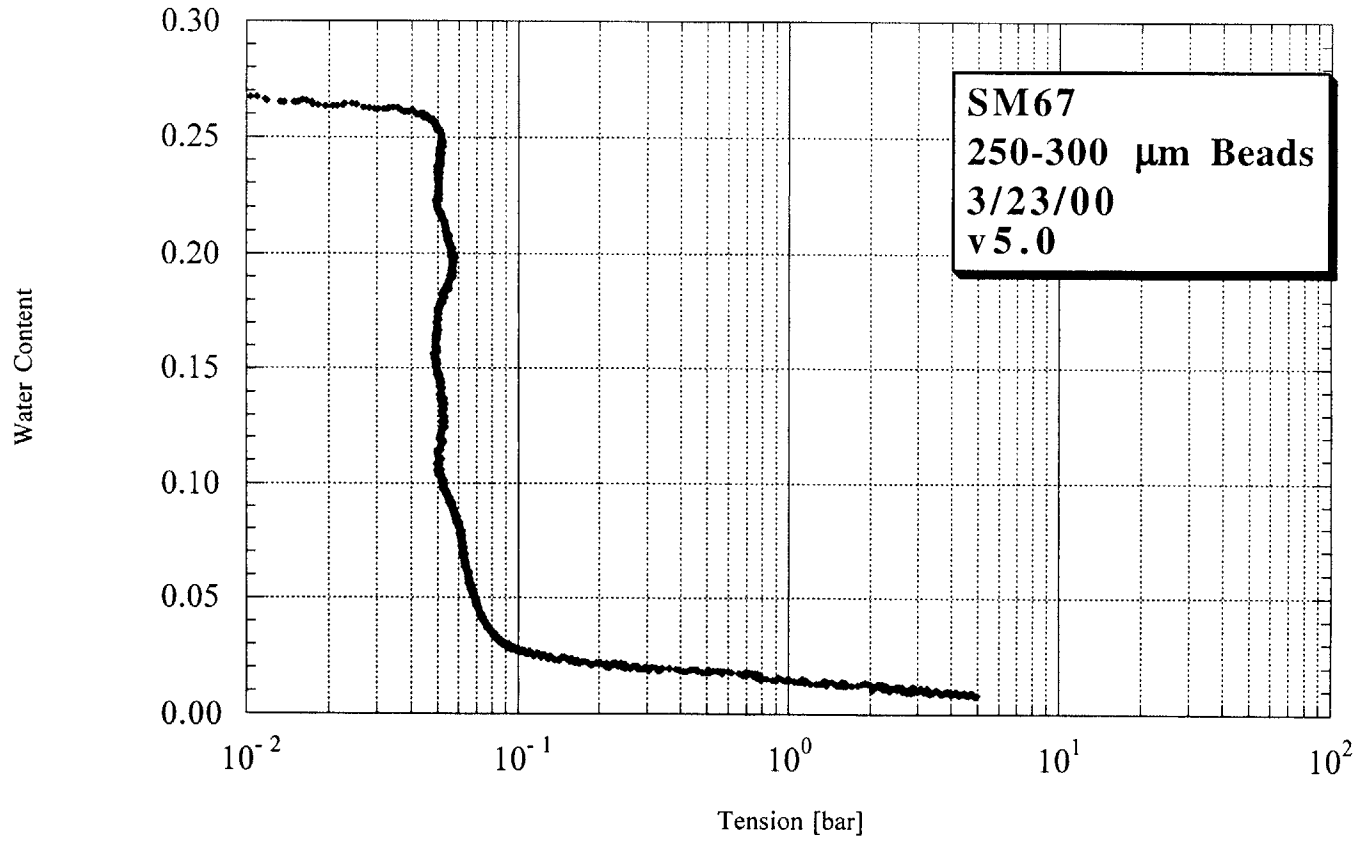

Figure D-37. SM67 testing results.

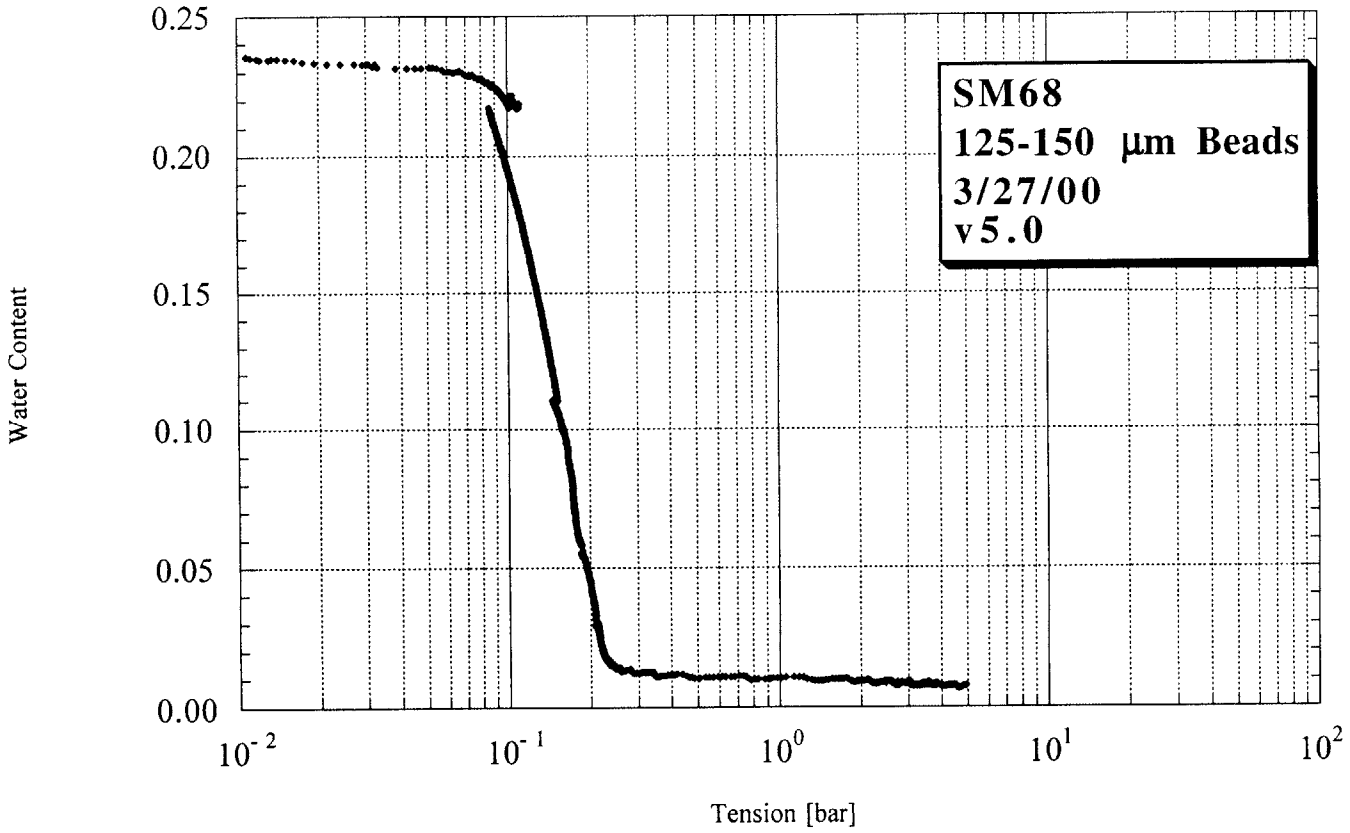

Figure D-38. SM68 testing results.

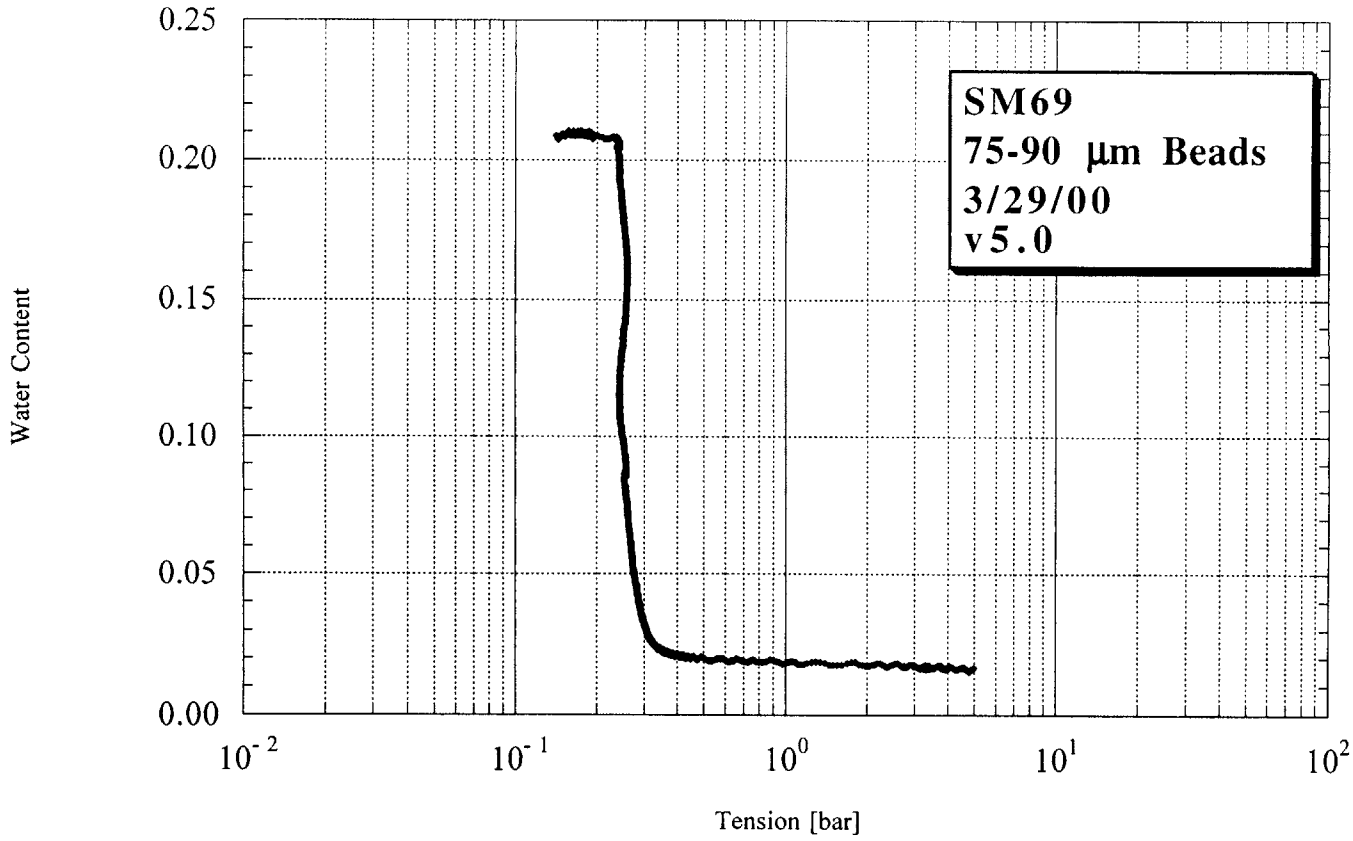

Figure D-39. SM69 testing results.

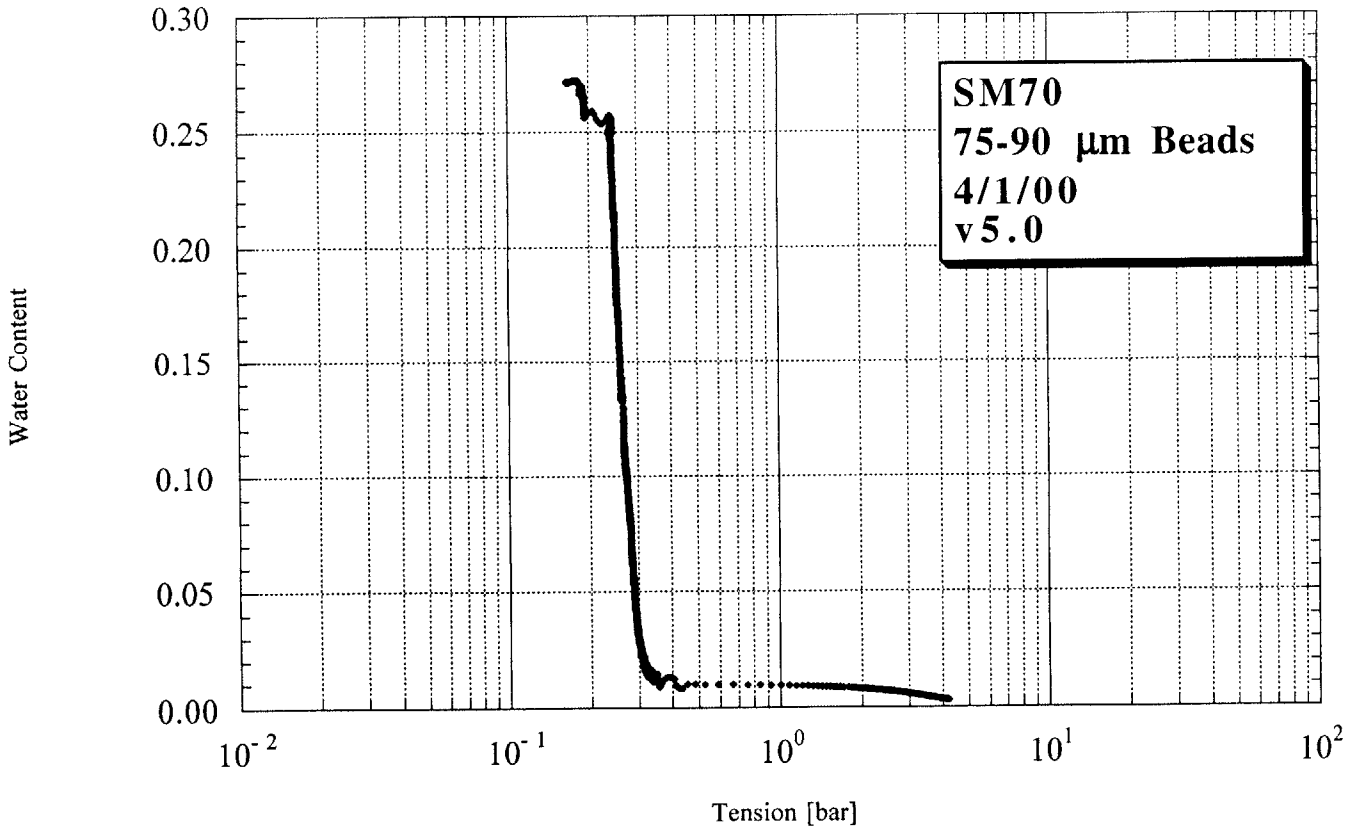

Figure D-40. SM70 testing results.

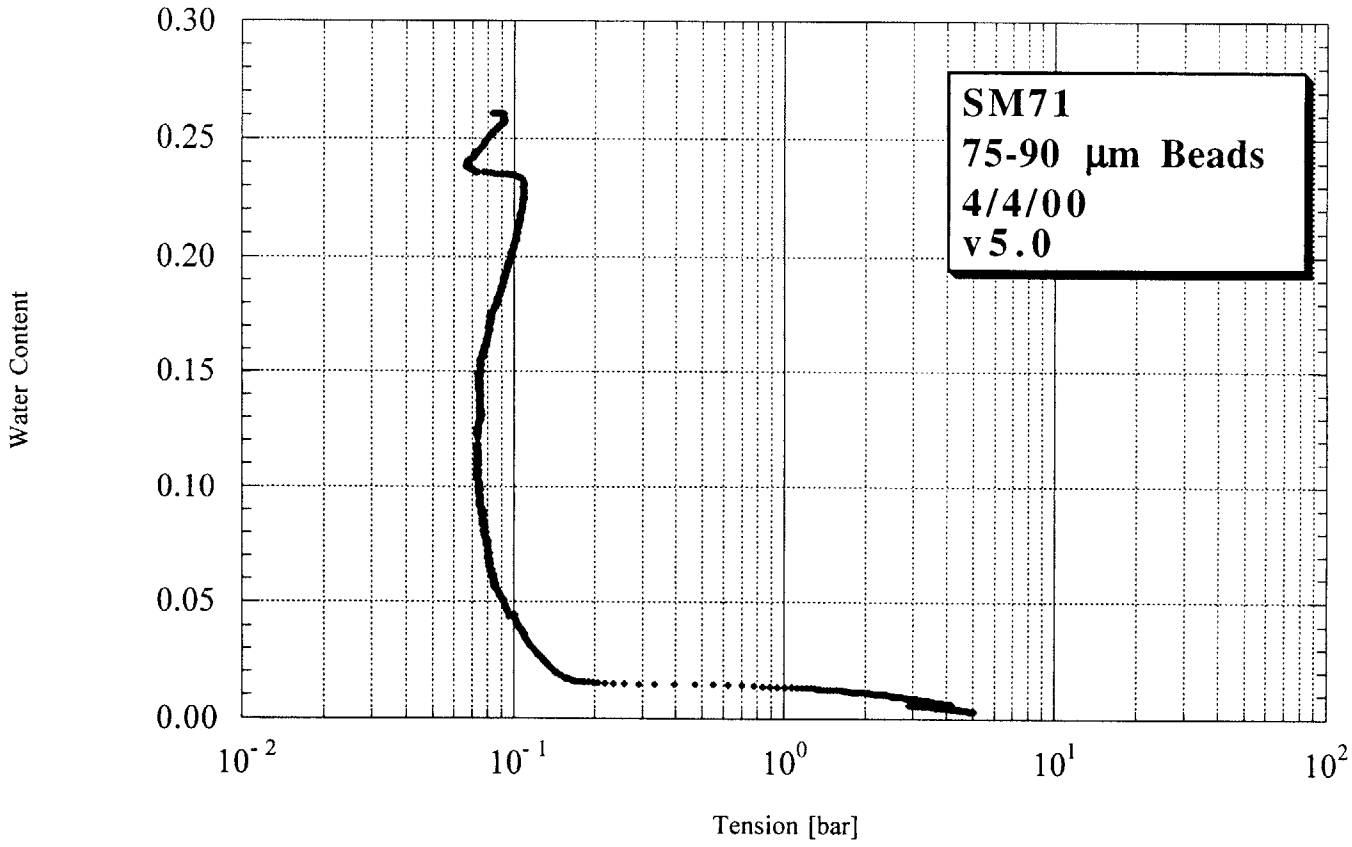

Figure D-41. SM71 testing results.

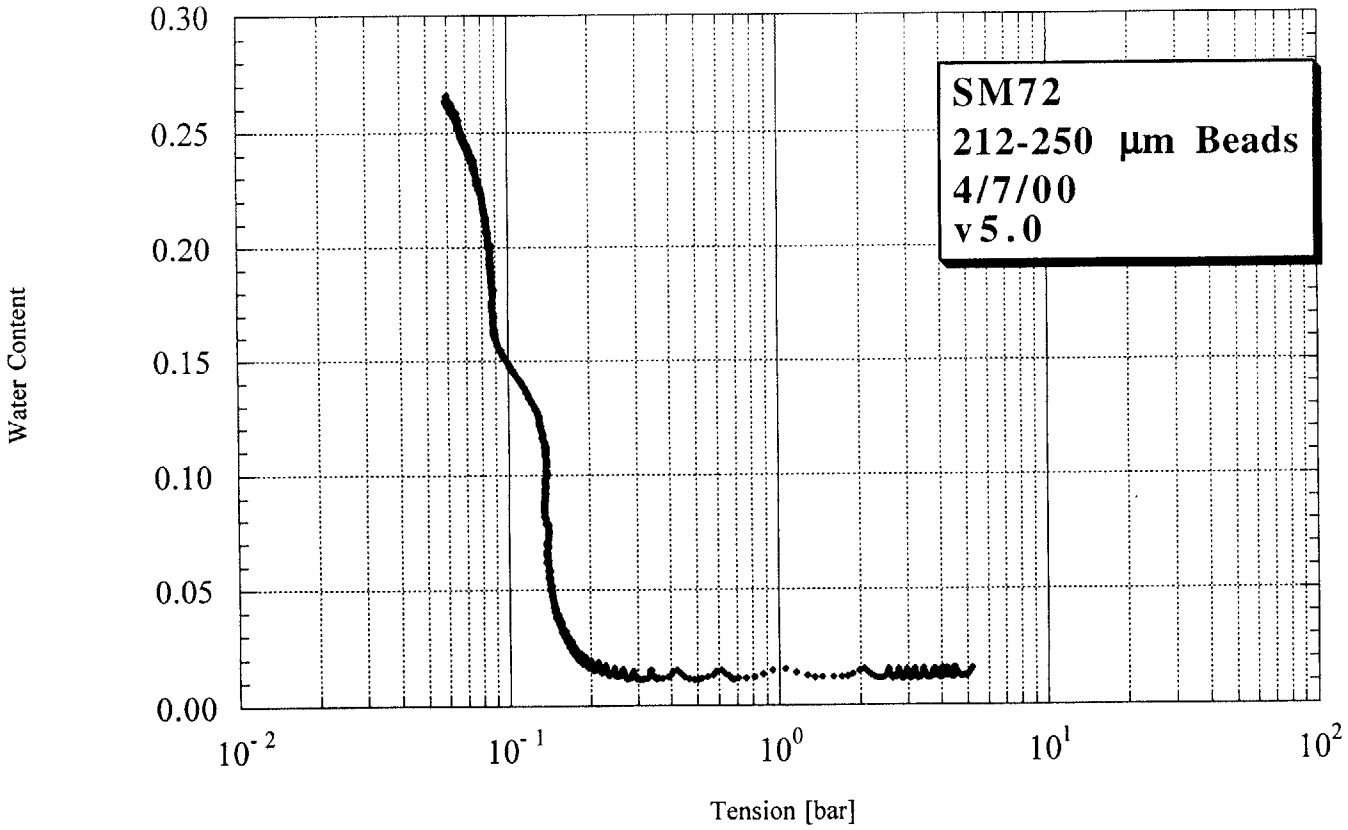

Figure D-42. SM72 testing results.

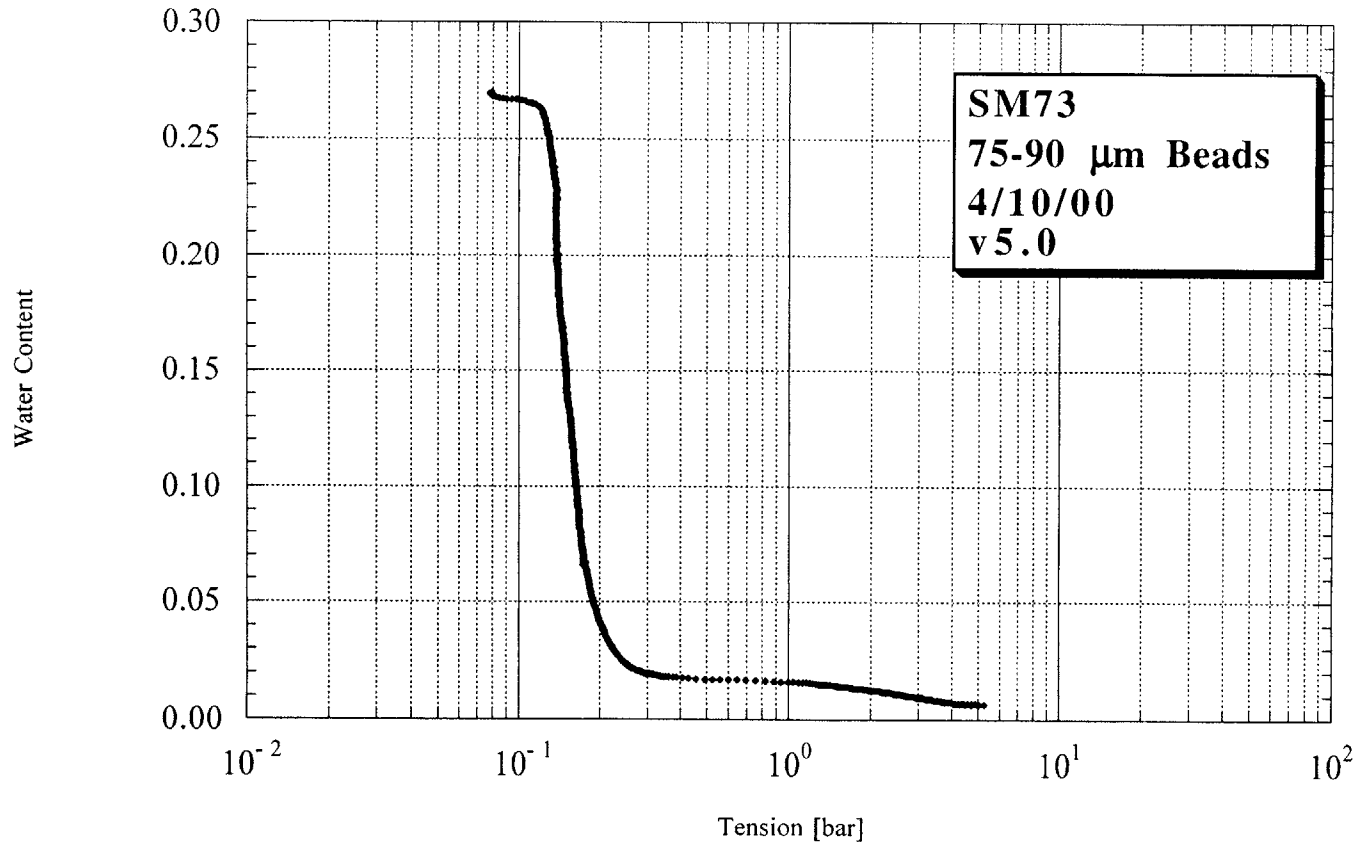

Figure D-43. SM73 testing results.

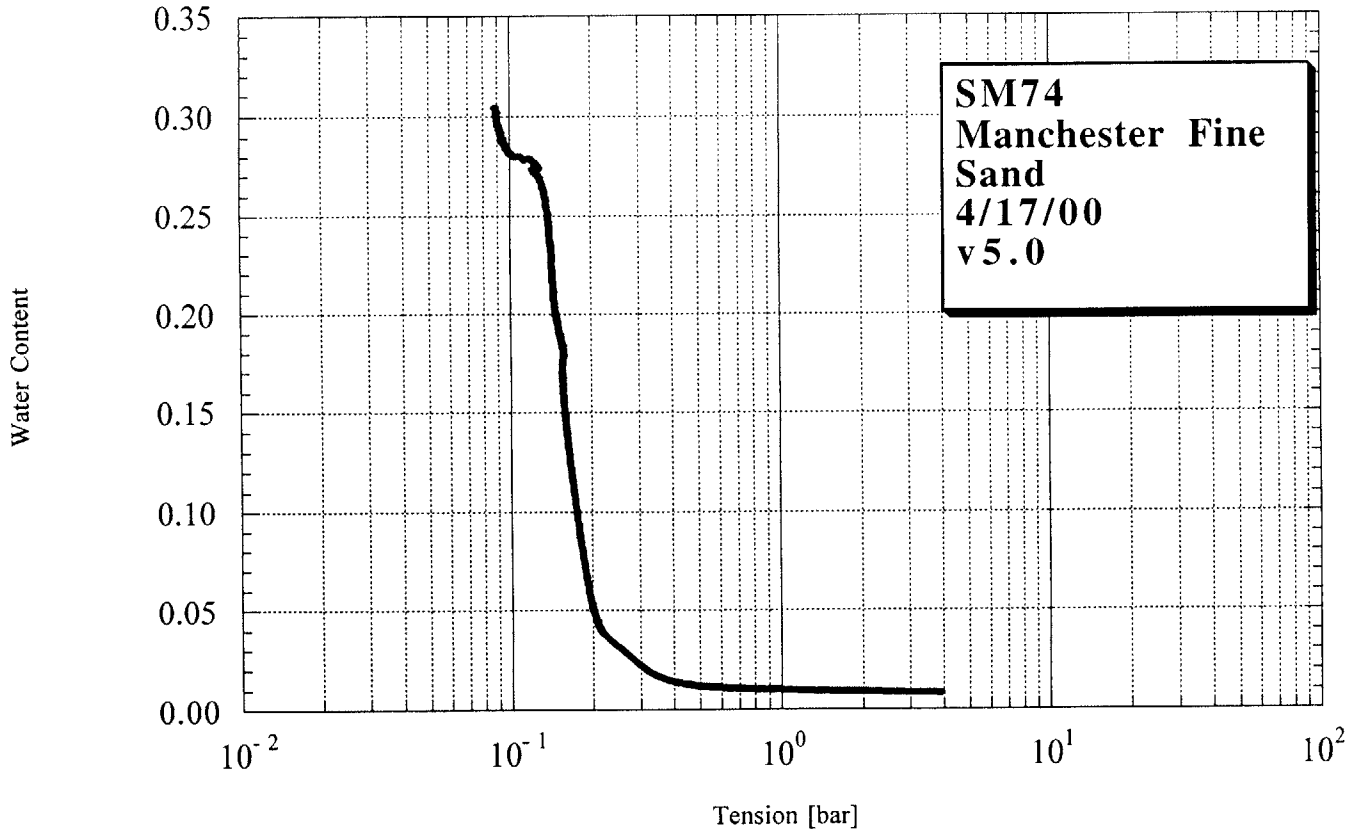

Figure D-44. SM74 testing results.

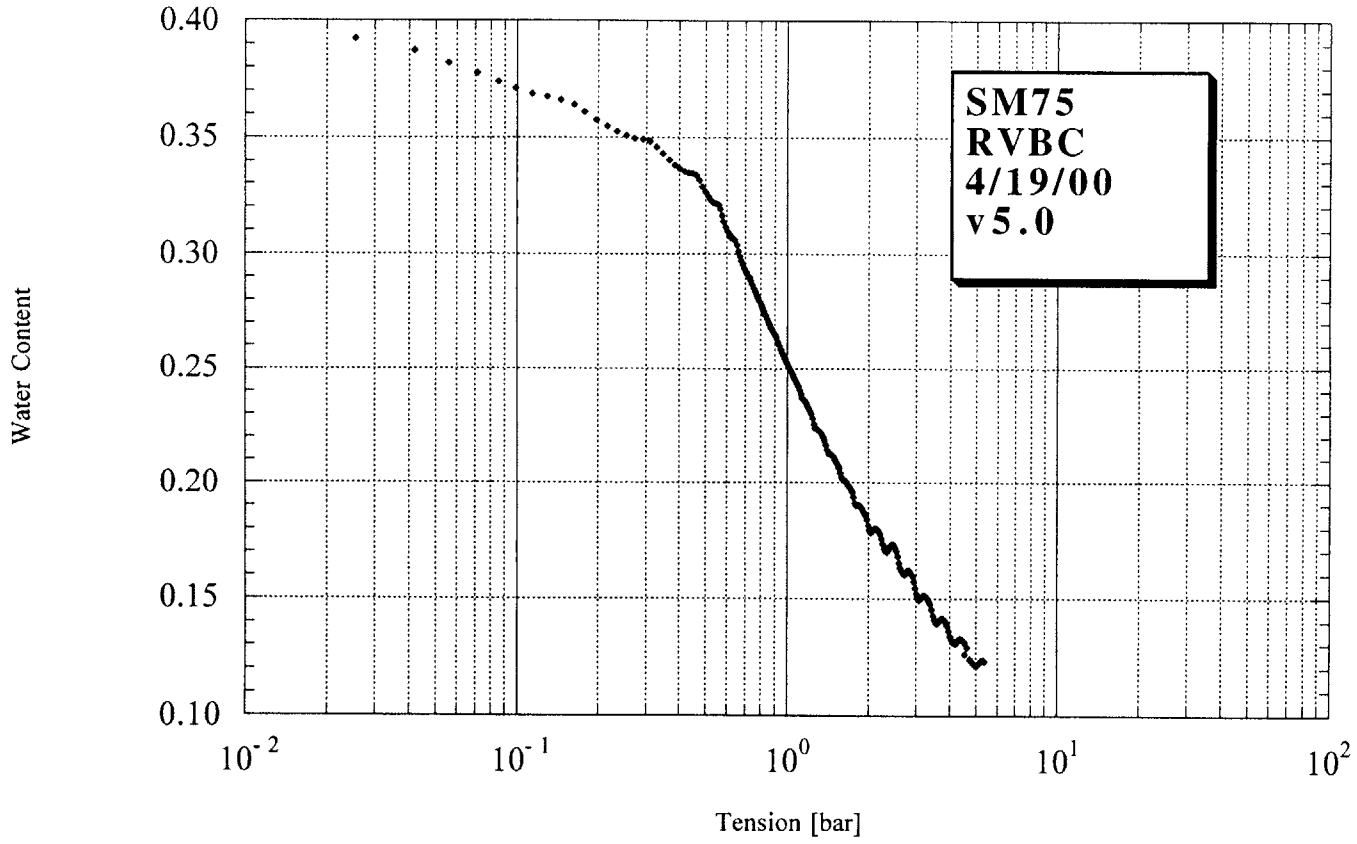

Figure D-45. SM75 testing results.

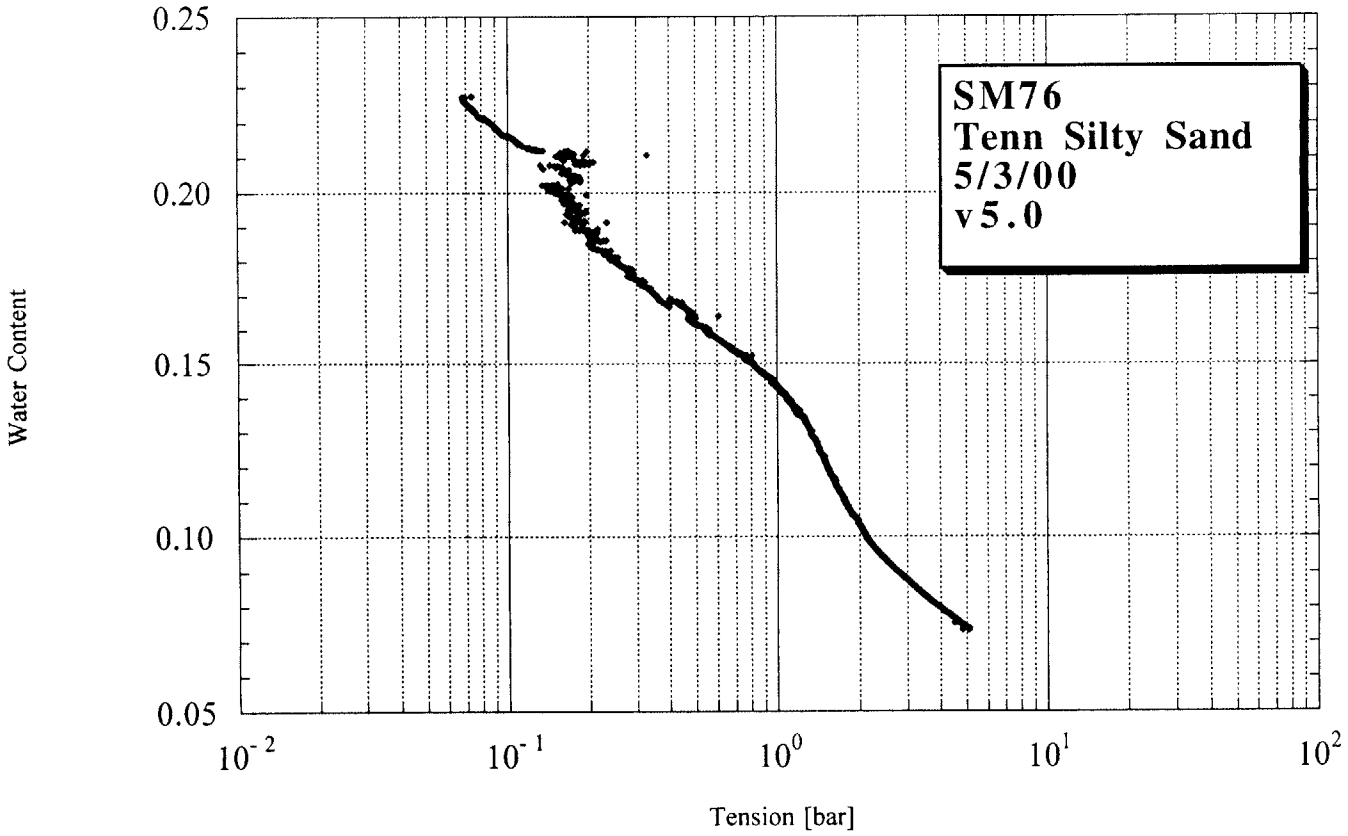

Figure D-46. SM76 testing results.

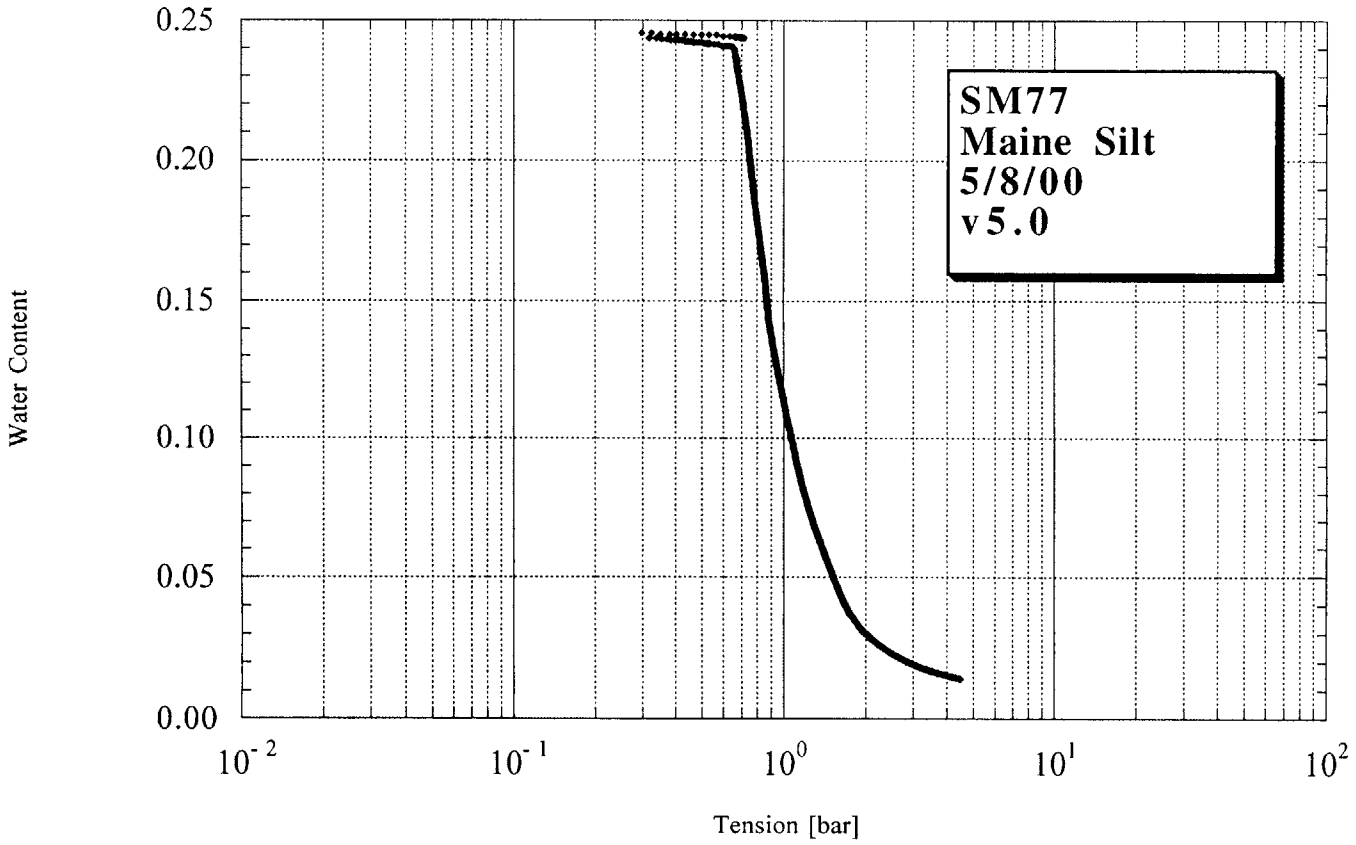

Figure D-47. SM77 testing results.

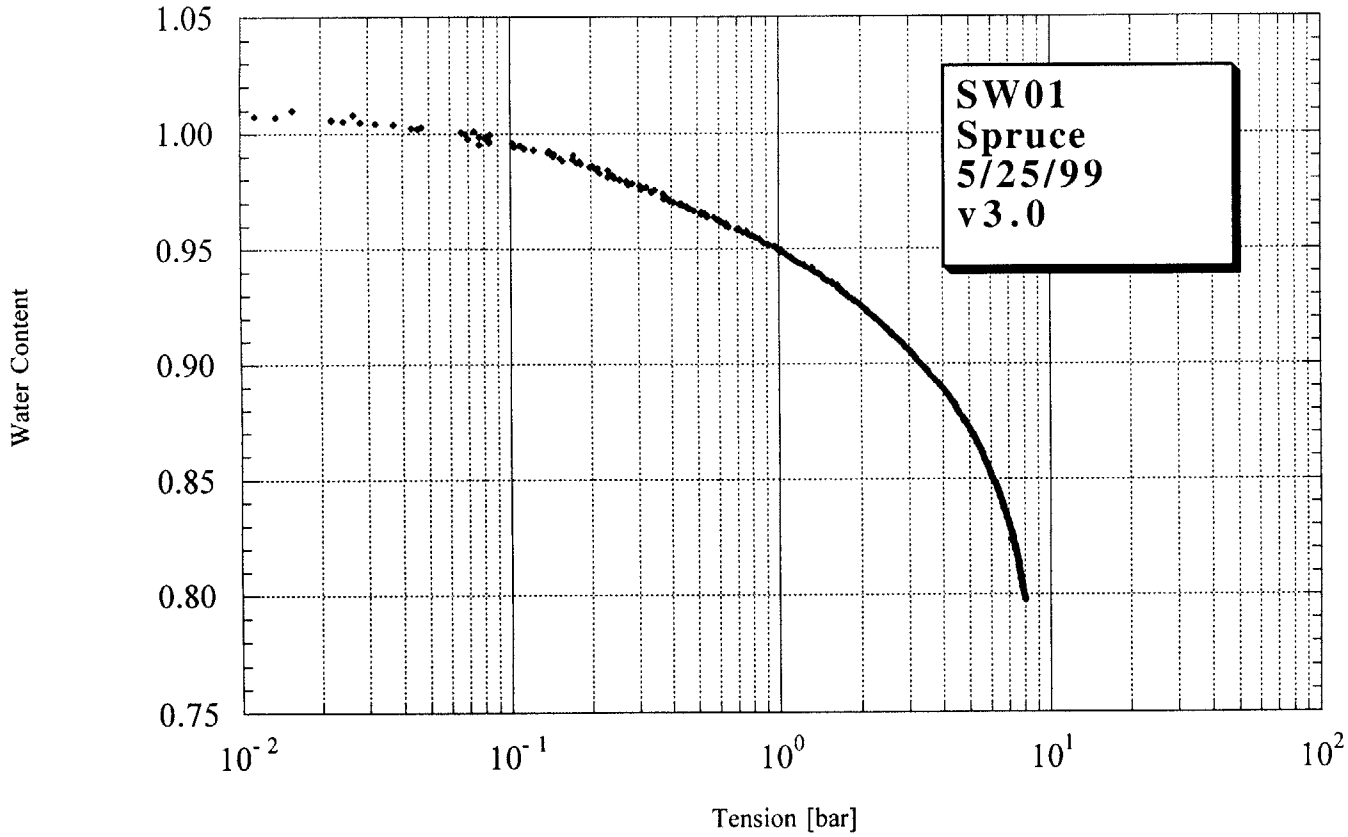

Figure D-48. SW01 testing results.

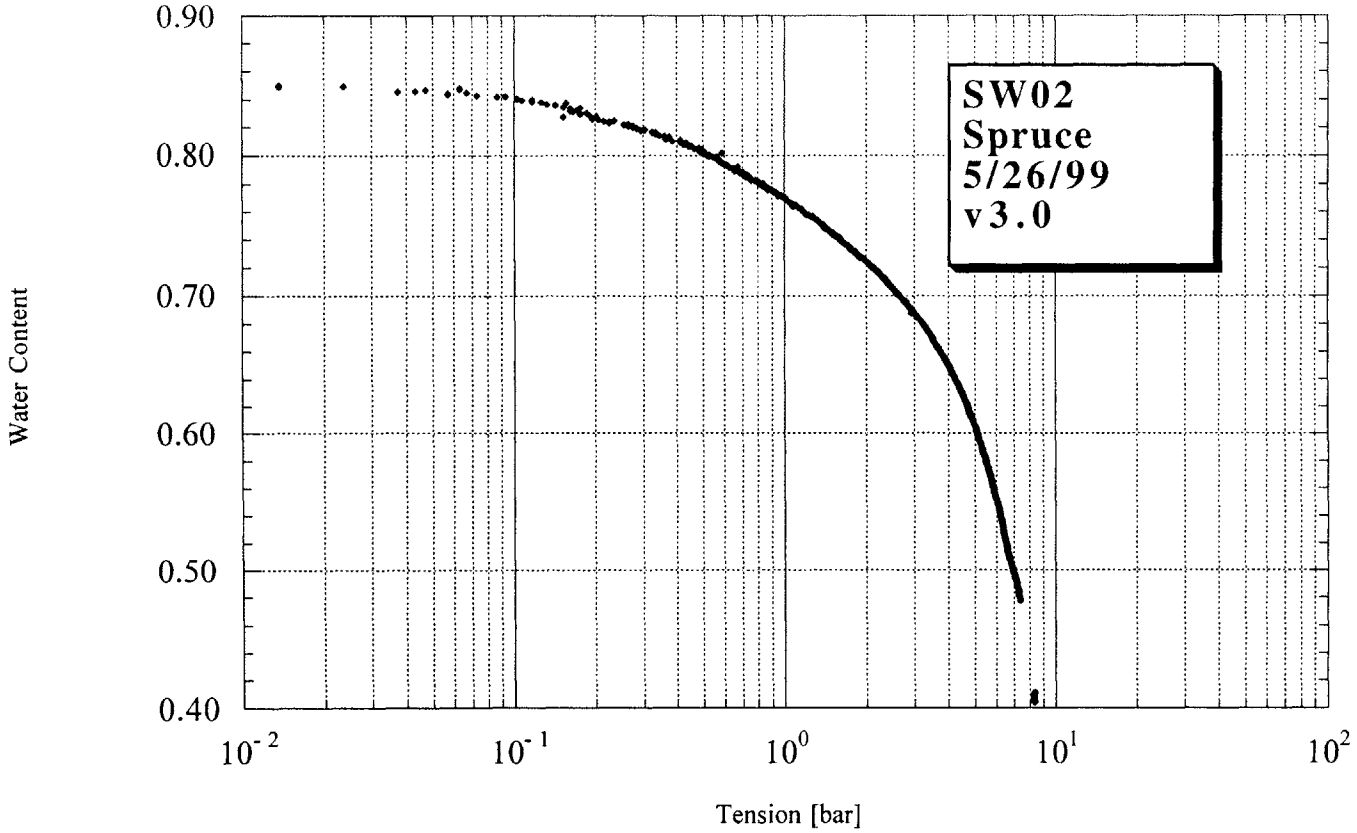

Figure D-49. SW02 testing results.